

EXPERIMENTAL STUDY ON A HEAVY FILM COOLED NOZZLE GUIDE VANE WITH CONTOURED PLATFORMS

THÈSE N° 2602 (2002)

PRÉSENTÉE À LA FACULTÉ STI SECTION DE GÉNIE MÉCANIQUE

ÉCOLE POLYTECHNIQUE FÉDÉRALE DE LAUSANNE

POUR L'OBTENTION DU GRADE DE DOCTEUR ÈS SCIENCES TECHNIQUES

PAR

Gregory VOGEL

**Ingénieur mécanicien diplômé EPF
et de nationalité suisse**

acceptée sur proposition du jury:

**Prof. Dr J. Giovanola, Président
Prof. Dr A. Bölcs, Directeur de Thèse
Dr M. Gritsch, Rapporteur
Prof. Dr J. Thome, Rapporteur
Prof. Dr B. Weigand, Rapporteur**

Lausanne, EPFL

2002

Quote:

"As far as the laws of mathematics refer to reality, they are not certain, and as far as they are certain, they do not refer to reality. "

Albert Einstein, 20th-century Swiss mathematician, physicist and public philosopher

Translated in French as follow:

"La théorie c'est quand on sait tout et que rien ne fonctionne. La pratique, c'est quand tout fonctionne et que personne ne sait pourquoi. "

Acknowledgements:

The present thesis work has been conducted at the Laboratoire de Thermique Appliquée et de Turbomachines (LTT) of the Ecole Polytechnique Fédérale de Lausanne (EPFL) during my employment as a research engineer. The research project has been subsidized by Alstom Power Switzerland and the Commission pour la Technologie et l'Innovation (CTI) of Switzerland.

First, I would like to thank Prof. Albin Bölcs who placed trust in me and has given me the opportunity to work at his lab. He followed my work with much interest and gave me encouragement and efficient technical guidance whenever needed. Although less significant, I am glad I was sometimes able to repay the favor somewhat by helping him with his macintosh computer.

I would also like to thank Prof. Bernhard Weigand of the university of Stuttgart, who also followed my work with very much interest and who gave me excellent theoretical and practical support in the domain of film cooling. I have very much respect for and admiration of his tremendous knowledge. From the same university, I would like to thank Prof. Jens von Wolfersdorf who inspired me to develop a new electrical heater-foil technique and who helped me with the numerical simulations. Regarding the measurement technique, I would like first to thank Serge Scholer with whom I started using heater foils in the frame of his diploma work. I would also like to particularly thank Arnulf Graf who did his training at the LTT. His availability and his aptitude to juggle mathematical equations helped me a lot in the developments of the novel measurement technique.

Of course, I wouldn't have been able to do my experimental work without my former colleagues, Dr. Alexander Hoffs, Dr. Uwe Drost and Dr. Hans Reiss who helped me with the operation of the linear test facility and the application of the transient liquid crystal technique. Huge thanks also to Carmine Capone who helped me reduce the important amount of data collected in the frame of this work. Thanks also to Guillaume Wagner with whom I did the PSP measurement and who is going to continue the work already developed in this area. I wish him good luck for his thesis. Many thanks also to all my other colleagues who provided a good atmosphere in the lab and with whom I had fruitful discussions. Thanks a lot also to the research technicians for their efficient work and availability. And last but not least, thanks a lot to my mom, my sister and of course to my "baby" Kini :-P for their patience and support.

Abstract

Nowadays, efficiency improvement of the modern gas turbines is usually achieved by increasing the pressure ratio which leads to an increase of the gas temperature in the combustion chamber. As a consequence, the temperature conditions imposed on the first stages of the turbine are well beyond the maximum allowable material of the engine. Therefore, it is necessary to effectively cool on these parts.

Some of the highest thermal loading is applied to the nozzle guide vane located just behind the combustion chamber. Its function is to efficiently direct the hot and high-pressure gas on the rotor blades of the turbine in order to extract maximum work. From the aerodynamic side, the loss level generated during the hot gas deviation defines the nozzle guide vane efficiency. From the thermodynamic side, an efficient nozzle guide vane is characterized by its cooling protection against the hot gas coming out of the combustion chamber. For this reason, the vane is internally cooled by coolant fluid circulating in channels; but it is also externally cooled by injection of coolant fluid on the surface. This process is usually called "film-cooling". If it is well designed, the film efficiently protects the vane airfoil and platforms of the engine; but if badly designed (unfavorable holes injections positions or inadequate blowing ratios), then the overall performance of the engine is reduced.

Recently, studies have shown a decrease in the aerodynamic losses for nozzle guide vanes with contoured platforms. Moreover, it has also been noticed that temperature profiles at the exit of the combustion chamber are more and more flattened and consequently require a better cooling of the platforms. The problem is to efficiently film-cool a nozzle guide vane airfoil and its contoured platforms. A numerical approach of this problem is yet not possible as the numerical codes are not accurate enough to take into account all the physics governing such situations. Therefore, an experimental approach is required.

So far, many film cooling studies have been performed but on relatively simple geometries (flat plates, cylinders etc). The innovative part of this present work was to study film cooling on a complex nozzle guide vane geometry equipped with contoured platforms. For this, as well the aerodynamic side and the thermodynamic side related to film cooling were considered. The experiments were divided into two parts. The first part was dedicated to the study of the vane airfoil. The second part was dedicated to the film-cooling study on the contoured platforms.

In both cases, heat transfer coefficients and film-cooling effectiveness were determined by transient measurement techniques using liquid crystals. For the vane airfoil, a preconditioning system followed by a rapid insertion was used. This installation was already used during previous projects, but in the frame of this research work, the liquid crystal technique was improved. For this, a new signal analysis and image processing system was developed.

For the measurements on the platforms, a new measurement technique based on the use of a thin electrical heater-foil was developed. The innovation of this technique comes from the fact that it can be applied on complex geometries for which inhomogeneous heat fluxes are produced (curved surfaces, introduction of cooling holes). This novel measurement technique was first tested and validated on a simple geometry consisting of a film-cooled flat plate. The same technique was then applied to the film-cooled contoured platform and allowed obtaining interesting results of heat transfer coefficient and film-cooling effectiveness distributions. The latter result was also compared to values obtained from another innovative measurement technique based on Pressure Sensitive Paint with Nitrogen injection.

The results obtained in the frame of this experimental work dedicated to film cooling applied on a complex geometry were obtained thanks to the development of novel measurement techniques. These measurement techniques provide the opportunity to perform systematic tests in order to gain further insight into the physics of the film cooling process on complex geometries such as contoured platforms.

Résumé

De nos jours, l'amélioration du rendement des turbomachines modernes, notamment des turbines à gaz, s'obtient principalement en augmentant leur niveau de températures dans la chambre de combustion. Les conditions ainsi imposées aux premiers étages de la turbine sont bien au-dessus des températures maximums admissibles par les matériaux de la machine, d'où la nécessité d'appliquer un refroidissement efficace sur les parties fortement sollicitées en températures.

Une des parties les plus sollicitée est certainement l'aubage directeur juste en sortie de la chambre de combustion. Son rôle est d'amener les gaz chauds et à haute pression sur les aubes du rotor de la turbine de manière efficace afin d'en extraire le maximum de travail. L'efficacité de l'aubage directeur, au niveau aérodynamique est essentiellement défini par le niveau de perte de charge généré lors du passage des gaz chauds. Au niveau thermique, une bonne aube directrice est caractérisée par un refroidissement efficace la protégeant des gaz extrêmement chauds sortant de la chambre de combustion. Pour cette raison, l'aube est refroidie de manière interne par un fluide de refroidissement circulant dans des canaux, mais aussi de manière externe, par l'injection d'un fluide de refroidissement à la surface et communément appelé « refroidissement par film ». Si ce dernier est bien conçu, le film protège de manière très efficace les aubes et les parois de la machine. Par contre si il est mal conçu, telle que : mauvaise position géométrique des trous d'injection, taux d'injection inadéquats, il se produit alors une baisse des performances de la machine.

Récemment, des études ont montré une baisse des pertes aérodynamiques des aubages directeurs possédant des parois formées. De plus, il a aussi été remarqué que les profils de températures en sortie des chambres de combustions sont de plus en plus homogènes, nécessitant par conséquent un meilleur refroidissement des parois. Se pose alors le problème d'effectuer correctement un important refroidissement par film sur l'aubage directeur et sur ses parois formées. Une approche numérique de ce problème n'est pour l'instant pas possible, les codes de calculs n'étant pas encore assez performants pour tenir compte des phénomènes physique présent dans une telle situation. Par conséquent une approche expérimentale s'impose.

Jusqu'à présent, de nombreuses études ont été effectuées sur le refroidissement par film mais sur des géométries relativement simples telles que plaque plane, cylindres etc. L'originalité du présent travail fut d'étudier une configuration d'injection

sophistiquée sur une géométrie d'aubage directeur muni de parois formées. Pour cela, aussi bien l'aspect aérodynamique que thermique associé au refroidissement par film fut considéré. Les essais furent partagés en deux parties, la première fut dédiée à l'étude de l'aubage directeur même, la deuxième à l'étude du refroidissement par film sur les parois formées.

Dans les deux cas, les mesures de transfert de chaleur et d'efficacité de refroidissement par film furent effectuées à l'aide d'une technique de mesure transitoire utilisant des cristaux liquides. Pour l'aubage directeur, un système de pré-conditionnement suivi d'une insertion rapide fut utilisé. Ce dernier fut déjà appliqué lors d'autres projets, mais dans le cadre de ce travail de recherche, la technique des cristaux liquides fut améliorée. Pour cela, un nouveau système de traitement d'image et d'analyse du signal furent conçus.

Pour les mesures sur les parois, une nouvelle technique de mesure transitoire basée sur l'utilisation d'une fine feuille électrique chauffante fut développée. L'originalité de cette nouvelle technique réside dans son application à des géométries complexes pour lesquelles un flux de chaleur non homogène est produit (parois courbes, présence de trous de refroidissement). Cette nouvelle technique de mesure fut tout d'abord testée et validée sur une géométrie simple, consistant en une plaque plane refroidie par film. Cette même technique fut ensuite appliquée aux parois formées et refroidies par film et permit d'obtenir des résultats très intéressants de coefficient de transfert de chaleur (h) et d'efficacité de refroidissement par film (η). Ce dernier résultat fut aussi comparé à des valeurs obtenues à l'aide d'une technique de mesure tout aussi innovante basée sur une peinture PSP avec injection d'azote.

Les résultats de ce travail expérimental sur le refroidissement par film et appliqué sur une géométrie complexe, ont été obtenus grâce au développement de nouvelles techniques de mesures. Ces dernières permettent maintenant d'effectuer des essais systématiques afin de mieux comprendre l'aspect physique du procédé de refroidissement par film sur des configurations complexes telles que des parois formées.

Nomenclature

| | | |
|--------------------------------|------------------------|---|
| A | [m ²] | surface area |
| Bi | [-] | Biot number $h\delta/k$ |
| BR | [-] | local blowing ratio $u_c\rho_c/u_g\rho_g$ |
| C _d | [-] | discharge coefficient |
| c | [J/kgK] | specific heat |
| c _p | [J/kgK] | specific heat at constant pressure |
| c _v | [J/kgK] | specific heat at constant volume |
| DR | [-] | coolant-to-gas density ratio ρ_c/ρ_g |
| D | [mm] | hole diameter |
| G | [-] | heat flux gain |
| h | [W/(m ² K)] | local heat transfer coefficient |
| I | [-] | light intensity |
| k | [W/mK] | thermal conductivity |
| L | [mm] | true airfoil chord |
| L _D | [mm] | hole length |
| L _{AR} | [mm] | diffuser length for shaped holes |
| Ma | [-] | Mach number $u/(\kappa RT)^{0.5}$ |
| m | [kg/s] | mass flow rate |
| m _c /m _g | [%] | specific coolant mass flow rate |
| Nu _s | [-] | Nusselt number hs/k |
| P | [m] | vane pitch |
| Pr | [-] | Prandtl number $(\rho v c_p)/k$ |
| p | [mbar] | pressure |
| q | [W/m ²] | specific heat flux |
| R | [J/kg/K] | ideal gas constant |
| R3z | [μm] | 3 points peak roughness profile DIN ISO 1302 |
| Ra | [μm] | mean roughness profile deviation DIN ISO 1302 |

| | | |
|-------------|-------|------------------------------|
| Re_L | [-] | Reynolds number $(uL)/\nu$ |
| r_0 | [-] | recovery factor |
| s | [m] | surface coordinates distance |
| T | [K] | temperature |
| Tu | [%] | turbulence intensity |
| t | [s] | time |
| u | [m/s] | velocity |
| v | [m/s] | velocity |
| x | [m] | axial coordinate |
| \tilde{x} | [-] | dimensionless distance |
| y | [m] | pitch-wise coordinate |
| z | [m] | span-wise coordinate |

Greek Symbols

| | | |
|-----------|----------------------|--|
| α | [m ² /s] | thermal diffusivity $k/(\rho c_p)$ |
| β | [-] | eigenvalues |
| δ | [m] | wall thickness |
| Φ | [-] | overall effectiveness |
| φ | [°] | stream-wise inclination angle |
| γ | [°] | compound angle |
| η | [-] | adiabatic film-cooling effectiveness $(T_{aw}-T_{rg})/(T_{tc}-T_{tg})$ |
| κ | [-] | isentropic coefficient c_p/c_v |
| μ | [Ns/m ²] | dynamic viscosity |
| ν | [m ² /s] | kinematic viscosity |
| Θ | [-] | dimensionless temperature |
| ρ | [kg/m ³] | density |
| τ | [-] | dimensionless time |
| ζ | [-] | loss coefficient |

x

Subscripts

| | |
|----------|--------------------------------|
| 0 | reference, initial |
| 1 | inlet |
| 2 | exit |
| aw | adiabatic wall |
| c | coolant gas |
| f | with film cooling |
| g | main stream gas |
| i | injection |
| is | isentropic |
| L | based on chord length |
| LC | liquid crystal |
| max | maximum value |
| r | recovery |
| S | steady part solution |
| s | static conditions, surface |
| T | transient part solution |
| t | total conditions |
| th | theoretical |
| wall | for $x=0$ (upper wall surface) |
| ∞ | approach conditions |

Superscripts

| | |
|---|---------------------|
| i | index of experiment |
|---|---------------------|

Abbreviations

| | |
|---------|--|
| AVI | Audio Video Interleave |
| BL | Boundary Layer |
| CCD | Charge-Coupled Devices |
| DV | Digital Video |
| HSI | Hue Saturation Intensity |
| IEEE | Institute of Electrical and Electronics Engineers |
| LE | Leading Edge |
| LED | Light Emitting Diode |
| LTT | Laboratoire de Thermique Appliquée et de Turbomachines |
| PAL | Phase Alternating Line |
| PS | Pressure Side |
| PSP | Pressure Sensitive Paint |
| RGB | Red Green Blue |
| SLPM | Standard Liter Per Minute |
| SS | Suction Side |
| S-Video | Super-Video |
| TE | Trailing Edge |
| TIFF | Tagged Image File Format |
| TIT | Turbine Inlet Temperature |
| VHS | Video Home System |

Table of Contents

| | | |
|-------|---|----|
| 1 | Introduction | 1 |
| 1.1 | Gas Turbines | 1 |
| 1.2 | Nozzle Guide Vane | 3 |
| 1.3 | Film Cooling | 4 |
| 1.4 | State of the Art | 5 |
| 1.5 | Objective of this Work | 6 |
| 2 | Test Configuration..... | 9 |
| 2.1 | Geometry Configuration | 9 |
| 2.1.1 | 3D Model Extraction | 9 |
| 2.1.2 | Linear Cascade Test Facility | 11 |
| 2.2 | Experimental Conditions | 17 |
| 2.2.1 | Vane Configuration..... | 17 |
| 2.2.2 | Platform Configuration..... | 23 |
| 2.3 | Conclusion of Test Configurations | 24 |
| 3 | Transient Measurement Technique | 25 |
| 3.1 | Basic Principle | 25 |
| 3.2 | Hardware and Video Signal..... | 25 |
| 3.3 | Digital Image Processing System (DIPS)..... | 28 |
| 3.4 | Transient Time Experiment | 33 |
| 3.5 | Conclusion of Transient Measurement Technique | 37 |
| 4 | Vane Experiments..... | 39 |
| 4.1 | Aerodynamic Measurements on the Vane | 39 |
| 4.1.1 | Flow Periodicity | 39 |
| 4.1.2 | Mach Number Distribution | 42 |
| 4.1.3 | Loss Measurements | 46 |
| 4.1.4 | Conclusion of Aerodynamic Measurements on the Vane..... | 51 |
| 4.2 | Baseline Heat Transfer Measurements on the Vane | 52 |

| | | |
|-------|---|-----|
| 4.2.1 | Baseline Experiment Setup for the Vane..... | 52 |
| 4.2.2 | Baseline Vane Heat Transfer Measurement Procedure..... | 55 |
| 4.2.3 | Baseline Results..... | 57 |
| 4.2.4 | Comparison with Correlations and Calculations..... | 61 |
| 4.2.5 | Conclusion of Baseline Heat Transfer Measurements on the Vane..... | 64 |
| 4.3 | Film-Cooled Heat Transfer Measurements on the Vane..... | 65 |
| 4.3.1 | Film-Cooled Experiment Set-Up for the Vane..... | 65 |
| 4.3.2 | Film-Cooled Vane Heat Transfer Measurement Procedure..... | 68 |
| 4.3.3 | Film-Cooled Results..... | 72 |
| 4.3.4 | Conclusion of the Film-Cooled Vane..... | 92 |
| 5 | Transient Measurement Technique with Heater Foil..... | 93 |
| 5.1 | Introduction to Heater Foil Techniques..... | 93 |
| 5.2 | Basic Principle of Film-Cooled Experiments with Heater Foils..... | 94 |
| 5.3 | Heater-Foil Experiment Set up for a Film-Cooled Flat Plate..... | 95 |
| 5.4 | Film-Cooled Flat Plate Results..... | 99 |
| 5.5 | Measurement Error Analysis..... | 104 |
| 5.6 | Conclusion of Transient Measurement Technique with Heater Foil..... | 107 |
| 6 | Platform Experiments..... | 109 |
| 6.1 | Aerodynamic Measurements on the Platform..... | 109 |
| 6.1.1 | Description of Aerodynamic Measurements on the Platform..... | 109 |
| 6.1.2 | Mach Number Distribution on the Casing Platform..... | 110 |
| 6.1.3 | Pressure Sensitive Paint (PSP)..... | 110 |
| 6.2 | Heat Transfer Measurements on the Platform..... | 112 |
| 6.2.1 | Platform Baseline and Film-Cooled Experiments Set-up..... | 112 |
| 6.2.2 | Heater Foil Film-Cooled Measurement Procedure..... | 115 |
| 6.2.3 | Platform Heat Transfer Results..... | 119 |
| 6.2.4 | Measurement Uncertainties..... | 138 |
| 6.3 | Conclusion of the Platform Experiments..... | 140 |

| | | |
|---|------------------|-----|
| 7 | Conclusion | 141 |
| 8 | References..... | 145 |

Appendix

| | |
|---|-----|
| Appendix A : Step Heating, Baseline Case, Finite Model | 151 |
| Appendix B : Step Heating Generated by Rapid Insertion, Baseline Case, Semi-Infinite Model..... | 155 |
| Appendix C : Step Heating Generated by Rapid Insertion, Film-Cooled Case, Semi-Infinite Model..... | 157 |
| Appendix D : Step Heating Generated by Heater Foil, Baseline and Film-Cooled Cases, Semi-Infinite Model | 161 |
| Appendix E : PSP, Iterative Correction on the Surface Temperature Distribution .. | 167 |
| Appendix F : PSP Technique with N ₂ Injection for Film-Cooling Effectiveness Determination..... | 169 |

Table of Figures

| | |
|---|----|
| Figure 1-1: Example of a Modern Industrial Gas Turbine | 1 |
| Figure 1-2: Turbine Inlet Temperature Evolution | 2 |
| Figure 1-3: Film-Cooled Nozzle Guide Vane | 4 |
| Figure 2-1: Geometry Process from 3D to a Linear Cascade | 10 |
| Figure 2-2: Extracted Airfoil and Platforms Vane Geometries | 11 |
| Figure 2-3: Front Disc: Hub Side Test Section..... | 12 |
| Figure 2-4: Rear Disc: Casing Side Test Section..... | 13 |
| Figure 2-5: Linear Cascade Test Facility Equipped with Four Tailboards..... | 14 |
| Figure 2-6 : Different Inflow Angle Configurations From the Casing Wall Side..... | 15 |
| Figure 2-7: Rapid Insertion of the Mobile Central Vane | 16 |
| Figure 2-8: Position of the Film Cooling Rows | 20 |
| Figure 2-9: Unwrapped Surface of the Film-Cooled Nozzle Guide Vane..... | 20 |
| Figure 2-10: Fan-Shaped Hole Configuration and Notation..... | 21 |
| Figure 2-11 : Projected 2D Surface of the Film-Cooled Casing Platform..... | 22 |
| Figure 3-1: Format of the Transient Liquid Crystal Video Signal | 26 |
| Figure 3-2: Transient Liquid Crystal Video Sequence of the Nozzle Guide Vane Leading Edge View | 28 |
| Figure 3-3: RGB and HSI Color Modes..... | 29 |
| Figure 3-4: Light Inhomogeneities Filtering..... | 30 |
| Figure 3-5: Temperature Level Filtering..... | 31 |
| Figure 3-6: Reference Grid and Image Transformation | 32 |
| Figure 3-7: Semi-Infinite and Finite Wall Configurations..... | 34 |
| Figure 3-8: Dimensionless Heat Transfer Coefficients Determined by the Finite and Semi-Infinite Model for Different Time Experiments | 35 |
| Figure 3-9: Dimensionless Wall Temperature on the Lower Surface ($x=\delta$) for the Finite Model, the Semi-Infinite Model and Measurements..... | 35 |
| Figure 3-10: Dimensionless Wall Temperature on the Upper Surface ($x=0$) for the Semi-Infinite and Finite Models, with Rough Bi_c Estimations..... | 36 |

| | |
|--|----|
| Figure 4-1: Flow Periodicity Check for the Three Inflow Angle Configurations | 40 |
| Figure 4-2: Static Pressure Taps Locations | 41 |
| Figure 4-3: Central Vane Ma and Acceleration at Mid-Span TE | 41 |
| Figure 4-4: Outlet Ma Distribution on the Casing Wall | 41 |
| Figure 4-5: Surface Flow Visualization on the Vane with the Use of Liquid Crystal Sensitive to Shear Stress..... | 43 |
| Figure 4-6: Ma Surface Distribution for the Three Inflow Angles | 44 |
| Figure 4-7: Ma Distribution Close to the Contoured Walls | 45 |
| Figure 4-8: Span-Wise Ma Distribution at $s/L=+0.5$ and $s/L=-0.5$ | 45 |
| Figure 4-9: Traversing Probe System | 46 |
| Figure 4-10: Pneumatic Pressure Probe Positions in the Linear Cascade | 47 |
| Figure 4-11: Position of the Probe Measured Section | 47 |
| Figure 4-12: Loss Measurements at Three Different Inflow Angles | 48 |
| Figure 4-13: Pitch Averaged Loss Measurements | 49 |
| Figure 4-14: Loss Measurements Comparison at Mid-Span TE Position | 49 |
| Figure 4-15: Pitch Averaged Pitch Angle | 50 |
| Figure 4-16: Picture and Drawing of the Global Optical Access for the Measurements on the Central Vane | 53 |
| Figure 4-17: Typical Liquid Crystal Coating Roughness | 55 |
| Figure 4-18: Coordinate Transformations and View Assembly | 57 |
| Figure 4-19: Baseline Heat Transfer Coefficients on the Vane | 58 |
| Figure 4-20: Span-Wise Averaged Heat Transfer Coefficients on the Vane..... | 59 |
| Figure 4-21: Flow Stagnation Line and Heat Transfer Coefficient on LE..... | 60 |
| Figure 4-22: Comparison with Laminar and Turbulent Nusselt Numbers Correlations | 61 |
| Figure 4-23: Comparison with Numerical Simulations (Texstan code) | 63 |
| Figure 4-24: Camera Views for the Film-Cooled Vane Experiments | 66 |
| Figure 4-25: The Three Different Operating Modes of Coolant Gas Supply for the Film-Cooled Vane | 69 |

| | |
|--|-----|
| Figure 4-26: Transient Liquid Crystal Video Sequence on the Surface of the Film-Cooled Vane | 70 |
| Figure 4-27: Typical Discharge Coefficients of Cooling Holes | 72 |
| Figure 4-28: Averaged Film-Cooled Heat Transfer Coefficients on the Vane | 75 |
| Figure 4-29: Averaged Film Cooling Effectiveness on the Vane..... | 77 |
| Figure 4-30 Averaged Film-Cooled and Un-Cooled Heat Flux Ratios | 79 |
| Figure 4-31: Film-Cooled Heat Transfer Coefficients for Independent PS LE SS Zones | 80 |
| Figure 4-32: Film-Cooled Heat Transfer Coefficients for Combined PS LE SS Zones | 81 |
| Figure 4-33: Film-Cooling Effectiveness for Independent PS LE SS Zones | 82 |
| Figure 4-34: Film-Cooling Effectiveness for Combined PS LE SS Zones..... | 83 |
| Figure 4-35: Film-Cooled and Un-Cooled Heat Flux Ratios for Independent PS LE SS Zones | 84 |
| Figure 4-36: Film-Cooled and Un-Cooled Heat Flux Ratios for Combined PS LE SS Zones | 85 |
| Figure 4-37: Pressure Ratio at the Different Rows of Coolant Gas Injection | 88 |
| Figure 4-38: Density Ratio at the Different Rows of Coolant Gas Injection | 88 |
| Figure 4-39: Blowing Ratio at the Different Rows of Coolant Gas Injection..... | 89 |
| Figure 4-40: Coolant Mass Flow Distribution of the Different Rows..... | 89 |
| Figure 4-41: Detailed Measurement Uncertainties for the Heavy Film-Cooled Vane | 91 |
| Figure 5-1: Model Configuration of Heater Foil and Film-Cooled Experiments..... | 94 |
| Figure 5-2: Schematic Drawing of the Flat Plate Test Facility | 95 |
| Figure 5-3: Film-Cooled Flat Plate Heater Foils Configurations..... | 98 |
| Figure 5-4: Dimensionless Reference Heat Flux Distribution Measurements (upper) and Calculations (lower) | 100 |
| Figure 5-5: Surface Distribution of Heat Transfer Coefficients on the Plate | 102 |
| Figure 5-6: Lateral Averaging of Heat Transfer Coefficients on the Plate..... | 102 |

| | |
|--|-----|
| Figure 5-7: Surface Distribution of Adiabatic Film Cooling Effectiveness on the Plate | 103 |
| Figure 5-8: Lateral Averaging of Adiabatic Film-Cooling Effectiveness on the Plate | 103 |
| Figure 5-9: Relative Error Evolution for Different Number of Experiments Used in Regression Analysis | 106 |
| Figure 6-1: Tubing Arrangement for the Casing Wall Static Pressure Distribution Measurements | 109 |
| Figure 6-2: Mach Number Distribution Issued From Pressure Taps..... | 110 |
| Figure 6-3: Comparison of Mach Number Distribution Issued from PSP (colors) and from Pressure Taps (black contour lines) | 111 |
| Figure 6-4: Video Image Transformation for the Baseline Case Platform..... | 113 |
| Figure 6-5: Video Image Transformation for the Film-Cooled Case Platform | 113 |
| Figure 6-6: Picture and Drawing of the Film-Cooled Casing Platform | 114 |
| Figure 6-7: Liquid Crystal Signals on Platform for a Baseline (left) and a Film-Cooled (Right) Transient Experiment..... | 116 |
| Figure 6-8: The Three Different Operating Modes of Coolant Gas Supply for the Film-Cooled Casing Platform..... | 118 |
| Figure 6-9: Improvement of the Heat Flux Distribution by Different Bus Bars Connections (streamlines represent the electrical current lines) | 120 |
| Figure 6-10: Reference Heat Flux Ratio Distribution Measured for the Baseline Case | 122 |
| Figure 6-11: Heat Flux Ratio Calculated for the Baseline Case..... | 122 |
| Figure 6-12: Reference Heat Flux Ratio Distribution Measured for the Film-Cooled Case..... | 123 |
| Figure 6-13: Heat Flux Ratio Calculated for the Film-Cooled Case | 123 |
| Figure 6-14: Comparison of the Baseline Heat Flux Ratio | 124 |
| Figure 6-15: Comparison of the Film-Cooled Heat Flux Ratio | 124 |
| Figure 6-16: Comparison with Laminar and Turbulent Nusselt Number Correlations | 125 |

| | |
|--|-----|
| Figure 6-17: Platform Vortex Pattern (Goldstein & Spore, 1988)..... | 127 |
| Figure 6-18: Baseline Heat Transfer Coefficients Measurement | 128 |
| Figure 6-19: Surface Flow Visualization on the Baseline Casing Platform | 128 |
| Figure 6-20: Film-Cooled Heat Transfer Coefficients Measurement..... | 129 |
| Figure 6-21: Surface Flow Visualization on the Film-Cooled Casing Platform..... | 129 |
| Figure 6-22: Film-Cooling Effectiveness Distribution with the Transient Technique | 130 |
| Figure 6-23: Film-Cooling Effectiveness Distribution for PSP with N ₂ Injection | 130 |
| Figure 6-24: Comparison of the Transient and PSP Film-Cooling Effectiveness Results..... | 131 |
| Figure 6-25: Film-Cooled and Un-Cooled Heat Flux Ratios Distribution..... | 133 |
| Figure 6-26: Pressure Ratio at the Different Coolant Gas Injection Positions | 136 |
| Figure 6-27: Density Ratio at the Different Coolant Gas Injection Positions..... | 136 |
| Figure 6-28: Blowing Ratio at the Different Coolant Gas Injection Positions | 137 |
| Figure 6-29: Coolant Mass Flow Distribution of the Different Holes | 137 |
| Figure 6-30: Detailed Measurements Uncertainties of the Film-Cooled Platform Results..... | 139 |

Appendix

| | |
|---|-----|
| Figure b-1: Typical Wall Temperature Evolution of a Transient Liquid Crystal Experiment..... | 156 |
| Figure c-1: Multiple T_{tc} Experiments and the Resulting T_w | 159 |
| Figure d-1: Multiple G and T_{tc} Experiments and the Resulting T_w | 165 |

Tables

| | |
|--|----|
| Table 2-1: Main Flow Conditions for Aerodynamic Measurements..... | 18 |
| Table 2-2: Main Flow Conditions for Baseline Heat Transfer Measurements..... | 18 |
| Table 2-3: Main Flow Condition for Vane Film-Cooled Measurements..... | 21 |
| Table 2-4: Film-Cooled Area Configurations..... | 22 |

| | |
|---|----|
| Table 2-5 : Main Flow Condition for Platform Measurements | 23 |
| Table 4-1: Mass Averaged 5-Hole Probe Measurements | 51 |
| Table 4-2: Liquid Crystal Coating Roughness Results..... | 54 |

1 INTRODUCTION

1.1 Gas Turbines

Large-scale energy consumption is common nowadays in modern society. Natural resources give us this energy, but machines are required to extract this energy from the resources. Since our natural resources are limited, our goal is of course to develop and use the best machines that exploit energy. The gas turbine is one of these machines that uses fossil fuels to produce mechanical or electrical energy. Its most important applications are for aircraft propulsion (also called jet-engine) or in industrial power generations. The working principle is based on the thermodynamic Brayton cycle, which can be described as follows. The working fluid, typically air, is compressed to high pressure by series of rotor and stator blades. The compressed fluid is then heated by passing through a combustion chamber where fuel is injected and burned. The high pressure, high temperature working fluid then expands through the turbine part; hence it delivers power output. One part of this energy drives the compressor mounted on the same shaft as the turbine. The rest of this energy is either used to drive a generator for electrical power production, or a fan for aero-engines propulsion.

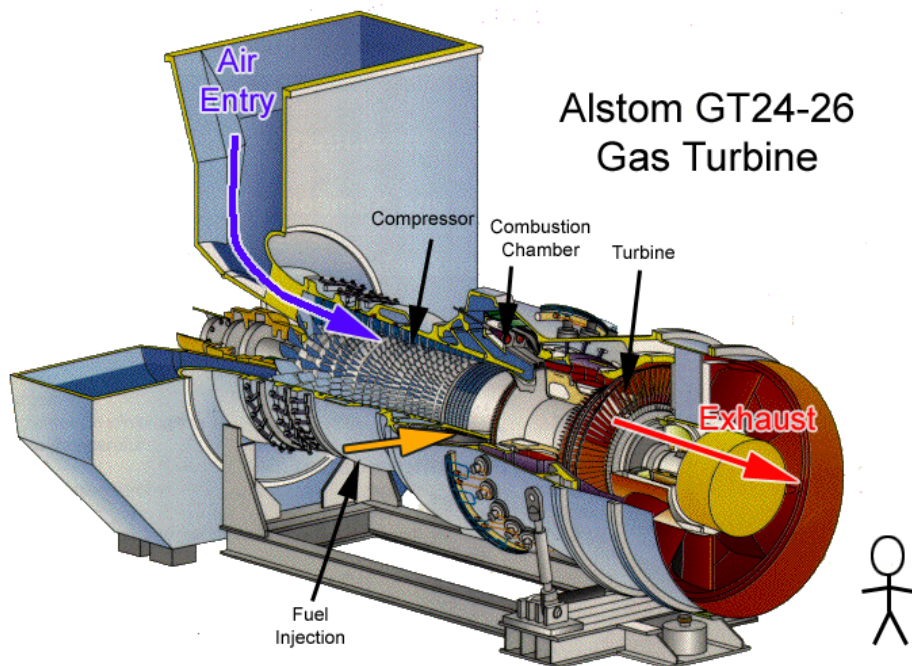


Figure 1-1: Example of a Modern Industrial Gas Turbine

The principal advantage of these engines is their large amount of useful power production for their relatively small size and weight. However, fifty years ago, the maximum thermal efficiency was only around 18%. Today, modern industrial gas turbines (see Figure 1-1) are able to deliver an electrical output of 265MW with a thermal efficiency that can reach about 40% for a simple cycle and up to 55% for a combined cycle. In the near future, the goal is to reach up to 60% thermal efficiency. This could be achieved by increasing the turbine inlet temperature; but since this temperature often exceeds the maximum allowable material temperature, the turbine parts have to be cooled to guarantee safe operating conditions.

In the past, efforts to increase the turbine inlet temperature were dedicated to the development of higher temperature resistant alloys. It was during the Second World War that German engineers started the idea to compensate for the poor quality of their alloys by cooling the critical parts (Cohen et al., 1996). Nowadays, the turbine parts in current engines use the best nickel based superalloys, covered by TBC coatings like zirconia based ceramics, and are combined with the most efficient internal convective cooling and external film cooling configurations to satisfy the always more demanding turbine inlet temperature (TIT) conditions. Figure 1-2 shows the turbine inlet temperature evolution of the last fifty years thanks to the improved material but above all from advanced cooling methods.

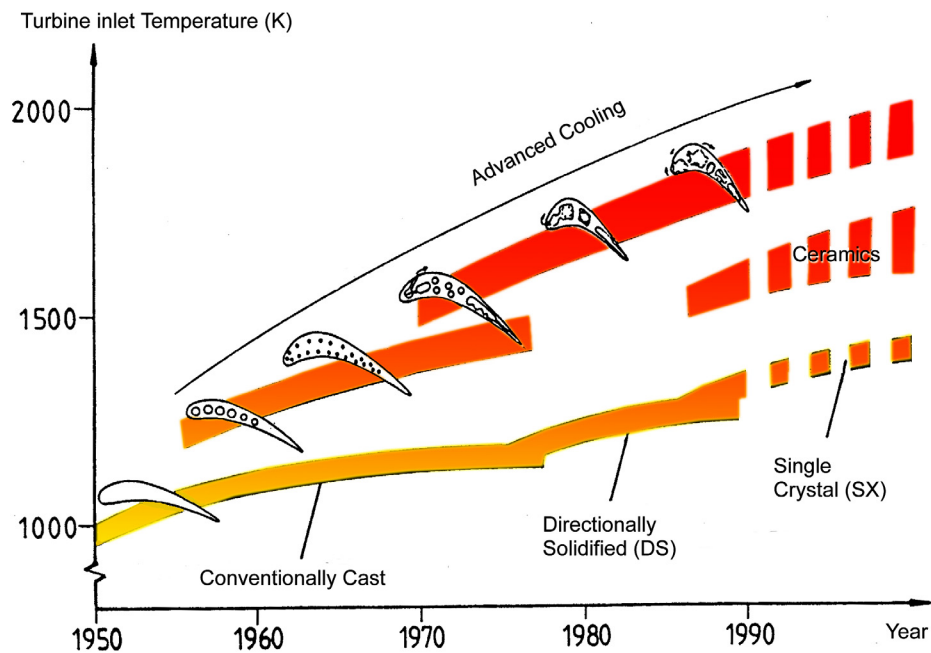


Figure 1-2: Turbine Inlet Temperature Evolution

1.2 Nozzle Guide Vane

In order to perform work, the hot gas discharged from the combustion chamber must be suitably processed. This is the task of the nozzle guide vane, which has two principal functions. First, it must convert part of the energy of hot gas into kinetic energy in order to sufficiently elevate the flow velocity when it impinges the rotor blades. Second, the nozzle guide vane must change the direction of the gas flow in a manner such that the circumferential forces generated on the turbine rotor blades are maximized for the production of shaft power. The required acceleration is accomplished by narrowing the passage between adjacent blades (nozzle effects). As velocity increases, static pressure and temperature decrease; thus heat and pressure energy are converted into kinetic energy. The efficiency of the nozzle guide vane is determined by the aerodynamic losses caused during this process; and recent research on vane with contoured platforms has shown reduced losses by the secondary flow changes (Dossena et al, 1998).

In modern gas turbines, due to the high turbine Inlet temperature, the nozzle part is subject to high thermal load as the hot gas directly exits the combustion chamber. For this reason, the vane is internally cooled but also heavily externally film-cooled. Typically it uses about 38% of the total amount of cooling air used in the turbine. Film cooling has to be highly efficient because of the fact that a too large cooling mass flow would degrade the thermal efficiency of the thermodynamic cycle. Moreover, in some cases it also decreases the nozzle performances by increased aerodynamic losses (Day et al, 1998). Indeed one of the most important issues is to improve film-cooling designs to minimize cooling air consumption.

In addition to the high turbine inlet temperature, Chyu (2000) notes that today's combustors generate also a flatter radial temperature profile, and as a consequence increase the thermal load on the vane platform. This now imposes a higher platform-cooling requirement.

Hence, there is a real need to improve film-cooling designs of new nozzle guide vanes with contoured platform geometries. The goal is to accurately predict heat-transfer coefficient as well as the local vane temperature of new developed film-cooling configurations in order to prevent a local hot spot, which would otherwise reduce the life of the turbine components. Note that the vane life will be reduced by half if the vane metal temperature is only 10 K higher than the predictions (Han et al. 2000).

1.3 Film Cooling

The film cooling process is characterized by the injection of air through holes in the surface (Figure 1-3), in such a way that it forms a protective layer against the hot mainstream gas (Goldstein, 1971; Leontiev, 1999). The precise knowledge of the heat transfer characteristics is required for the design of improved film-cooled nozzle guide vanes.

Principal parameters influencing the heat transfer coefficient along the turbine vane are: airfoil curvature, film cooling injection geometry, Reynolds and Mach numbers, free-stream turbulence, temperature and density ratios of the fluids. Moreover, the linear or contoured platforms geometries of the vane generate special secondary flows that also have an influence on the heat transfer coefficient.

Film cooling depends primarily on the coolant to hot mainstream pressure ratio p_{tc}/p_{tg} , temperature ratio T_{tc}/T_{tg} and the film cooling hole location, configuration and distribution on the surface. In a typical first vane gas turbine airfoil, the p_{tc}/p_{tg} ratios vary from 1.02 to 1.1 while the corresponding blowing ratios vary approximately from 0.5 to 2.0, whereas, the T_{tc}/T_{tg} values vary from 0.5 to 0.85 and the corresponding density ratios vary approximately from 2 to 1.5. In general, the higher the pressure ratio is, the better the film-cooling protection is. However, a too high-pressure ratio (i.e. blowing too much) may reduce film-cooling protection because of jet lift-off from the surface. Therefore it is important to optimize the amount of coolant for film cooling under engine operating conditions. For a nozzle guide vane it is usually around an exit Reynolds number based on chord length of $Re_{2L}=1e+6$ and a downstream isentropic Mach number of $Ma_2=0.8$. It is also important to determine the effect of free stream turbulence on the film-cooling performance (i.e. film-cooling effectiveness and heat transfer coefficient distributions).

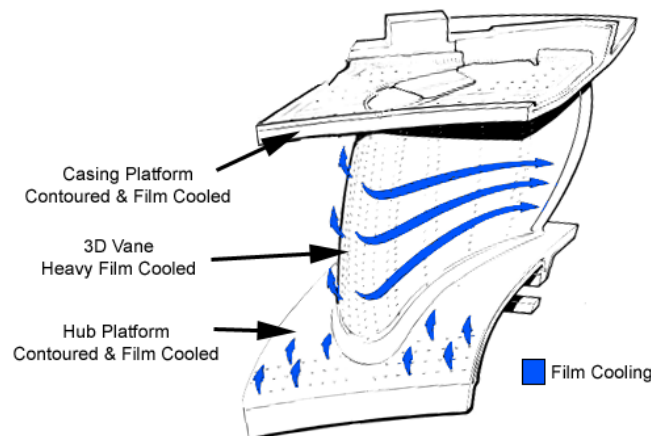


Figure 1-3: Film-Cooled Nozzle Guide Vane

1.4 State of the Art

Current turbine designs are characterized by an inability to accurately predict heat transfer coefficient distributions under turbomachinery flow conditions. This results in a non-optimized design using inordinate amounts of cooling air, which ultimately causes significant penalties to the cycle in term of efficiency. Factors which hinder the accurate prediction of the nozzle guide vane heat transfer include the inlet temperature profile, high turbulence effect (up to 20%) and the secondary flows produced near the platforms.

For the last fifty years, several studies have been focused on heat transfer measurements on un-cooled vane airfoil configurations. The techniques used were based on heat flux sensors for measurements at discrete locations. For higher spatial resolutions, the naphthalene technique (Håring, 1996) based on the heat and mass transfer analogy was applied. More recently, convenient methods such as the liquid crystal coating for steady or unsteady experiments, or the use of infrared cameras have been used for baseline experiments on vane airfoils or simplified geometries such as flat plates or cylindrical models.

Film-cooled vane airfoil configurations for simplified geometries have been studied by the use of the aforementioned measurement techniques (Goldstein, 1971; Leontiev, 1999). Due to the significant numbers of parameters characterizing the film-cooling configurations, experiments on simplified geometries are still being performed. It is expected that the accurate correlations obtained from these complex cooling holes geometries on simplified physical models can be applied on real vane airfoil geometries.

Vane airfoil studies are usually performed in a linear cascade with flat platforms. A flat wall configuration was, and in some cases is still quite representative from the platform geometry of the engine. However, in 1960 Deich introduced contoured platforms in order to reduce the aerodynamic losses of the nozzle guide vanes.

Some baseline studies were then performed on contoured (Harvey, 1990) or non-contoured platforms (Goldstein et al., 1988). The measurement technique for the determination of the local heat transfer coefficient was based on the heat to mass transfer analogy with the naphthalene technique. Results have shown that heat transfer distribution on the platforms is very complex and can be closely correlated with the vortex system set up by the secondary flows.

Flat platform film-cooling was first applied by coolant gas Injection upstream the cascade through slots (Farmer et al., 1997) or rows of holes (Seager et al. 1997) and showed beneficial interactions with the secondary flows that sometimes decreased or increased the aerodynamic losses. Similar cooling configurations have then been tested on contoured platforms (Burd & Simon, 2000). For these configurations, the measurement technique is based on infrared or transient liquid crystal techniques applied with an electrical heater foil on the measured wall (von Wolfersdorf & al., 1993).

More recently, film-cooling on flat or contoured platforms is being performed by rows of holes present in the vane passage. The introduction of film-cooling sets up a complex interaction between the cooling jets and the secondary flow system (Harasgama et al., 1992). For these configurations, new measurement techniques for the determination of the film-cooling effectiveness have been developed. Results obtained by the Ammonia Diazo technique are obtained by Friedrichs (2000) who points to the need for careful design of platform film-cooling configurations since a poor design may actually strengthen the secondary flow in some cases. Zhang et al. (2001) use a quite promising measurement technique based on the pressure sensitive paint technique with nitrogen injection to obtain results of film-cooled platforms.

The effect of platform contouring on the film coolant interaction with the main flow needs further description. Most of the available experimental data in this field has been obtained using either non-contoured walls or relatively simple film cooling configurations. There is now an urgent need for detailed film cooling experimental data on actual realistic nozzle guide vanes geometries that model the effect of curvature, stream-wise acceleration, and secondary flows.

Besides heat transfer and effectiveness measurements, it is important to take measurements quantifying aerodynamic losses in film-cooled situations, especially for contoured nozzle guide vanes.

1.5 Objective of this Work

As it has been indicated in the previous paragraphs, one of the most critical parts in a modern gas turbine in term of heat transfer is certainly the Nozzle Guide Vane, which is nowadays heavily cooled and equipped with special contoured platforms. It is this part of the engine that is experimentally studied in the present work, as there is a real need for data experiments on such complex film-cooled geometries.

In addition to the creation of a physical test model that accurately represents the nozzle guide vane present in modern gas turbines, the flow conditions during the experiments have to be similar to engine conditions. Concerning the flow conditions, this study replicated the Reynolds and Mach numbers found in gas turbine engines. It did not replicate the absolute temperature levels found in gas turbine engines. However, coolant gas-to-mainstream pressure and temperature ratios are kept as similar as possible to the engine conditions, by using CO₂ as the coolant gas, for instance.

This experimental work can be subdivided into two major parts. The first part focuses on the heavy film-cooled airfoil vane and consists of aerodynamic and heat transfer measurements. While the second and really innovative part is dedicated to the film-cooled contoured platform experiments for which a novel transient measurement technique has been developed.

2 TEST CONFIGURATION

The challenge of this work is to perform experiments on a model being as close as possible to the real engine design leading to a complex test section geometry; with similar secondary flow conditions. For this, a nozzle guide vane geometry model issued from a last generation gas turbine is extracted and mounted in the so-called “linear cascade test facility” of the LTT for experiments. This chapter describes both the geometry of the film-cooled vane and platform configuration used in this work, as well as the different film-cooling test conditions.

2.1 Geometry Configuration

This sub-chapter describes the steps and process that are performed in order to obtain a physical model for the linear test facility of an engine representative nozzle guide vane geometry.

2.1.1 3D Model Extraction

The actual 3D geometries of the blades and the platforms chosen for the experiments have been given in electronic format by ALSTOM Power Switzerland, one of the world leaders in modern gas turbine manufacturing. The centrifugal effects and pressure gradients issued in a radial configuration can be neglected for vane height to radius ratios inferior to 0.4 (Bölcs,1993). This is the case of the nozzle guide vane given by ALSTOM, so that similar flow conditions can be obtained in a linear cascade configuration. As the linear cascade requires prismatic vanes with a constant profile, adequate airfoil geometry is extracted from the 3D nozzle guide vane. To obtain the best analogy, the 3D vane is cut conically, the cone angle corresponding to a cut going from the mid-span position of the leading edge to the mid-span position of the trailing edge. The 3D curve obtained from this conical cut is then projected onto a reference plane perpendicular to the radial direction and then extruded to obtain the required cylindrical vane.

By doing so, the extracted cylindrical vane does not intersect the original contoured platforms at the same positions as for the 3D vane; and because the contoured platform geometry is closely related to the 3D vane geometry, it is then necessary to adapt both of the original platforms by stretching or un-stretching them in the stream-wise direction x .

To obtain a periodic flow, the linear cascade is equipped with at least five vanes. Since the size of the linear channel is unmodifiable, it is necessary to apply a scaling factor to the extracted geometry. The resulting downscaling factor is 3:4, giving a model vane pitch of 63.4 mm.

Moreover, as the casing platform is at the rear of the test facility and the hub is at the front (for optical access reasons), and because the exit of the test facility is on the left, the extracted blade cascade is flipped (the inversion has no influence) in order to change the direction of deviation with respect to the 3D design.

Figure 2-1 summarises the steps performed on the extraction of the engine nozzle guide vane cascade to a linear cascade.

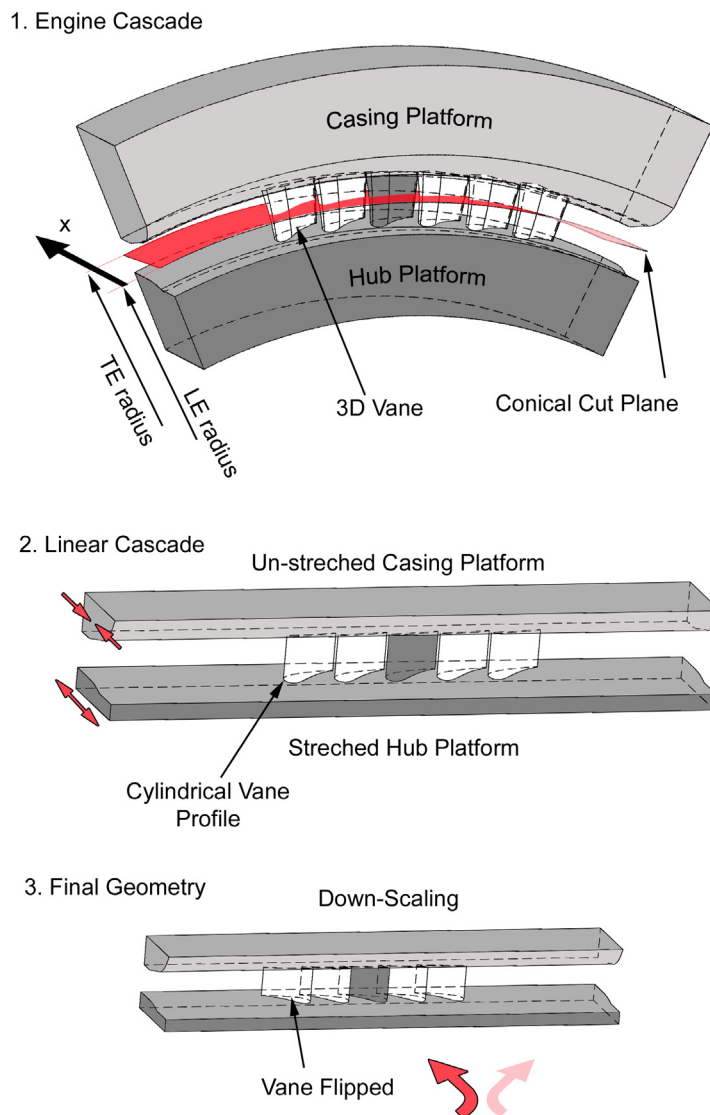


Figure 2-1: Geometry Process from 3D to a Linear Cascade

This linear cascade geometry at the bottom of Figure 2-1 is mounted in the linear cascade test facility for the experiments of the present work. Details of the vane and contoured platform profiles and the coordinate system used are given in Figure 2-2.

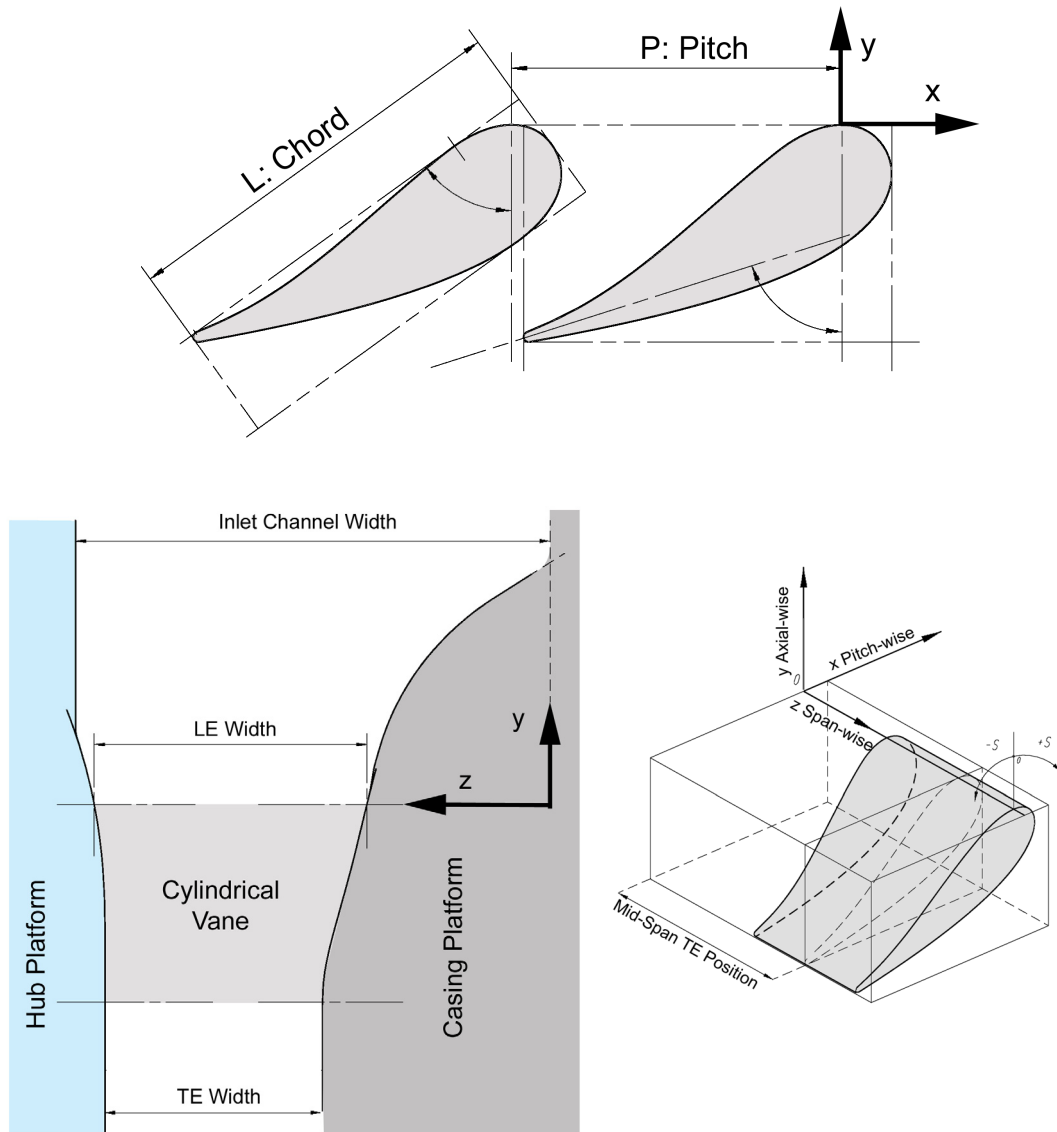


Figure 2-2: Extracted Airfoil and Platforms Vane Geometries

2.1.2 Linear Cascade Test Facility

The complete test section is mounted on two large discs on each side (front and rear) of the wall of the flow channel, keeping a maximum flexibility for the construction and easier installation. These discs can be turned in order to perform experiments with variable inflow angles for the cascade. However, the contoured platforms mounted on these discs interfere with the sidewalls of the flow channel. To avoid this problem, design of adapted lateral blocs of the hub and casing platforms have to be

manufactured for specific angular position. The number of inflow angle configurations for the experiments of this work was then limited to three (Figure 2-6).

2.1.2.1 Hub Platform

The hub platform being less contoured than the casing platform, it is used for optical access in the linear cascade. For this reason, the hub platform is mounted on the disc at the front side of test facility; and the main platform part is used as a window as it is made out of Perspex. Additional windows are placed on the front disc at specific locations. One is located upstream the cascade and can be un-mounted from outside to provide an easy and large access to the linear cascade. Another window, in a circular shape and located downstream the cascade, allows verifying the large tailboard position used for flow periodicity adjustment.

The front disc represented in Figure 2-3 contains only the contoured hub platform and is simply pushed on the vanes of the cascade. Complete access of the cascade is then obtained by simply un-mounting this front disc.

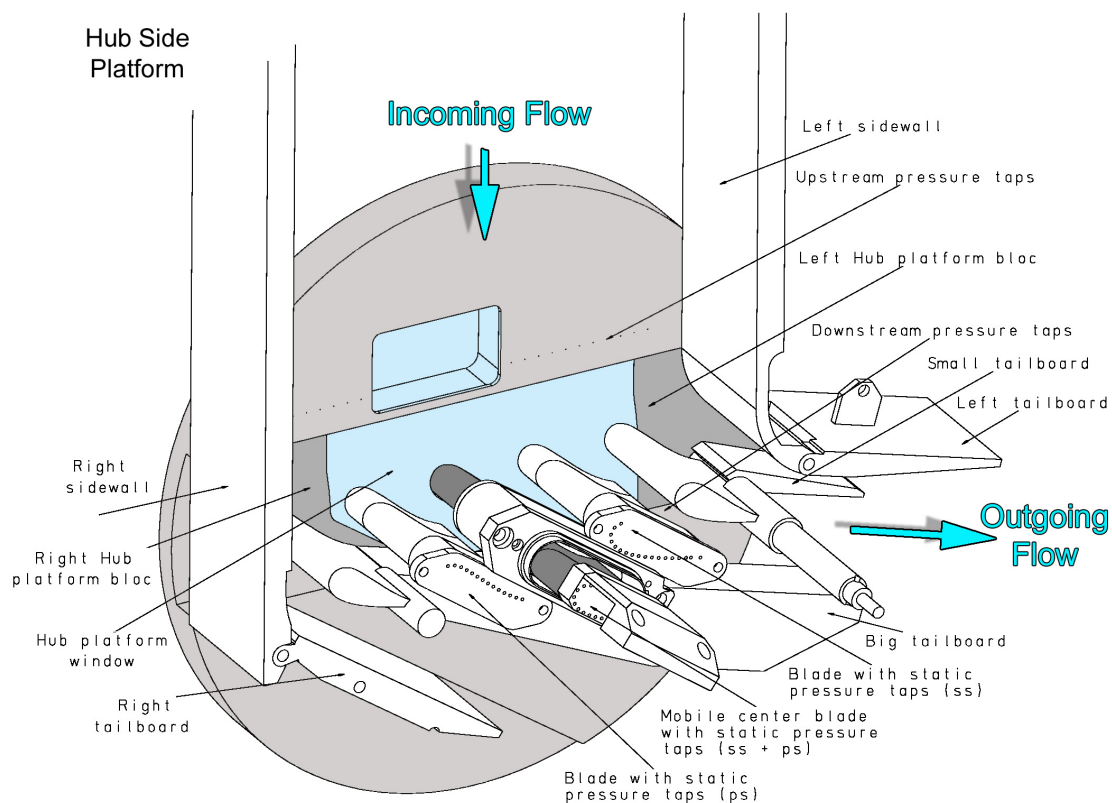


Figure 2-3: Front Disc: Hub Side Test Section

2.1.2.2 Casing Platform

The casing platform, more contoured than the hub platform, is mounted on the rear disc of the test facility. It contains the vanes airfoils and tailboards. Pressure taps used for flow conditions adjustments are located on this side. For rigidity reasons, this disc is mounted from inside the channel test facility, which makes it more difficult to access. For this reason the large main wall of the test facility has to be unmount when changing the lateral platform blocks of the inflow angle configurations. Since this opening process is relatively time consuming, most of the last experiments presented in this work were performed for only one inflow angle configuration.

With its large contouring profile, the casing platform is well suited for being equipped with a plenum chamber for platform film-cooled experiments. Hence, for improved flexibility the mid-casing platform part (see Figure 6-1 and Figure 6-6) can be directly unmounted from the rear disc when the front disc is removed. Figure 2-4 represents the casing side test section and its associated rear disc.

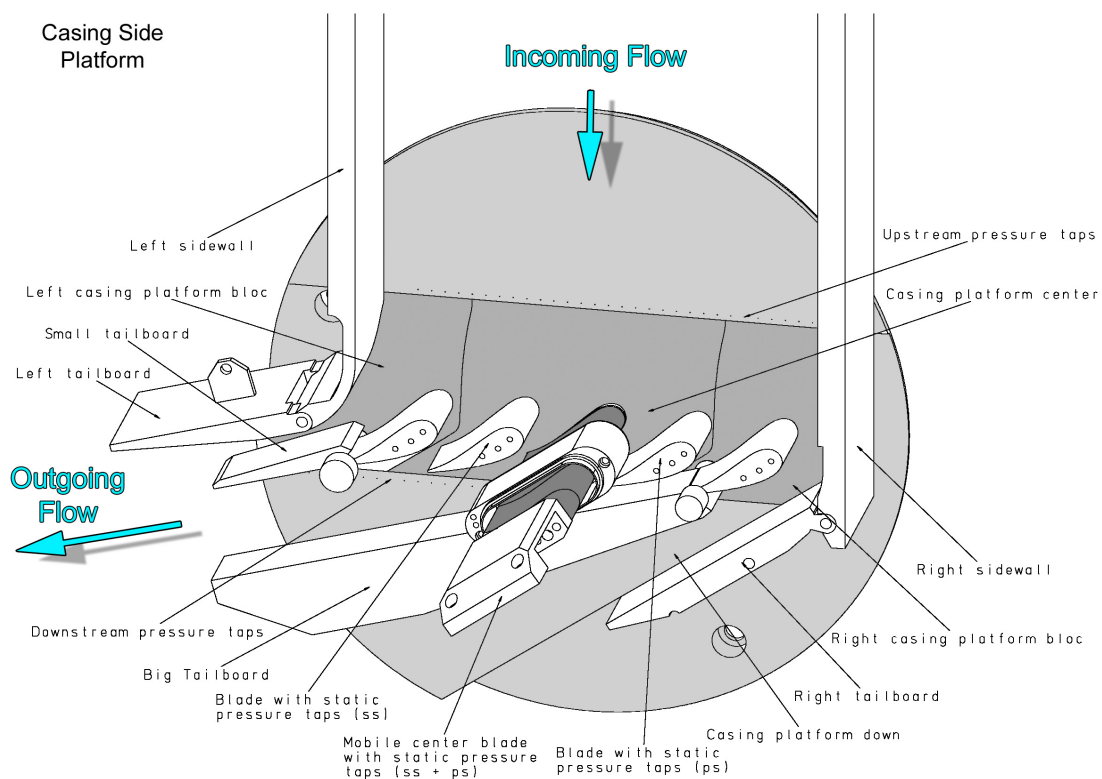


Figure 2-4: Rear Disc: Casing Side Test Section

2.1.2.3 Periodic Flow Adjustment: Tailboards

In order to ensure periodicity in the five vanes linear cascade, the channel is equipped with four tailboards as shown in Figure 2-5.

Two large size tailboards (in blue on the figures) located at the extreme left and right walls of the linear cascade allow controlling the incoming flow distribution. The walls can be adjusted vertically for different cascade angles of deviation (Figure 2-6).

The two other tailboards (in red on the figures) located at the trailing edges of the extreme right and left vanes are thinner as they are located downstream the cascade at the reduced section issued from the contoured platforms. The angles of these tailboards allow controlling the outgoing flow distribution. The longest tailboard has special slots covering about 40 % of its surface in order to avoid reflections of shocks issued from a transonic flow in the cascade or of a pressure loss measurement probe inserted downstream the cascade.

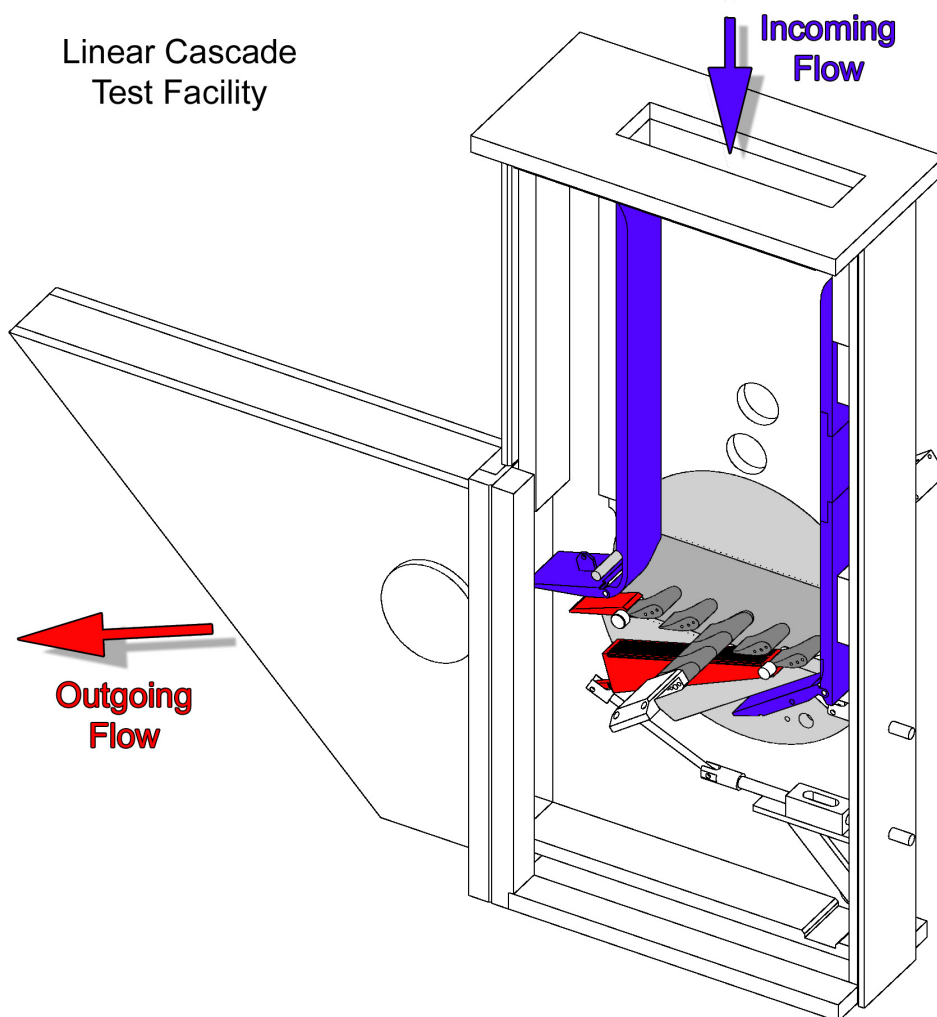


Figure 2-5: Linear Cascade Test Facility Equipped with Four Tailboards

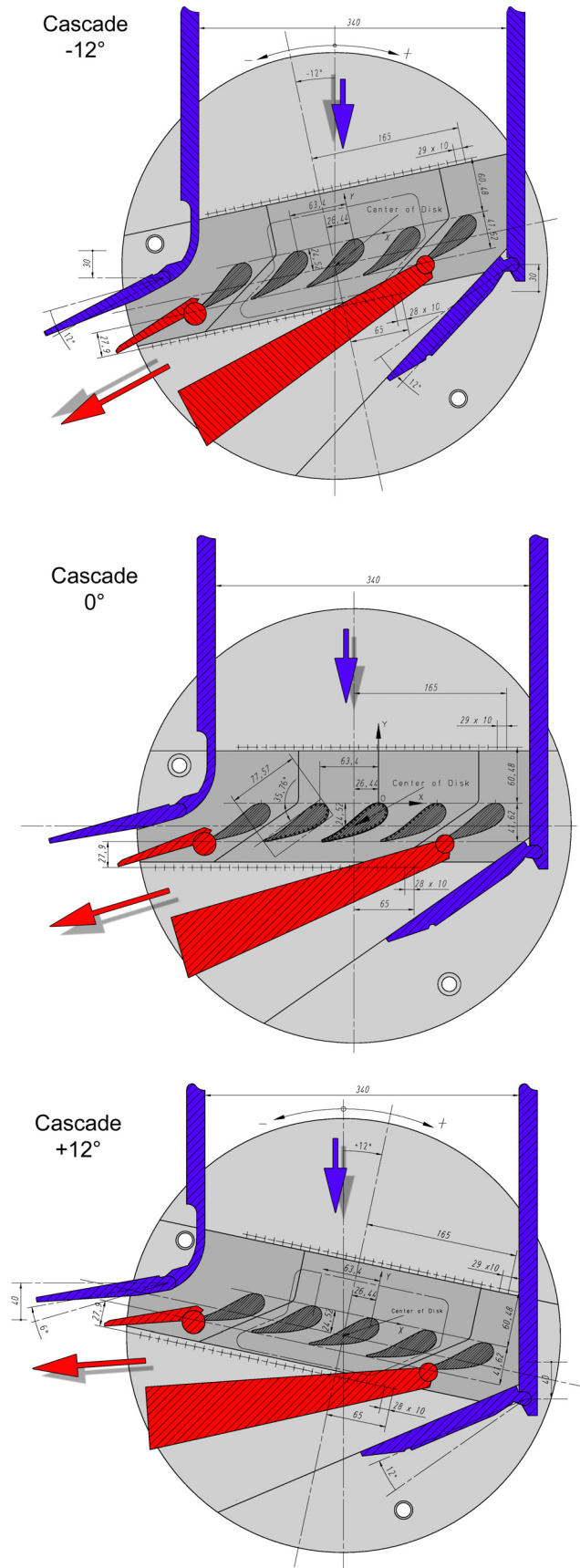


Figure 2-6 : Different Inflow Angle Configurations From the Casing Wall Side

2.1.2.4 Rapid Insertion Mechanism

The linear test facility is equipped with a rapid insertion pneumatic device for the central cylindrical vane of the cascade. It allows performing transient experiments by preconditioning the test section in a box outside of the channel test facility and then by rapidly inserting it into the main flow. Before insertion, a dummy part of the cylindrical vane is present in the main flow. Figure 2-7 shows the two positions of the so-called mobile central vane made out of several Perspex and aluminium parts. The Perspex test sections can either be a full solid model for baseline experiments or a complex vane model with a plenum chamber feeding multiple rows of holes for film-cooling experiments.

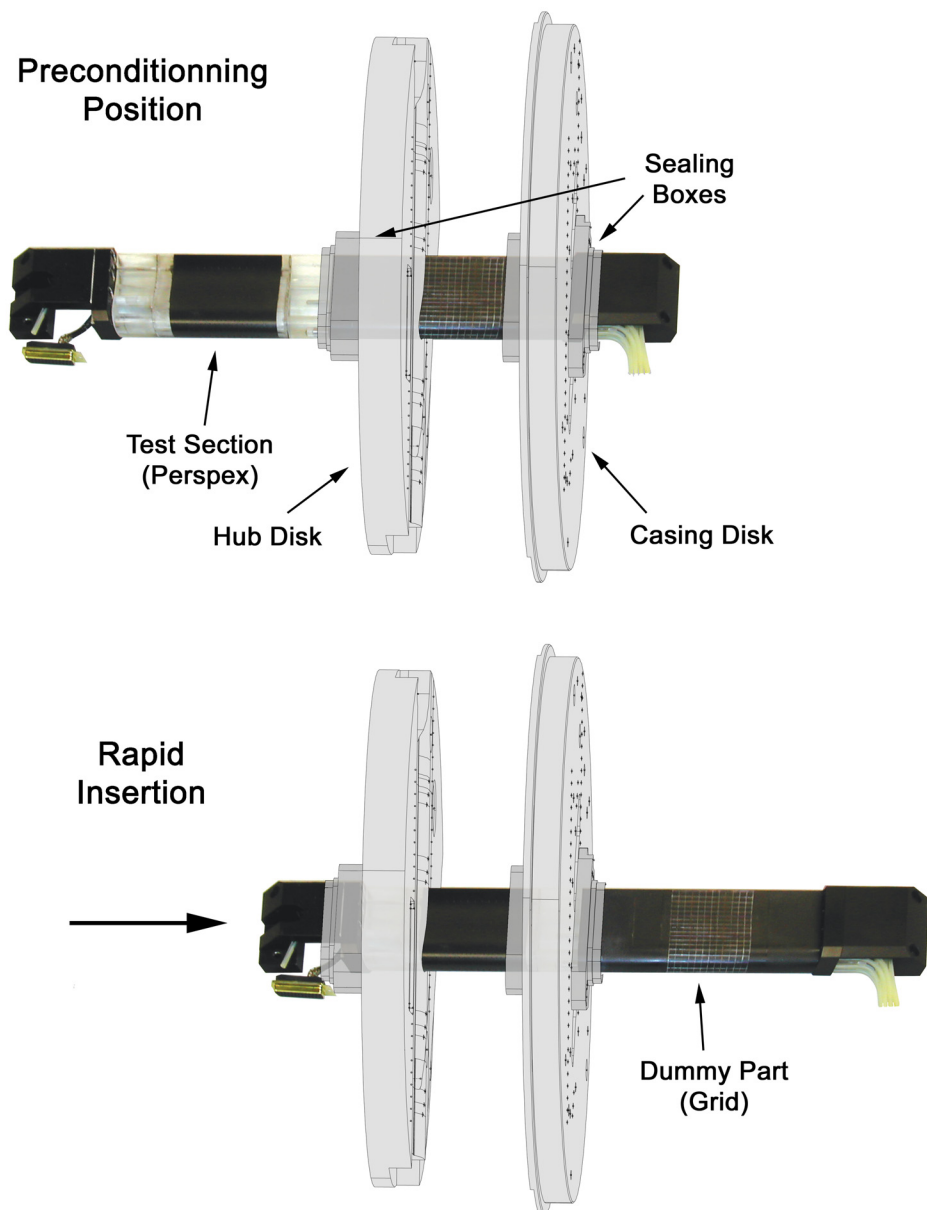


Figure 2-7: Rapid Insertion of the Mobile Central Vane

A Teflon protection layer covers the profiled passages on the platforms where the central vane translates in the span-wise direction. It helps reducing the clearances required for the vane translation without damaging its surface. However, it is necessary to seal the main flow channel from the rest of the test facility at these locations. This is accomplished by two sealing boxes equipped with rapid inflating tubes, which deflate before the central vane moves and inflate again when the vane has reached its position.

2.2 Experimental Conditions

This sub-chapter presents the vane and platform test conditions for both aerodynamic and heat transfer measurements, baseline and film-cooled cases. The different experimental conditions such as inflow angle, main flow velocity and coolant gas injection are specified. Cooling holes schemes applied for the film-cooled heat transfer measurements on the airfoil and the platform of the vane are detailed.

2.2.1 Vane Configuration

2.2.1.1 For Aerodynamic and Baseline Heat Transfer Measurements

The dummy part of the central vane is equipped with 30 pressure taps, which allow determining of the velocity profile. The coordinate system used for the representation of the data is attached to the leading edge of the vane on the casing platform wall before the contraction; hence, x is for the pitch-wise direction, $-y$ for the axial-wise direction and z for the span-wise direction (see Figure 2-2). It should be noted that results in this work are presented in dimensionless form with the vane pitch reference length P used for the x,y,z coordinate system, and with the vane chord reference length L used for the surface coordinate system s .

A complete span-wise pressure distribution is measured by moving the central vane to variable span-wise positions. The fixed neighbouring blades have pressure taps located only at the mid-span position of the trailing edge. The central vane is then shifted to have the pressure taps at the same span-wise position during flow periodicity check measurements.

Aerodynamic measurements including flow periodicity check, span-wise Mach number distribution and pressure loss measurements, and baseline heat transfer measurements are performed for three different inflow angles. For all cases, the coordinate system used is the same and turns with the cascade. The two tailboards

located downstream the cascade are for all the inflow angle configurations inclined to 74° relative to the (axial) y axis in order to achieve good flow periodicity. Orientations of three different inflow angle configurations -12° , 0° and $+12^\circ$ used for the experiments are shown in Figure 2-6.

All the aerodynamic and heat transfer measurements are performed at the nominal flow condition only, given by a downstream isentropic Mach number of about 0.77. A turbulence grid is mounted upstream the cascade assuming a turbulence inflow level of about 10% (Drost, 1998). The different conditions tested are given in the following tables:

| Inflow angle | P_{t1} [mbar] | T_{t1} [K] | Re_{2L} | Ma_2 |
|--------------|-----------------|--------------|-----------|--------|
| -12° | 1409 | 303 | 1.45E+06 | 0.8 |
| 0° | 1410 | 303 | 1.42E+06 | 0.77 |
| $+12^\circ$ | 1415 | 302 | 1.42E+06 | 0.76 |

Table 2-1: Main Flow Conditions for Aerodynamic Measurements

| Inflow angle | P_{t1} [mbar] | T_{t1} [K] | Re_{2L} | Ma_2 |
|--------------|-----------------|--------------|-----------|--------|
| -12° | 1449 | 333 | 1.26E+06 | 0.78 |
| 0° | 1463 | 333 | 1.31E+06 | 0.77 |
| $+12^\circ$ | 1463 | 332 | 1.35E+06 | 0.74 |

Table 2-2: Main Flow Conditions for Baseline Heat Transfer Measurements

Due to temperature steps for the transient measurement technique, the heat transfer measurements are performed at a slightly higher main flow temperature than for the aerodynamic measurements.

2.2.1.2 For vane film-cooled heat transfer measurements

The film cooling hole design is extracted from the geometry of the engine nozzle guide vane. For each row of cooling holes, the airfoil coordinate positions s and the exit flow angles φ are obtained by the vector line defined by the projection on the reference plane perpendicular to the radial direction of the inlet and exit lines of the rows.

For the compound angle, the cooling holes of the engine vane have values of about $+5^\circ$ on the upper mid-span side (casing) and -5° on the other side (Hub). This is

essentially due to manufacturing constraints, and as these angle values are relatively small, no compound angle is considered on the tested model.

Distribution of the holes along the span-wise direction is set by specifying the position of the first hole of each row from the casing wall. The scaled hole diameter D and the pitch between the holes P_D as well as the number of holes for each row are identical to the original 3D vane. It represents a heavily film-cooled configuration with fifteen rows and a total of 188 cooling holes. There are: six rows of fan-shaped holes on the suction side located upstream the channel throat position, four rows of cylindrical holes on the leading edge area (so called “showerhead”), and five very inclined rows of cylindrical holes on the pressure side.

Two plenum chambers feed the film-cooling holes of the actual nozzle guide vane. It allows two main different pressure ratios for a better coolant distribution of the fifteen rows. This is unfortunately not the case of the tested model as it is made out of Perspex, thus with less mechanical resistance. Instead, only one plenum chamber is present with a wall thickness of the physical model large enough to provide sufficient mechanical resistance and an acceptable time period of the transient experiment for the assumption of a semi-infinite thickness model; nor too large for avoiding any hole inlet interferences or too important coolant hole discharge coefficients. A thickness of $\delta=3\text{mm}$ is a good compromise although it implies some modifications of the extracted cooling holes geometries for the physical model. As a consequence, the holes of rows #6 and #11 have an increased exit angle φ of respectively $+2^\circ$ and $+7^\circ$ in order to avoid inlet hole interferences.

Mechanical resistance of the physical model is acceptable but critical for performing high blowing ratios on the leading edge (higher pressure in the plenum chamber).

A geometrical description of the cooling holes is given in Figure 2-8 and Figure 2-9. The two vertical lines on Figure 2-9 denote the distribution of the rows for the three considered areas: SS (suction side), LE (leading edge) and PS (pressure side). As rows of holes on the suction side are fan-shaped, Figure 2-10 gives the corresponding notation as well as the characteristics of the fan-shaped hole geometry. This fan-shaped geometry is similar to the one used on the vane of the engine. It has a certain lateral and forward angle and a small backward angle. L_{AR} is the shaped part length of the hole giving the requisite area ratios S_e/S_i .

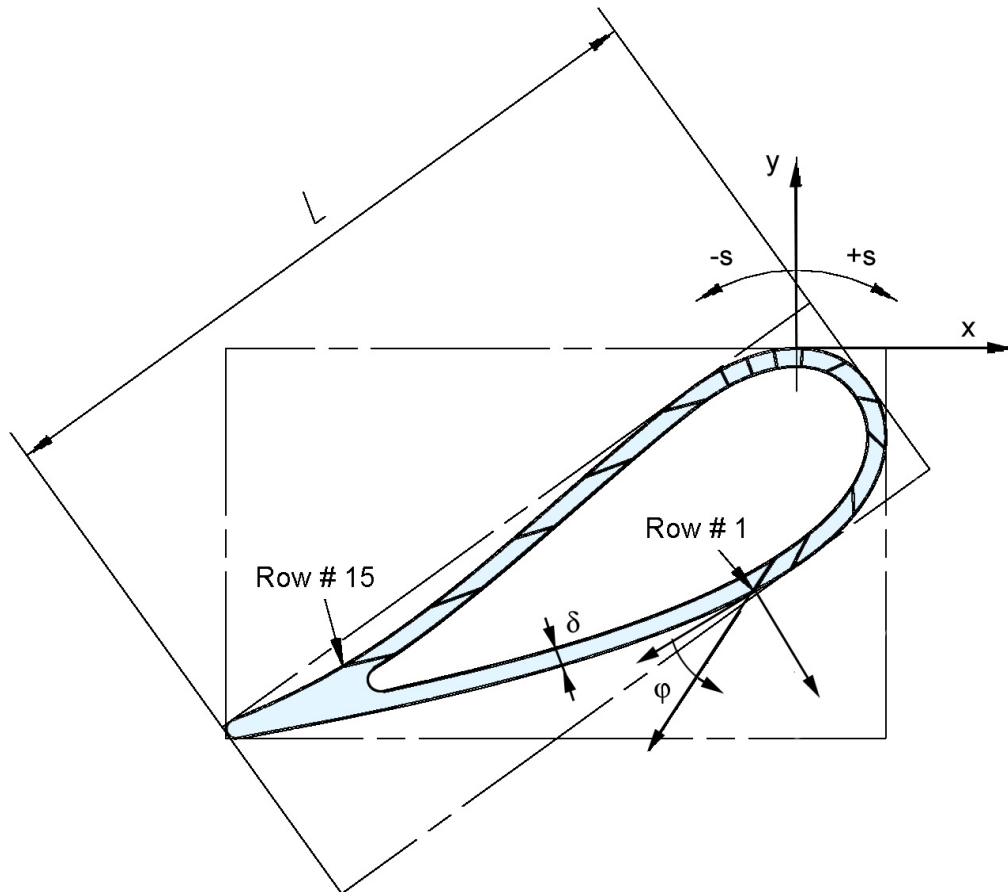


Figure 2-8: Position of the Film Cooling Rows

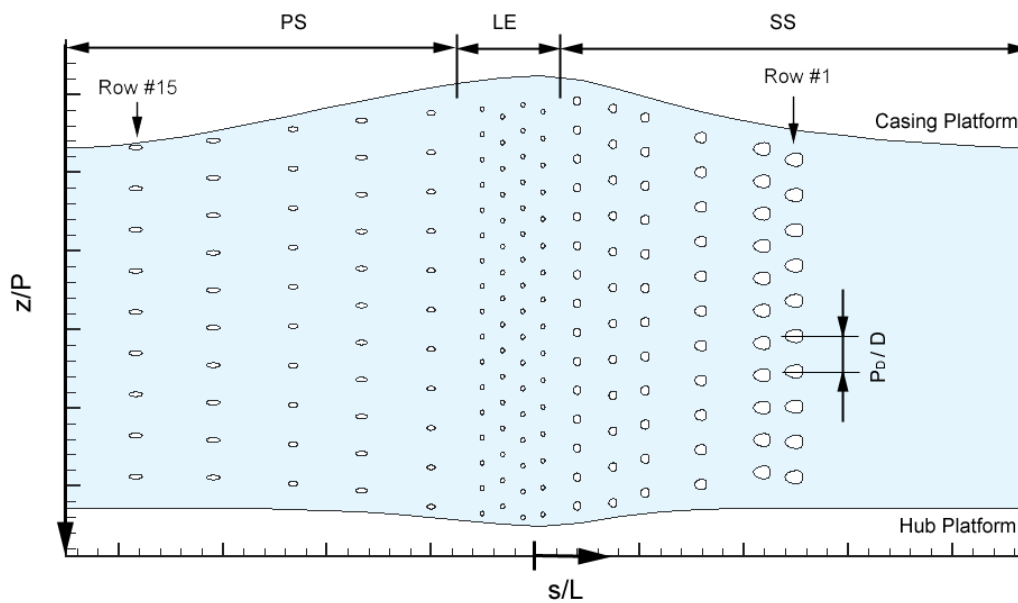


Figure 2-9: Unwrapped Surface of the Film-Cooled Nozzle Guide Vane

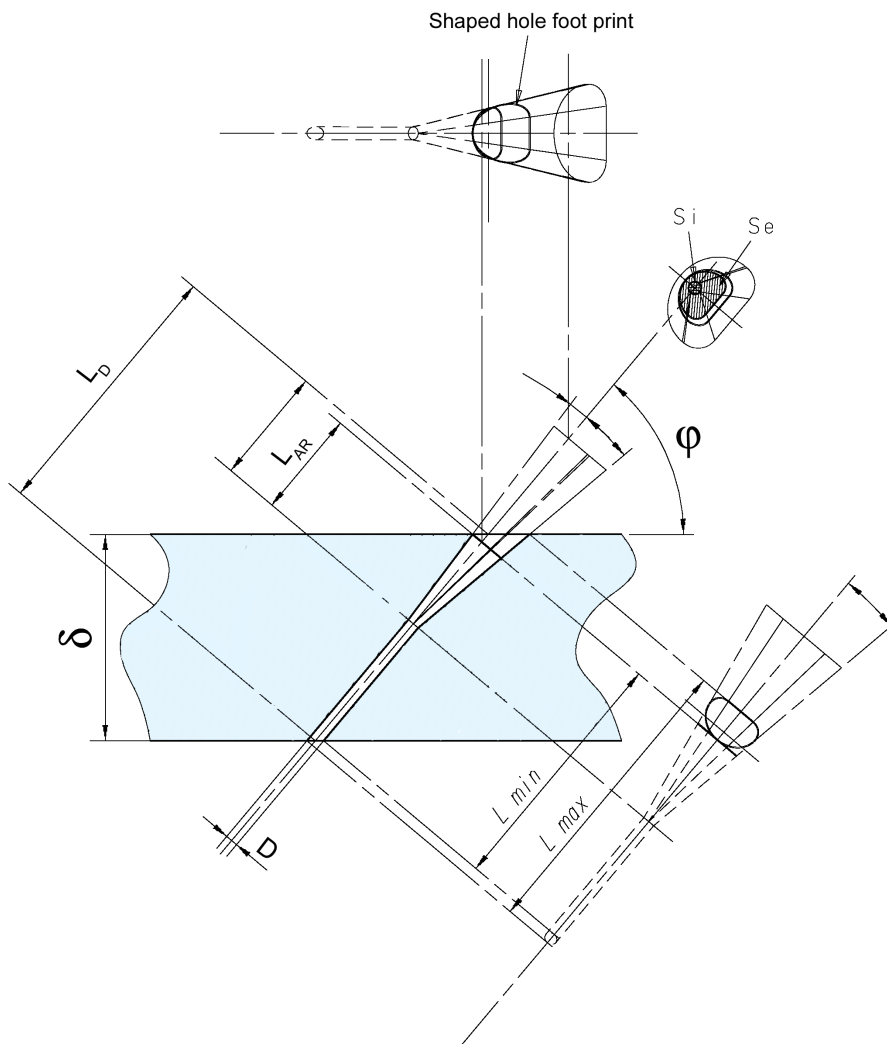


Figure 2-10: Fan-Shaped Hole Configuration and Notation

All the film-cooled measurements are performed at the nominal flow conditions and for a unique mainstream inflow angle of 0° (Table 2-3).

| Inflow angle | P_{t1} [mbar] | T_{t1} [K] | Re_{2L} | Ma_2 | $m_{g \text{ channel}}$ [Kg/s] |
|--------------|-----------------|--------------|-----------|--------|--------------------------------|
| 0° | 1450 | 324 | 1.31E+06 | 0.77 | 0.218 |

Table 2-3: Main Flow Condition for Vane Film-Cooled Measurements

Experimental variations are performed on the film cooling configurations. It consists of a series of six different and combined film-cooled areas opened. The active areas

are noted in Table 2-4 where PS stands for the rows #11 to #15 on the pressure side, LE for the rows #7 to #10 on the leading edge and SS for the rows #1 to #6 on the suction side. The total pressure of the coolant gas in the plenum chamber is adjusted in order to have about the same coolant gas distribution for the different configurations.

| Film Cooling Configuration | PS | LE | SS |
|---|----|----|----|
| Rows on pressure side only open | x | | |
| Rows on leading edge only open | | x | |
| Rows on suction side only open | | | x |
| Rows on pressure side and leading edge open | x | x | |
| Rows on leading edge and suction side open | | x | x |
| All rows of cooling holes open | x | x | x |

Table 2-4: Film-Cooled Area Configurations

The objective is to determine the influence of a film-cooled area to another and to find out if any superposition principle can be applied. However, because of the reduced material resistance of the Perspex and because of the use of only one plenum chamber, representative blowing ratios for certain areas could only be provided when rows of other areas were closed.

For the experiments, a unique film-cooled Perspex model is used. A 3M-Kapton tape, very resistant to the temperature and the pressure levels applied during the measurements, is used to seal the non-active rows.

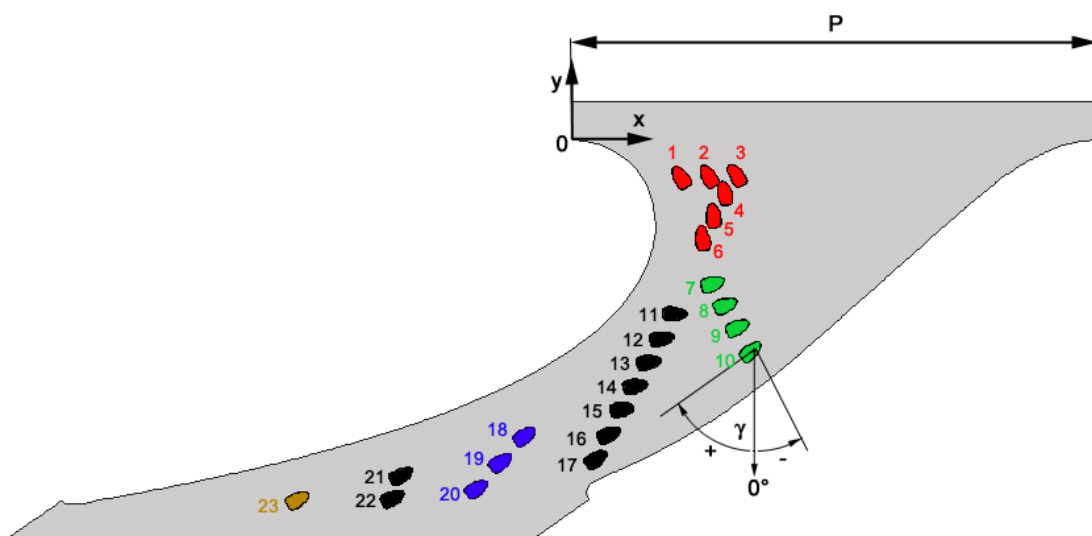


Figure 2-11 : Projected 2D Surface of the Film-Cooled Casing Platform

2.2.2 Platform Configuration

The platform film cooling hole design of the tested model is similar to the engine nozzle guide vane configuration. The extracted geometry requires a few modifications:

Compare to the original film-cooled vane platform, the hole pitch of holes #1 to #3 is slightly reduced in order to avoid exit hole interferences with hole #4. A similar pitch reduction is applied to holes #7 to #10 so that the two last holes have their inlet connected to the plenum chamber of the model. Compound angle φ of these two last holes as well as of the holes #16 and #17 are slightly reduced for the same reason. These modifications essentially imply holes close to the vane profile and are a consequence of a specific thickness of the platform models. The wall thickness is set to $\delta=3$ mm giving a $\delta/D=5$. The exit angle of the holes relative to the tangent of the surface is set to 30° for all rows, giving an $L_p/D>7$ preferably required for surface film-cooling injection (Burd et al, 1996).

The exit hole positions on the film-cooled platform surface (x,y) and the exit compound angle γ relative to the axial direction (y) are shown in Figure 2-11. All cooling holes are identically fan-shaped with a cylindrical inlet section. The type of fan-shaped hole is similar to the one present on the suction side of the vane airfoil with the same notations as in Figure 2-10.

The film-cooled nozzle guide vane platform on the casing side of the engine is fed by two plenum chambers allowing different pressure ratios between the holes close to pressure side (holes #7 to #17) and the other holes close to the suction side. For limited space reasons, it is not possible to design two separate plenum chambers on the model so that only one is considered for the experiments. However, both adjacent channels of the central vane are equipped with film-cooled platforms.

For the measurements on the platforms, only one baseline and one film-cooled experiments are performed at engine representative conditions given in Table 2-5.

| Inflow angle | P_{t1} [mbar] | T_{t1} [K] | Re_{2L} | Ma_2 | $m_{g\ channel}$ [Kg/s] |
|--------------|-----------------|--------------|-----------|--------|-------------------------|
| 0° | 1450 | 296 | 1.31E+06 | 0.77 | 0.218 |

Table 2-5 : Main Flow Condition for Platform Measurements

2.3 Conclusion of Test Configurations

- The geometry of a new generation gas turbine nozzle guide vane has been carefully extracted into a physical model for a linear cascade test facility. Steps of the geometry extraction, consisting of a vane airfoil conical cut, platforms stretching and a cascade flipping and scaling, have been described.
- The resulting linear cascade mounted on two discs has been presented. The hub side disc is used for optical access while the vanes and tailboards are mounted on the casing side disc. Four mobile tailboards allow adjusting flow periodicity, and a rapid insertion mechanism for the central vane allows performing transient experiments.
- Film-cooled vane and platform holes geometries have been detailed, and the different experimental conditions such as mainstream flow conditions and the different coolant gas injection configurations have been specified.

3 TRANSIENT MEASUREMENT TECHNIQUE

The transient measurement technique used for the heat transfer experiments is presented here, with a special focus on the transient liquid crystal signal analysis.

3.1 Basic Principle

The transient measurement technique consists of monitoring the surface temperature evolution in time triggered by a heat step. This heat step can be generated by electric heater foils on surfaces or with heater grids in the flow, or by rapidly exposing a preconditioned model to a different temperature level. Transient experiments have the advantage of avoiding conduction problems and being of short duration; hence more measurements can be performed in a limited amount of time compared to steady state techniques.

The transient surface temperature can be accurately measured by thermocouples or thin film gauges (on discrete positions) but with a known drawback of a poor spatial resolution. In order to obtain a higher spatial resolution, field methods need to be employed such as the thermo-chromic liquid crystal technique that consists of monitoring the surface temperature evolution by acquiring the color signal of a liquid crystal coating. By using a single layer of narrow-band thermo-chromic liquid crystals (Ireland & Jones, 2000), the evolution of the local surface temperature noted $T_w(x,y,t) = T_{LC}$ is obtained from a hue capturing technique of the color play.

Depending on the configuration of the experiment, a data analysis, usually based on transient one-dimensional heat conduction into a semi-infinite model, allows the calculation of local parameters such as heat transfer coefficient h and adiabatic film cooling effectiveness η .

With the goal of further increasing the quality of the measurements, and because of the deformed and limited optical access due to the nozzle guide vane platform geometries in this work, a novel hardware and image processing system has been developed. It uses multiple digital camera signals combined with powerful image processing software to obtain larger detailed liquid crystal surface measurements.

3.2 Hardware and Video Signal

During the transient liquid crystal experiment, the color variation of the liquid crystal signal coating is captured with several miniature color CCD cameras (TELI Tokyo

Electronic Industry Co) through access windows located around the test section (Figure 4-16). Placement of the small camera heads (diameter 12mm, length 40mm) in reduced area is being simplified, as they are separated from the signal processing electronic module boxes. Four camera views are typically used on the linear cascade test facility in order to capture the entire central vane surface. However, multiple cameras use can become problematic since the amount of data collected during the measurements may increase rapidly. In the past, a specific device was used during the experiment with maximum two camera views filtering the liquid crystal signal in real time. Hence the amount of data was reduced; but if the signal was of a too poor quality or the filtering parameters were not well adjusted, the experiment had to be repeated again. It is due to these problems that the real time signal processing has been avoided for the new system. Instead of this, each camera views the complete video signal, which is independently recorded on a digital support during the transient experiment. The Digital Video (DV) format storage has the advantage of ensuring precise color image signal restitution at a constant image frequency and without any noise generation. Moreover, the DV signal automatically contains the frame, time and recording date information that allows automatic search of a specific transient experiment video sequence.

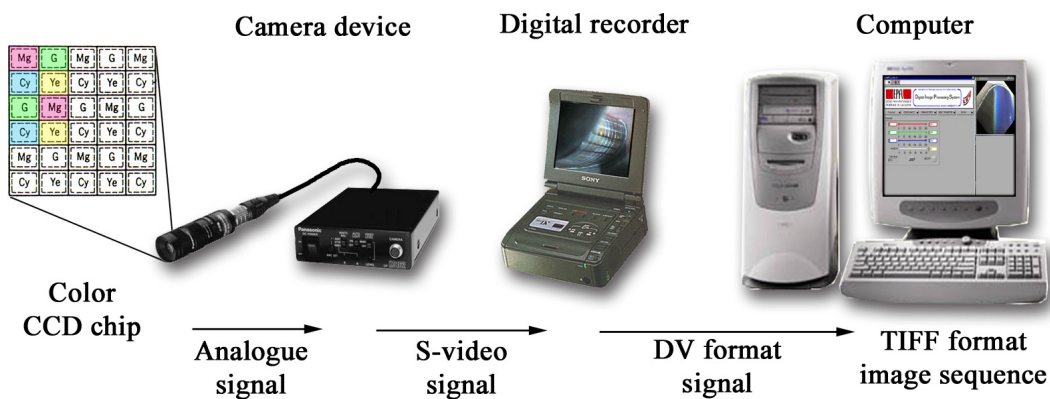


Figure 3-1: Format of the Transient Liquid Crystal Video Signal

Video sequences of the different camera views and transient experiments are then transferred after the measurements to a computer for image processing and data reduction. The format of the transient liquid crystal signal, from the camera view to the computer, is resumed in Figure 3-1.

The CCD camera chip is composed of 752 x 582 pixels with a mosaic structure of complementary color filters (Cyan, Magenta, Yellow plus Green). True color is obtained on each pixel location by combining interpolated color plane values of the neighboring pixels. Hence, the color value resolution depends essentially on the proximity of the different color filtered pixels (Theuwissen, 1995). A camera with three CCD (one for each basic color) has a higher resolution but the size is too large to be directly used for reduced optical access. In the future, the promising X3 chips from Foveon Inc. will capture the three basic color lights at the same pixel position thus with very high resolution and minimum size.

The liquid crystal color play, acquired by the CCD chip is converted into an analogue signal. The electronic camera device restitutes this information out to a so-called "S-video" signal. For standard PAL video format, the S-video signal has a resolution of 720 x 576 pixels at a frame rate of 25 images per second.

This S-video signal is then transmitted to a digital video recorder device where it is converted into a digital 24 bits RGB mode, compressed and recorded on a tape in the standard DV format.

After the transient experiments, DV format sequences are transferred onto a computer by a DV in/out IEEE 1394 standard data link. Transfer is executed in real time and coded in a standard PAL DV format (i.e. 25 images per second with a spatial resolution of 720 x 576 pixels). In order to be compatible with the image-processing program, the movie file is finally converted into a set of image files in a 24 bits RGB TIFF format. For one experiment and for one camera view, considering a maximum spatial resolution of 720 x 576 with the color coded on 3 bytes ($3 \times 8 = 24$ bits) it gives an image size of 1,24 Mbytes. By considering a transient experiment duration of 5 seconds with 25 images per second, it represents 125 images leading to an image sequence size of 155 Mbytes stored on the computer. By lowering the spatial resolution to 320 x 240, which still gives very good data resolution, the same image sequence is reduced to a size of 28 Mbytes. Hence, depending on the capacity and performances of the computer, either lower or higher resolutions can be used.

3.3 Digital Image Processing System (DIPS)

An image treatment of the digital video sequences allows one to automatically follow the time evolution of a color signal converted into a temperature level. This data reduction is performed on a personal computer with in-house programs written in the commercial LabView[®] language and using the IMAQ[™] image processing functions from National Instruments. Powerful coordinate transformations and image filtering functions (Jähne, 1993) are applied on the digital video sequences for noise signal filtering of undesired zones or light in-homogeneities. A hue color value threshold of the calibrated liquid crystal signal gives very precise temperature levels of the recorded surface. It is then possible on the tested surface to determine the time it takes to reach a specific temperature value along the transient experiment.

Figure 3-2 shows a typical transient liquid crystal TIFF image sequence recorded during a transient experiment issued from a baseline experiment on the nozzle guide vane. A heat step is here generated by the rapid insertion of the preconditioned cold vane model into the hot air main-flow.

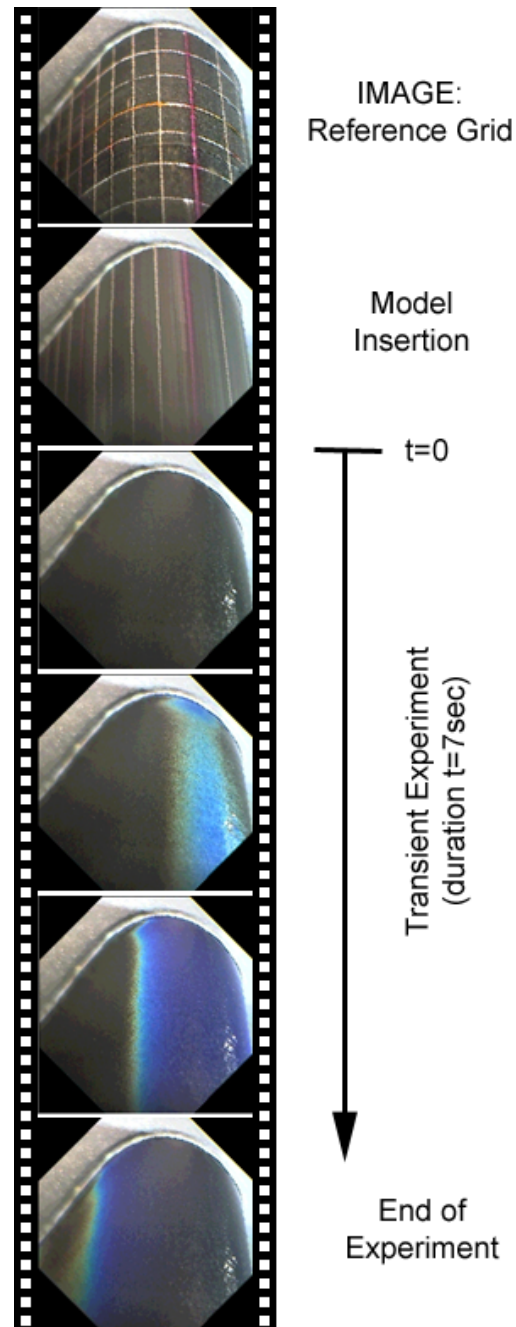


Figure 3-2: Transient Liquid Crystal Video Sequence of the Nozzle Guide Vane Leading Edge View

This sequence, representing the leading edge of the nozzle guide vane, is only one of the four views that are acquired in parallel during the experiments. The first image of the sequence shows the dummy vane part containing the reference grid. At the start of the transient experiment the dummy part of the central vane is replaced by the Perspex part coated by narrow-band reacting encapsulated thermo-chromic liquid crystals from Hallcrest™. Color signal appears first on the leading edge area and progressively develops on the rest of the surface.

Image signal can be coded in different color modes. The standard RGB mode, often used in video systems, is based on a combination of red, green and blue color planes. For the color liquid crystal filtering a more physical color-coding related to hue values is used. The HSI mode is based on hue, saturation and intensity planes (Kunt, 1993). Both color modes are coded in 24 bits i.e. 8 bits per plane corresponding to 255 discrete levels of each component as shown in Figure 3-3.

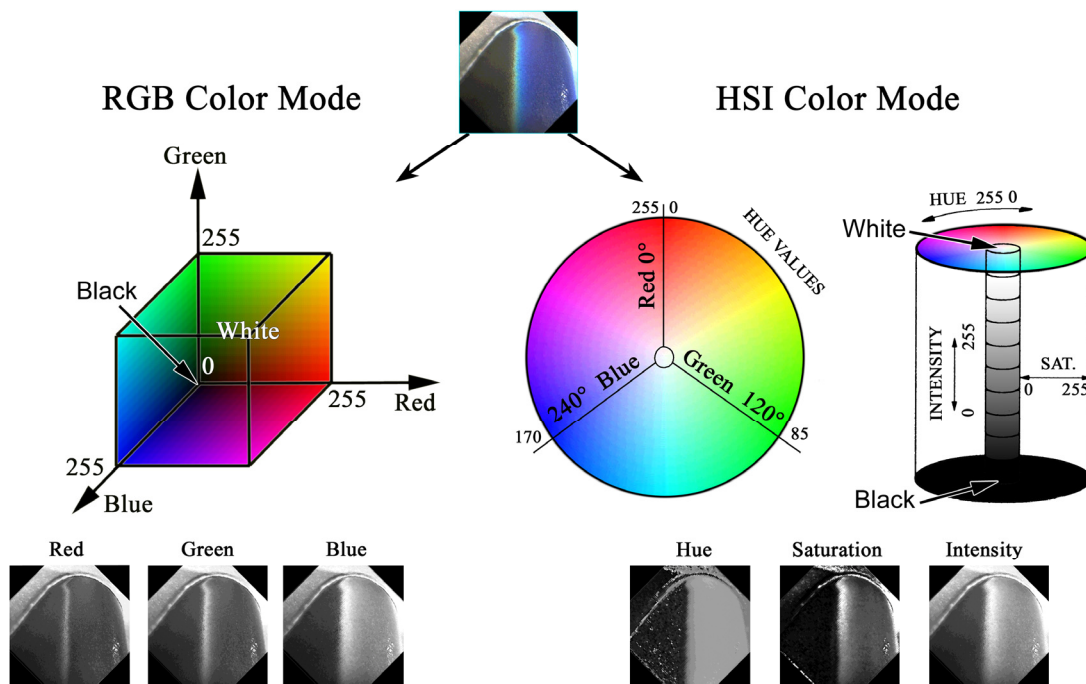


Figure 3-3: RGB and HSI Color Modes

In order to eliminate light reflections and inhomogeneities, a difference operation is performed on all the images of the sequence with a reference image usually taken just after the vane insertion that does not contain any liquid crystal signal. Very good results are obtained by performing the difference in HSI color mode on the saturation

and intensity planes only so that the hue information of the liquid crystals is not altered. Figure 3-4 shows such a difference operation for one image of the sequence.

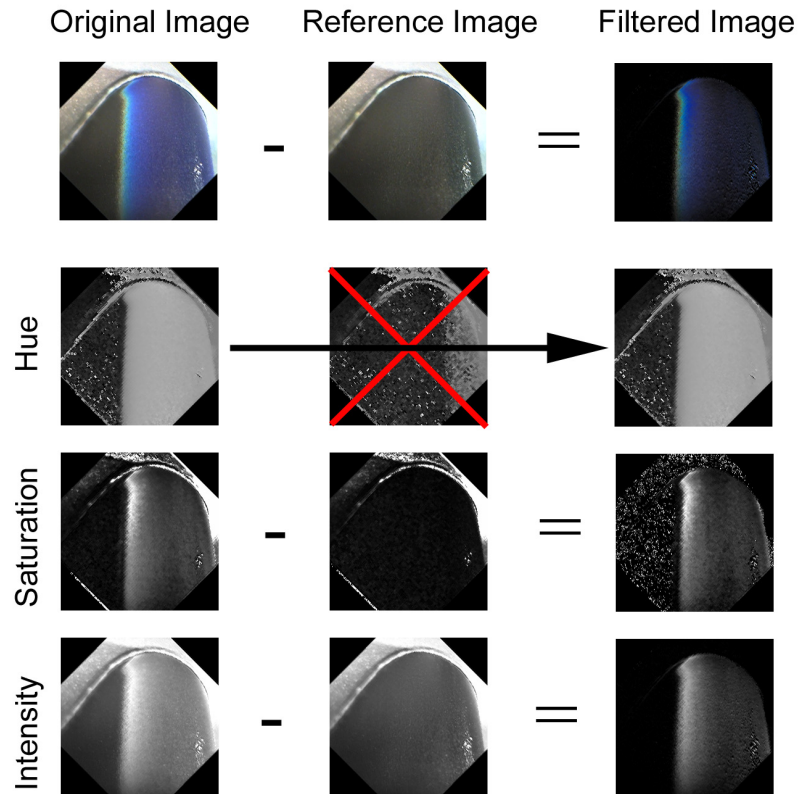


Figure 3-4: Light Inhomogeneities Filtering

By using a steady state calibration, a specific hue value of the liquid crystal signal can be related to a specific temperature level. Typically, the green color signal with a hue level of around 85 (on a scale of 0 to 255) and a margin of ± 5 is taken into account. For narrow-band liquid crystals (0.7K), this gives accuracy on the surface temperature detection of about $\pm 0.03\text{K}$. Hue filtering can be combined with a saturation and intensity threshold in order to avoid either too low or too high levels that are often sources of noise. Figure 3-5 shows a typical hue filtered image result.

Threshold can either be directly applied on the images of the original sequence or on the previously obtained light inhomogeneities filtered sequence. In this case, a combined saturation and intensity threshold is not necessary, as noise signal is already eliminated. Note that as all the color play of the liquid crystal signal is acquired with the new digital system, hue threshold can also be applied on multiple

hue levels, hence for multiple temperature levels (especially in the case of using wide band liquid crystals).

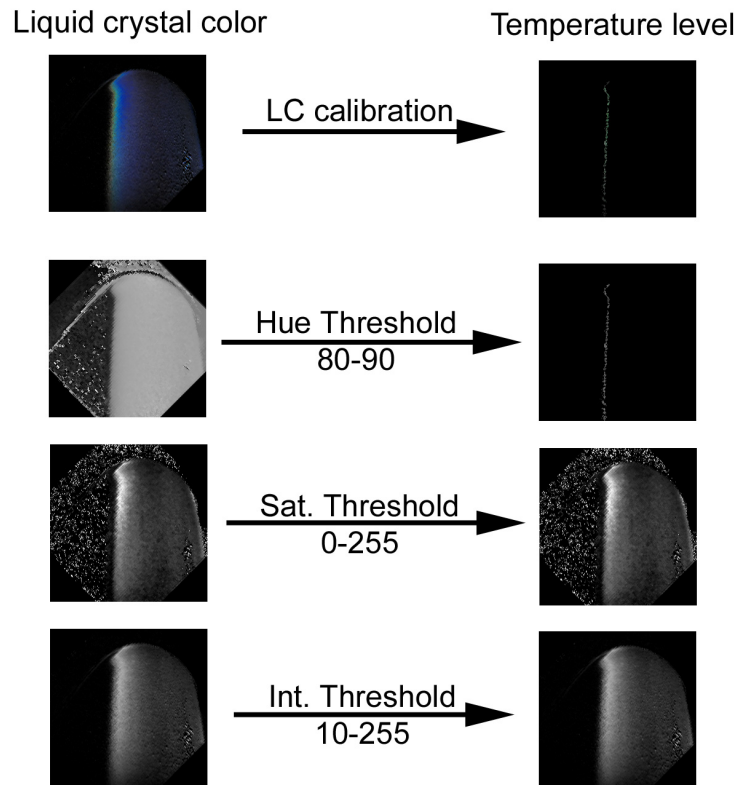


Figure 3-5: Temperature Level Filtering

Once the images of the sequence contain only events of the chosen hue filtered color (hence of the specific calibrated temperature level) the time lap between the start of the transient experiment and a local event appearance can be extracted. As color band filtered images are of good quality, time event detection is performed for each pixel position leading to a higher spatial resolution, and not on a group of pixels as it was with the previous system. Moreover, in the past, due to non noise-filtered data, the hue filtered signal needed to appear over a consecutive number of images in order to be considered as an event. The new developed image processing system allows taking into account every event of individual pixels on each image. Hence, it provides a better acquisition of fast evolution signals that appear only on one image of the sequence.

The camera views inevitably contain a perspective and/or deformed image representation. It is therefore practical to perform a coordinate transformation so that

each pixel position of the image is referenced to the surface coordinate of the physical model. Each view has its own coordinate transformation but on the same final coordinate system so that they can be assembled all together for a complete surface representation. For the rapid insertion system, a simple square reference grid of 5mm spacing on the dummy vane part is acquired from each camera point of view before the transient experiment. These grid lines are then used to define a set of spline interpolation functions to transform the views into a surface reference coordinate system (usually corresponding to an unwrapped surface). The figure below shows this operation for the leading edge camera view.

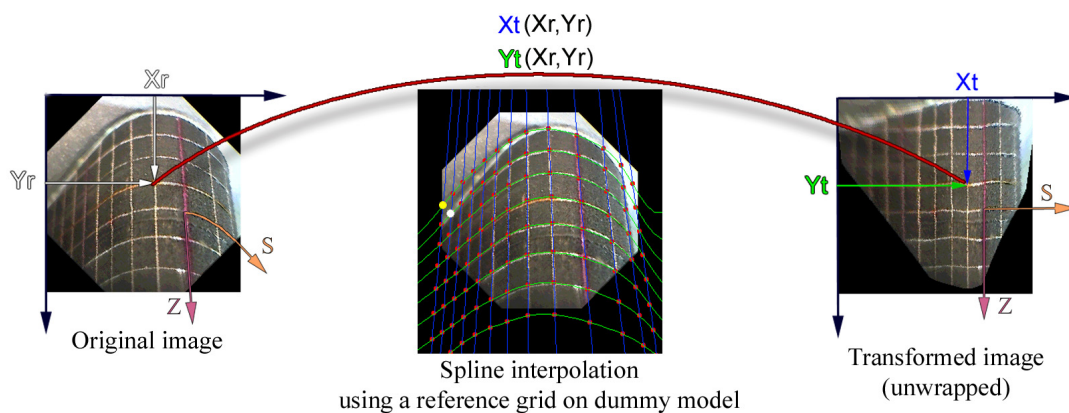


Figure 3-6: Reference Grid and Image Transformation

Coordinate transformation is usually applied on the final reduced time event detection data only, rather than on all the images of the original un-filtered sequence. It gives the same result in both cases.

Coordinate transformation is also performed in order to combine over the same area other such data as the initial surface temperature measured by thermocouples or the static pressure distribution on the vane surface issued from pressure taps. Therefore, these discrete measurements are interpolated on the same coordinate system. They are necessary for the data analysis giving the heat transfer results. When assembling the measurements of the different views altogether the overlapped zones give identical results with less than 2% variations. This indicates there is almost no influence of the different camera view angles on the T_{LC} temperature calibration or that the error is very small for narrow band liquid crystals.

However, the overlapped zones usually have different spatial resolutions. The

average spatial resolution of each view is defined by the total number of pixels used for the total surface covered by the camera after coordinate transformation. For the final result, results of the different views are interpolated on a global mesh with an averaged spatial resolution. On the overlapped zones, the views with less noise or higher resolution are usually taken into account.

3.4 Transient Time Experiment

Being for the baseline case or for the film-cooled case, with the rapid test section insertion or with the heater-foil activation, data analysis of these transient experiments are all based on theoretical models with some specific assumptions. One of them is the maximum time duration for which the experiment is still considered transient.

Several years ago, a lot of research focused on transient measurement methods that were dedicated to shock tubes test facilities. The goal was to obtain accurate temperature measurement transducers that had to be used for very short time periods. Experiments and theoretical analysis on these transducers had given specific correlations for the determination of the maximum time for correct data acquisition. As some of the layers combining these transducers were of relatively large thicknesses, analysis of the transient effects was based on the assumption of semi-infinite models. Schultz and Jones (1973) estimated the maximum allowable measurement time for such experiments to be:

$$t_{\max} \leq \frac{\delta^2}{16\alpha} \quad (3.1)$$

where δ is the wall thickness and α the thermal diffusivity of the material.

More recently, the semi-infinite model assumption and its associated criterion have been applied for larger time scales measurement methods such as the transient liquid crystal technique. The inconvenience of this criterion application is that for certain experiments, very thick walls are required or the maximum measurement time is very limited.

In order to determine the validity of this criterion for the correct use of the semi-infinite model assumption, analysis of the latter is performed and compared to a finite wall thickness model. Configurations of the two physical models are shown in Figure 3-7 with typical temperature profile evolutions in the material.

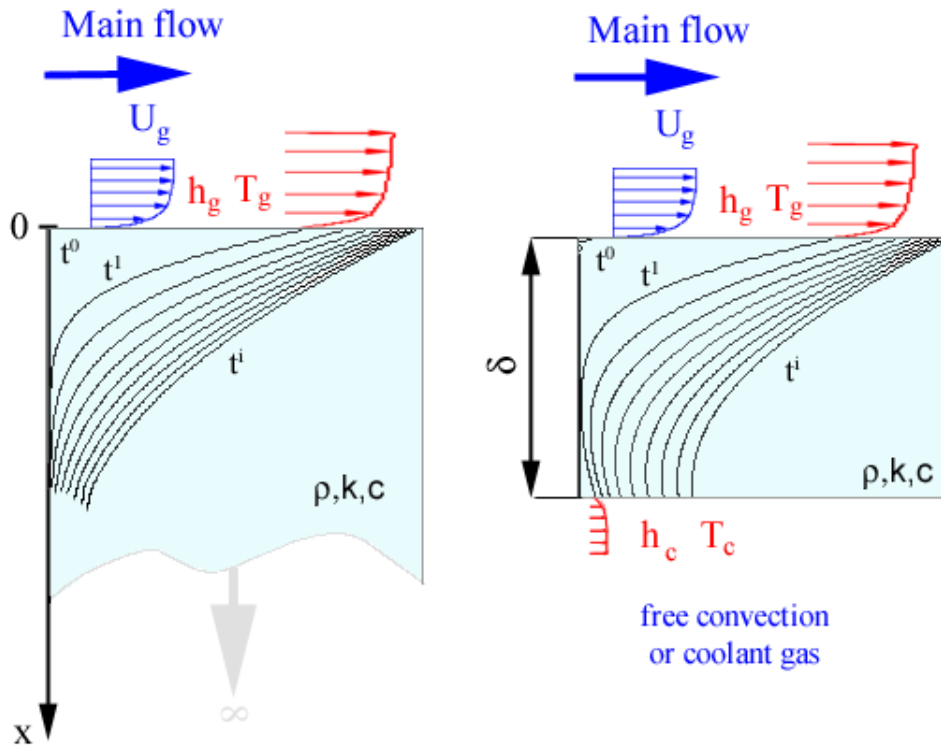


Figure 3-7: Semi-Infinite and Finite Wall Configurations

The theoretical developments of the finite and semi-infinite wall models are respectively given in Appendix A and Appendix B. These models allow one to determine the main flow heat transfer coefficient h_g (or Bi_g in dimensionless form) from a transient liquid crystal experiment where t , T_{LC} , T_i , T_g , T_c (or τ , θ_{LC} , θ_c in dimensionless form) are known. For the finite wall model, however, a rough approximation of h_c (hence of Bi_c) is also required. Results of a typical transient liquid crystal experiment determined by the two models are given in Figure 3-8.

It shows that both models give the same result for transient dimensionless times τ lower than 1/4 (solid black vertical line on the graph). The semi-infinite criterion of 1/16 (dashed red vertical line on the graph) previously used is here not representative and thus not appropriate for the transient liquid crystal experiments.

Indeed, when looking at temperature evolution on the lower part ($x=\delta$) (Figure 3-9), it is obvious that the 1/16 criterion corresponds to the very restrictive case for which no alteration of the lower wall temperature is required.

For the transient liquid crystal technique, it is not the temperature level but the heat transfer coefficient Bi_g that has to be considered. Moreover, Figure 3-8 shows that despite a temperature change of the lower wall of the model given in Figure 3-9, the

heat transfer coefficient determination is still accurate for $\tau < 1/4$. Above this value, the temperature levels between the representative finite case and the semi-infinite approximation are so different that the latter over-determines the heat transfer coefficient.

Figure 3-9 also shows that the finite model, being more accurate than the semi-infinite one, is in very good agreement with the measurements.

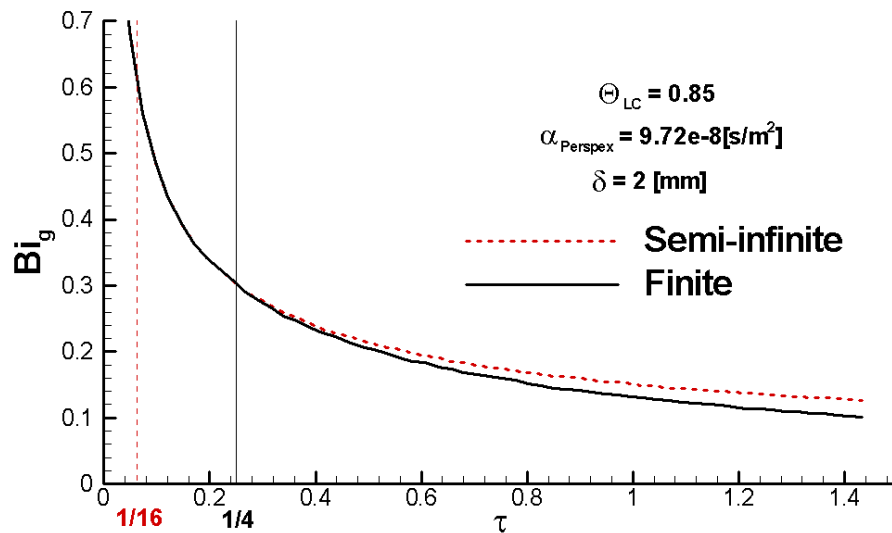


Figure 3-8: Dimensionless Heat Transfer Coefficients Determined by the Finite and Semi-Infinite Model for Different Time Experiments

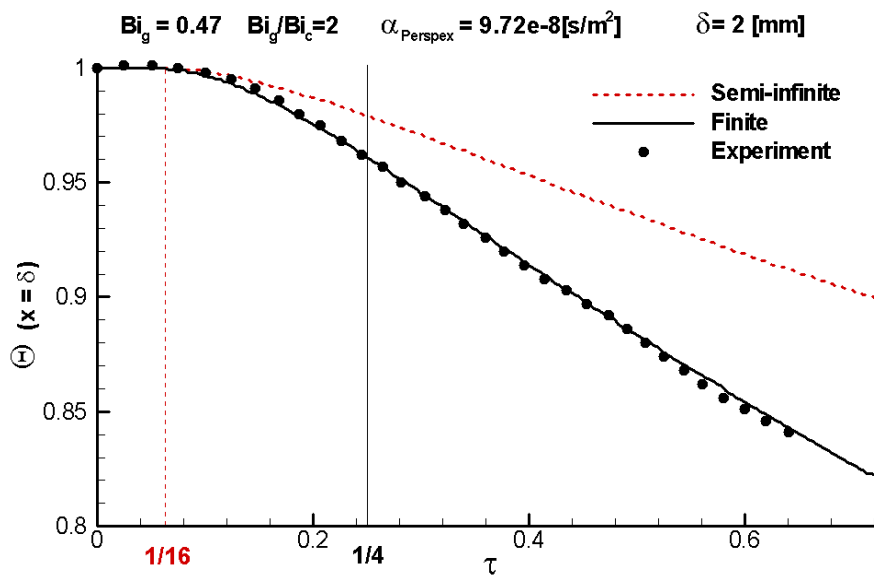


Figure 3-9: Dimensionless Wall Temperature on the Lower Surface ($x=\delta$) for the Finite Model, the Semi-Infinite Model and Measurements

Considering the temperature evolution on the upper surface ($x=0$), Figure 3-10 shows that variations of Bi_c of an order of magnitude only affect Θ_{wall} values for τ greater than 0.35 (black vertical bold line).

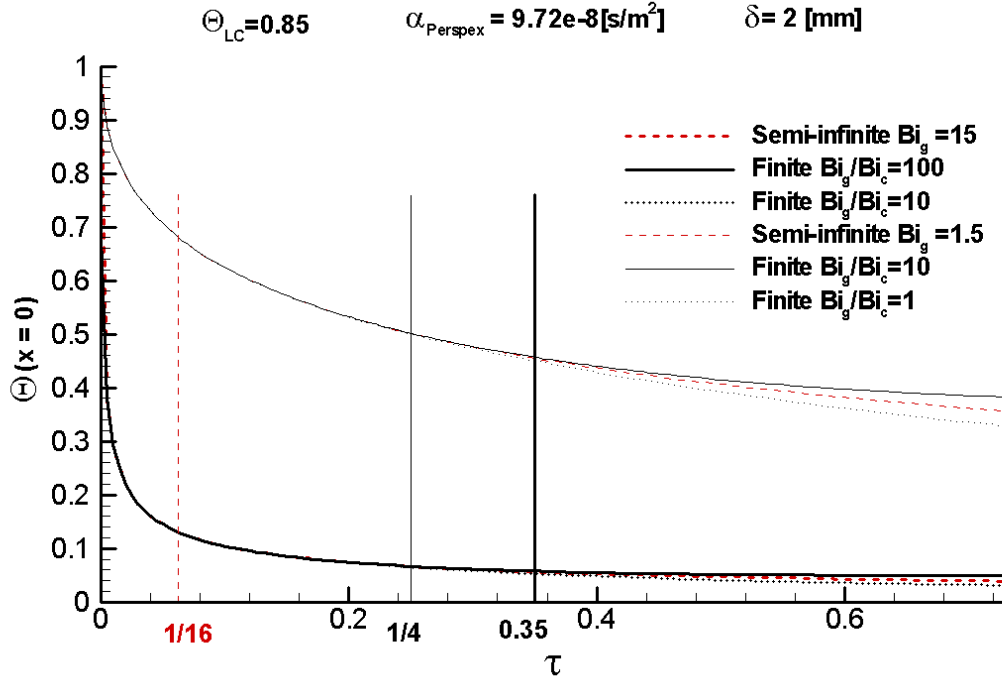


Figure 3-10: Dimensionless Wall Temperature on the Upper Surface ($x=0$) for the Semi-Infinite and Finite Models, with Rough Bi_c Estimations

In conclusion, for a specific wall material and thickness δ , the semi-infinite model applied for the heat transfer coefficient determination is valid for $\tau < 1/4$ and not for $\tau < 1/16$ as considered in the past. The finite model with a rough approximation of Bi_c is valid for $\tau < 0.35$. If the model with the finite wall thickness assumptions shall be used for longer times, then values for Bi_c have to be accurately known.

Alternatively, it means that for a specific experiment with the maximum transient time t_{max} , the semi-infinite model is only valid for wall thicknesses larger than:

$$\delta > \sqrt{\frac{\alpha t_{max}}{0.25}} \quad (3.2)$$

By using the finite model with a rough approximation of Bi_c , the wall thickness can be reduced to:

$$\delta > \sqrt{\frac{\alpha t_{max}}{0.35}} \quad (3.3)$$

and can be reduced even more with the finite model if the approximation of Bi_c is

more precise.

For the transient liquid crystal experiments performed on the vane airfoil and on the platform, because of the higher complexity and longer time iteration of the finite model, the maximum transient time experiment and the minimal wall thickness are chosen so that they satisfy the use of the semi-infinite model for the data analysis. Hence, for a typical Perspex ($\alpha=9.72\text{e-}8$ s/m²) material of $\delta=3$ mm wall thickness, it gives a maximum time period of the transient experiment of $t_{max}=23$ seconds. Then, the conditions of the transient experiments such as the main flow temperature, the initial wall temperature, and the temperature reaction of the transient liquid crystal have to be adjusted so that data are measured within a maximum time period of 23 seconds.

3.5 Conclusion of Transient Measurement Technique

- The basic principles of a transient experiment have been introduced with the data analysis developments given in Appendix A and Appendix B.
- A novel digital image acquisition and processing system for the transient liquid crystal technique has been presented. It allows performing experiments with multiple cameras. It is combined with a Digital Image Processing computer program, which provides powerful post-processing filtering, coordinate transformations and data reductions. In addition, with this very low noise filtered signal, data analysis can be performed on each pixel. Hence, it results in a higher spatial resolution and a better acquisition of fast transient liquid crystal signals.
- The criterion of the maximum allowable transient time has been analyzed and compared to a new model, which makes use of the fact that the wall at which the liquid crystal coating is applied is of finite thickness. However, due to the finite model complexity, the preference goes to the use of the semi-infinite model but with an increased dimensionless time τ criterion that is adapted for transient liquid crystal experiments.

4 VANE EXPERIMENTS

This chapter covers the measurements dedicated to the vane airfoil. It starts first with the aerodynamic experiments presented in sub-chapter 4.1, and continues with the development of the heat transfer experiments. The latter is divided into two parts, one dedicated to the baseline measurements given in sub-chapter 4.2, and another one dedicated to the film-cooled vane results described in sub-chapter 4.3.

4.1 Aerodynamic Measurements on the Vane

Aerodynamic measurements related to the vane airfoil for three different inflow angles: -12° , 0° and $+12^\circ$ consist of a flow periodicity check as well as a downstream isentropic Mach number distribution measured by static pressure taps on the casing wall. The surface Mach number distribution on the central vane, used by the heat transfer data analysis for the recovery gas temperature determination, is also measured. In addition, a 5-hole probe mounted on an automatic traversing system is used for aerodynamic loss measurements through the cascade. Results are compared between the different cases.

4.1.1 Flow Periodicity

In order to check the flow periodicity through the cascade, pressure taps measurements of the central vane are compared to the values of the neighbouring vanes. Locations of the static pressure taps are specified in Figure 4-2 and the results are given in Figure 4-1. These graphs show a very good flow periodicity for all inflow angle configurations, especially on the pressure side. On the suction side, a very small difference is noticeable at the maximum flow velocity, indicating that at this location the left channel flow is slightly less accelerated than the right one. Differences are however acceptable and the flow can be considered periodic.

In order to see how the aerodynamic characteristics of the nozzle guide vane change with the inflow angle, it is interesting to compare on the same graph the central vane velocity profile at the TE mid-span position. The three sets of measurements are performed with the same relative tailboards positions and with about the same mainstream total inlet pressure. At 0° inflow angle it gives an isentropic downstream Mach number close to 0.77 (nominal flow condition); And at -12° and $+12^\circ$ inflow angles, the exit Mach numbers are slightly different as shown in Figure 4-3.

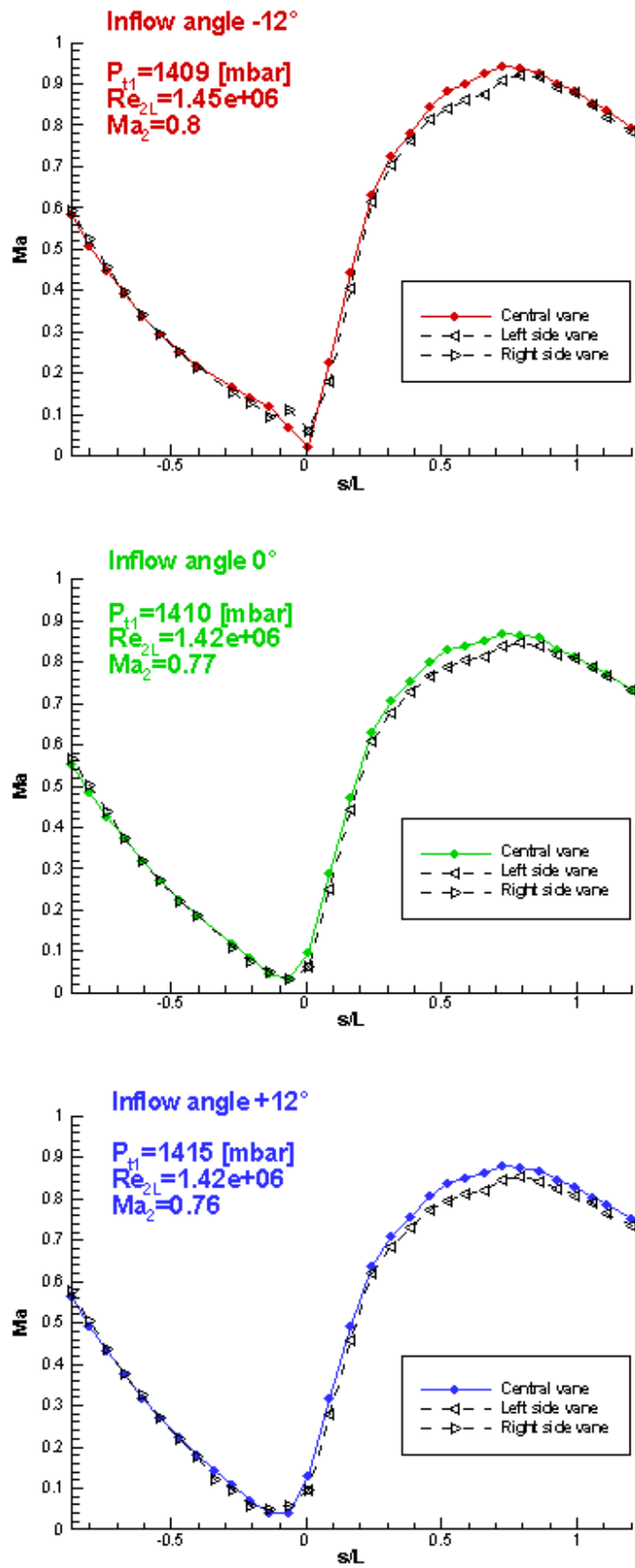


Figure 4-1: Flow Periodicity Check for the Three Inflow Angle Configurations

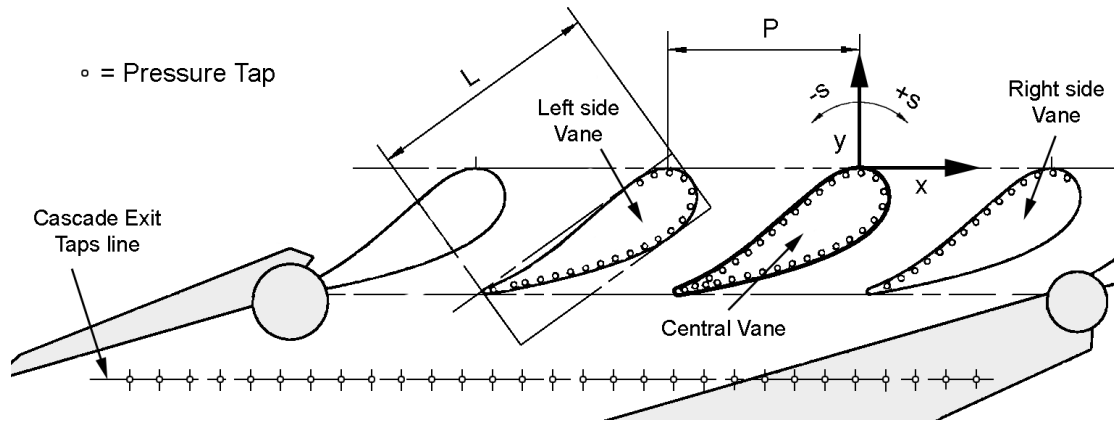


Figure 4-2: Static Pressure Taps Locations

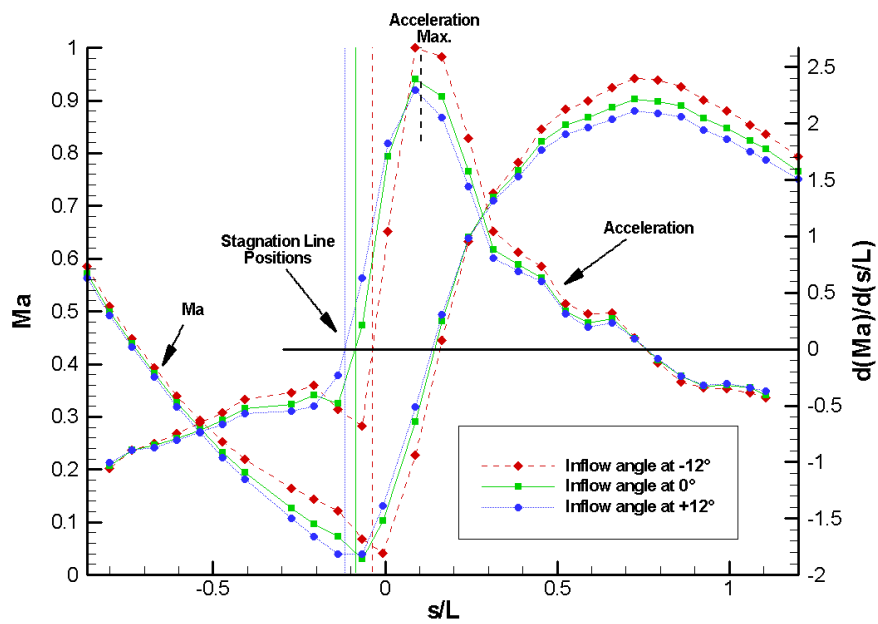


Figure 4-3: Central Vane Ma and Acceleration at Mid-Span TE

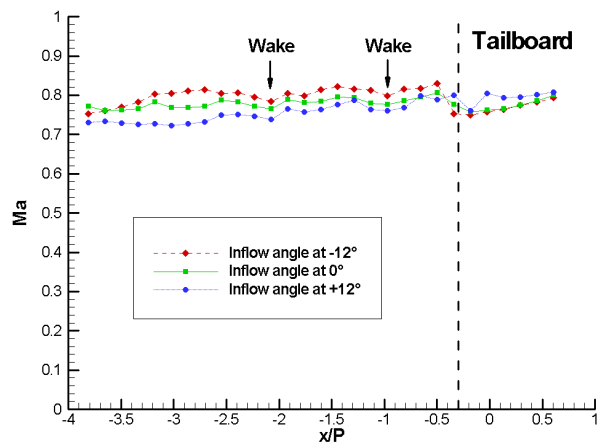


Figure 4-4: Outlet Ma Distribution on the Casing Wall

For a given total inlet pressure level of the flow, a decrease of the cascade angle produces less blockage effect. As a consequence, the Mach number on the suction side increases slightly when the flow deviation decreases. As expected, the stagnation line locations (s/L positions represented by vertical lines on the graph) move to the pressure side when the mainstream inflow angle increases.

The Mach number acceleration curves are represented on the same graph. Acceleration has to be positive on the pressure side when considering the flow going to the negative s/L direction. However, for graphical reasons the acceleration curves are given for the flow going to the positive s/L direction. The stagnation line positions (vertical lines in the graph) are then given by the curves crossing the zero $dMa/d(s/L)$ line. Maximum acceleration occur on the suction side around $s/L=0.1$ for the three inflow angle cases.

The downstream isentropic Mach number distributions measured on the casing wall are given in Figure 4-4. The discrepancy at $x/P > -0.3$ is due to the obstruction of the pressure taps by the large tailboard. For $x/P < -0.3$, the curves are quite parallel with a vertical offset due to the increase of the exit Mach number for a decreased inflow angle as already noticed in Figure 4-3. In this region, the small oscillations every vane pitch length $x/P=1$ are due to the wake passage of the vane airfoils.

4.1.2 Mach Number Distribution

The mobile central vane has a plane of static pressure taps distributed all around the profile. The span-wise surface pressure distribution can then be measured by shifting the central vane at different span-wise positions. However, as already mentioned in chapter 2, to allow the displacement, a small gap filled by Teflon tape is present between the central vane and the contoured platforms up to the sealing boxes. In order to check that there is no undesired leakage flow circulation in this area, liquid crystals sensitive to shear stress are applied on the central vane airfoil. The flow is then visualized by the traces left on the surface. The traces of Figure 4-5 show that there is no undesired flow recirculation at the walls junctions. Only the vane separation lines induced by the horseshoe vortices on the suction side very close to the contoured platforms are present. More details about the secondary flows of the contoured platforms are given in chapter 6.

The detailed isentropic Mach number distributions on the surface of the airfoil vane for the three different inflow angle configurations are present in Figure 4-6. Results are given with the vane surface and platform contours unwrapped as defined by

Figure 2-2 (bottom left). The complete pressure surface measurement on the central vane shows that the flow cannot be considered two-dimensional due to the contoured platforms. The concept of platform contouring as a reduction of the airfoil span between the leading edge and the trailing edge (Deich et al., 1960) results in a reduction of velocity in the region of highest turn and a shift of the diffusion part of pressure distribution on the suction surface toward downstream. This can be observed between the less contoured hub side and the more contoured casing side in Figure 4-7 where the Mach number distributions are represented at two different z/P span positions.

Looking in the span-wise direction on Figure 4-8 where the span-wise Mach number profile is presented for two specific positions, one on the suction side at $s/L=+0.5$ and another on the pressure side at $s/L=-0.5$; for the suction side, it leads to a faster flow velocity on the casing side than on the hub side. The opposite tendency is observed on the pressure side. The offset values between the three cases are a consequence of an accelerated flow when the mainstream inflow angle decreases.

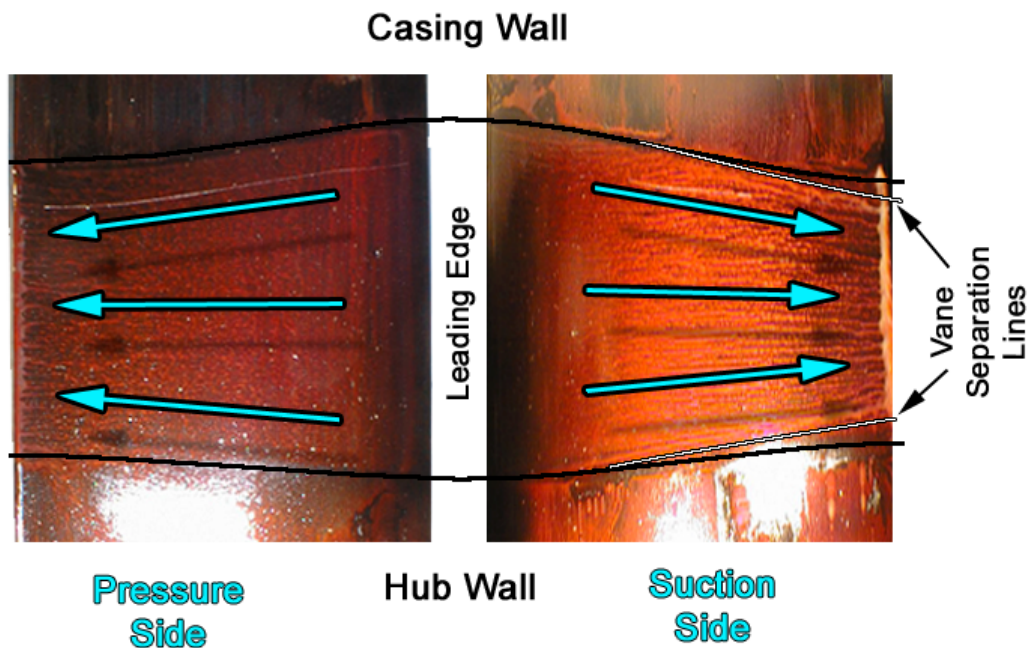


Figure 4-5: Surface Flow Visualization on the Vane with the Use of Liquid Crystal Sensitive to Shear Stress

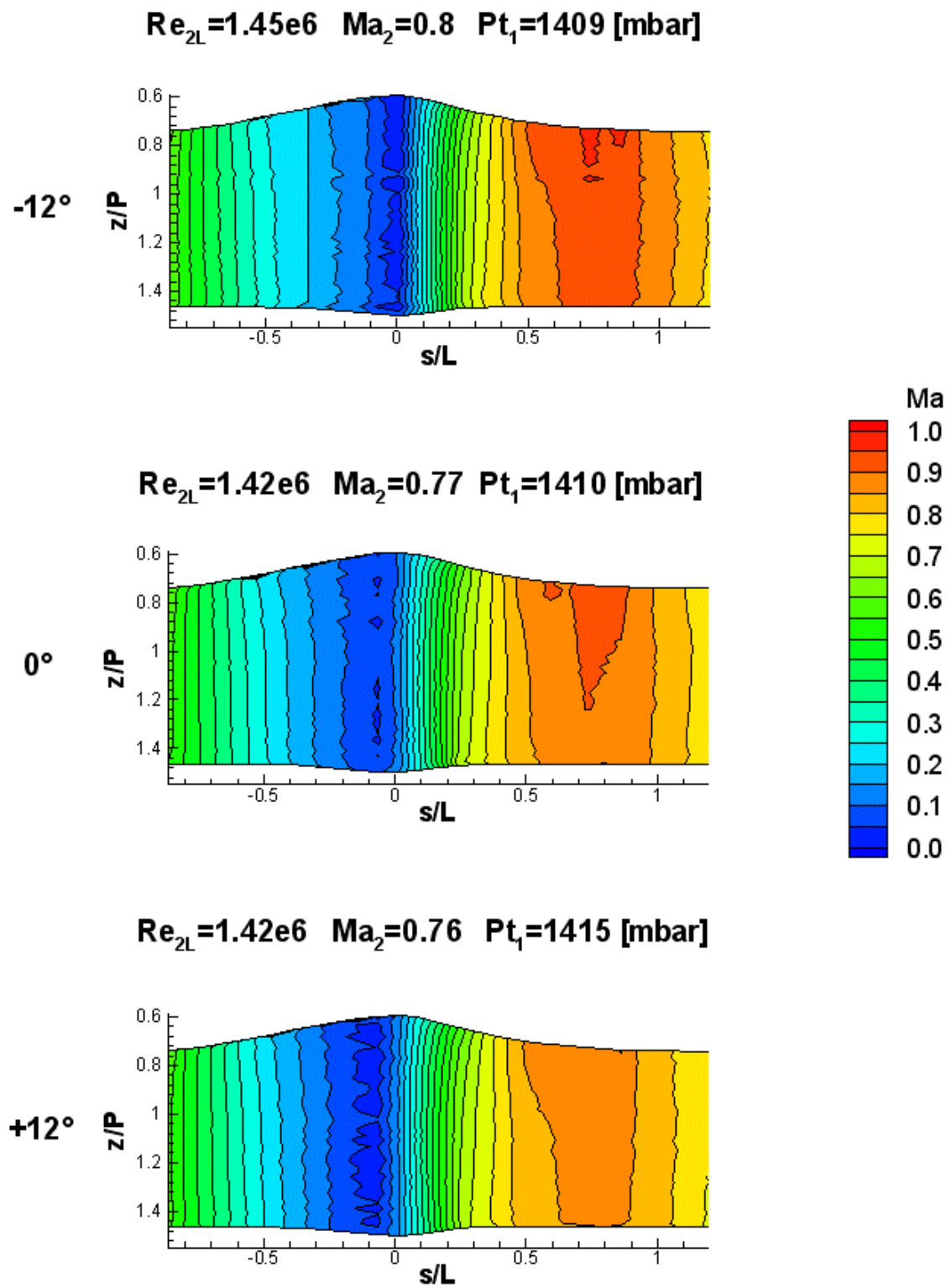


Figure 4-6: Ma Surface Distribution for the Three Inflow Angles

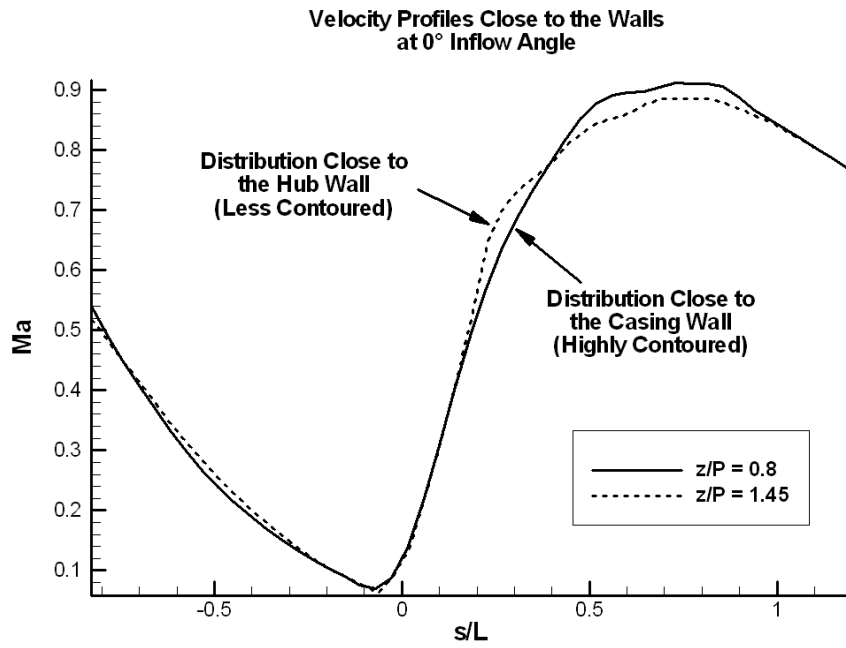


Figure 4-7: Ma Distribution Close to the Contoured Walls

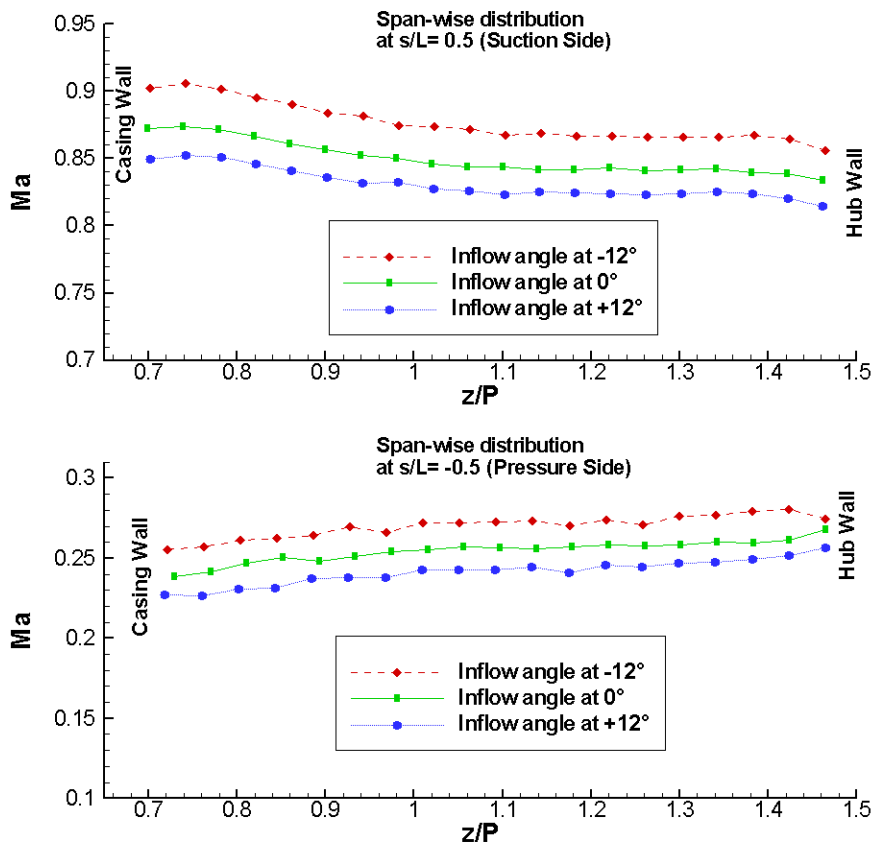


Figure 4-8: Span-Wise Ma Distribution at $s/L = +0.5$ and $s/L = -0.5$

4.1.3 Loss Measurements

For contoured platforms, the more favourable pressure gradient induced by the span-wise contraction impedes the growth of the boundary layers on both the airfoil surface and the platforms. This is the major benefit of platform contouring and offers an effective means for controlling the secondary flow and reducing the aerodynamic losses (Dossena et al., 1998).

To measure the losses of the nozzle guide vane studied in this work, a traversing probe system shown in Figure 4-9 is mounted on the hub side of the test section. A special ribbon protected by a very thin wall translates with the probe and ensures sealing at any probe position. For geometrical compatibility, this probe sealing box system is mounted just under the contoured hub wall.

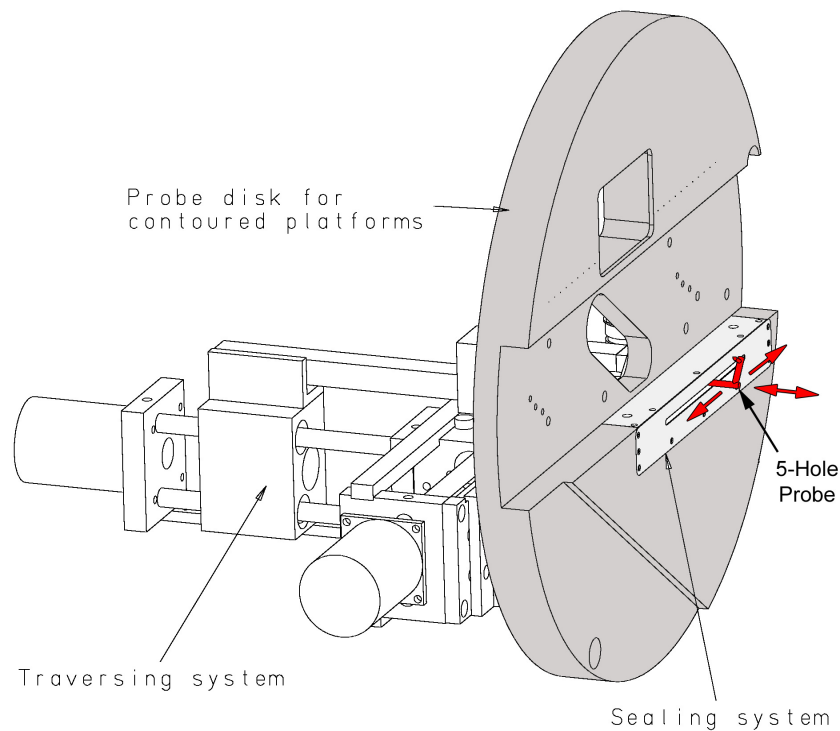


Figure 4-9: Traversing Probe System

The position of the probe relative to the linear cascade is indicated on Figure 4-10. Due to the lack of space, a flow periodicity check on the loss measurements with complete traverse on two channels (2P) is not possible. It is, however, sufficient by the use of an L shaped probe, to have measurements in the wake of the central vane. Because of the flow deviation generated by the contoured platforms, a 5-Hole probe is used to determine the correct total pressure downstream the cascade as

well as the flow direction. It is located at about 86% chord length downstream of the vane trailing edge, assuming an exit flow angle of 74° .

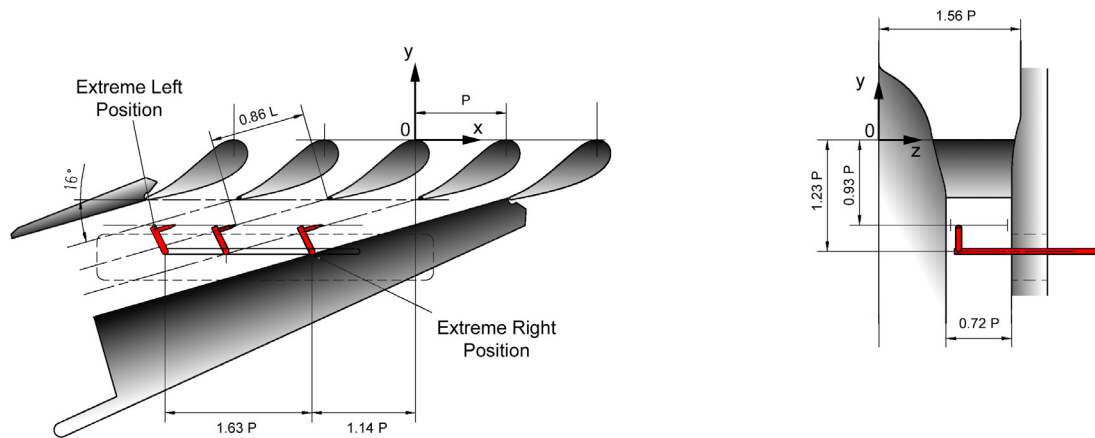


Figure 4-10: Pneumatic Pressure Probe Positions in the Linear Cascade

The spatial representation and relative position of the plane measured by the 5-Hole probe as well as the definitions of the angles for the flow direction are given in Figure 4-11. Despite the size of the probe, loss measurements are performed as close as possible to the contoured walls (90% of the exit span).

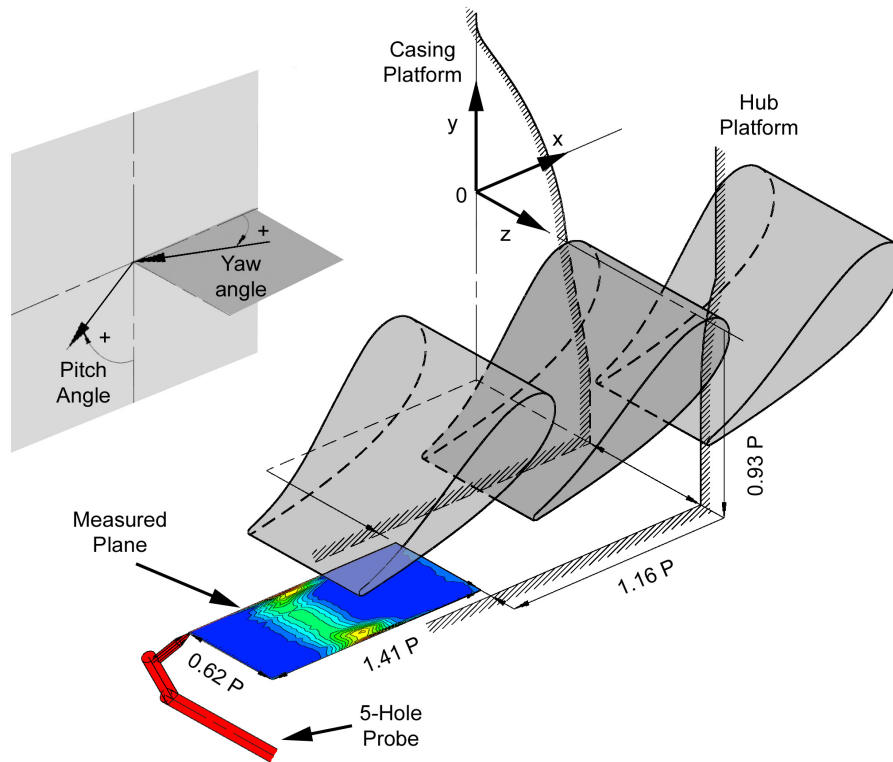


Figure 4-11: Position of the Probe Measured Section

Measurements are performed at nominal flow conditions for the three inflow angles. Figure 4-12 represents the enthalpy loss coefficient defined as follow (Denton, 1993):

$$\zeta_{loss} = 1 - \frac{u_2^2}{u_{is2}^2} = \frac{\left(\frac{p_{s2}}{p_{t2}}\right)^\theta - \left(\frac{p_{s2}}{p_{t1}}\right)^\theta}{1 - \left(\frac{p_{s2}}{p_{t1}}\right)^\theta} \quad \theta = \frac{\kappa - 1}{\kappa} \quad (4.1)$$

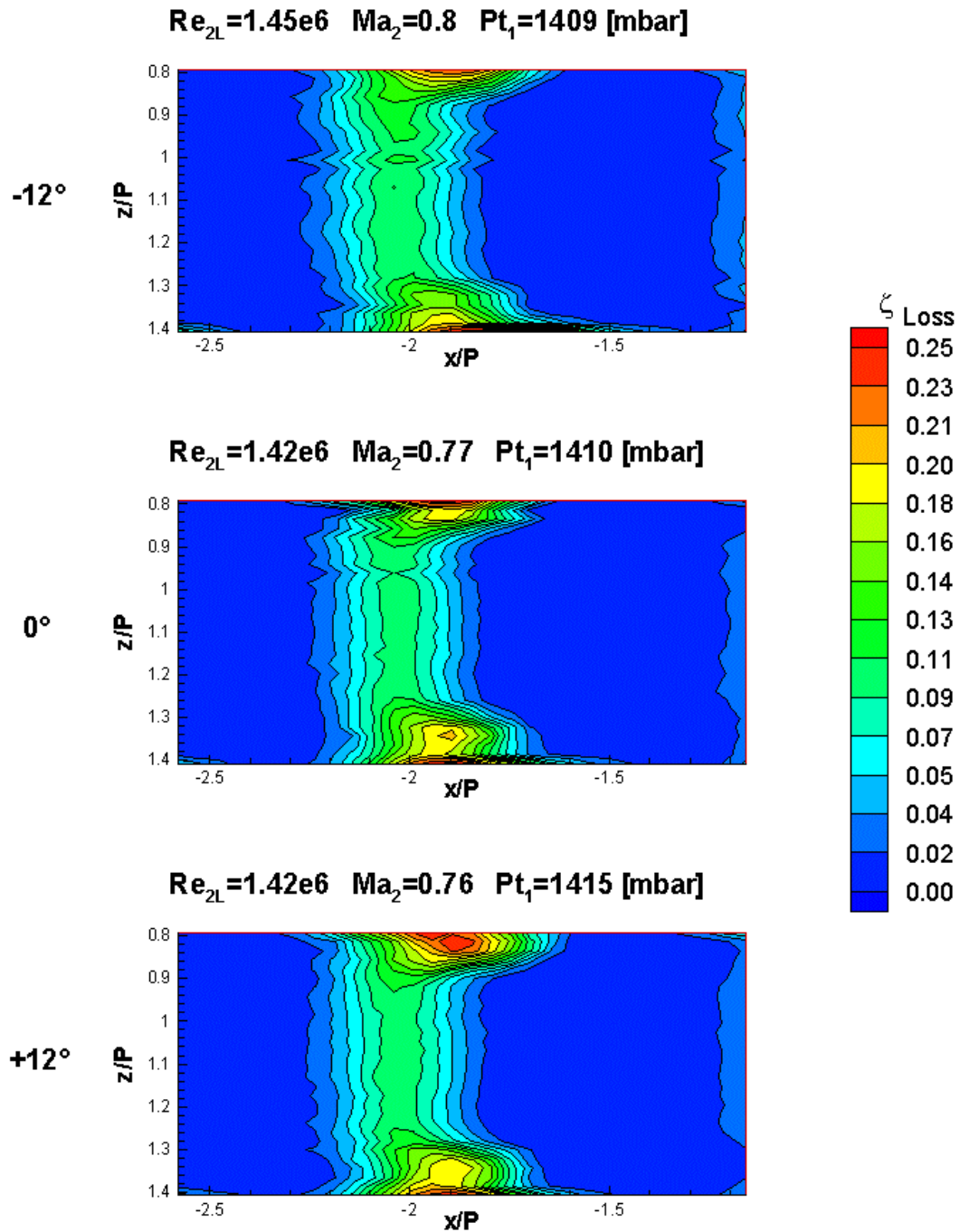


Figure 4-12: Loss Measurements at Three Different Inflow Angles

The results show a typical wake signal with two core zones close to the walls coming from the suction side. These core zones extend and increase in intensity as expected when the inflow angle is increased. Local loss coefficient reaches up to 25% on the high contoured casing wall of the +12° case where the flow deviation is maximum.

For the nominal configuration at 0° inflow angle, the core size is smaller on the casing side than on the hub side. This demonstrates the beneficial effect of the contoured platform and is a consequence of the reduced boundary layer due to the higher acceleration on the more contoured casing wall.

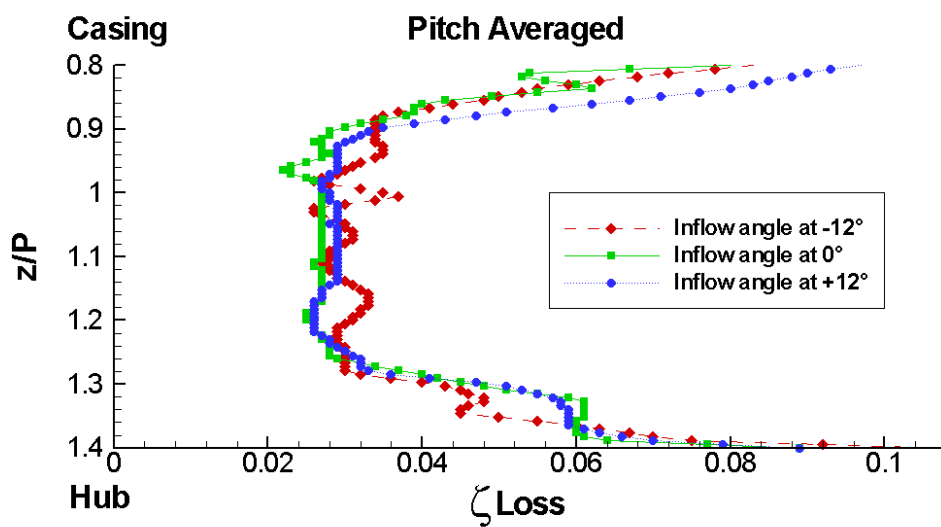


Figure 4-13: Pitch Averaged Loss Measurements

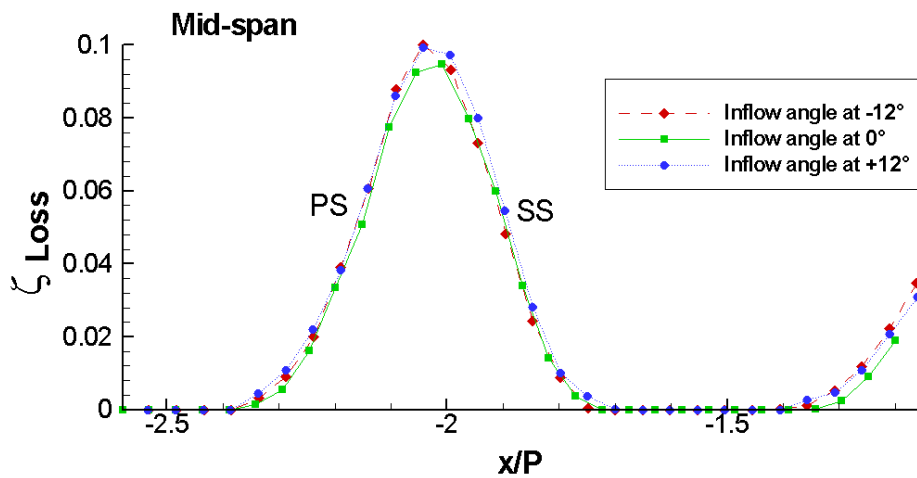


Figure 4-14: Loss Measurements Comparison at Mid-Span TE Position

Despite the core zones, in order to see the difference of the three inflow angles, the values of the losses are pitch-averaged in Figure 4-13. It shows a quasi-identical averaged loss distribution with a more important zone on the hub side ($1.25 < z/P < 1.4$).

In order to see if there is any wake position difference between the three inflow cases, loss values are extracted at the trailing edge mid-span position. The curves are presented in Figure 4-14. It shows that for all the different inflow angles, position of the wake downstream the cascade is identical. Moreover, at mid-span position, loss intensity and profile do not change. However, the pitch averaged downstream flow direction is different. Figure 4-15 shows a slightly higher flow deviation on the casing side than on the hub side, again as a consequence of the high contoured casing wall. The offsets between the cases are due to the accelerated flow when the mainstream inflow angle decreases.

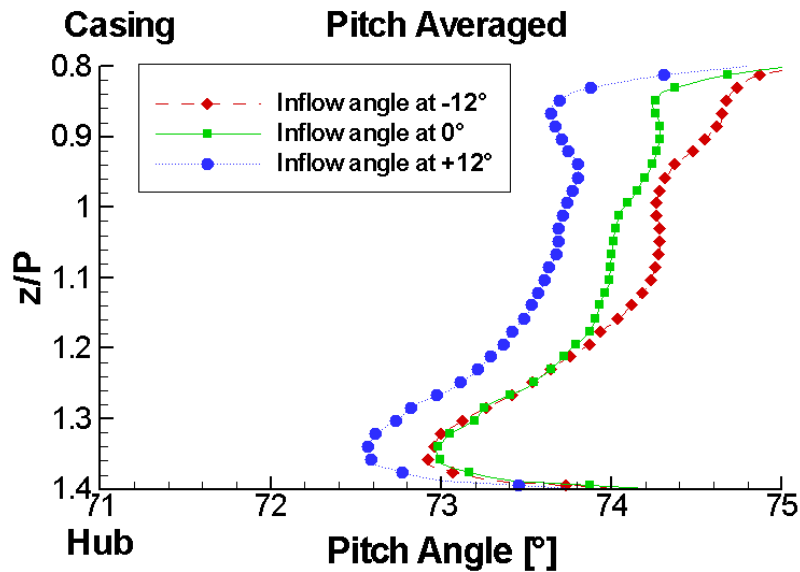


Figure 4-15: Pitch Averaged Pitch Angle

In order to determine the global difference between the three inflow cases, results are mass averaged over one pitch length and the maximum span-wise section (Table 4-1). Despite the lack of measurements very close to the walls due to the size of the probe, averaged values are quite representative, as the mass flow is lower there.

The averaged pitch outflow angle decreases with an increase of the inflow angle. The averaged yaw outflow angle stays constant and is negative due to the highly

contoured casing platform. The averaged mass flow loss is about the same for the three different inflow angles with a minimum of 3.29% for the 0° case. The total mass flow (of a channel passage) being slightly different between the three inflow cases, no clear tendency can be extracted from the results, except that the averaged loss increases with the mass flow. However, principally due to the contoured platforms, the levels of losses obtained on the nozzle guide vane studied in this work are quite low compared to similar vanes geometries but with non-contoured platforms (Reiss, 2000).

| Inflow angle | P _{t1} [mbar] | T _{t1} [K] | Re _{2L} | Ma ₂ | m _{g channel} [Kg/s] | Average exit Pitch angle | Average exit Yaw angle | Average loss % |
|--------------|------------------------|---------------------|------------------|-----------------|-------------------------------|--------------------------|------------------------|----------------|
| -12° | 1409 | 303 | 1.45E+06 | 0.8 | 0.219 | 74.01 | -1.81 | 3.46 |
| 0° | 1410 | 303 | 1.42E+06 | 0.77 | 0.218 | 73.89 | -1.77 | 3.29 |
| +12° | 1415 | 302 | 1.42E+06 | 0.76 | 0.225 | 73.41 | -1.87 | 3.59 |

Table 4-1: Mass Averaged 5-Hole Probe Measurements

4.1.4 Conclusion of Aerodynamic Measurements on the Vane

- Three sets of measurements have been performed at nominal flow conditions with three different inflow angles: -12°, 0° and +12°.
- For each flow condition, flow periodicity has been checked and surface Mach number distribution has been obtained. Flow is non-two-dimensional due to the presence of the contoured platforms.
- Loss measurements have been performed with traverses of a 5-Hole probe downstream the cascade. A typical loss coefficient distribution behind a vane cascade was observed. However, due to the contoured platforms, the core zones were less pronounced. Wake profile and mass averaged losses were almost identical for the three inflow angle configurations.

4.2 Baseline Heat Transfer Measurements on the Vane

This sub-chapter describes the baseline heat transfer measurements on the vane. Baseline measurements are essentially used for comparisons with the film-cooled configurations. Moreover, as the experimental process is simpler, it allows for a check of the geometry set-up and the transient liquid crystal technique before performing the more complex film-cooled measurements. Heat transfer coefficients are measured and compared to correlations found in literature and to numerical simulations.

4.2.1 Baseline Experiment Setup for the Vane

4.2.1.1 Optical Access

The first step of the heat transfer measurements for this specific geometry consists of finding an optical access for the central vane. When using the transient liquid crystal technique, the better the optical access is, the better the heat transfer measurements are. For this reason, as already presented in chapter 2, a quite large part of the hub platform is made out of Perspex and used as a window. This allows the maximum optical access but because of the hub-contoured platform, the window has some deformations and a small lack of visibility on a region situated at the beginning of the contour on the wall. Therefore, another window upstream from the cascade provides an optical access to the leading edge area of the vane. Windows in blue in Figure 4-16 represent the optical access used where all the cameras and light sources needed for the heat transfer measurements are pointing to the central vane test section. At least four camera views are necessary to have proper coverage of the central vane test section. One camera is fixed left to the central vane for recording a large pressure side surface. Another small camera is fixed on the window upstream of the cascade for recording the leading edge region, and two more cameras are used on the right of the central vane for recording the suction side area. An advantage of the new digital video system is that each recorder device has a monitor display showing in real time the view associated to its camera. It makes it easier to perform the adjustment of the cameras and lights, and ensures a good coverage verification of the measured zones. For the liquid crystal signal detection, the required light illumination is brought to the windows through fiber optics connected to so called “cold halogen light sources” with adjustable intensities. The positions and directions of the light spots are set in order to avoid any reflections as well as shadow

zones on the test section. Installation of the photographic equipment (cameras and lights) is an important part of the experiment, as it directly influences the quality of the heat transfer measurements. If the liquid crystal signal on some regions is not visible with the camera, even with powerful filtering, determination of the heat transfer coefficient is not possible. Experience with liquid crystal measurement equipment is necessary to be able to take sufficient high quality measurements.

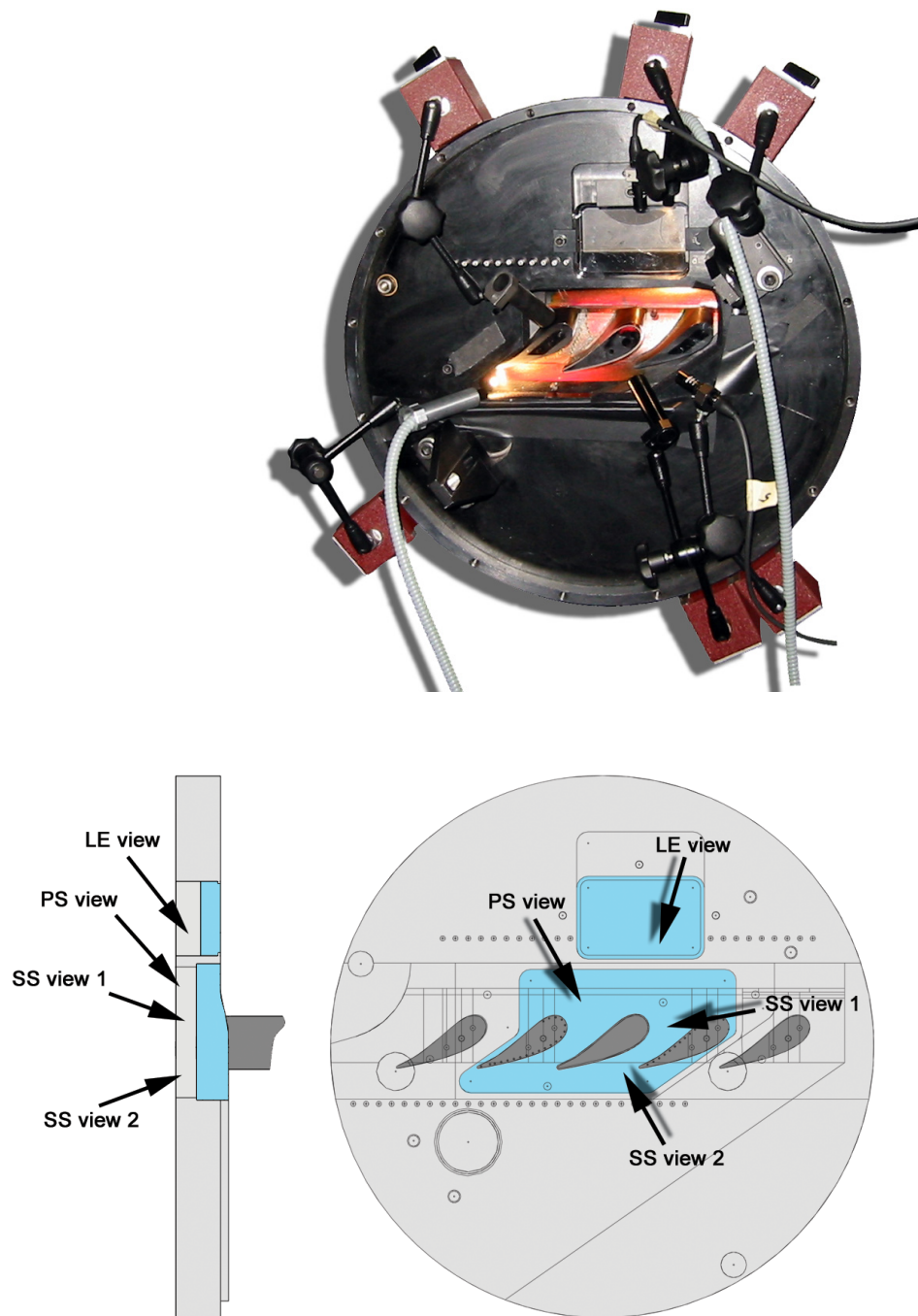


Figure 4-16: Picture and Drawing of the Global Optical Access for the Measurements on the Central Vane

4.2.1.2 Liquid Crystal Coating

Heat transfer measurements quality depends also on the liquid crystal coating applied on the test surface, which usually consists of three different layers applied in the following order:

- one black backing acrylic layer: Hallcrest BB-G1.
- one liquid crystal layer: Hallcrest BM/R30C1W/C17-10
(quantity: 3 ml LC + 1,5 ml water)
- one varnish protection layer: Hallcrest binder AQB-2

Coating is performed with a professional spray device with very small particles coming out of the spray but with many passages in order to get the most homogeneous surface in thickness. As liquid crystal particles are quite transparent, light reflection is used during spraying for checking the homogeneity of the layer. During the coating application, any dust deposit has to be avoided, as any irregularity on the surface would lead to undesired turbulent spot transition during the measurements.

In order to have information about the homogeneity of the coating and some roughness parameter estimations, the liquid crystal coating roughness is measured by a Mitutoyo Surftest 301 device on different regions of the central vane before the experiments.

| Suction side | | | | Pressure side | | | |
|--------------|------|----------------------|-----------------------|---------------|------|----------------------|-----------------------|
| s/L | z/P | Ra [μm] | R3z [μm] | s/L | z/P | Ra [μm] | R3z [μm] |
| 0.1 | 0.8 | 0.59 | 2.7 | -0.1 | 0.8 | 0.67 | 3.1 |
| 0.1 | 1.45 | 0.7 | 3.3 | -0.1 | 1.45 | 0.8 | 3.2 |
| 0.6 | 0.8 | 0.64 | 2.9 | -0.5 | 0.8 | 0.66 | 2.9 |
| 0.6 | 1.45 | 0.55 | 2.7 | -0.5 | 1.45 | 0.96 | 3.5 |
| 1.1 | 0.8 | 0.73 | 3.4 | -0.9 | 0.8 | 0.8 | 2.6 |
| 1.1 | 1.45 | 0.67 | 3.2 | -0.9 | 1.45 | - | - |

Table 4-2: Liquid Crystal Coating Roughness Results

Values are given in Table 4-2 with one typical roughness profile (of position 2 on Suction side) represented in Figure 4-17. They demonstrate a very good roughness homogeneity and a low roughness level of the liquid crystal coated surface.

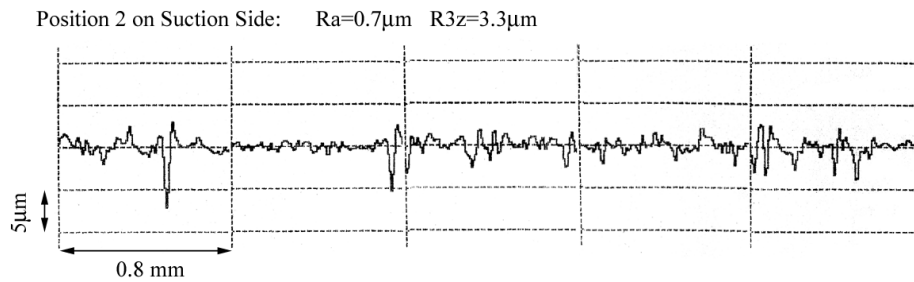


Figure 4-17: Typical Liquid Crystal Coating Roughness

Once applied on the tested surface, the lifetime of the liquid crystal is quite short, depending on the intensity of the main flow. In addition, after a certain number of temperature cycles, the reaction time is increasing. Moreover, when exposed to high light intensities (especially UV light) for a long amount of time, the liquid crystal signal intensity decreases. Therefore before each set of measurements, a new coating is applied. As a result, it provides a liquid crystal signal with the best quality.

4.2.2 Baseline Vane Heat Transfer Measurement Procedure

The test vane is made out of cast Perspex for its small heat transfer conductivity, allowing relatively long transient time experiment for thin material thickness. It has the following properties:

| | | |
|------------------------------------|----------|-----------------------------|
| Thermal conductivity | k | 0.17 [W/mK] |
| Density | ρ | 1189 [Kg/m ³] |
| Specific heat at constant pressure | c_p | 1500 [J/KgK] |
| Thermal diffusivity: | α | 9.53e-8 [m ² /s] |

For a minimum thickness of 3 mm at the trailing edge of the vane, the maximum allowable time given by equation (3.2) is about 23 seconds.

The Perspex test section of the central vane is first placed in a pre-conditioning box where the temperature is set to approximately 270 K. The cooling box is supplied by pressure air (adjusted to about 1200 mbar), which is dried and cooled through two coolant devices. The preconditioning temperature level is adjusted so that the unsteady measurements last less than the maximum time allowed for the semi-infinite model assumption. Liquid crystal signal detection depends on the type of narrow band liquid crystal used (typically reacting at around 303 K), on the adjusted initial temperature level, on the total gas temperature level (around 333 K) and

principally on the heat transfer coefficient distribution induced by the flow conditions around the physical model.

Eight thermocouples mounted at two different span-wise positions around the vane airfoil give the temperature homogeneity of the pre-conditioned model and check that the required initial level T_0 is reached. Homogeneity is of about ± 2 K but a surface interpolation is accounted for during the data analysis to reduce the measurement uncertainty on T_0 to ± 0.5 K. Once the main flow condition is attained, and the initial temperature level and homogeneity reached, the unsteady experiment can start. The video recording systems are first activated and the Perspex vane test section is rapidly shifted from the preconditioning box to the main flow of the linear cascade (Figure 2-7).

Heat transfer measurements consist of recording the liquid crystal signal evolution on the test section from the different camera views. Once the signal has been detected on the entire surface, the vane test section is re-inserted in the cooling box for the preparation of the next experiment. Video recording is then stopped or paused until the next transient test. For every experiment, it is important to have the vane insertion sequence recorded as well as the reference grid captured as shown in Figure 3-2. The grid allows performing the coordinate transformation, and the last image of the insertion sequence gives the start of the transient experiment.

Once the video sequences are transferred to the computer, the heat transfer coefficients are determined by a signal analysis as described in chapter 3 and with a data reduction based on the theory of the semi-infinite model developed in Appendix B. Including the transient liquid crystal signals, the parameters required for the determination of the heat transfer coefficients are as follows:

Mainstream: Total pressure p_{tg} , total temperature T_{tg}

Physical model: Static pressure distribution p_s (for the recovery gas temperature), Initial surface temperature T_0 , temperature calibration of the filtered liquid crystal colour T_{LC}

The static pressure distribution, the initial surface temperature and the locations of the liquid crystal temperature detection are all specified in a reference coordinate system representing the vane airfoil surface unwrapped. Figure 4-18 shows the corresponding coordinate transformation of each camera view and their location on the unwrapped vane surface.

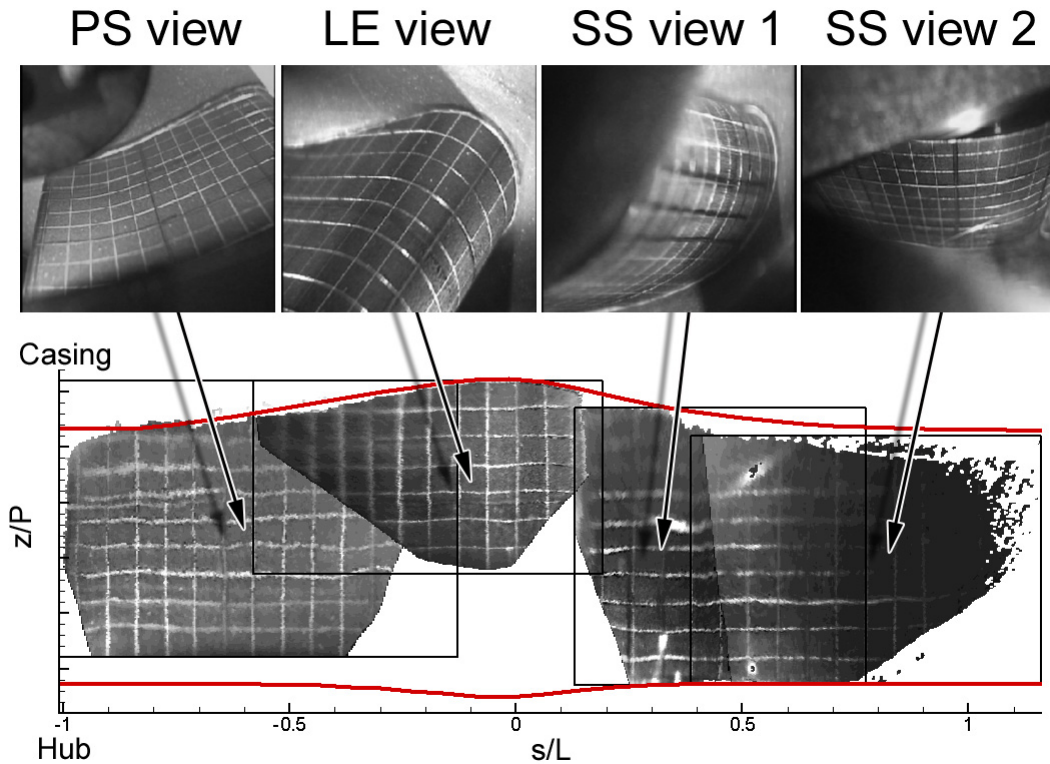


Figure 4-18: Coordinate Transformations and View Assembly

The lack of coverage close to the leading edge on the hub side is due to the presence of the sealing box on the window. On the suction side, close to the casing wall, there is also a lack of recorded data. This is due to a poor liquid crystal signal because of difficult light access. On some views, small white spots or lines are due to light reflection problems that could not be filtered.

4.2.3 Baseline Results

As for the aerodynamic experiments, three sets of measurements are performed corresponding to three different inflow angles: -12° , 0° and $+12^\circ$. Each inflow angle configuration implies a partly un-mounting and re-mounting of the test facility, which conducts to some slight changes in the camera set-up, thus on the covered areas given in the results.

Compared to the aerodynamic measurements, the main flow total temperature is increased by 30K for the transient liquid crystal measurements. This increase in temperature does not significantly change the aerodynamic flow conditions. However, in order to be as precise as possible, the span-wise static pressure distribution on the surface of the vane is re-measured and used for the determination

of the recovery gas temperature. Based on the method described in the previous paragraph, the baseline heat transfer coefficient distribution on the vane airfoil is obtained (Figure 4-19).

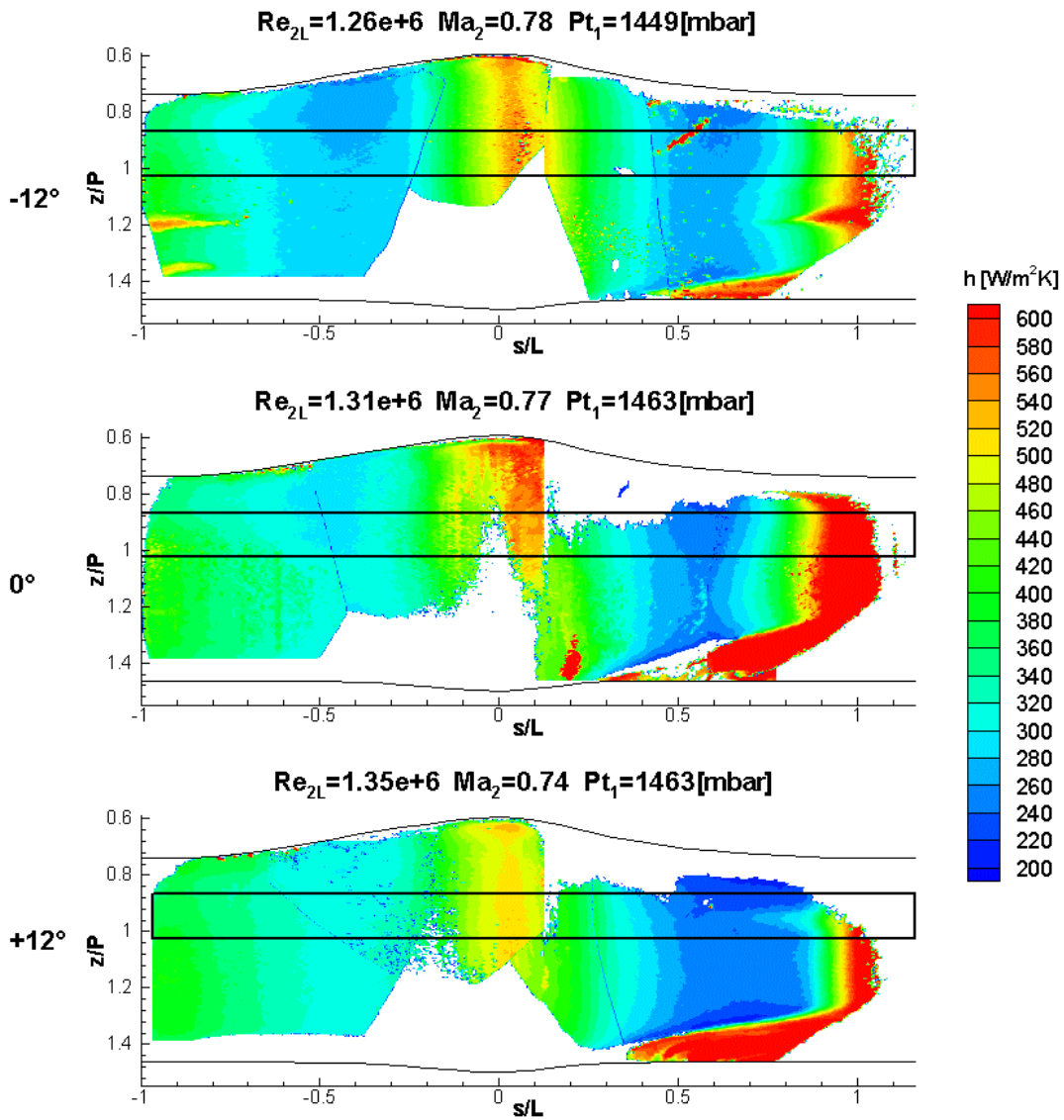


Figure 4-19: Baseline Heat Transfer Coefficients on the Vane

The quality of the results here obtained is acceptable despite the fact that on the suction side, close to the hub wall, there is a zone with a quite high heat transfer coefficient level. It is unfortunately not due to the horseshoe vortex but principally due to the presence of a slightly larger than expected Teflon gap (see paragraph 2.1.2.4). Indeed, for the heat transfer experiments, the gap was slightly increased in order to be sure that the liquid crystal coating would not be damaged during the model insertion. Based on this observation, the Teflon coating was then increased for the

film-cooled heat transfer measurements on the vane. Indeed, results close to the casing wall are not influenced and can be taken into account. On the rest of the surface, for the -12° and $+12^\circ$ cases, close to the trailing edge, there are zones with regrettable cones of higher heat transfer coefficient due to so-called “turbulent spots” generated by particles or dust embedded in the liquid crystal coating.

In order to better see the difference of the heat transfer coefficient levels for the three inflow cases, a span-wise averaging is calculated on a representative surface area (black rectangle on Figure 4-19) and is presented in Figure 4-20.

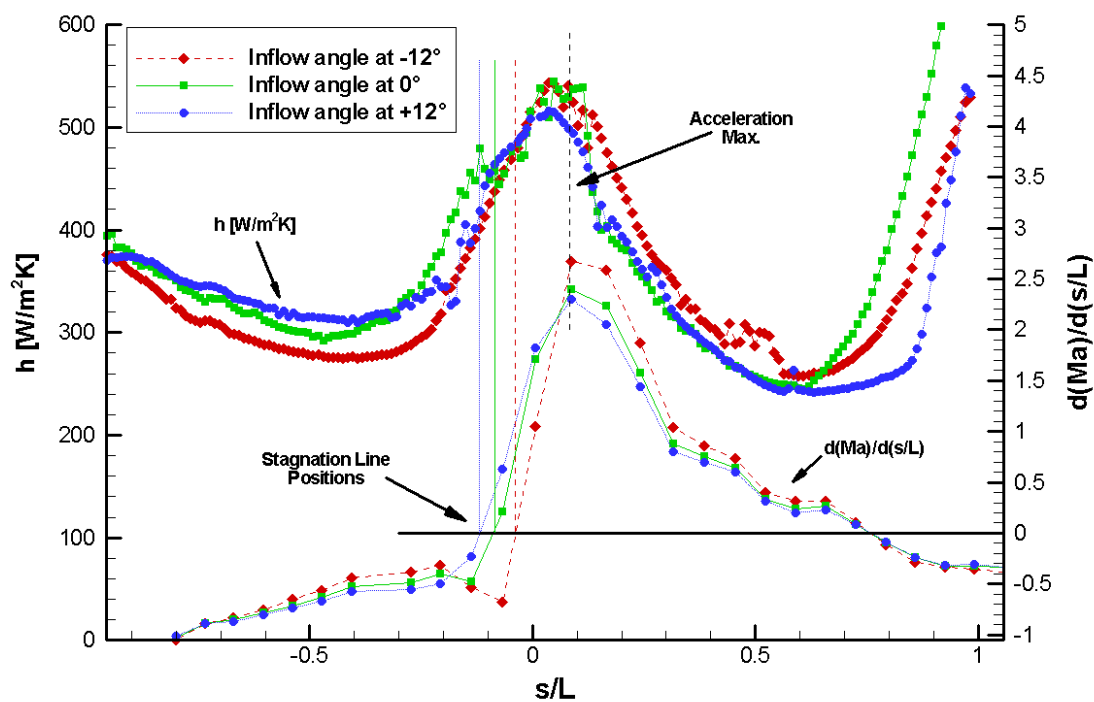


Figure 4-20: Span-Wise Averaged Heat Transfer Coefficients on the Vane

For all the cases, the maximum heat transfer coefficient occurs close to the leading and trailing edge areas. However, it can be seen that the highest heat transfer coefficient on the leading edge area does not occur at the stagnation line positions but is slightly shifted on the suction side (see also Figure 4-3). To verify this, the less pronounced case of -12° is checked by the two images in Figure 4-21. The left one is a liquid crystal shear stress picture taken during the experiment to verify the stagnation line position; and the right one is a liquid crystal temperature picture issued from the beginning of the transient experiment. Assuming an homogeneous

initial temperature and recovery gas temperature in this area, the liquid crystal signal appears first at the highest heat transfer coefficient. It shows clearly that this signal apparition is shifted from the stagnation line position. The reference grid is numerically superposed to these images in order to help the localisation on the surface.

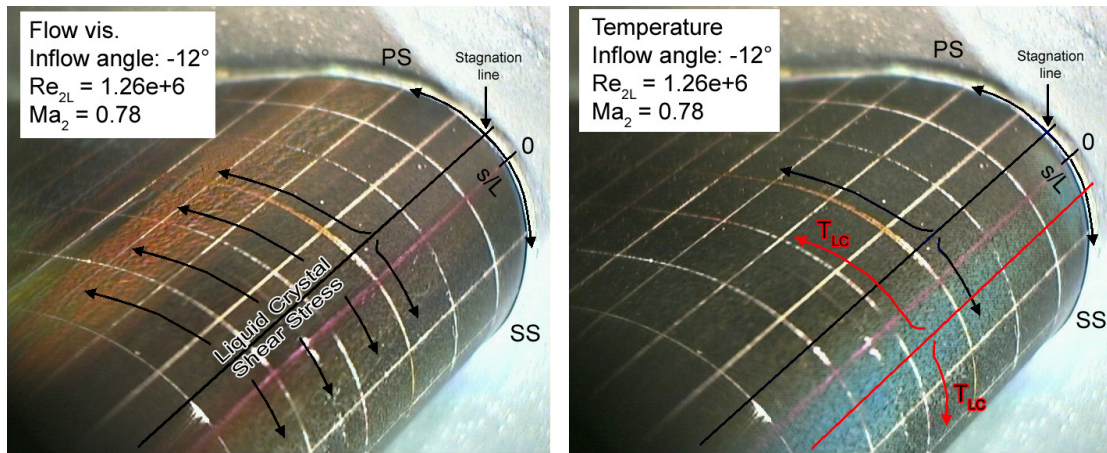


Figure 4-21: Flow Stagnation Line and Heat Transfer Coefficient on LE

Indeed, the maximum heat transfer coefficient around the leading edge occurs at the position on the vane where the flow is the most accelerated (see Figure 4-20), as the aerodynamic boundary layer is getting very thin, thus offering less protection. A less pronounced but similar leading edge peak heat transfer coefficient shifting to the suction side was also observed by Dullenkopf et al. (1991).

After the peak, the heat transfer coefficient decreases first along the suction side as the thickness of the laminar boundary layer increases. A minimum level is then reached before a rapid increase due to a laminar-turbulent transition that occurs in a region where the flow on the vane airfoil decelerates.

Along the pressure side, the heat transfer coefficient decreases first before increasing again smoothly until the trailing edge region. The decrease around the leading edge area can be explained by the increase of the laminar boundary layer, as the flow does not accelerate much. Then, for $s/L < 0.2$, as the flow starts accelerating along the pressure side surface, the boundary layer thickness is reduced. The latter offers less protection to the surface so that the heat transfer coefficient increases also along the surface without any noticeable laminar to turbulent transition.

A comparison between the three inflow angles shows that on the pressure side, the heat transfer coefficient is less for the -12° than for the 0° or $+12^\circ$ cases, which is coherent with the flow acceleration (see Figure 4-20). An accelerated flow decreases the laminar boundary layer and thus offers less protection. On the suction side, the laminar to turbulent boundary layer transition occurs on an earlier s/L position for the 0° case, then for the -12° case and finally for the $+12^\circ$ case. The latter may be not directly compared to the two others, as the downstream isentropic Mach number is a little lower than for the two other cases.

4.2.4 Comparison with Correlations and Calculations

4.2.4.1 Laminar and Turbulent Nusselt Correlations Comparisons

In order to verify the correct order of magnitude of the results obtained from these specific vane airfoil measurements, heat transfer coefficients are compared in dimensionless form with laminar and turbulent (Kays et Crawford, 1993) Nusselt numbers correlations for a flat plate. Figure 4-22 shows the measured Nusselt numbers function of the Reynolds number on the pressure and suction sides for the three different inflow cases. On the same graphs, the laminar (large solid line) and the turbulent (large dashed line) correlations normally applied for the flat plates and defined by (4.2) and (4.3) are also represented.

$$Nu_{s,lam.} = 0.332 Pr^{\frac{1}{3}} Re_s^{\frac{1}{2}} \quad (4.2)$$

$$Nu_{s,turb.} = 0.0287 Pr^{0.6} Re_s^{0.8} \quad (4.3)$$

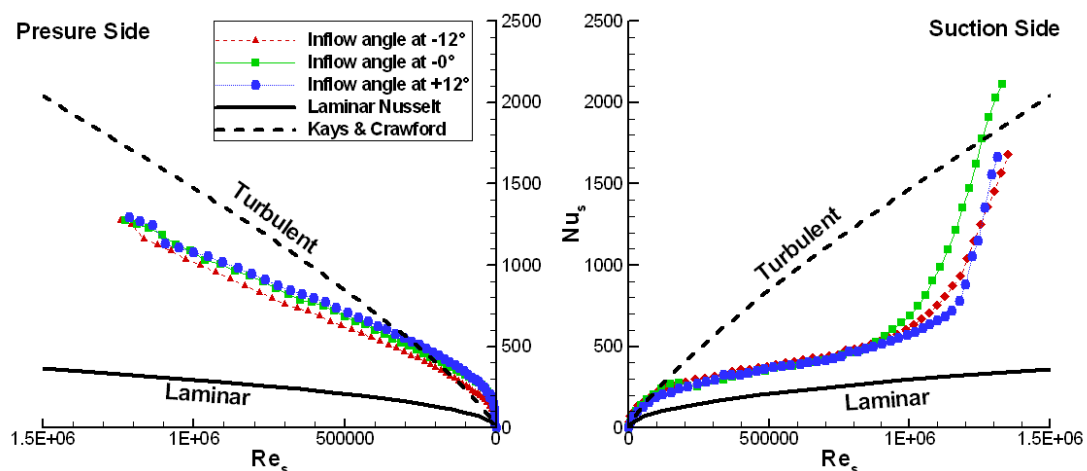


Figure 4-22: Comparison with Laminar and Turbulent Nusselt Numbers Correlations

Although the vane cannot be considered as a flat plate, the Nusselt numbers correlations given here are essentially used as indicators of the typical heat transfer coefficient intensities obtained for specific local Reynolds numbers. As expected, the results of the vane are in the same order of magnitude.

On the pressure side for each inflow angle case, the curves are about the same for the different inflow conditions. However, on the suction side, Nusselt numbers vary with the different inflow conditions. All curves are first closer to the laminar side and then rise to the turbulent side at different Reynolds numbers corresponding to different locations of laminar to turbulent transition.

4.2.4.2 *Texstan Code Calculations Comparisons*

In order to have a better verification of the heat transfer coefficient profiles obtained by the measurements, some numerical simulations are performed with boundary layer code. Figure 4-23 shows the comparison between the measurements and the Texstan code calculations for the three different inflow angles.

The measured velocity profile is used for the calculations. Texstan calculations are performed with the Lam-Bremhorst turbulence model and with a laminar-turbulent transition zone s/L position on the suction side imposed manually.

Results show a similar tendency between the calculations and the measurements. However, for the suction side, the calculations underestimate the heat transfer coefficients, particularly in the laminar region.

For the leading edge area, calculations are not very well defined so it is quite difficult to compare them with the measurements.

It is essentially on the pressure side that the intensity of the heat transfer coefficients calculations show very good agreement with the measurements, this for the three different inflow cases.

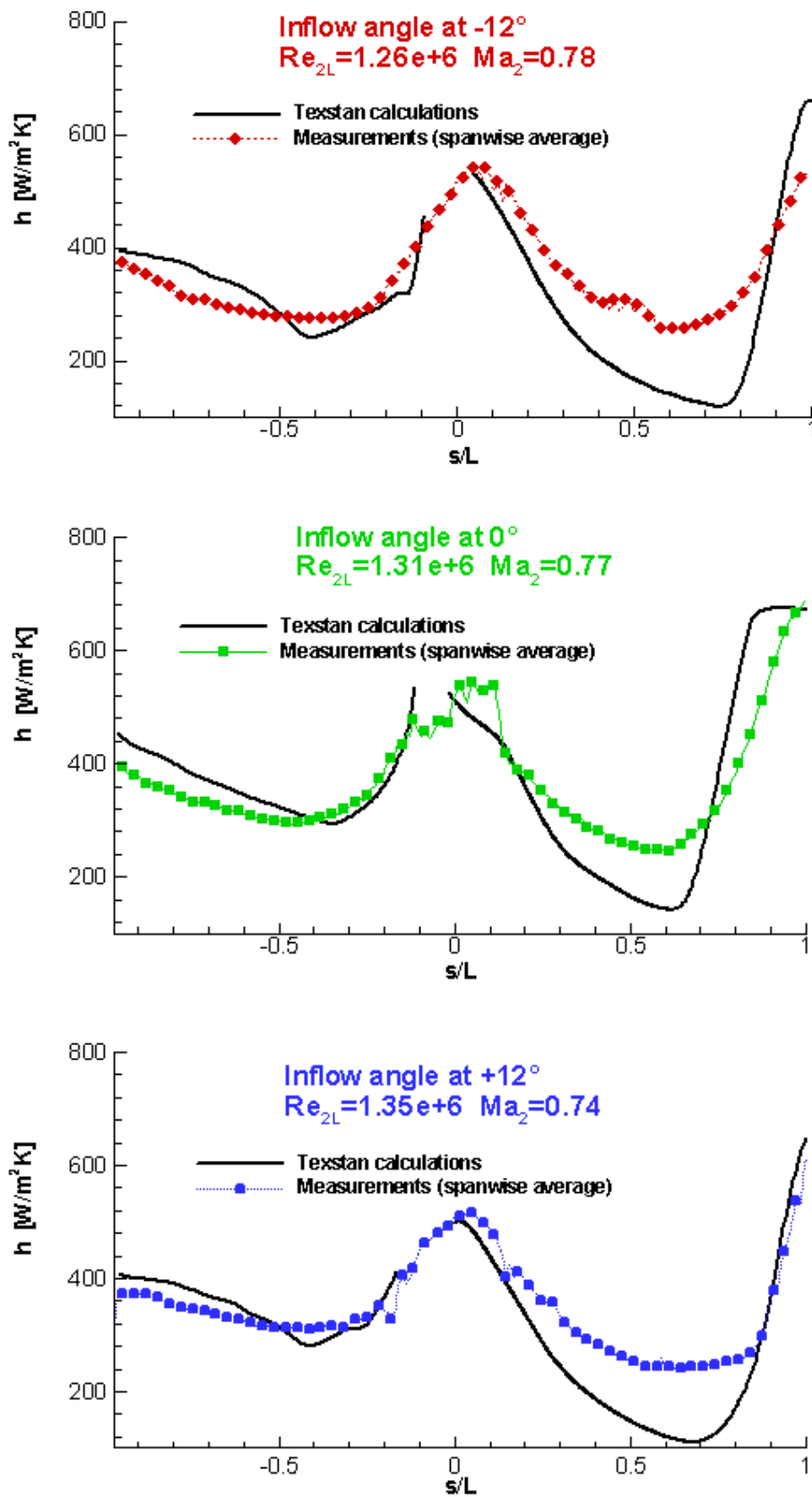


Figure 4-23: Comparison with Numerical Simulations (Texstan code)

4.2.5 Conclusion of Baseline Heat Transfer Measurements on the Vane

- The heat transfer measurement procedure has been explained and some basic remarks have been given about camera views set up and the new data reduction program based on a digital image processing system.
- Liquid crystal signal acquisition was performed with four different camera views. The assembled views gave a global heat transfer coefficient surface distribution. For a specific area, curves have been extracted by a span-wise averaging.
- Like for the aerodynamic measurements, three sets of measurements have been realized corresponding to the three different inflow angles: -12° , 0° and $+12^\circ$. Very small variations were obtained between the different cases.
- Validity of the results has been checked by laminar and turbulent correlations of Nusselt numbers issued from literature.
- The profiles of the baseline heat transfer coefficients curves have been compared with numerical simulations by using the boundary layer Texstan code.

4.3 Film-Cooled Heat Transfer Measurements on the Vane

This paragraph describes the film-cooled heat transfer measurements on the nozzle guide vane. The regression of multiple transient liquid crystal experiments for the measurements of the film cooling performances is explained with the help of the theory given in Appendix C. The geometry of the film cooling hole configuration has already been detailed in chapter 2. The nozzle guide vane is cooled by fifteen rows of holes. Six different film cooling holes configurations are tested for different areas of rows opened (PS, LE, SS, PS-LE, LE-SS and PS-LE-SS). For all cases, four camera views are used and assembled. The film-cooled heat transfer coefficient h_f and the film cooling effectiveness η results are presented in a two-dimensional unwrapped surface coordinate system and with span-wise averaged curves. A heat flux ratio between film-cooled and baseline case is estimated, giving information on the performances of the film cooling holes design. Discharge coefficients of each row of holes are measured and used to determine the distribution of the coolant flow injection. Parameters characterising the cooling configuration, such as density ratio and blowing ratio, are presented.

4.3.1 Film-Cooled Experiment Set-Up for the Vane

The first challenging step for the film-cooled vane experiments was to design a manufacturable Perspex model with the same cooling hole schemes as in the real engine. The latter having a double plenum chamber for feeding the cooling rows of holes, an attempt was made to use a double carbon-fibre plenum chamber with the Perspex model. Unfortunately, due to some sealing problems it was not used. Hence, the film cooling experiments are performed on a Perspex model with a unique plenum chamber. However, several experimental configurations are tested by sealing some of the rows with 3M-Kapton tape. This allows reducing the cost of the experiments by avoiding the manufacture of a model for each configuration of active rows of cooling holes.

4.3.1.1 Optical Access

Geometry set-up and optical access for the film-cooled heat transfer measurements are similar to those used for the baseline heat transfer measurements. Some improvements are performed by changing the view angles and lenses of the cameras, as well as by applying more homogeneous light sources. Despite these efforts, some areas close to the walls are still difficult to take measurements from.

Focus is on the mid-span area with a global overview of the surface rather than with zoom views close to the holes. At least four cameras are necessary to have a good coverage of the central vane test section during heat transfer measurements. Figure 4-24 shows the vane surface area covered by the different views as well as the corresponding image of the reference grid present on the dummy test section. This reference grid is then used for a coordinate transformation in order to present the measurements of the four views altogether on an unwrapped surface.

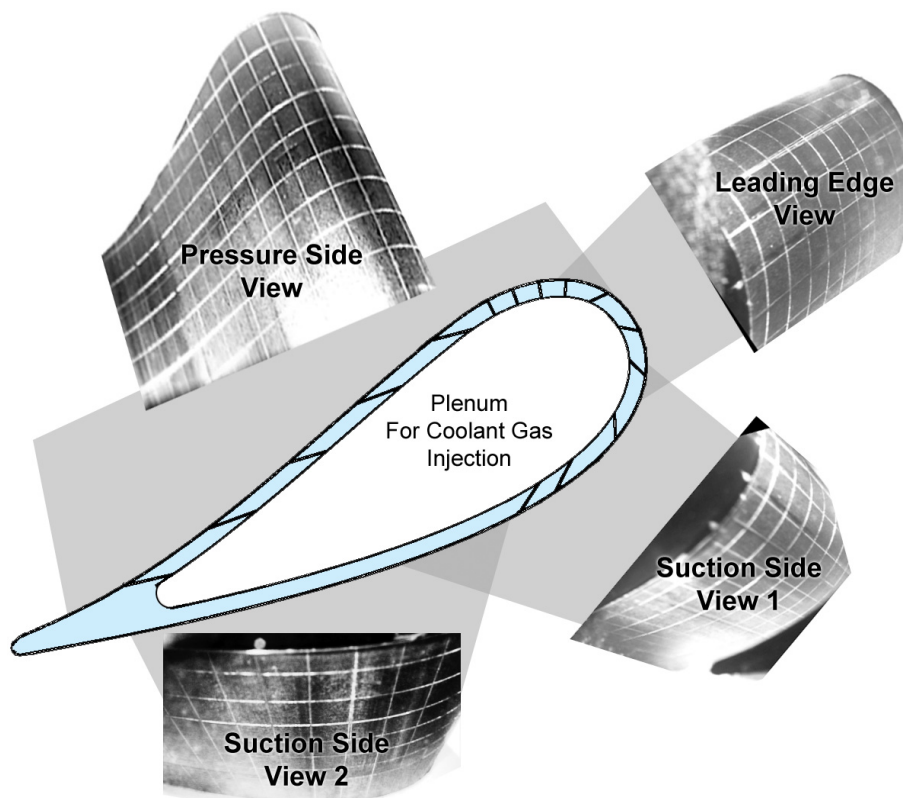


Figure 4-24: Camera Views for the Film-Cooled Vane Experiments

4.3.1.2 Central Vane Set Up

The film-cooled test blade is, as for the baseline vane, made out of cast Perspex with the same properties. Hence, for a wall thickness of 3mm, the maximum allowable time for transient experiments is also of about 23 seconds to satisfy the semi-infinite model criterion. Indeed, the longest experiment performed for the film-cooled measurements did not exceed 10 seconds.

Despite the increased complexity due to the presence of the plenum chamber, eight thermocouples are placed around the profile at two span-wise positions as for the

baseline model. They are also used to verify that the chosen level of the initial vane model temperature T_0 is reached and that it is sufficiently homogeneous to start a transient experiment. A new preconditioned cooling box has been manufactured with a different jet impingement configuration producing a more homogeneous initial temperature level. Variations of the initial surface temperature on the model are now on the order of about ± 1 K.

4.3.1.3 Liquid Crystal Coating

With about the same temperature levels as those used in the baseline case ($T_{ig} \approx 333$ K, $T_0 \approx 273$ K), the narrow band liquid crystal coating is also chosen to give a signal at around $T_{LC} = 303$ K. Application of the liquid crystal coating on the Perspex model consists, as for the baseline case, of the three following layers:

- Black backing acrylic layer: Hallcrest BB-G1
- Liquid crystal layer: Hallcrest BM/R30C07W
(Quantity: 3 ml LC + 1,5 ml water)
- Varnish protection layer: Hallcrest binder AQB-2

Although reacting at the same temperature than for the baseline case, the liquid crystals here applied have a slightly narrower band of 0.7K (instead of 1K). As a consequence, it gives finer temperature signal accuracy and less view angle variation effects. Coating of the layers is again applied with the same technique as for the baseline vane; hence, it results in similar surface roughness.

It should be noted that a new coating is applied before each new set of experiments. For this, the deteriorated liquid crystal coating was first carefully removed by using water (as it is acrylic based painting) on the complete surface, including the areas in and around the holes.

4.3.1.4 Coolant Supply

A large reservoir supplies the coolant flow via a series of mass flow meters, vanes, and heater tubes as shown in Figure 4-25. The bottle can either be filled with air or by CO_2 . For the present work CO_2 is used as coolant gas due to a higher gas density ratio that is found in the engine due to much higher gas temperature differences (Ekkad et al., 1997).

Two laminar flow elements with very sensitive pressure transducers are able to measure mass flow of up to 2×200 [SLPM] with an accuracy of 0.2% (at full scale).

An electrical heater tube is used to make small changes in the total coolant gas temperature T_{tc} before being injected into the plenum chamber during the transient experiment. Note that there are three different operating modes of the coolant gas injection:

- The preconditioning mode requires setting up all the tubing installation so that the transient experiment is performed at the desired coolant gas temperature. Preconditioning usually takes some time compared to the transient experiment so air is used in order to save CO₂. Moreover, a higher mass flow is used in the preconditioning mode so that the required conditions are obtained faster.
- The pre-injection mode is then used a few minutes before the transient experiment starts. CO₂ replaces air and the mass flow regime is set to the required blowing ratio for the experiment. All the conditions are similar to the transient test except that the flow does not go through the Perspex model (still in the preconditioning box for the initial model temperature), but through an adjustable orifice that simulates the same counter pressure as if the flow was passing through the cooling holes of the vane.
- The injection mode is the same as the previous one, but this time with flow coming out of the cooling holes as soon as the vane is inserted into the main flow channel for the start of the transient experiment.

During the transient experiment a pressure tube and two thermocouples measure the pressure and the temperature of the coolant gas injected. Combined with additional discharge coefficients measurements of each row, the local blowing ratio distribution is determined.

4.3.2 Film-Cooled Vane Heat Transfer Measurement Procedure

The heat transfer measurement technique for the determination of the heat transfer coefficient and the adiabatic film cooling effectiveness consists of the regression of multiple transient liquid crystal experiments by small changes in the coolant gas temperature. For one experiment, thus for one coolant gas temperature, the transient heat flux and the coolant gas injection create a surface temperature evolution of the tested model. The latter is monitored as in Figure 4-26 by the use of the same transient liquid crystal technique applied for the baseline case experiments and is already described in chapter 3.

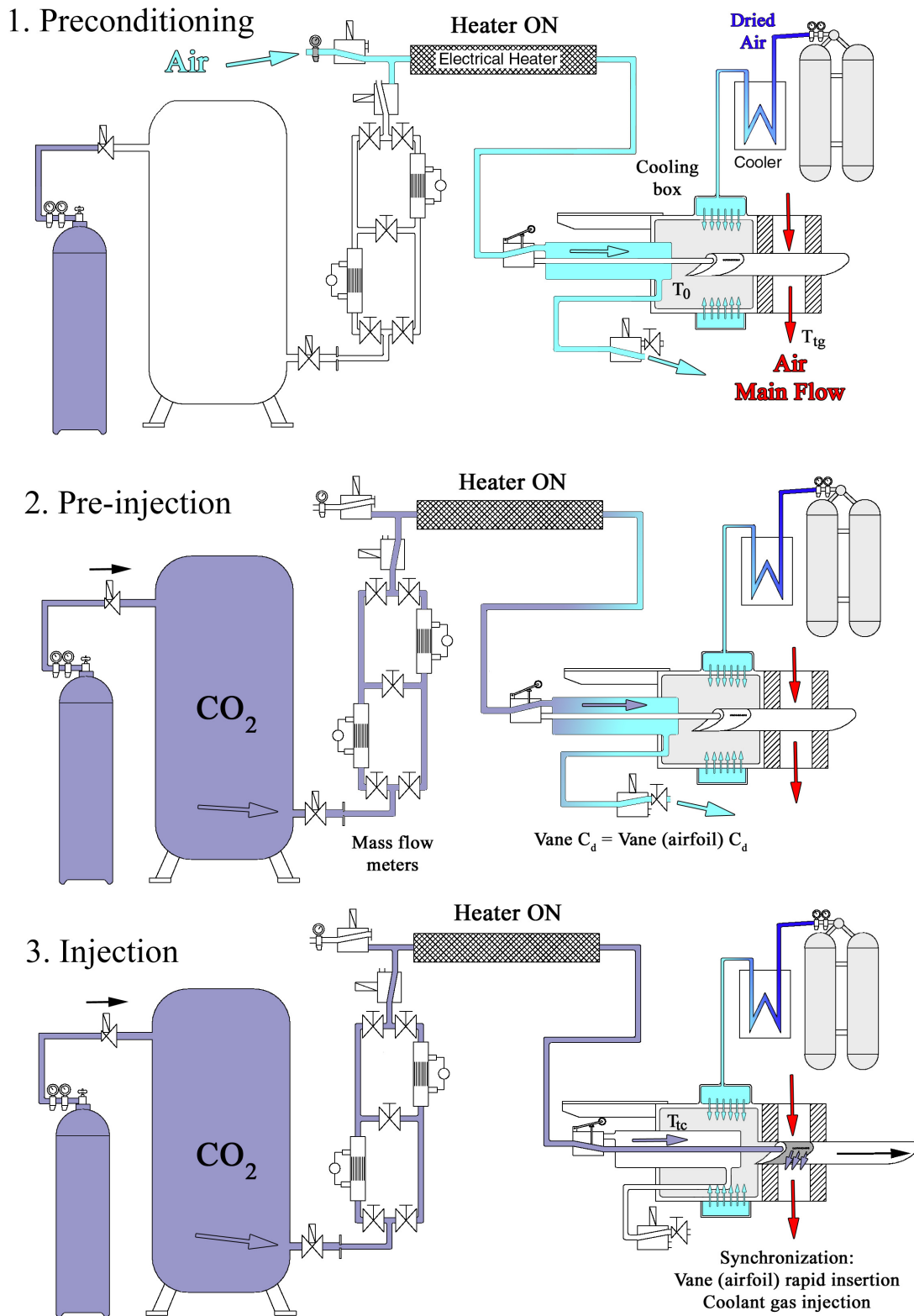


Figure 4-25: The Three Different Operating Modes of Coolant Gas Supply for the Film-Cooled Vane

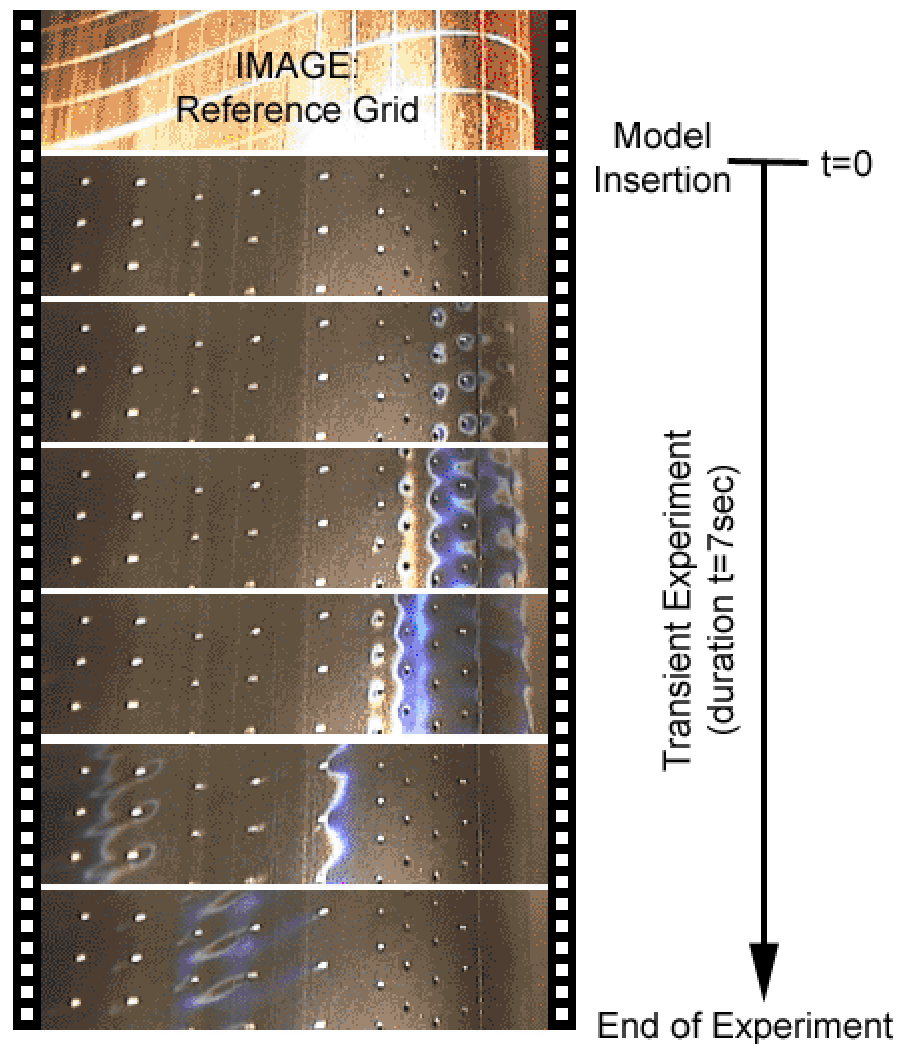


Figure 4-26: Transient Liquid Crystal Video Sequence on the Surface of the Film-Cooled Vane

4.3.2.1 Multi Experiments for Regression

For each film-cooling configuration, about ten transient tests are realized with all the same main flow and film cooling conditions except for the temperature of the coolant gas that slightly vary in order to apply the regression method described in Appendix C. Due to the heat exchange with the plenum chamber during the transient experiment, the coolant gas temperature T_{tc} injected is not kept constant. This is accounted for in the regression analysis by using a coolant gas temperature function defined by equation (c.8). This type of function is representative from the temperature evolution measured by the thermocouples in the plenum chamber, hence performing a more accurate regression analysis than the one used for the previous experiments

(Drost 1998, and Reiss, 2000) for which polynomial functions were used. Preconditioning of the coolant temperature varies from 293K to 338K with typical steps of 5K as it can be seen in Figure c-1 in Appendix C. Pressure ratio is kept constant for the different coolant gas temperatures making a variation on the blowing ratio of maximum 5%.

Due to the configuration of one plenum chamber for multiple rows, it is not possible to specify an independent blowing ratio per row. Indeed, the only parameters to adjust are the numbers of rows open (see Table 2-4) and the total coolant gas pressure of the plenum chamber p_{tc} . The resulting local blowing ratio distribution of the different opened rows configurations is then calculated by the help of the discharge coefficients measured for each row.

4.3.2.2 Discharge Coefficients

To measure the discharge coefficient of one row, the others are sealed by 3M-Kapton tape. The experiments consist of applying different pressure levels in the plenum chamber. For each level, the effective coolant mass flow is measured by the laminar flow elements and compared to the theoretical mass flow (eq. (4.5)). The discharge coefficient is defined as follow:

$$C_d = \frac{m}{m_{th}} \quad (4.4)$$

with:

$$m_{th} = n \frac{\pi D^2}{4} \frac{p_{tc}}{\sqrt{RT_{tc}}} \left(\frac{p_{sc}}{p_{tc}} \right)^{\frac{1}{\kappa}} \sqrt{\frac{2\kappa}{\kappa-1} \left[1 - \left(\frac{p_{sc}}{p_{tc}} \right)^{\frac{\kappa-1}{\kappa}} \right]} \quad (4.5)$$

and n the number of holes per row and D the diameter of the hole.

It must be noted that the static coolant gas pressure p_{sc} (at hole exit location) used for the theoretical mass flow determination is issued from the local static main flow pressure on the vane surface from the baseline aerodynamic measurements, and not from the total pressure in plenum chamber at no coolant gas injection as the inclined cooling holes do not capture the static pressure at the injection location.

Discharge coefficient profiles vary with both the local geometry and flow conditions as it can be seen on Figure 4-27. For a constant wall thickness δ and hole diameter D , a hole with a lower exit angle conducts to a higher L_D/D ratio thus to a lower C_d . For the same configuration, fan-shaped holes usually have higher C_d than cylindrical

holes (Gritsch et al., 1998). This is due to the pressure recovery occurring in the diffuser section of the fan-shaped hole. The typical discharge coefficients curves obtained of the film-cooled holes on the different areas on the vane are given in Figure 4-27.

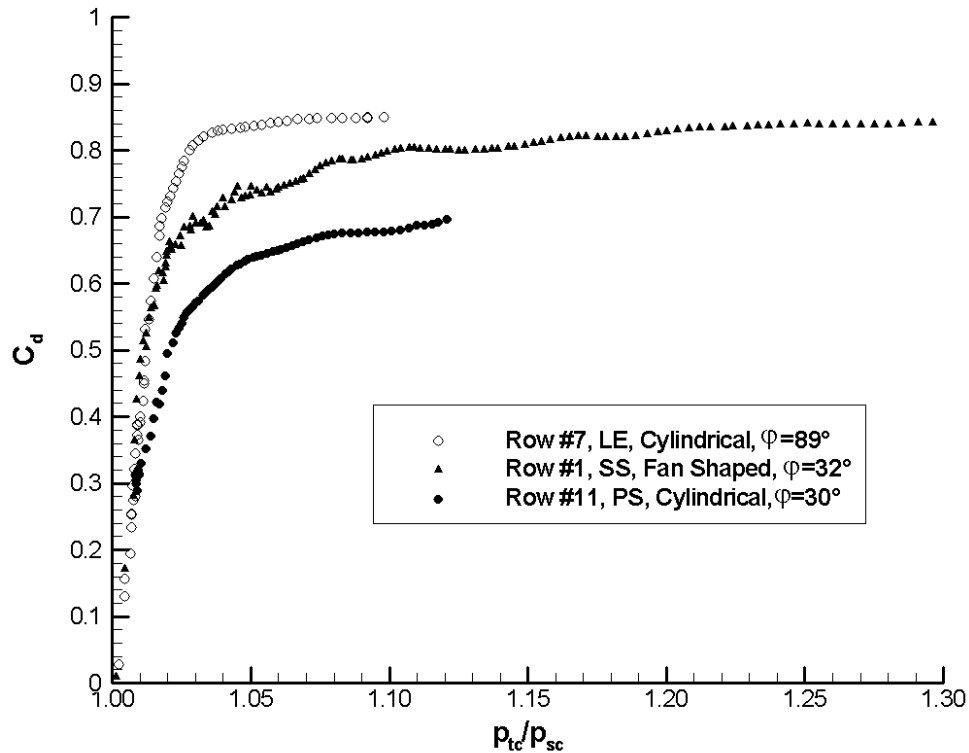


Figure 4-27: Typical Discharge Coefficients of Cooling Holes

When applying the thin liquid crystal coating or the Pressure Sensitive Painting on the surface of the model but also around or even in the cooling holes, experiments did not show any significant variation of the discharge coefficients. Moreover, for holes of 0.6mm diameter, no significant variations in C_d were observed due, for instance, to dilatation effects produced by the injection of different coolant gas temperatures.

4.3.3 Film-Cooled Results

For each camera view presented in Figure 4-24, video signal data analysis and regression calculations are performed independently and finally assembled together in a coordinate system given by the unwrapped vane surface. Film-cooled heat transfer coefficients as well as adiabatic film cooling effectiveness are presented in

the following paragraphs. The average spatial resolution of these results is of 8 pixels/mm, thus at least 5 pixels for a hole diameter of 0.6 mm.

In order to better analyse these results, span-wise averaged curves are extracted on a mid-span area where enough liquid crystal signals were detected. These zones are noted by black rectangles on the 2D results ($1.03 < z/P < 1.26$ and $-0.82 < s/L < 0.86$). In addition, a special data filtering was applied on the 2D results so that values inside the holes were not considered in the averaging operation. A span-wise averaging on a specific hole-pitch was not possible since P_D is different for each row.

Footprints of the holes are indicated on the 2D results showing the different film cooling configurations (Figure 4-31, Figure 4-32, Figure 4-33, Figure 4-34, Figure 4-35, Figure 4-36).

For the averaged curves, arrows on the graphs show the locations of the rows of cooling holes (Figure 4-28, Figure 4-29, Figure 4-30).

Characteristics of the local coolant injections of each row associated to these results are calculated by the discharge coefficient measurements and given in separate graphs (Figure 4-37, Figure 4-38, Figure 4-39, Figure 4-40).

4.3.3.1 Film-Cooled Heat Transfer Coefficients

Surface film-cooled heat transfer coefficients of the different configurations are presented in Figure 4-31 for the independent PS LE SS areas of cooling holes opened and in Figure 4-32 for the combined PS-LE, LE-SS and full film-cooled configurations. For all cases, a specific region of the 2D results (noted by a black rectangle on the graphs) is used for a span-wise averaging. The curves obtained are all plotted in the same graph in Figure 4-28. The dashed blue line in this figure represents the baseline heat transfer coefficient results issued from paragraph 4.2.3. Compared to the baseline case, film-cooled heat transfer coefficients are higher due to the increase in the turbulence level generated by the coolant jets. The value is even doubled on the suction side, certainly due to the fact that the baseline case has a laminar boundary layer while the film-cooled configuration is turbulent. However, in order to see the real beneficial effect of film cooling, it is the heat flux ratio (q_f / q_0), presented later, that has to be considered.

The superposition of the film-cooled heat transfer coefficient curves for the different configurations shows very close agreement. The results of the independent cases are quite similar to the combined cases. However, there are some small differences due to the fact that the pressure level p_{tc} of the total coolant gas in the plenum chamber was not kept constant. For the same active row, the variation of the blowing ratio between the different configurations is given in Figure 4-39. The corresponding coolant mass flow variation is given in Figure 4-40. Both graphs denote a certain coolant gas injection difference at the leading edge and for the first rows on the pressure side. The larger difference occurs for the combined LE-SS configuration, where the pressure ratio p_{tc}/p_{sc} was too low to provide representative injection through the holes of the leading edge (showerhead). Despite this, the level on the suction side was very close to the independent SS and combined PS-LE-SS configurations and gave similar heat transfer coefficient augmentation. On the suction side, the curves denote an increase at the hole-injection location followed by a progressive decrease until the next row.

This progressive decrease of heat transfer coefficient after the row is well represented for the independent LE configuration (solid black squared curve) and the combined PS-LE configuration (solid red squared curve) where the curves on the suction side tend to reach the same level as in the baseline case. A similar effect of the black squared curve is observed on the pressure side. On the leading edge area, the results of the PS-LE and LE configurations are very well superposed.

On the pressure side, for the independent PS and combined PS-LE and PS-LE-SS configurations, heat transfer coefficient curves are quite well superposed despite some small blowing rate and coolant mass flow distribution variations. Moreover, values are quite close to the baseline configuration, especially at the beginning of the pressure side where the pressure ratio is quite low. Here, no decreasing tendency is observed after the rows as for the suction side. Instead, the heat transfer coefficient is continuously increasing along the pressure side, probably due to the fact that the coolant gas injection does not significantly alter the supposed laminar boundary layer (see paragraph 4.2.3).

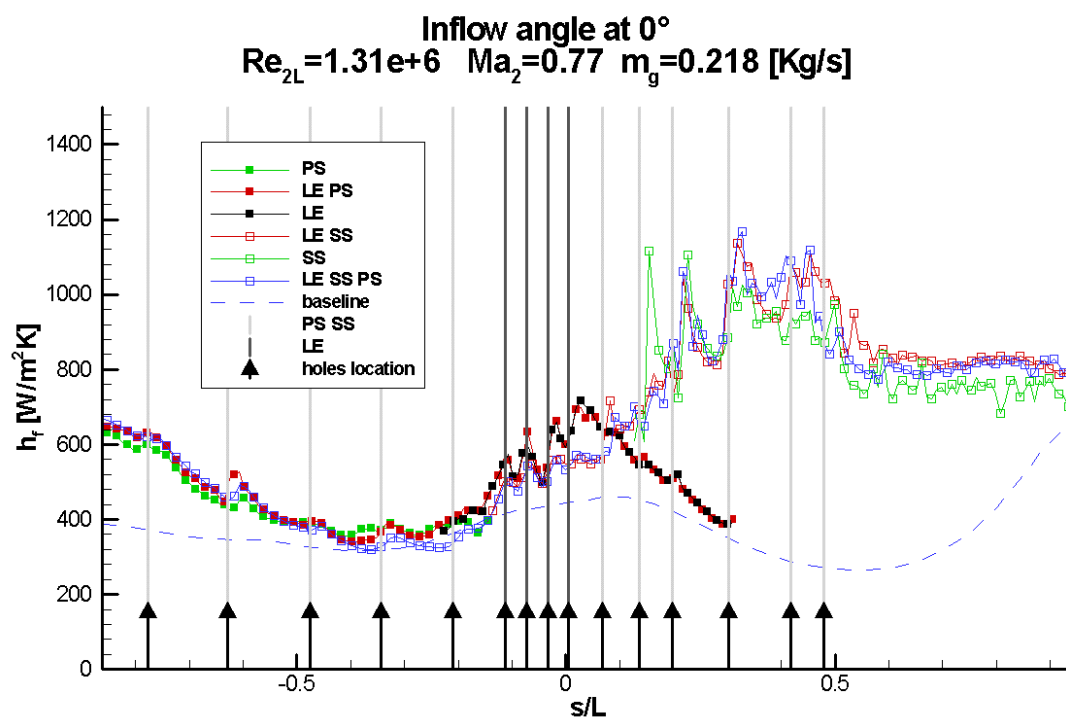


Figure 4-28: Averaged Film-Cooled Heat Transfer Coefficients on the Vane

4.3.3.2 Adiabatic Film Cooling Effectiveness

Surface film cooling effectiveness of the different configurations are presented in Figure 4-33 for the independent PS LE SS areas of cooling holes opened and in Figure 4-34 for the combined PS-LE, LE-SS and full film-cooled PS-LE-SS configurations. For all cases, a specific region of the 2D results (noted by a black rectangle on the graphs) is used for a span-wise averaging. The curves obtained are all plotted in the same graph in Figure 4-29.

On the 2D results, there is a clear indication of the direction of the cooling jets. In some areas, on the pressure side close to the casing wall, the flow is obviously not two-dimensional, as the jets tend to follow the wall profile. This indicates that, for rows geometrically staggered, the jets are not acting identically along the span-wise direction.

On the suction side, despite a poorer liquid crystal signal in some areas, there are interesting jet patterns of the fan-shaped holes. The holes of the first rows are not perfectly staggered and as a consequence, do not offer an optimum coverage. As it continues along the suction side in the direction of the trailing edge, though still not evenly staggered, the film coverage seems to benefit from the increased area ratio of the fan-shaped hole. Film cooling effectiveness values rise up to 50% and drops slowly to 20% close to the trailing edge. Globally, this area seems to be well film covered; moreover, the series of six rows present upstream from the vane throat location allow sufficient cooling effectiveness further downstream. This is also related to the fact that the rows on the suction side area use quite a large amount of coolant compared to the rest of the vane as shown in Figure 4-40.

Due to rigidity limitations, the total pressure of the coolant gas p_{tc} in the plenum chamber was not increased much during the experiments, resulting in lower coolant mass flow injection of rows located on the vane airfoil where the static pressure is high. As a consequence, the leading edge area is not film-cooled enough for the configurations with active rows on the suction side. For the LE-SS configuration, it is clearly shown on Figure 4-34 (middle) that there is almost no film cooling effectiveness on the leading edge area. The same effect but less pronounced occurs with the PS-LE-SS film-cooled configuration in Figure 4-34 (bottom). This poor film-cooling coverage must not be attributed to the cooling design but to the presence of a unique coolant plenum chamber that is responsible for a non-efficient coolant gas distribution as noted in Figure 4-40.

For the span-wise averaged results in Figure 4-29, film-cooling effectiveness increases at the injection location and is followed by a slow decrease downstream the row from an isolated row.

On the suction side, due to the longer surface footprints of the shaped holes and also probably due to the cooling jets interactions of the upstream rows, the film cooling effectiveness peak position is not very clear. However, the superposition of the film-cooling effectiveness curves for the different configurations shows very close results

This is not the case on the pressure side where the independent and combined configurations show quite different tendencies. This is quite surprising as the results of the film-cooled heat transfer coefficients in Figure 4-28 showed very good superposition for this area. The explanation of the difference in the film-cooling effectiveness comes from the significant variation of the blowing ratio distribution between the different cases as seen in Figure 4-39.

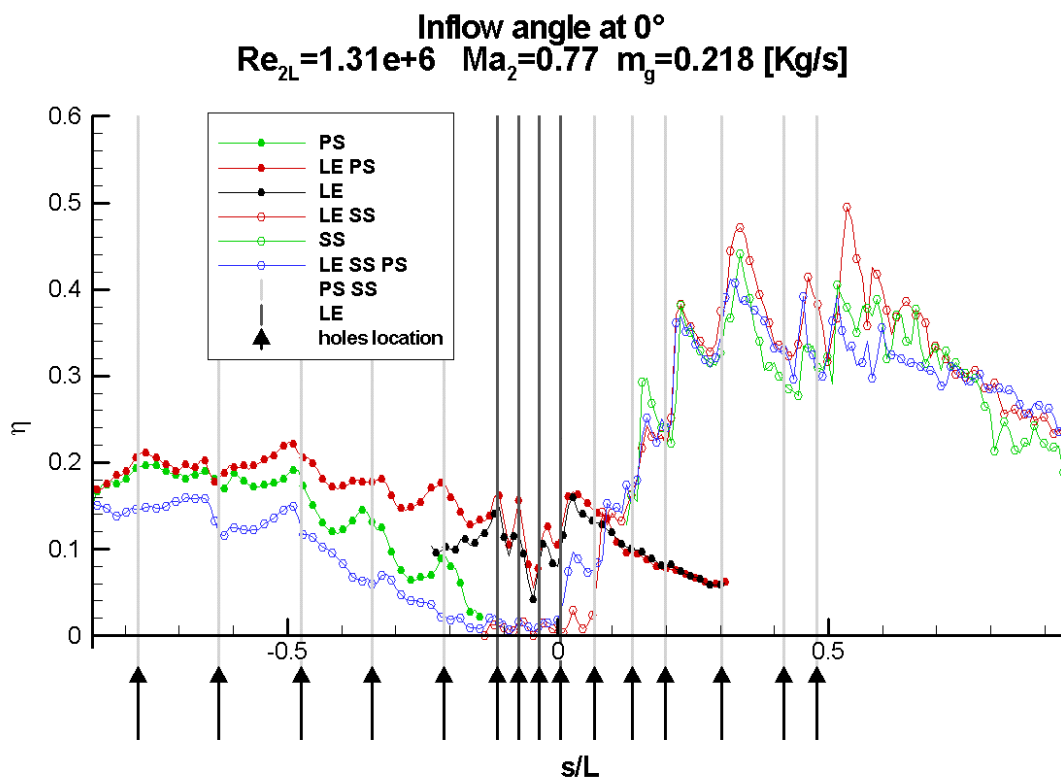


Figure 4-29: Averaged Film Cooling Effectiveness on the Vane

4.3.3.3 Heat Flux Ratio

To demonstrate the real advantage of film cooling, consider the heat flux ratio of the film-cooled and of the un-cooled case.

As mentioned in the film-cooled heat transfer coefficient results, the heat transfer coefficient increases from the un-cooled case due to higher turbulent flow conditions generated by the coolant jets. On the other hand, the coolant jets are cooler than the main flow, and if ideally spread on the surface, the heat flux q_f given to the film-cooled surface decreases compared to the un-cooled case q_0 .

Hence, the heat flux ratio can be defined as follow:

$$\frac{q_f}{q_0} = \frac{h_f}{h} \left(1 - \frac{\eta}{\Phi} \right) \quad (4.6)$$

with the overall cooling effectiveness Φ defined by:

$$\Phi = \frac{T_w - T_g}{T_c - T_g} \quad (4.7)$$

Unfortunately the latter is not known experimentally and varies over the surface, depending on the main flow conditions and the cooling parameters. However, an average value of $\Phi = 0.5$ can be considered typical for an engine environment. This value is then used and combined with the heat transfer coefficient and film-cooling effectiveness results obtained in this work in order to have an indication of the cooling performances of the nozzle guide vane.

Surface heat flux ratios of the different configurations are presented in Figure 4-35 for the independent PS LE SS areas of cooling holes opened and in Figure 4-36 for the combined PS-LE, LE-SS and full film-cooled configurations. In order to see if applying film cooling is giving better or worse protection, a special colour legend is chosen: with a blue to green gradient for improved performances ($q_f / q_0 < 1$), and a red to yellow gradient for decreased performances ($q_f / q_0 > 1$). For all cases, a specific region of the 2D results (noted by a black rectangle on the graphs) is used for a span-wise averaging. The curves obtained are all plotted in the same graph in Figure 4-30. An horizontal line at $q_f / q_0 = 1$ is traced on the same graph to determine the areas with improved performances obtained by film cooling.

It appears that the suction side is not as critical as can be concluded from the results of the film-cooled heat transfer coefficients where a relatively important increase was

measured compared to the baseline case. A heat transfer coefficients comparison on the suction side has to be done with care since the boundary layer seems to be laminar for the baseline case, and turbulent for the film-cooled case.

The superposition of the heat flux ratio curves for the different configurations shows close agreement for the suction side but not for the pressure side.

Overall, the vane film cooling does not have good performance at the leading edge area, the trailing edge pressure side area and the suction side area around the last two rows of injection. However, it must be noted that the experiments are performed on the model with a unique coolant plenum chamber that is responsible for a non-efficient coolant gas distribution. The latter is detailed in the next paragraph.

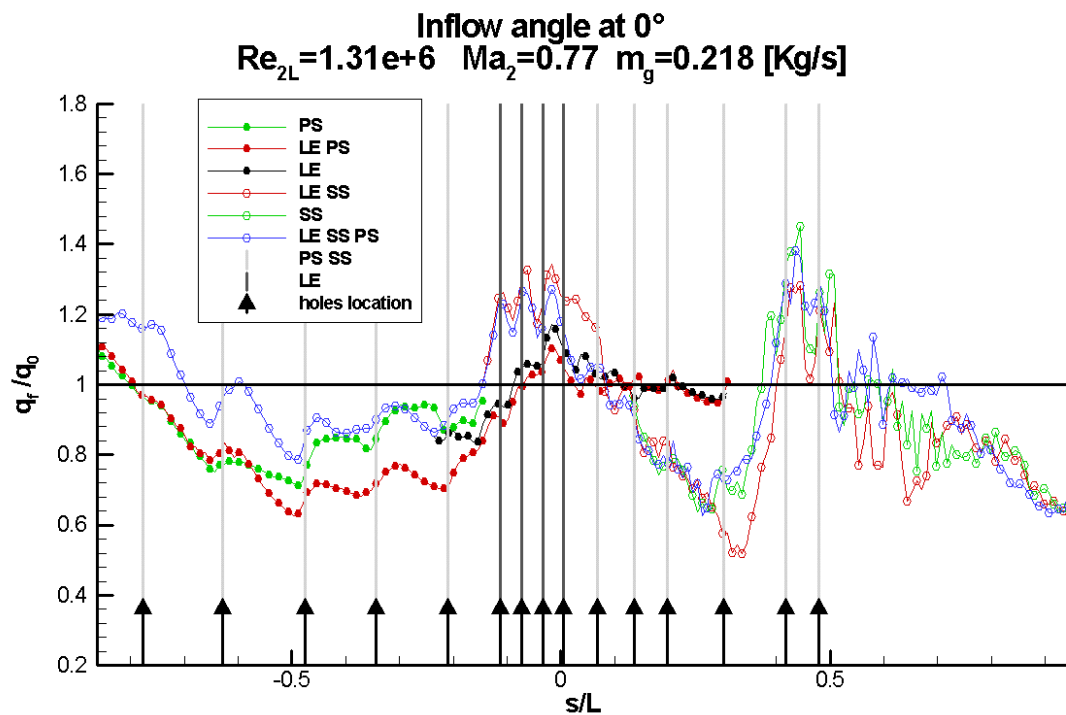


Figure 4-30 Averaged Film-Cooled and Un-Cooled Heat Flux Ratios

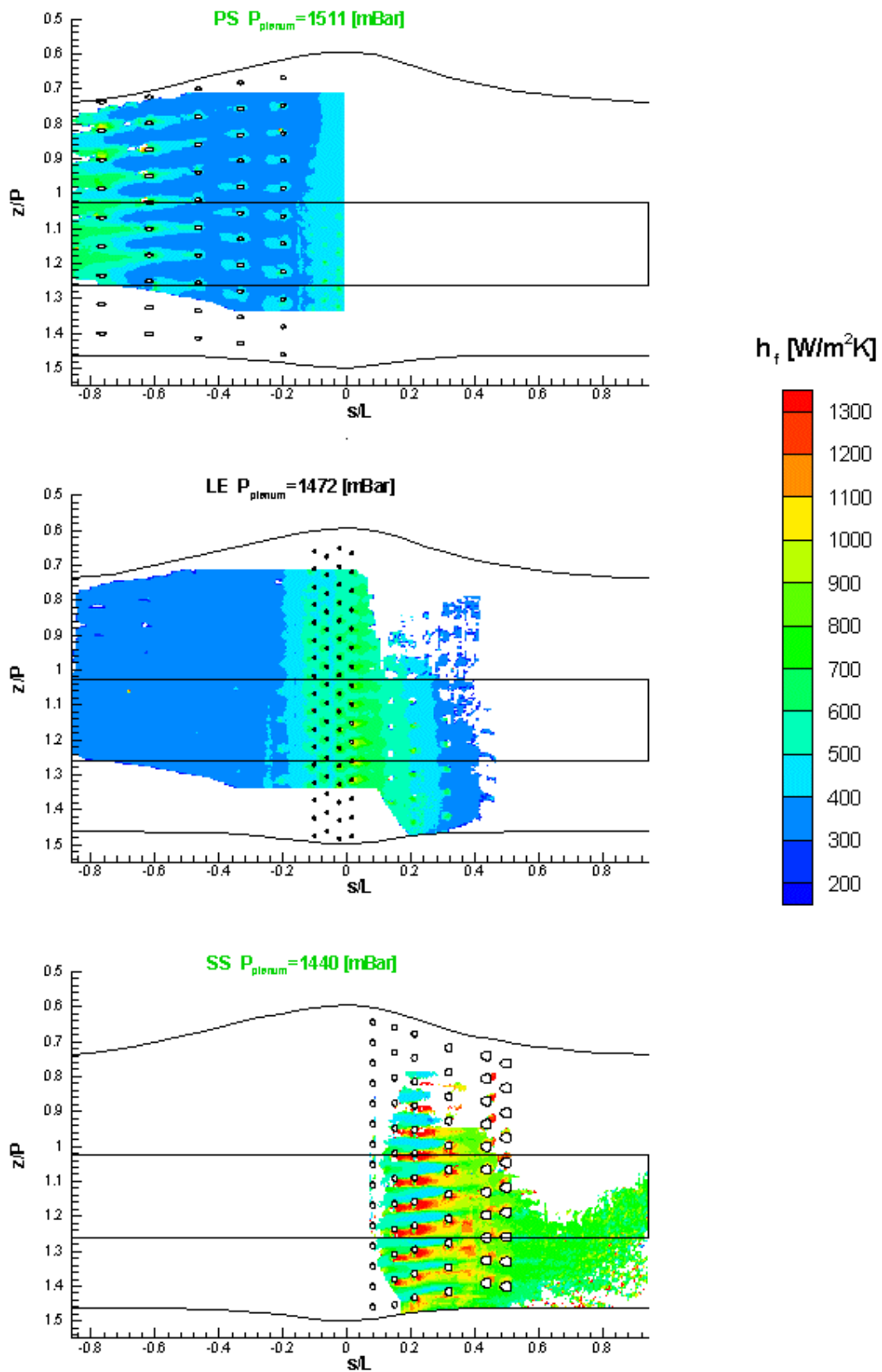


Figure 4-31: Film-Cooled Heat Transfer Coefficients for Independent PS LE SS Zones

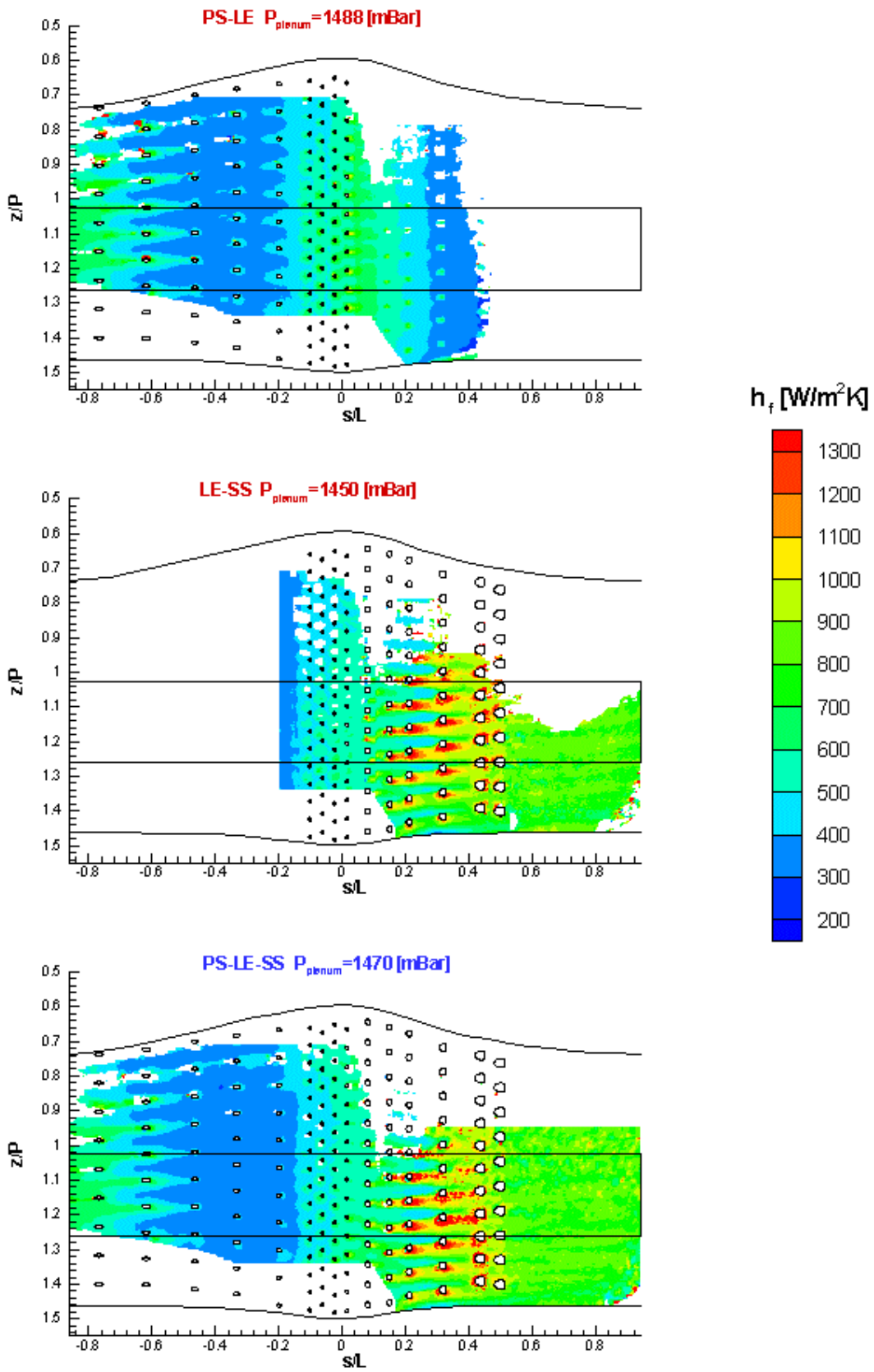


Figure 4-32: Film-Cooled Heat Transfer Coefficients for Combined PS LE SS Zones

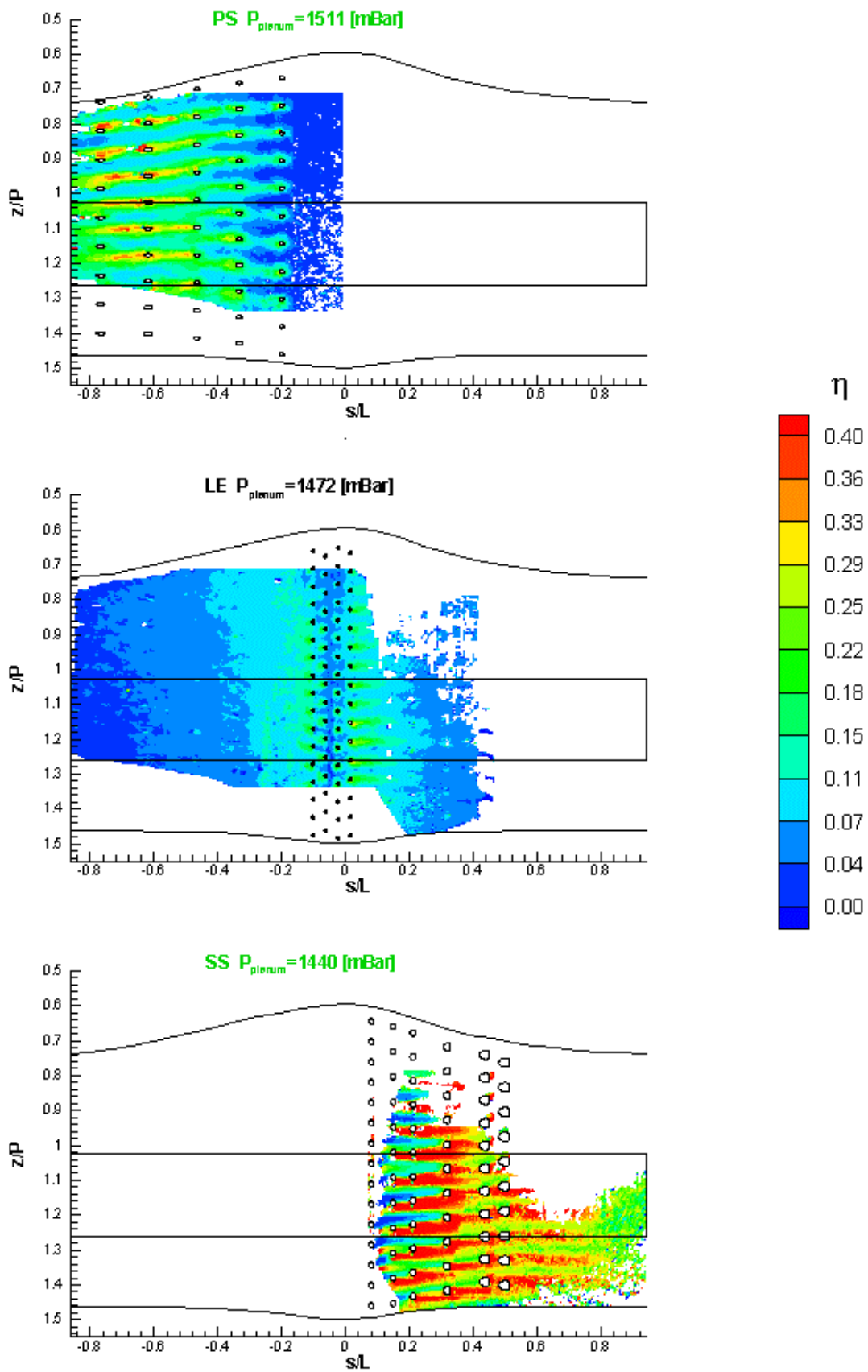


Figure 4-33: Film-Cooling Effectiveness for Independent PS LE SS Zones

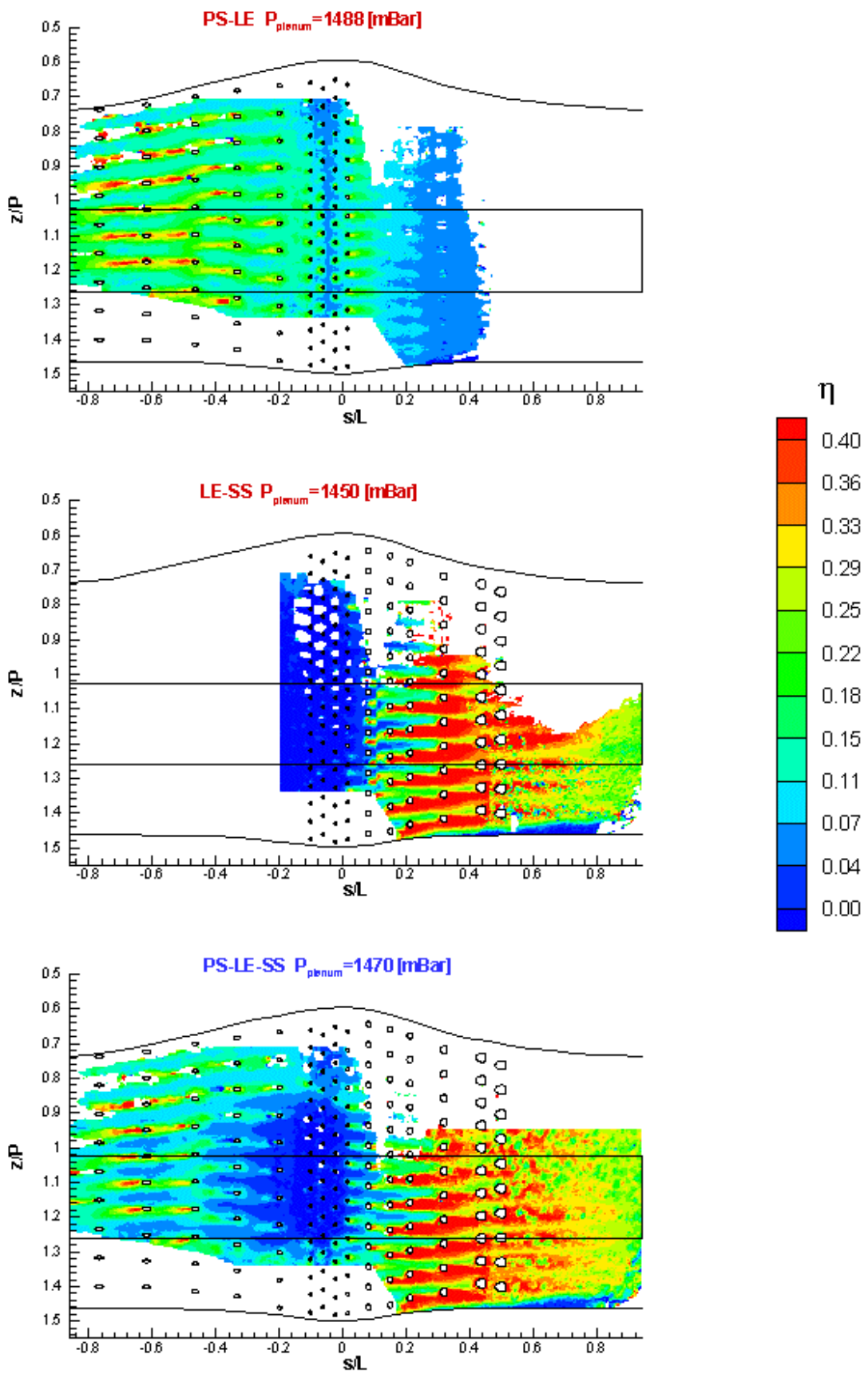


Figure 4-34: Film-Cooling Effectiveness for Combined PS LE SS Zones

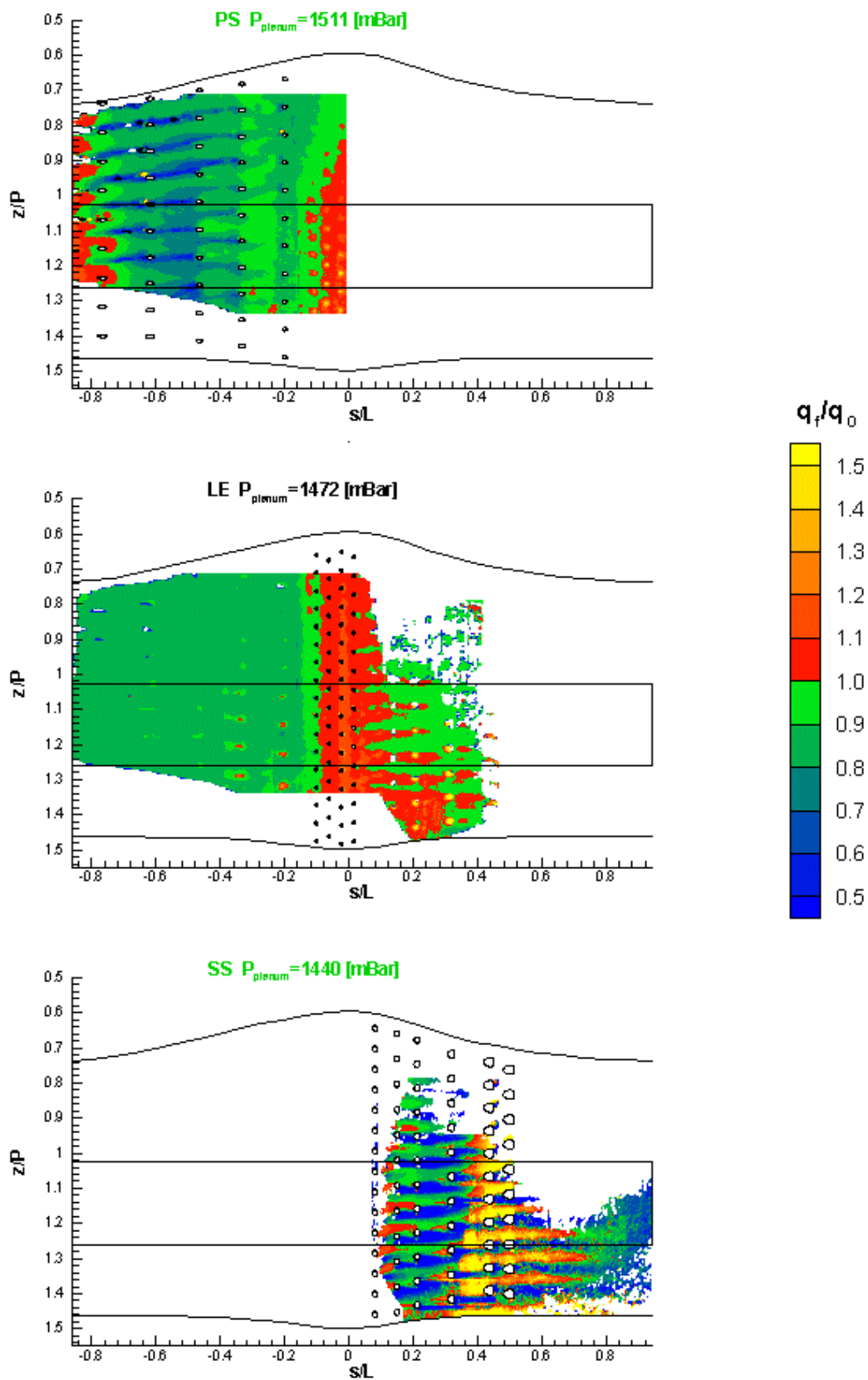


Figure 4-35: Film-Cooled and Un-Cooled Heat Flux Ratios for Independent PS LE SS Zones

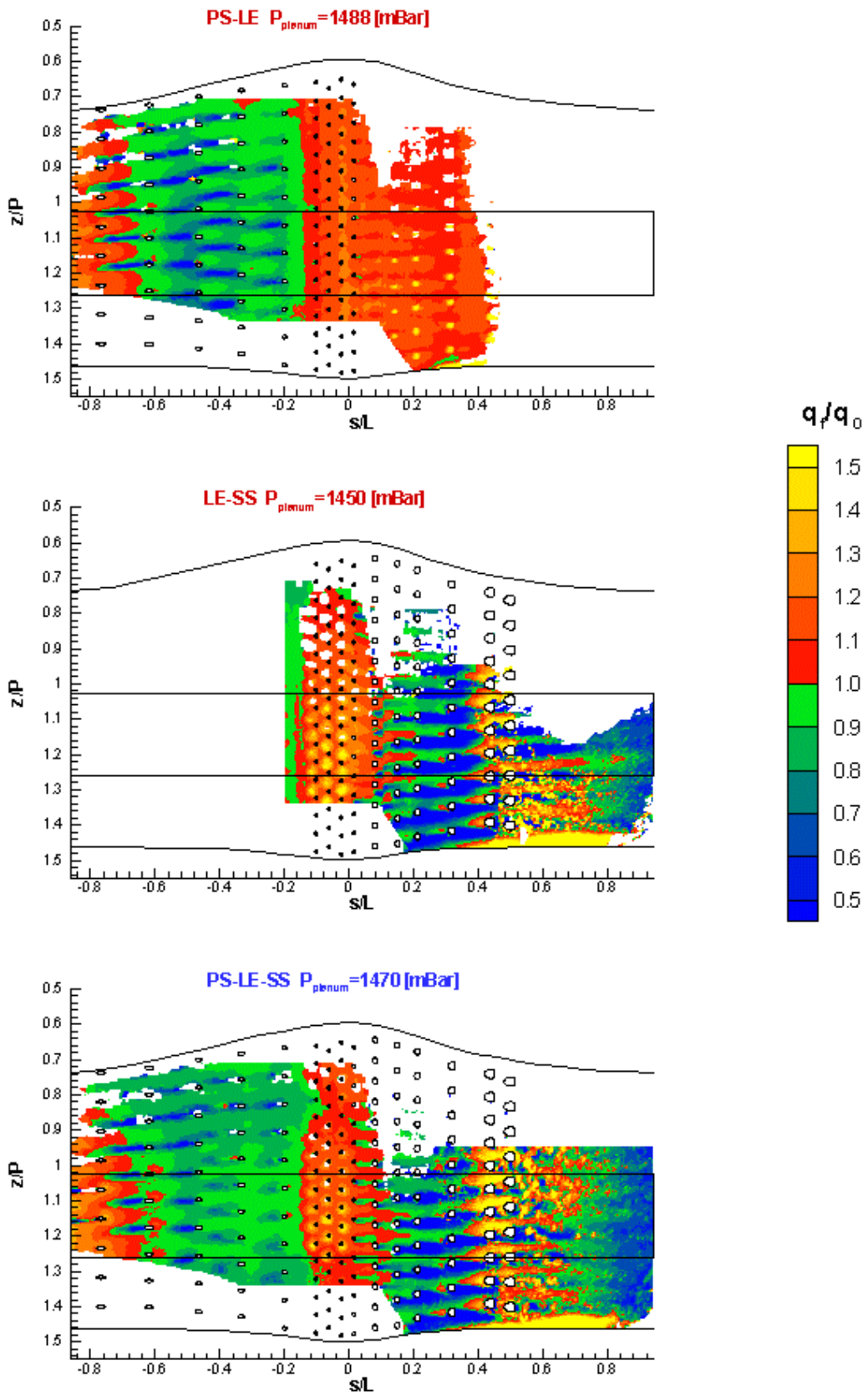


Figure 4-36: Film-Cooled and Un-Cooled Heat Flux Ratios for Combined PS LE SS Zones

4.3.3.4 Coolant gas distribution:

Based on the measurements of the discharge coefficient of each row separately and by considering the nominal main flow conditions and the averaging coolant flow condition from the nine to ten different transient experiments (max 5% variation on BR_i), it is then possible to determine the following parameters at each injection location for every film-cooled configuration:

1) p_{tc}/p_{sc} is the coolant gas pressure ratio and is given for each row of injection in Figure 4-37. p_{tc} is acquired by a pressure tap in the plenum chamber, while p_{sc} is obtained from the baseline aerodynamic measurements. The relatively low values for the leading edge rows denote the difficulty of maintaining high total pressure of coolant gas in the plenum chamber due to a lack of mechanical rigidity of the model. Moreover, even with a relatively low p_{tc} for an acceptable pressure ratio at the leading edge, the resulting pressure ratios on the suction side already give too high values. It must be noted that a pressure ratio that is too high (hence a coolant gas injection velocity that is too high) can conduct to lower film-cooling effectiveness. This is one of the reasons why fan-shaped holes are used on the suction side, as the diffusion effect decreases the coolant gas injection velocity (Takeishi et al., 2000).

2) DR present in Figure 4-38 is the coolant gas to main flow density ratio and is around 1.6 for a main flow gas of air at 333K and a CO_2 coolant gas at an average temperature of 303K. The results are given locally, with the main flow and the coolant gas densities based on the static conditions at local holes injection. The values are quite representative of the engine conditions, where the temperature levels of the mainstream and the coolant air give density ratios varying from 2 to 1.5. For the use of a unique plenum chamber feeding all rows of cooling holes with the same total coolant gas temperature T_{tc} and pressure p_{tc} , the density ratio should be kept constant at all locations in case of a coolant gas similar to that of the main flow. Slightly lower values of the density ratio on the suction side than on the pressure side (5%) are a consequence of CO_2 used as coolant gas in a main flow of air.

3) BR_i is the local (at injection location) coolant gas to local (also at injection location) main flow blowing ratio and is defined by:

$$BR_i = \frac{\rho_c u_c}{\rho_g u_g} \quad (4.8)$$

Values in Figure 4-39 go up to 3.5 or higher in the leading edge area since the local main flow velocity on the airfoil u_g tends to zero at the stagnation line. For these

regions, where the main flow velocity is very low or close to zero, it is normally preferred to use a blowing ratio based on the velocity conditions of approach. In this work, in order to be coherent with the rest of the rows using the local values due to significant velocity changes, values of the leading edge area are also presented with the local conditions. Hence, except for this area, the blowing ratios values applied during the experiments can be considered as representative engine conditions, as they usually vary from 0.5 to 2. It must be noted that for the LE-SS coolant case, the blowing ratio was not high enough and unfortunately resulted in quasi-zero effectiveness at the leading edge area as confirmed in Figure 4-34 (middle).

4) The coolant mass flow distribution relative to the main gas mass flow of one channel passage is given in Figure 4-40. Values are in %; hence, the total coolant mass flow used for the case with all the rows open (PS-LE-SS) is of 4.05% of the main gas mass flow. This is quite high compared to usual values of around 2.5% for typical engine conditions (Cohen et al., 1996). Indeed, a quite important part of the coolant gas goes to the suction side (2.54%), while the pressure side is fed by 0.81% and the leading edge by only 0.7%. This is a consequence of one plenum chamber configuration allowing a unique p_{tc} so that the coolant flow distribution is essentially driven by the static pressure distribution around the vane airfoil p_{sc} . For this reason, a coolant gas pressure that is too high in the plenum chamber leads to a dominating coolant mass flow injection on SS, and a pressure that is too low in the plenum chamber to a coolant gas injection that is too weak on LE, as already noted on Figure 4-34 (bottom graph). A better coolant gas distribution is applied in real engines thanks to the use of two plenum chambers. For complexity reasons, this was unfortunately not the case of the tested model and therefore compromises were made to have pressures in the plenum chamber giving acceptable coolant gas distributions.

The coolant flow distribution is only based on the pressure in the plenum chamber and on the discharge coefficient values of each row. The static pressure at the hole exit of each row is known; hence, the theoretical mass flow being injected can be calculated. The real mass flow is simply obtained by multiplying the theoretical mass flow with the discharge coefficient measured at the specific pressure ratio. Excellent agreement is found when comparing the total coolant mass flow obtained from the calculated distribution with the total coolant mass flow measured during the experiments. Hence, it confirms the accuracy of the discharge coefficient measurements (no or negligible coolant flow leakage).

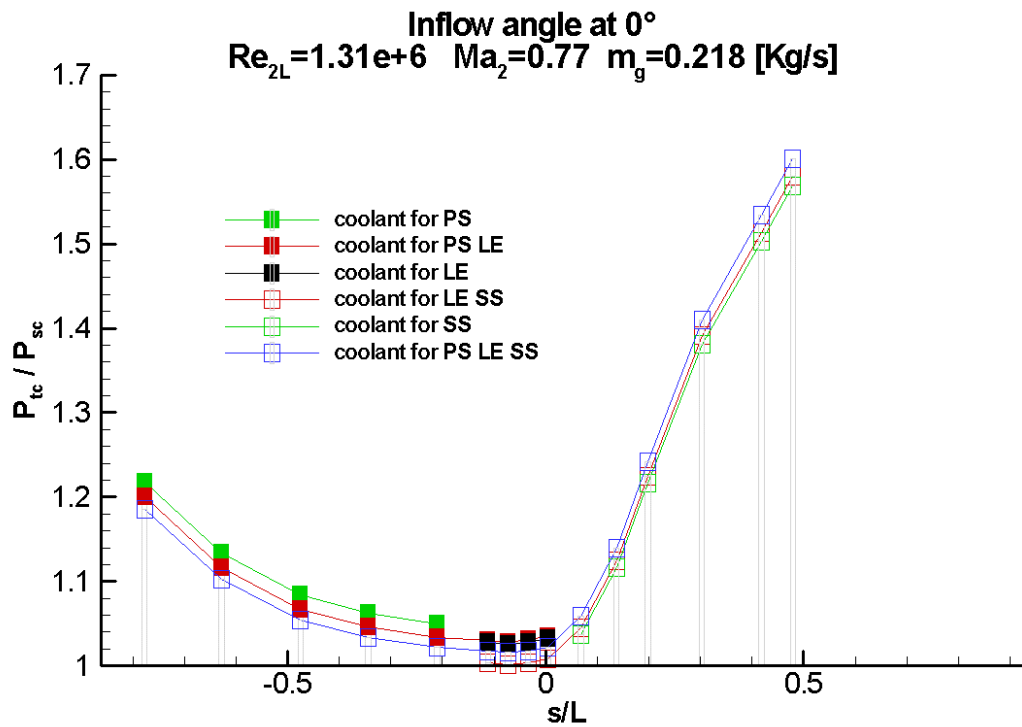


Figure 4-37: Pressure Ratio at the Different Rows of Coolant Gas Injection

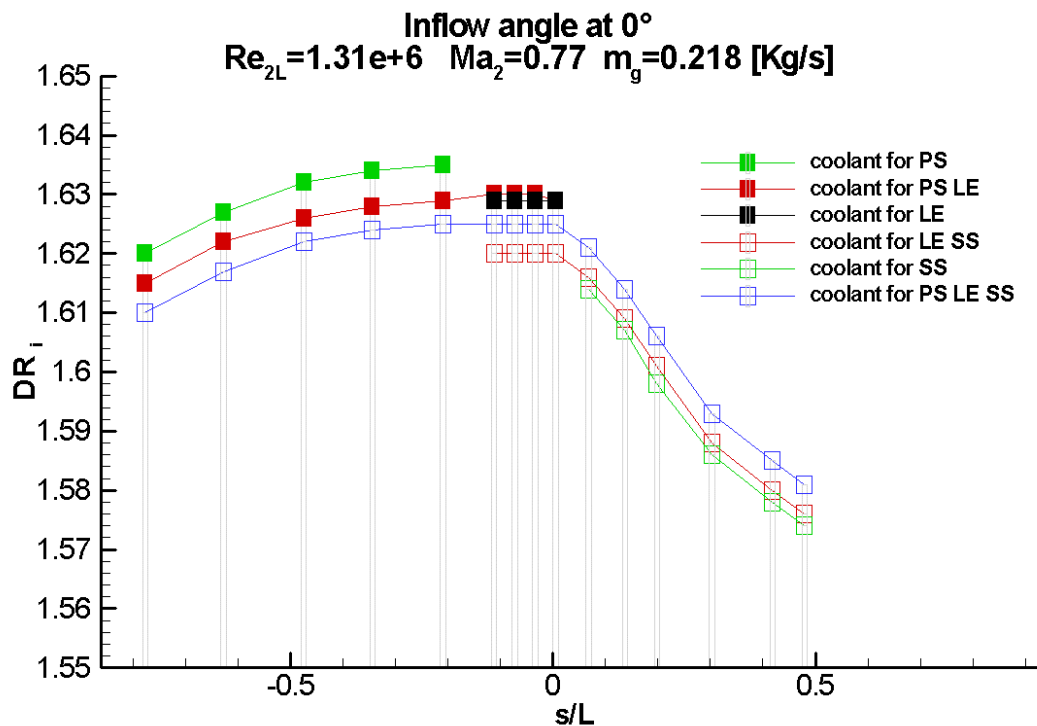


Figure 4-38: Density Ratio at the Different Rows of Coolant Gas Injection

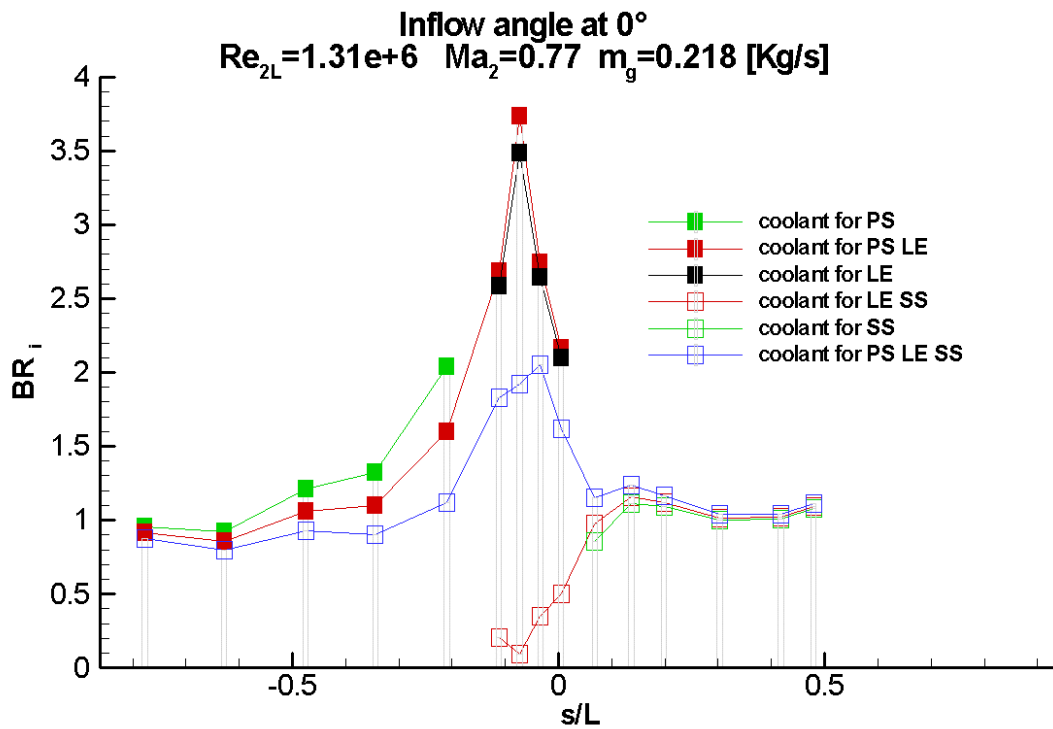


Figure 4-39: Blowing Ratio at the Different Rows of Coolant Gas Injection

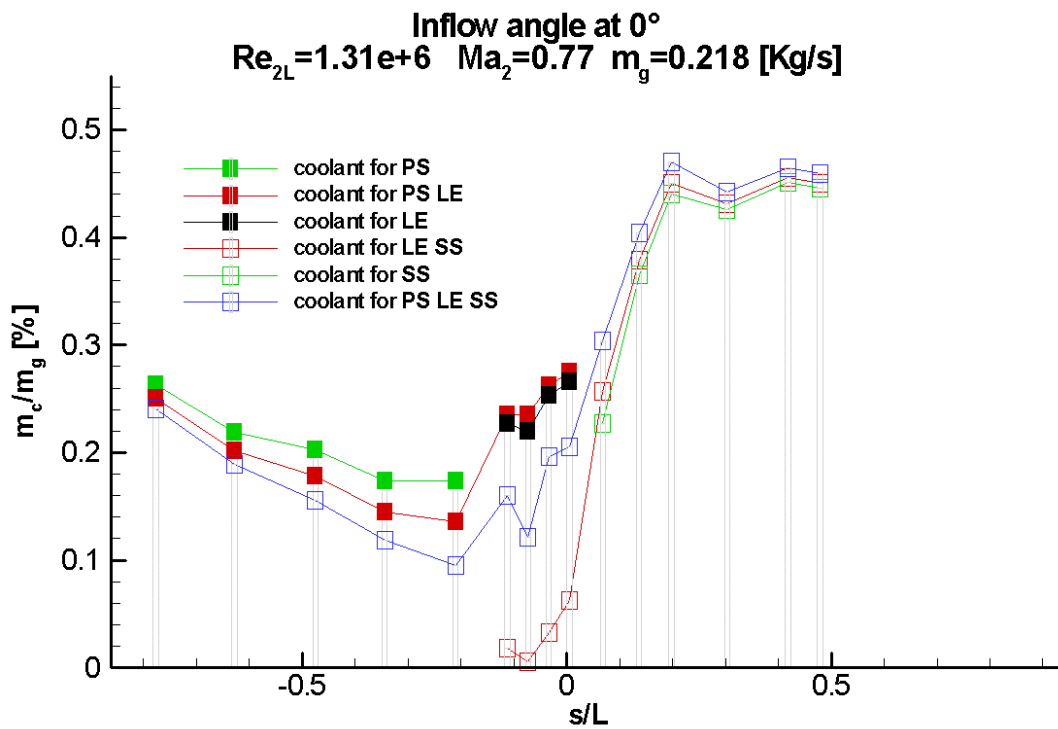


Figure 4-40: Coolant Mass Flow Distribution of the Different Rows

4.3.3.5 Measurements Uncertainties

Based on the existing measurement uncertainties for:

| | |
|---|--------------|
| Liquid Crystal Calibration T_{LC} | ± 0.1 K |
| Thermocouple Measurements T_{tg} T_o T_{tc} | ± 0.5 K |
| Time Resolution of Video Sequence | ± 0.04 s |

A statistical error estimation on the regression analysis as given by Drost (1998) is developed here for the new introduced coolant gas temperature evolution function defined in equation (c.8). For about the same test conditions and with an identical number of experiments used in the regression, the measurement uncertainty reduces from 6% to 4.5% for the heat transfer coefficients and with about the same magnitude for the film-cooling effectiveness. This improvement is essentially due to a lower measurement uncertainty of the liquid crystal signal detection obtained by the new developed Digital Video system, and also to the use of a more adequate function fitting the coolant gas temperature evolution.

Although very time consuming (about 120 hours on a Pentium IV 2 GHz), the measurement uncertainties were calculated for each measured pixel on the heavy film-cooled vane configuration. Figure 4-41 gives the detailed information on the quality of the film-cooled vane results.

For the heat transfer coefficient h_f , error values are not higher than 5% except very close to some suction side holes, where the semi-infinite model theory is no longer valid due to conduction effects. Despite this, the error level is slightly higher for higher heat transfer coefficients, which can logically be explained as a consequence of a faster transient liquid crystal signal during the experiments.

For the film cooling effectiveness, the error level is higher than for the heat transfer coefficients. This is especially the case for the leading edge region where error values can reach more than 24%. However, this has to be related to the fact that this area has very low or zero film-cooling effectiveness levels. The lower the film-cooling effectiveness is, the higher the measurement uncertainty is. So despite for the low film-cooled covered areas, uncertainties on the film-cooling effectiveness vary from 15% for $\eta=0.04$ to only 2% for $\eta=0.4$.

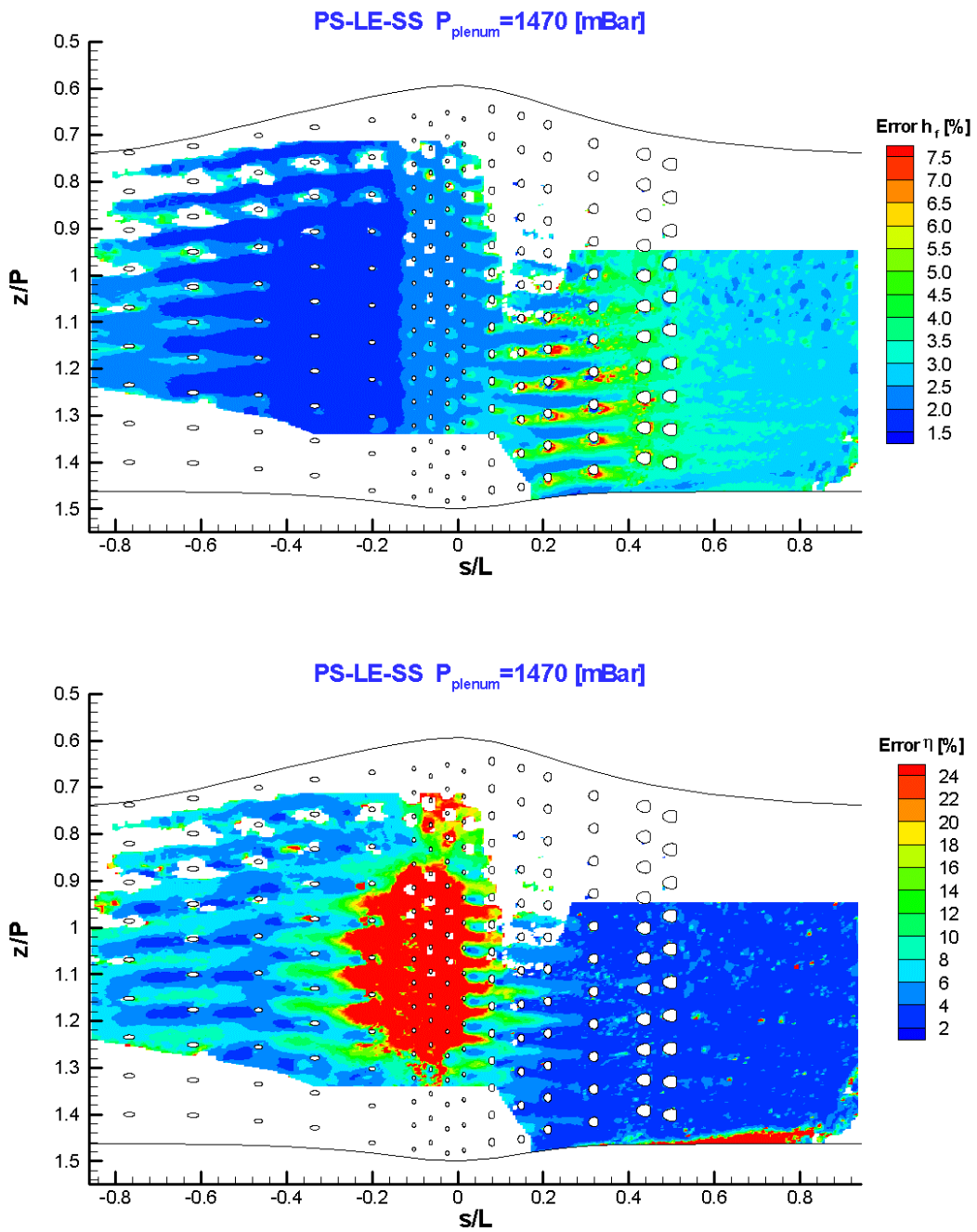


Figure 4-41: Detailed Measurement Uncertainties for the Heavy Film-Cooled Vane

4.3.4 Conclusion of the Film-Cooled Vane

- The regression of multi transient liquid crystal experiments for film cooling measurements has been introduced.
- All measurements were performed at nominal main flow conditions. Specific blowing ratios were used for the different configurations. For each configuration about ten transient experiments were performed with different coolant gas temperatures in order to apply the regression method.
- Four camera views were used for all cases and were assembled and presented on an unwrapped surface. Span-wise averaging were also performed and presented on graphs superposing the different cases. Due to the use of only one plenum chamber feeding all the rows of cooling holes, slight differences of blowing ratio between the different configurations occurred, especially on the leading edge area. Despite this, close agreement of the heat transfer coefficient curves was observed.
- The film-cooled heat transfer coefficient h_f and the adiabatic film cooling effectiveness η results have been given. Based on these results, a heat flux ratio between the film-cooled and the baseline cases have been estimated, giving information on the performance of the film cooling holes design.
- Discharge coefficients of each row have been measured and used to determine the coolant flow distribution related to the heat transfer results. Parameters such as coolant density ratio, coolant blowing ratio and coolant mass flow has been presented.
- Finally, a detailed error measurement analysis has been performed, giving precise information on the accuracy of the results.

5 TRANSIENT MEASUREMENT TECHNIQUE WITH HEATER FOIL

This chapter introduces the new measurement technique that is developed for the heat transfer experiments on the baseline and film-cooled platforms. It is based on a transient liquid crystal technique with the use of an electrical heater-foil. Preliminary tests of this technique are performed on a simple film-cooled flat plate configuration for validation.

First, an analytical model and its numerical resolution are derived. The experimental set-up is then described as well as the measurement errors analysis. Furthermore, the influence of four different heater foil configurations and therefore different thermal boundary conditions on the film cooling performance is studied.

5.1 Introduction to Heater Foil Techniques

Heat transfer measurements on the central vane airfoil are performed by the rapid insertion of a preconditioned model. For the cylindrical model, this technique does not disturb the flow conditions, as a dummy vane part is present before the transient experiment. This is not the case of a contoured platform model if a similar exposure system would be applied for heat transfer measurements. Therefore, another measurement technique has to be employed. For stationary models, von Wolfersdorf et al. (1993) and Turnbull et al. (1999) applied transient electrical heater-foil techniques with liquid crystal thermography for heat transfer investigations. Since no film cooling holes were considered, the full surface under investigation was covered with the heated layer. In case of film cooling, transient measurements using heater foils were applied for slots by Farmer et al. (1997) and for a row of holes by Seager et al. (1997), but with the heater-foil applied only in the area behind the holes. Heater-foil application has then the potential of heat transfer measurements on the platform. However, due to the film-cooled platform configuration of this work, it is not possible to apply a heater foil of homogeneous heat flux just behind the cooling holes. Therefore, a new transient heater foil method is introduced which is able to determine the film cooling effectiveness and the heat transfer augmentation simultaneously even for non-uniform heat flux situations (e.g. film cooling holes in the heater foil or curved surfaces) by using multiple transient experiments and a regression analysis. The applicability of this method is tested and validated on a film-cooled flat plate before its application on the casing wall platform.

5.2 Basic Principle of Film-Cooled Experiments with Heater Foils

The theoretical model of a transient film-cooled flat plate experiment using a thin electrical heater-foil is presented in Figure 5-1.

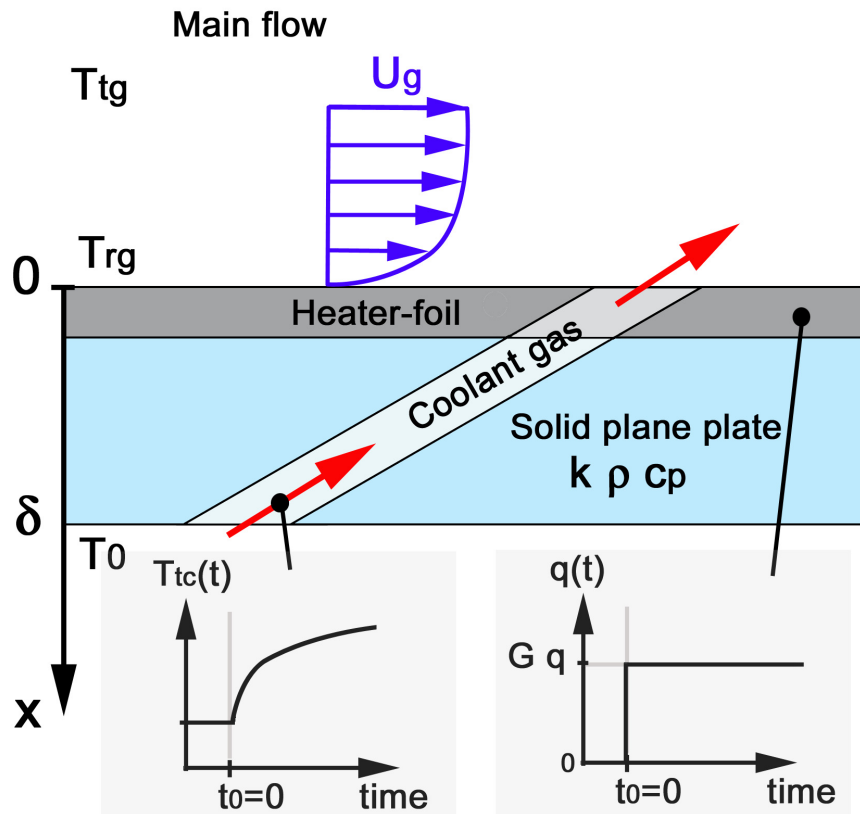


Figure 5-1: Model Configuration of Heater Foil and Film-Cooled Experiments

Before the experiment, no coolant gas is injected and the recovery temperature of the main gas gives the surface model temperature. At the start of the transient experiment, the coolant gas is injected on the surface. At the same time, a heat flux is generated by the heater-foil. Depending on the local heat flux, heat transfer coefficient, and film cooling effectiveness, the temperature at the surface of the model changes. If liquid crystals are applied on the surface, then the surface temperature evolution can be determined and used for heat transfer measurements. The theoretical development of this data analysis is given in Appendix D and as in Appendix C, is based on a regression of multiple transient experiments.

5.3 Heater-Foil Experiment Set up for a Film-Cooled Flat Plate

In order to validate the new developed transient heater-foil technique, experiments are carried out in an open low speed wind tunnel with a square cross-section of 100 mm x 100 mm and a total length of 1500 mm. The walls of the channel are made out of 15 mm thick Perspex which also provides a good optical access. The main air flow is coming from two electrical fans mounted in series, passing through a settling chamber and a convergent nozzle as represented in Figure 5-2.

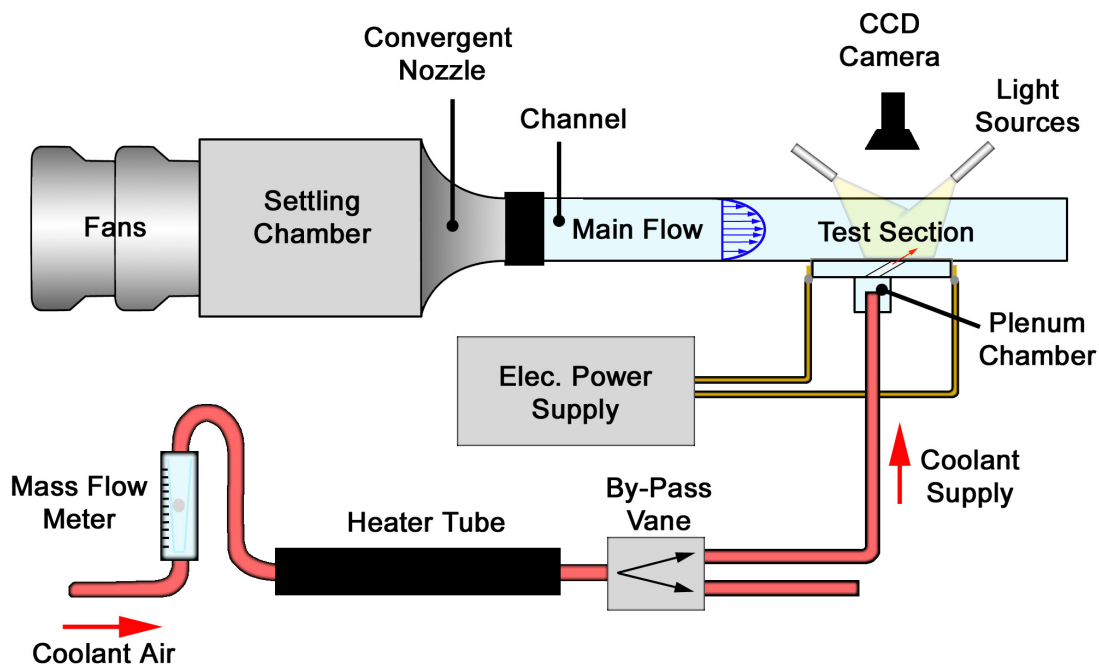


Figure 5-2: Schematic Drawing of the Flat Plate Test Facility

The flat plate test section is located on the bottom wall of the channel at about 10 hydraulic diameters from the square channel inlet. The latter consists of a flat plate of 250 mm in length and a wall thickness of $\delta=25$ mm film-cooled by a row of five cylindrical holes of $D=5$ mm diameter. This row of holes is located at 20 hole-diameters from the end of the plate. The five holes are centered in the transversal (span-wise) direction of the squared channel with a pitch of $P/D=3.5$. The axis of the holes is aligned to the channel flow direction (no compound angle) and with an exit angle of $\varphi=30^\circ$ from the surface of the flat plate. The ratio between the length of the hole L_D and its diameter D is $L_D/D>3$.

The plenum chamber feeding the coolant holes is fixed on the bottom part of the test section. Coolant is supplied to this plenum chamber by an orifice located on the lateral right-hand-side relative to the main flow direction in the channel. The coolant to mainstream blowing ratio is adjusted and measured by a graduated glass flow meter. The temperature of the coolant is adjusted by an electrical heater tube mounted downstream of the glass flow meter. A by-pass vane mounted at the exit of the heater tube allows the preconditioning of the coolant flow before its injection into the plenum chamber where a thermocouple measures the coolant temperature during the transient experiments.

A nickel-chrome heater-foil of 20 μm thickness is glued onto the upper surface of the test section. The foil is connected to an electrical power supply through copper cables and bus bars. Thermocouples electrically insulated with the heater foil are mounted on the upper and lower surface of the plate for monitoring the homogeneity of the initial surface temperature. A black coating layer (Hallcrest BB-G1) followed by a thermo-chromic narrow band liquid crystals layer (Hallcrest BM/R36C1W) and a varnish protection layer (Hallcrest AQB-2) are applied on the heater foil. A thermocouple mounted (with a 3M-Kapton tape) on top of these layers is used for the hue-temperature calibration of the liquid crystals T_{LC} .

Like for the transient liquid crystal experiments on the vane airfoil, cold light sources directed by fiber optics are used for the illumination of the test section. Hue value variations on the surface are recorded during the transient experiment by one color CCD camera mounted perpendicular to the test section and viewing through the upper wall of the channel. At any position on the plate, the time t_{LC} needed from the beginning of the transient experiment to reach a specific surface temperature T_{LC} is then obtained by performing a data reduction of the hue video sequence as already described in chapter 3. A LED, mounted close to the test section is triggered by the activation of the power supply connected to the heater-foil and is used to determine the beginning of the transient experiment on the video sequences. The same trigger signal is also used to activate the bypass vane; hence, synchronizing the coolant flow injection with the surface heat fluxes generation.

Experiments are performed in the aforementioned wind tunnel with an exit flow velocity of about $U_g=22$ m/s and a total gas temperature of about $T_{tg}=296\text{K}$. Air is used as coolant gas and the film cooling blowing ratio is set to $BR=0.3$. The initial temperature of the test section is in the same range as the total gas temperature and a specific hue value of the narrow band liquid crystals is calibrated for $T_{LC}=309.2\text{K}$.

The coolant is pre-conditioned with temperatures varying from 298 K to 323 K. The variable amount of heat flux applied during the N transient experiments is chosen in order to have time event samples neither too short ($t_{LC} > 2$ s) because of the rapid evolution of T_w at the beginning of the transient test, nor too long ($t_{LC} < 1600$ s) in order to respect the semi-infinite criterion. Numerical simulations of the temporal evolution of T_w for estimated values of heat transfer coefficient and film cooling effectiveness are first performed in order to assess the range of t_{LC} for the experiments. An example of the T_w numerical simulation is given in Figure d-1 of Appendix D.

Four different film-cooled flat plate heater-foil configurations as shown in Figure 5-3 are investigated and for every case, a total of nine experiments ($N=9$) are performed, consisting of three different heat flux ratios combined with three different preconditioned coolant temperatures.

Case 1: Longitudinal Electrical Current: One pair of bus bars is connected perpendicular to the flow direction forcing a global, longitudinal electrical current in the foil. This configuration generates an inhomogeneous heat flux distribution with higher values in-between the holes as a consequence of the reduced conductible surface (conservation of electric charge).

Case 2: Transversal Electrical Current: One pair of bus bars is connected parallel to the flow direction forcing a global transversal electrical current in the foil. This configuration also generates an inhomogeneous heat flux distribution with lower values in-between the holes.

Case 3: Upstream and Downstream Transversal Electrical Current: Two pairs of bus bars are connected parallel to the flow direction forcing a global transversal electrical current in two foils, one upstream and the other downstream of the row of cooling holes. This configuration generates two homogeneous heat fluxes, but of different levels.

Case 4: Downstream Transversal Electrical Current: One pair of bus bars is connected parallel to the flow direction forcing a global transversal electrical current in the foil downstream of the row of cooling holes; thus generating a homogeneous heat flux.

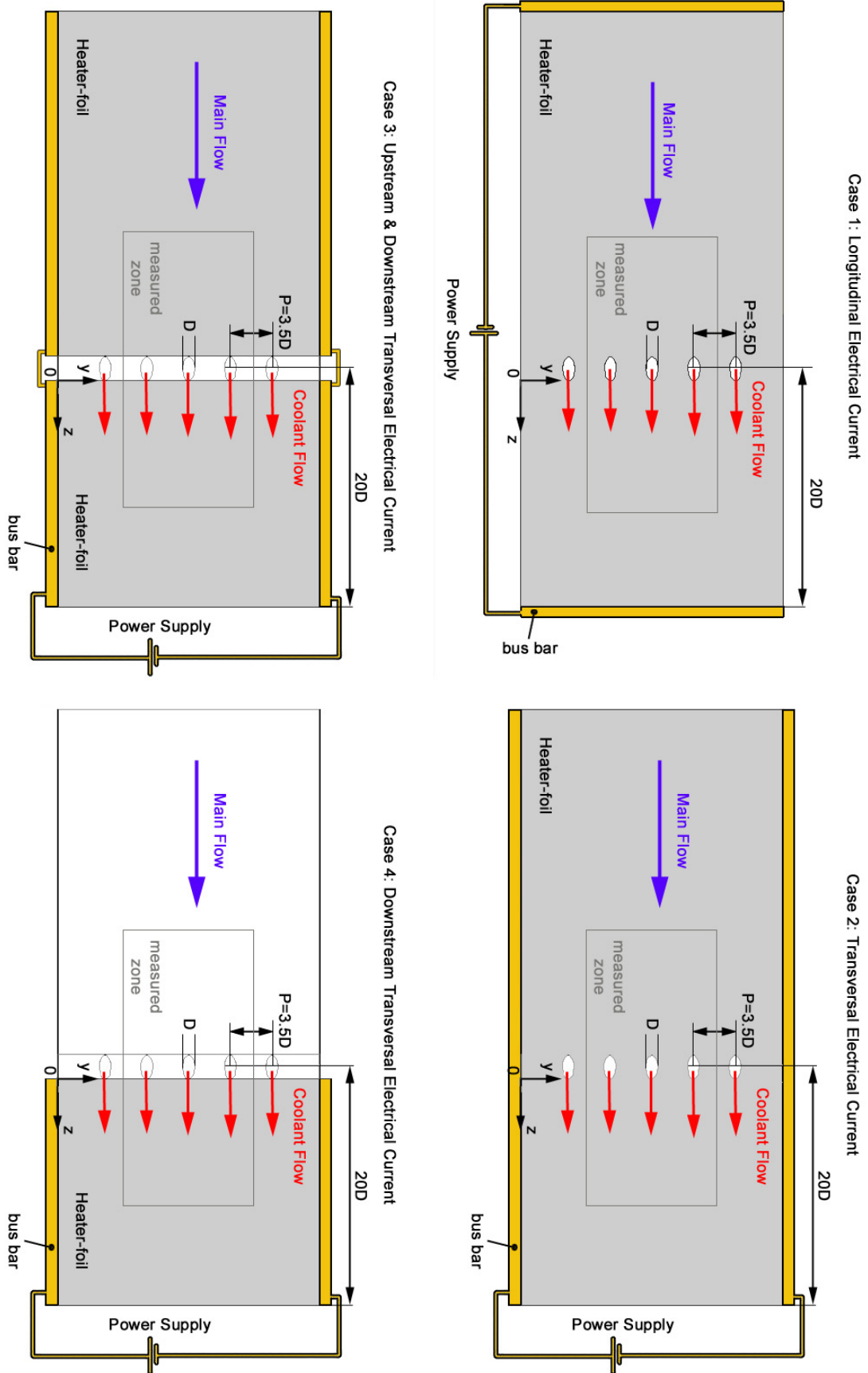


Figure 5-3: Film-Cooled Flat Plate Heater Foils Configurations

Case 3 and 4 are the usual heater-foil configurations of film-cooled experiments where a homogeneous heat flux is generated but can only be applied for simple geometries. For more complex geometries, like a film-cooled contoured platform considered later in this work, the only way to use heater-foils is to apply them on the complete surface, as for case 1 and 2, and to deal with an inhomogeneous heat-flux application due to the presence of the cooling holes. The new measurement technique presented in this chapter is developed for heater-foil experiments with an unknown surface heat flux distribution q . Hence, experiments of these four different cases allows the validation of the new heater-foil measurement technique as well as the determination of the influence or lack thereof of an inhomogeneous heat-flux on the heat transfer coefficient and adiabatic film cooling effectiveness results.

5.4 Film-Cooled Flat Plate Results

As it can be seen in Figure 5-3, the results on the flat plate are issued from different wall boundary conditions due to the heater-foil configuration. If cases 3 and 4 have a homogeneous heat flux, it is not the case for configuration 1 and 2 where the heater foil is also present around the holes. As the new measurement technique is able to determine the inhomogeneous reference heat flux (as a by-product) issued from the experiments (see Appendix D), it is then interesting to observe the distribution between case 1 and case 2 caused by different connections of the power supply to the heater foil. The reference heat flux q obtained by the regression of the measurements is presented in its non-dimensional form q/\bar{q} in Figure 5-4 (upper graphs). The effective surface heat flux generation applied during each experiment i is then the product of q by its gain factor G^i . For case 1, the local surface heat flux tends to increase in-between the holes and decreases in the longitudinal prolongation of the holes. The opposite is true for case 2 where the local surface heat flux is low or close to zero in-between the holes and increases in their longitudinal prolongation. This corresponds to the expected result when considering the local surface resistance of the foil and the path of the electrical current.

For case 2 Figure 5-4 (upper graph right), there are two kind of blank (white) areas on the surface. The small ones at the same y/D positions of the holes and surrounded by high heat flux levels, are blank areas of high heat flux levels that generated a too fast, hence non-captured, transient liquid crystal signal. The larger ones, located in-between the holes, have to be considered as blank areas of low heat

flux levels that did not produce enough increase of the surface temperature to be detected by the liquid crystal coating.

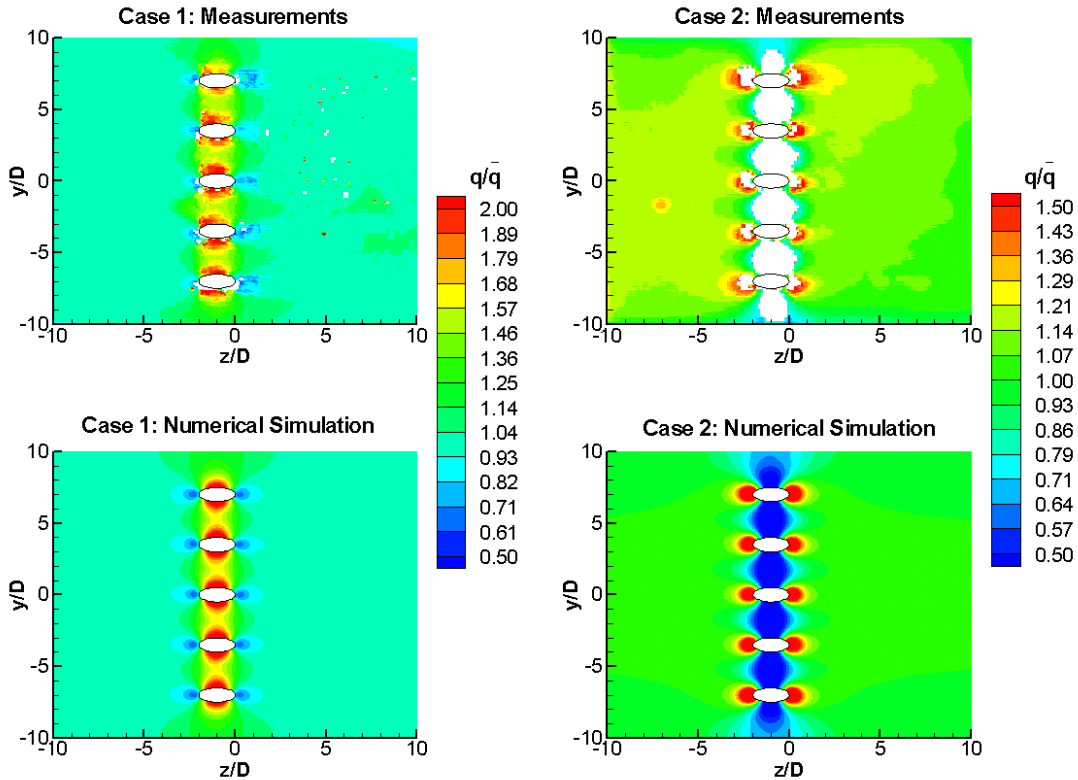


Figure 5-4: Dimensionless Reference Heat Flux Distribution Measurements (upper) and Calculations (lower)

The surface heat flux distributions in these two cases are compared to numerical simulations obtained by a method described by Wiedner and Camci (1996). These calculated values are shown in Figure 5-4 (lower graphs) and present excellent agreement with the experimental values. Hence, they validate the regression approach of multiple transient heater-foil experiments and the development of the new measurement technique described above regarding the heat flux determination. It should be added that with this measurement technique, the heat flux losses (electrical wiring, lateral conduction) are automatically accounted for without an explicit knowledge of them. These losses if determined by assessing the difference between the power given by the power supply and the heated surface yield a difference of ~25%.

Figure 5-5 shows the spatial distribution of the measured heat transfer coefficient and Figure 5-7 the adiabatic film cooling effectiveness, for the four heater foil configurations. For a better discussion of the results, the heat transfer coefficients and the film cooling effectiveness values are laterally averaged over one pitch of hole (see black rectangles, $-1.75 < y/D < +1.75$ and $0 < z/D < 10$) and presented in Figure 5-6 and Figure 5-8 respectively.

The observed changes in the heat transfer distribution are due to the changed thermal boundary conditions between the individual cases. If the near hole region is not taken into account, the difference between the heat transfer coefficients of case 1 and case 2 is quite small and can be generally neglected. This is explained by the fact that these two configurations have the same heater-foil coverage but a different power supply connection in order to produce the surface heat flux distribution, yielding only a slight change in the thermal boundary layer. Indeed, both configurations lead to the same starting point of the thermal boundary layer (at the starting of the plate). Case 2 however has a slightly lower heat flux levels at the row location but still more than for case 3 where the disruption in heat flux from the surface to the flow locally changes the thermal boundary layer thickness. In case 4, the start of the thermal boundary layer is delayed to $z/D > 0$ (after the film cooling holes) and results in a much higher heat transfer coefficients after the row of holes than for the other cases. Except for case 4, the change in thermal boundary conditions on the heat transfer coefficients can be neglected. This important outcome thus validates the use of complete heater-foil coverage with inhomogeneous heat flux distribution compared to the often-used film cooling studies in literature using homogeneous heat flux distribution similar to case 3. Moreover the results for the heat transfer coefficients of case 4 show clearly that care has to be taken in selecting appropriate thermal wall boundary conditions for film cooling experiments.

Concerning the distribution of the adiabatic film cooling effectiveness, only small differences can be observed between the individual cases. Additionally, Figure 5-8 also shows values from a film cooling effectiveness correlation given by Baldauf et al. (1997) based on a large set of experimental data. The results obtained here are in good agreement with those found in literature, further validating the present measurement method.

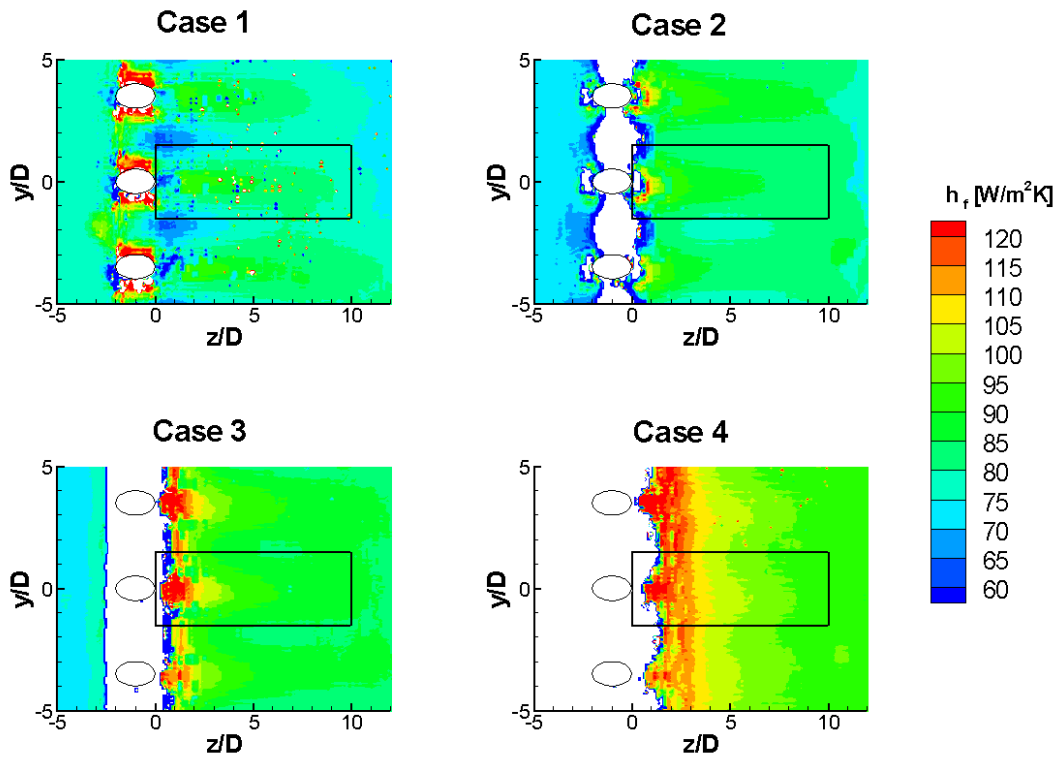


Figure 5-5: Surface Distribution of Heat Transfer Coefficients on the Plate

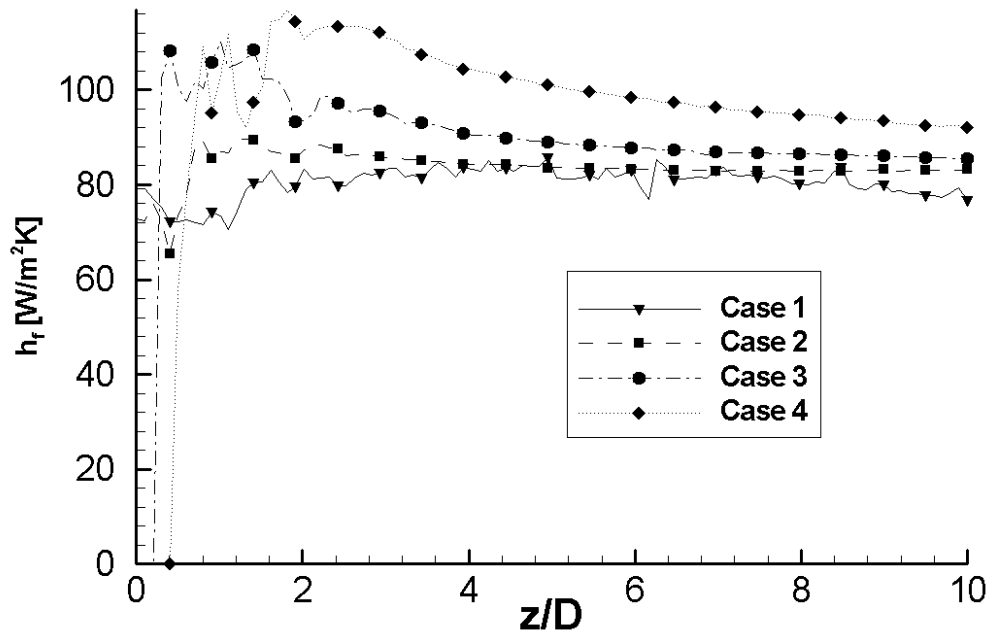


Figure 5-6: Lateral Averaging of Heat Transfer Coefficients on the Plate

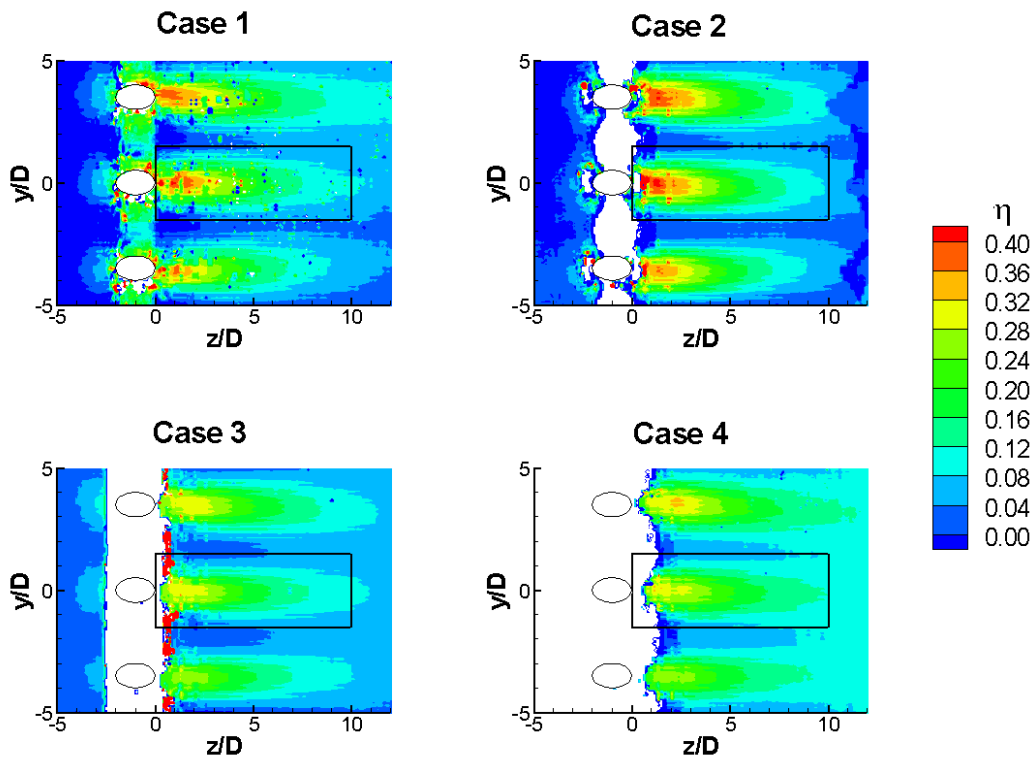


Figure 5-7: Surface Distribution of Adiabatic Film Cooling Effectiveness on the Plate

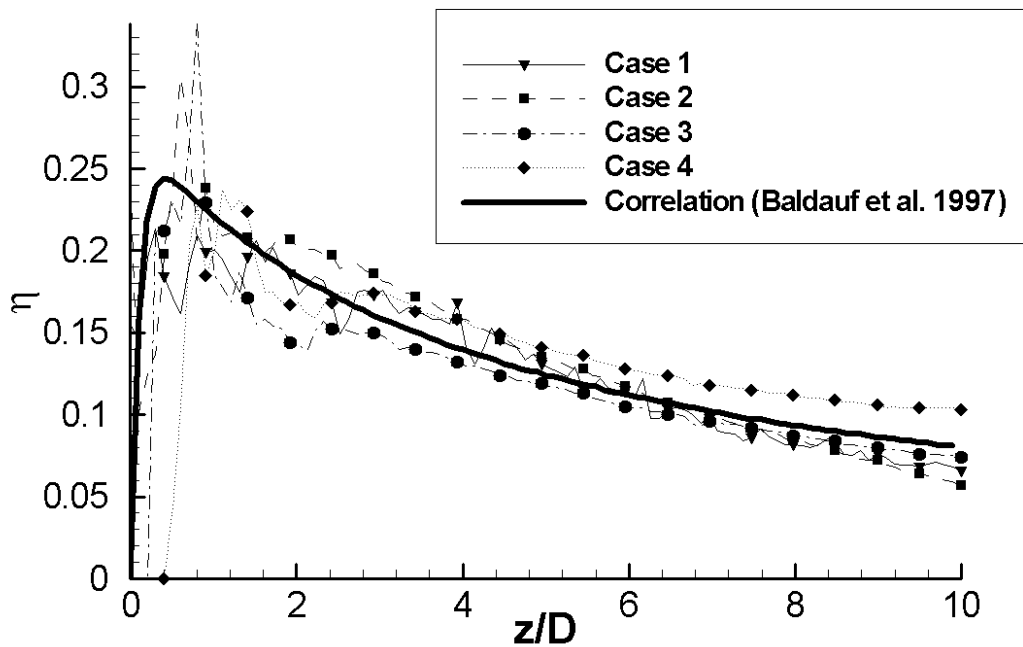


Figure 5-8: Lateral Averaging of Adiabatic Film-Cooling Effectiveness on the Plate

5.5 Measurement Error Analysis

The approach used for the measurement error analysis is similar to the one described in Kline and McClintock (1953). The values h_f , η and q are obtained from a regression analysis as described in Appendix D and have thus the subsequent dependencies: (form(d.15) (d.17) and (d.18))

$$h_f = h_f(T_{LC}^i, t_{LC}^i, T_{ig}^i, T_{rg}^i, T_0^i, T_{ic}^i, G^i), \quad q = q(h_f), \quad \eta = \eta(h_f, q) \quad (5.1)$$

In the following equation, the absolute error Δx_j of the above variables is considered identical across the different experiments. The following absolute errors can then be computed:

$$\Delta h_f = \sqrt{\sum_{i=1}^N \left[\left(\frac{\partial h_f}{\partial T_{LC}^i} \Delta T_{LC} \right)^2 + \left(\frac{\partial h_f}{\partial t_{LC}^i} \Delta t_{LC} \right)^2 + \left(\frac{\partial h_f}{\partial T_{ig}^i} \Delta T_{ig} \right)^2 + \left(\frac{\partial h_f}{\partial T_{rg}^i} \Delta T_{rg} \right)^2 + \left(\frac{\partial h_f}{\partial T_0^i} \Delta T_0 \right)^2 + \left(\frac{\partial h_f}{\partial T_{ic}^i} \Delta T_{ic} \right)^2 + \left(\frac{\partial h_f}{\partial G^i} \Delta G \right)^2 \right]}$$

$$\Delta q = \left| \frac{\partial q}{\partial h_f} \Delta h_f \right| \quad (5.2)$$

$$\Delta \eta = \sqrt{\left(\frac{\partial \eta}{\partial h_f} \Delta h_f \right)^2 + \left(\frac{\partial \eta}{\partial q} \Delta q \right)^2}$$

A centered scheme is used to approximate the above partial derivatives as:

$$\frac{\partial f}{\partial x_j} \approx \frac{f(x_1, \dots, x_j + \Delta x_j, \dots, x_j) - f(x_1, \dots, x_j - \Delta x_j, \dots, x_j)}{2 \Delta x_j} = \frac{\tilde{f}(x_j)}{2 \Delta x_j} \quad (5.3)$$

where $x_j, j=1 \dots J$, are the variables of a function f . The discretization step of the numerical scheme for a given variable is assumed to be identical to the absolute error of this variable and the following is then obtained:

$$\Delta h_f = \frac{1}{2} \sqrt{\sum_{i=1}^N \left[\tilde{h}_f(T_{LC}^i)^2 + \tilde{h}_f(t_{LC}^i)^2 + \tilde{h}_f(T_{ig}^i)^2 + \tilde{h}_f(T_{rg}^i)^2 + \tilde{h}_f(T_0^i)^2 + \tilde{h}_f(T_{ic}^i)^2 + \tilde{h}_f(G^i)^2 \right]} \quad (5.4)$$

Subsequently the errors for q and η become:

$$\Delta q = \frac{1}{2} |\tilde{q}(h_f)| \quad \Delta \eta = \frac{1}{2} \sqrt{\tilde{\eta}(h_f)^2 + \tilde{\eta}(q)^2} \quad (5.5)$$

For the experimental measurements, a relative error of 1% on the heat flux ratios G^i is considered. The liquid crystal band T_{LC} is calibrated with a precision of ± 0.1 K. For all the other temperature measurements an absolute error of ± 0.5 K is taken into account. This holds for the coolant gas temperature evolution where this error on the temperature can also be interpreted as a time error. The time detection of the transient liquid crystal signal is based on an absolute error of ± 0.04 seconds corresponding to one frame of the video sequence.

The error analysis is then based upon a total of nine tests resulting from a combination of three typical coolant gas variations T_{tc} combined with three typical heat flux ratios G^i as applied during the measurements on the film-cooled flat plate. For a representative result issued from the four flat plate configurations ($h_f=100$ W/m²K, $\eta=0.15$ and $q=1500$ W/m²), this leads to a maximum relative error on h_f of <8%, on η of <2% and on q of <3%.

As the measurement errors are based on the regression of multiple experiments, it is interesting to see (at this representative condition) the influence of the number of experiments taken into account. Simulations of the regression are then performed for G^i combined either with one, two, three or four different coolant gas temperatures injections T_{tc} . Results are presented in Figure 5-9 and show that in all cases the errors decrease with an increasing number of experiments, albeit to different levels depending on the number of coolant gas variations used. The optimum configuration appears to be the use of three different heat flux ratios combined with three different coolant gas temperature variations. This was the configuration used for the four film-cooled flat plate cases presented earlier in this chapter.

In addition to the measurement errors, the initial and the liquid crystal temperatures, the coolant gas preconditioning, and heat fluxes levels applied have to be chosen in accordance with the expected values of h_f , η and q . This may be assessed using numerical simulations of the temporal evolution of T_w in order to have acceptable t_{LC} values during the experiments. Indeed, a transient liquid crystal signal that is too fast leads to higher errors due to a limited time resolution for t_{LC} , and a transient signal that is too slow leads also to higher errors, since the semi-infinite model assumption is not satisfied anymore.

**Relative errors on the # of experiments used for regression
at $h_f=100 [W/m^2K]$, $\eta=0.15$, $q=1500 [W/m^2]$**

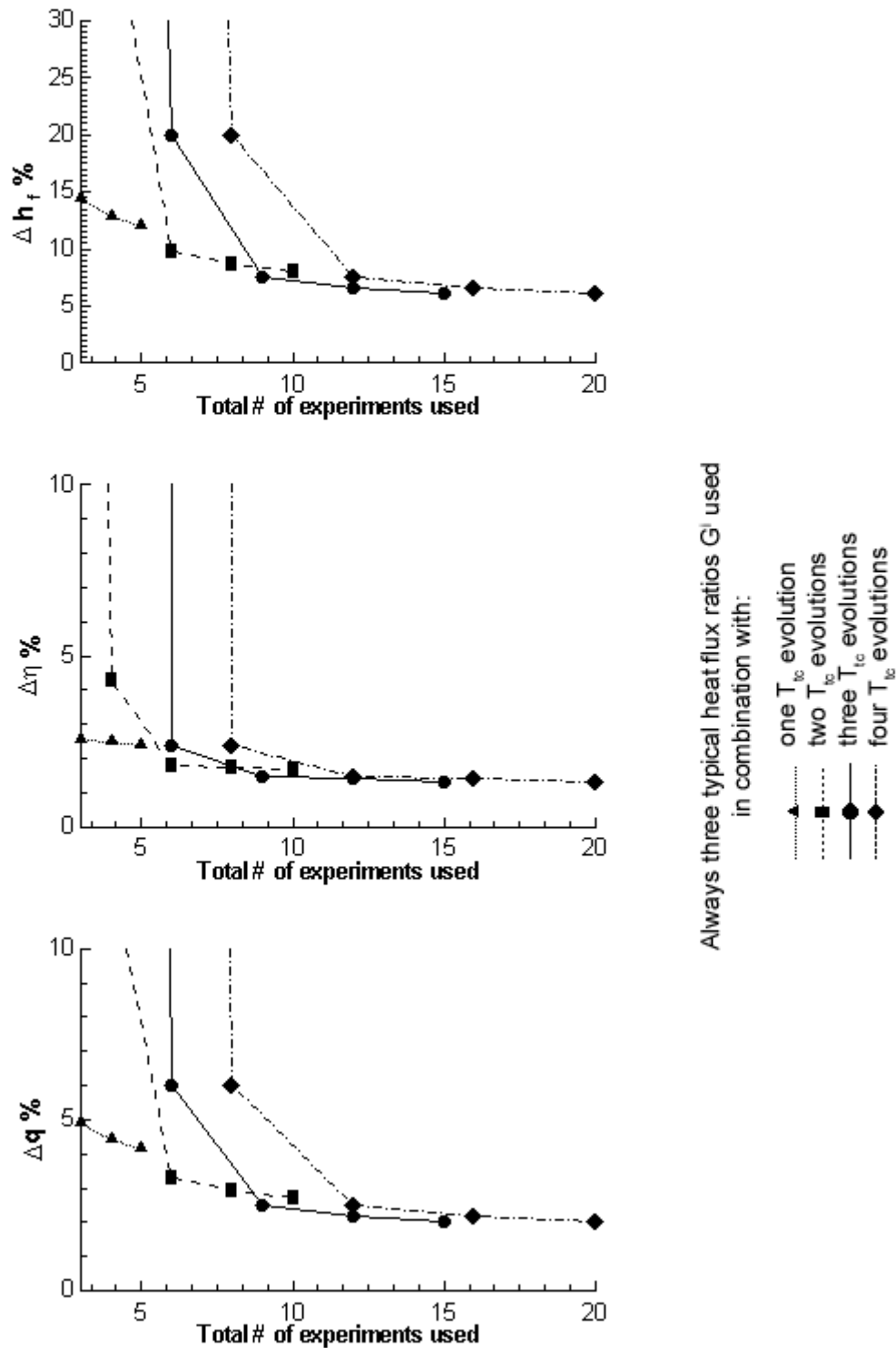


Figure 5-9: Relative Error Evolution for Different Number of Experiments Used in Regression Analysis

5.6 Conclusion of Transient Measurement Technique with Heater Foil

- A new measurement technique for transient liquid crystal experiments with heater-foil activation has been presented. It has the advantage of working for inhomogeneous heat flux distributions, which is usually the case of heater-foils applied to complex geometries.
- Experiments have been carried out on a film-cooled flat plate for configurations with homogeneous and inhomogeneous heat-flux distributions. Results show excellent agreement with numerical simulations and data from literature.
- A detailed error measurement analysis has verified the accuracy of this new measurement technique, hence validating its application for heat transfer measurements on the platform.

6 PLATFORM EXPERIMENTS

This chapter describes the baseline and film-cooled measurements on the casing platform of the nozzle guide vane geometry adapted for the linear cascade test facility. Some aerodynamic measurements on the platform are first presented, followed by the baseline and film-cooled heat transfer experiments.

6.1 Aerodynamic Measurements on the Platform

6.1.1 Description of Aerodynamic Measurements on the Platform

A total of 58 pressure taps are drilled into the initially used metallic platform in order to measure the casing wall static pressure distribution on the left and right channels of the central vane airfoil. Due to the limited space available behind the platform, it results in a quite impressive and complex tubing arrangement as shown in Figure 6-1. These 58 pressure tubes were then connected to an array of pressure transducers and allowed the determination of the isentropic Mach number distribution on the platform. To increase the spatial resolution of the data, the Pressure Sensitive Paint technique was used.



Figure 6-1: Tubing Arrangement for the Casing Wall Static Pressure Distribution Measurements

6.1.2 Mach Number Distribution on the Casing Platform

The Mach number distribution on the platform at nominal flow conditions is presented in Figure 6-2. The white dots indicate the pressure taps positions. These results allow determining the recovery gas temperature; hence, the initial wall temperature distribution used for the transient heat transfer measurement technique.

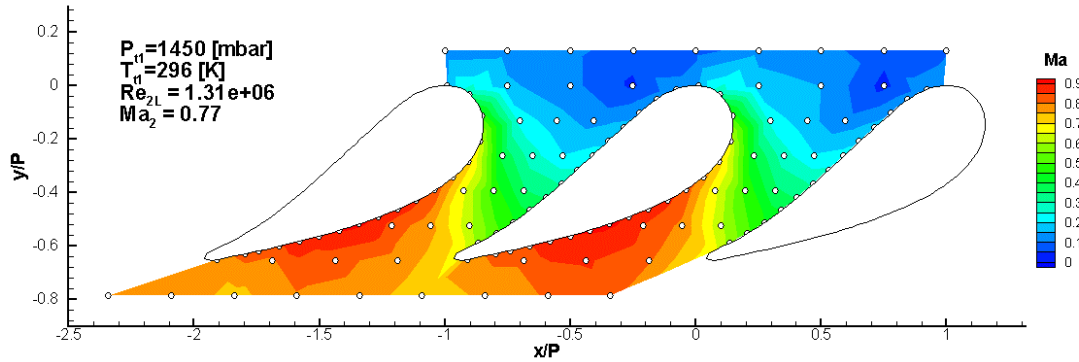


Figure 6-2: Mach Number Distribution Issued From Pressure Taps

In addition, casing wall measurements on the two adjacent channels are complementing the flow periodicity check of sub-chapter 4.1. As can be seen in Figure 6-2, the flow is very similar on both wall channel surfaces. On the right channel, the slightly larger high velocity area on the casing wall close to the suction side of the central vane is probably due to measurement errors of some pressure taps; color interpolation representation being issued from a limited number of points. Nevertheless, the flow on the suction side of the right channel is slightly more accelerated than the left one. The difference is small enough to still consider the flow periodic.

6.1.3 Pressure Sensitive Paint (PSP)

For a higher spatial resolution, complementary Pressure Sensitive Paint measurements are performed. PSP techniques are based on oxygen-quenched photoluminescence. After being illuminated by a suitable light source (high pressure Xe lamp), the intensity of light I emit by the PSP coating is depending on the partial pressure of oxygen. Hence, it is directly related to the pressure level of the surrounding gas containing oxygen. Pressure measurement can be expressed as a function of light emission I by:

$$\frac{p}{p_{ref}} = A(T) + B(T) \frac{I_{ref}}{I} + C(T) \left(\frac{I_{ref}}{I} \right)^2 \quad (6.1)$$

where (I_{ref}, p_{ref}) are reference values and $A(T)$, $B(T)$ and $C(T)$ are calibration coefficients (usually second order polynomial fit) depending on the temperature of the painted surface. A non-intensified scientific grade camera with 1024x1024 pixels of 16 bits on a black illuminated CCD is used for the light emission acquisition. For the PSP experiment, three images are captured: a dark image (no light, no flow), a reference image (light, no flow) and a flow image (light, flow).

The PSP emission is usually quite sensitive to temperature changes (Steiner, 2000); and as a consequence this technique is not well suited for measurements of surfaces with large variations of recovery gas temperatures like on the casing platform. For this reason, a novel PSP data analysis is applied. Results are accurately obtained by using the calibration coefficients with an iterative correction on the surface temperature distribution as explained in Appendix E.

Due to optical access limitation for the non-intensified camera, only the left channel of the platform is measured. Excellent agreement is found with the pressure taps measurements as it can be seen on Figure 6-3, where the black contour line levels issued from the pressure taps measurements are superposed with the color levels representing the PSP measurements.

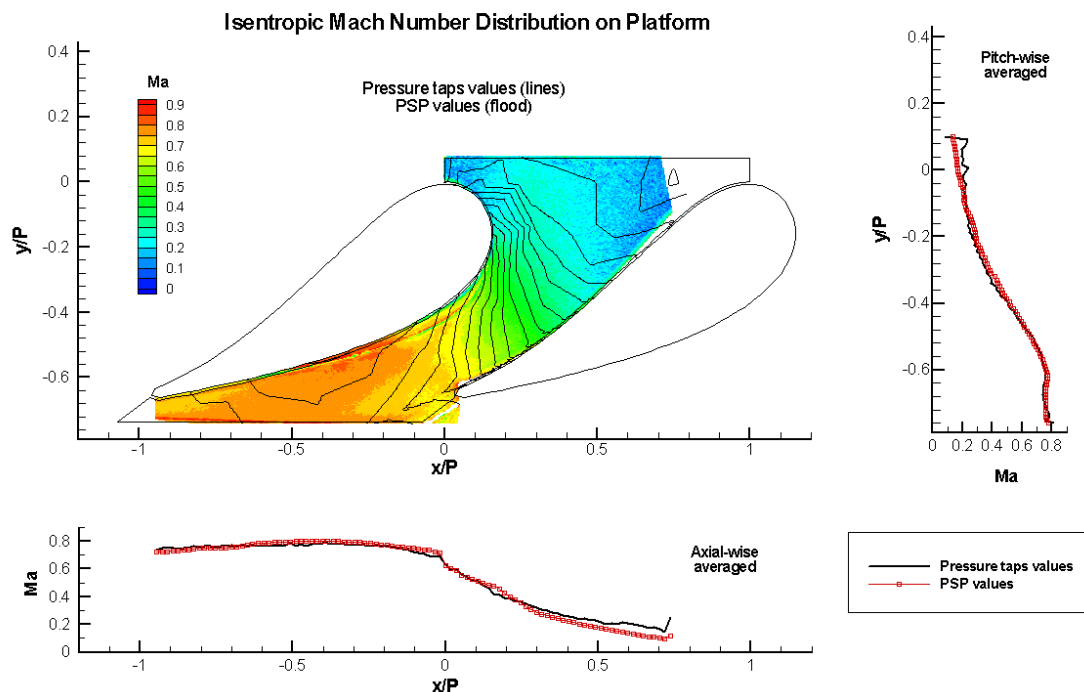


Figure 6-3: Comparison of Mach Number Distribution Issued from PSP (colors) and from Pressure Taps (black contour lines)

6.2 Heat Transfer Measurements on the Platform

6.2.1 Platform Baseline and Film-Cooled Experiments Set-up

For both the baseline and film-cooled experiments, the new measurement technique described in the previous chapter is used to obtain the distribution of the heat transfer coefficients and the adiabatic film cooling effectiveness on the platform. This technique can be used on the curved contoured wall channels with or without cooling holes on the foil as it works for inhomogeneous heat-flux distributions. The transient experiments are performed by applying some steps of heat-fluxes generated by an electrical heater-foil glued onto the surface of the platforms. The conception of the tested models is similar for the baseline and film-cooled casing platforms. It includes the heater-foils on the surface and bus-bars connections to the electrical power supply.

For the film-cooled experiments, the conception also includes the application of the cooling holes scheme extracted from the real geometry (see chapter 2) and the design of a plenum chamber feeding the cooling holes. Due to the lack of space, only one plenum chamber is considered instead of two present for the vanes in the engine.

6.2.1.1 Optical Access

The baseline and film-cooled experiments are performed with similar light and camera set-up. Compared to the vane airfoil experiments, the sealing boxes are removed for a better optical access and only two cameras are used. Each of them is recording the platforms of the channels adjacent to the central vane. However, it is not possible to video-record the experiments on both platforms simultaneously due to heavy light interferences and inhomogeneities. For this reason only one channel platform is illuminated during the experiments. Despite these efforts, some areas close to the vane airfoil are still difficult to acquire. Focus is put on the mid-pitch area of the platform with a global overview of the surface rather than zoom views close to the holes. The average spatial resolution hence obtained is of about 8 pixels/mm.

Compared to the transient experiments on the vane airfoil, where the transient startup time is given by the insertion of the model in the main flow, here an LED signal synchronized with the heater-foil activation and coolant gas injection is present on the video sequence. For the baseline case, the LED is directly mounted on the window in front of the neighboring vane profile, while for the film-cooled experiments, it is mounted inside the central vane profile as shown in the sequences of Figure 6-7.

Due to the absence of any dummy part, which contained a useful reference grid in the vane airfoil experiments, the coordinate transformation program has been improved so that it is directly possible to use the vane airfoil profiles and the cooling holes footprints as reference geometries. The resulting image transformation of the casing platforms to a 2D projected surface is shown in Figure 6-4 for the baseline case and in Figure 6-5 for the film-cooled case.

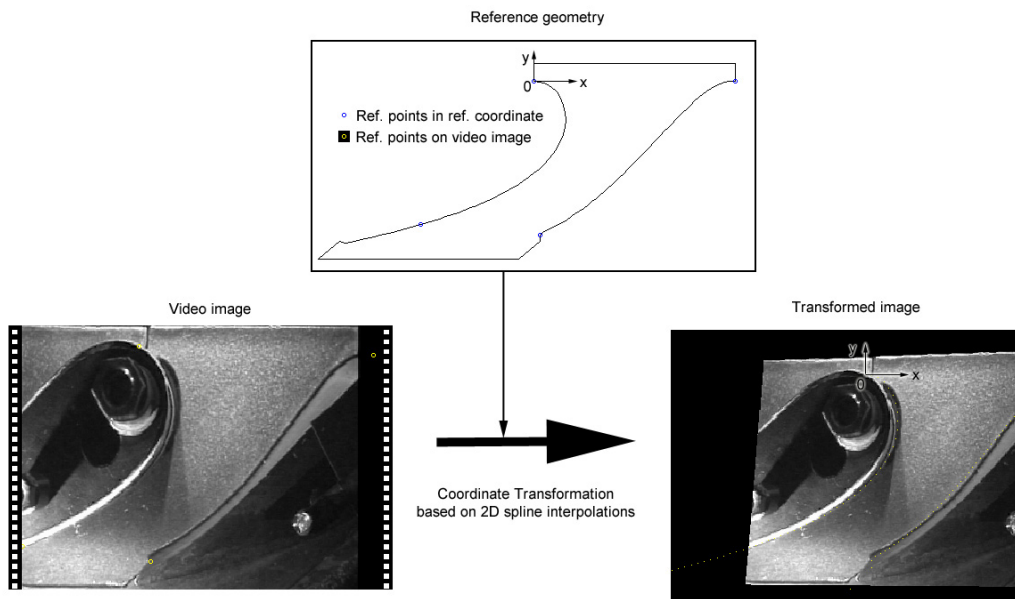


Figure 6-4: Video Image Transformation for the Baseline Case Platform

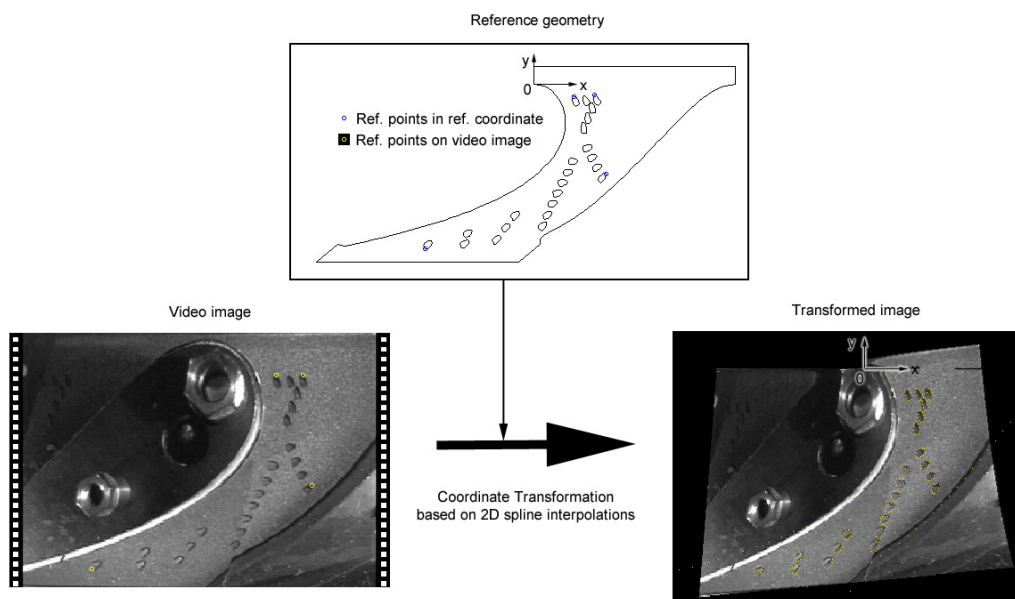


Figure 6-5: Video Image Transformation for the Film-Cooled Case Platform

6.2.1.2 Casing Platform Setup

The interchangeable baseline and film-cooled casing platform parts as well as the main casing part are made out of Perspex material for its low thermal conductivity. The Perspex used is the same as for the baseline and film-cooled vane models. Hence, for a wall thickness of $\delta \approx 3$ mm for the film-cooled platform, the maximum allowable transient time is about 23 seconds. Here the longest experiment performed on the platform did not exceed 20 seconds.

A nickel-chrome heater-foil of 20 μm thickness is glued on the interchangeable platform parts. The foil is bend at the upper and lower edges, and is connected to copper bus bars inside the casing. The voltage difference between these bus bars in order to generate the heat flux step is given by a 5000 W electrical power supply. A thin fillet on the lateral edges of the heater-foil is machined in order to avoid any electrical contact with the metallic neighboring vanes. Thermocouples inside the casing parts and on the outer surfaces are used to verify the initial temperature of the model and its homogeneity.

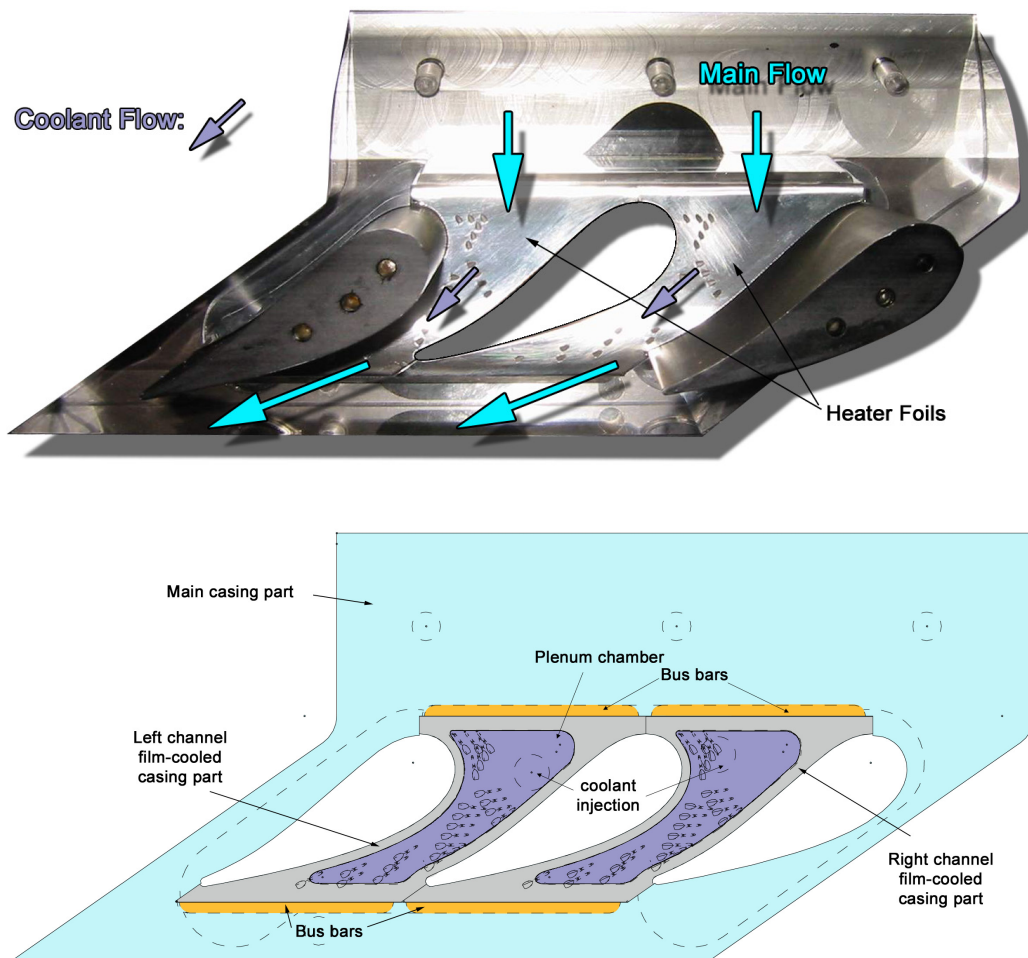


Figure 6-6: Picture and Drawing of the Film-Cooled Casing Platform

Film-cooled casing models are manufactured in two parts with a plenum chamber in the middle. Thermocouples are placed in the plenum chamber in order to record the coolant gas temperature evolution during injection. Pressure taps are also present in the plenum chamber allowing the checking of the blowing rate. Holes of the film-cooled casing platform are drilled with the heater-foil already glued on the Perspex, hence yielding a precise cutting around the holes. Figure 6-6 shows the different casing parts of the film-cooled configuration. The baseline case is similar, but without any cooling holes and plenum chambers.

With the novel measurement technique, there is no specific preconditioning of the measured surface required, except that the initial surface temperature is equal to the mainstream recovery gas temperature. The total temperature of the main flow supplied to the linear cascade is cooled to its maximum giving a T_{ig} of about 296K. At these conditions and by estimating the available heat flux that can be generated by the foils, the narrow band liquid crystals are chosen to give a signal at around $T_{LC}=301K$ for the baseline case and at around $T_{LC}=309K$ for the film-cooled case. Application of the liquid crystal coating on the Perspex model consists, like for the flat plate experiments, of the three following layers on the heater-foil:

| | |
|---|------------------------|
| Black backing acrylic layer: | Hallcrest BB-G1 |
| Liquid crystal layer (Quantity: 3 ml LC + 1,5 ml water) | |
| for baseline case: | Hallcrest BM/R28C07W |
| for film-cooled case: | Hallcrest BM/R36C07W |
| Varnish protection layer: | Hallcrest binder AQB-2 |

6.2.2 Heater Foil Film-Cooled Measurement Procedure

The transient heat transfer measurement procedure for the determination of the heat transfer coefficients and the adiabatic film cooling effectiveness on the contoured platform surface covered by the heater-foil is similar to the one described in chapter 5, with the theoretical model developed in Appendix D. It consists of the regression of multiple transient liquid crystal experiments by small changes in the heat flux steps for the baseline case and by small changes in the heat flux levels of the heater foil and the temperature levels of the coolant gas injected for the film-cooled case. For one baseline experiment, the transient step heat-flux applied to the physical model creates a temperature evolution on its surface. For the film-cooled case, it is the transient heat-flux and the temperature of the coolant gas injected on the model that

create a temperature evolution on its surface. In both cases, these evolutions are monitored as in Figure 6-7 with the help of the thermo-chromic liquid crystal coating. Again, their color is recorded by miniature CCD cameras, and the video sequences are then treated by a digital image processing system that determines the temporal evolutions of the local surface temperature (see chapter 3).

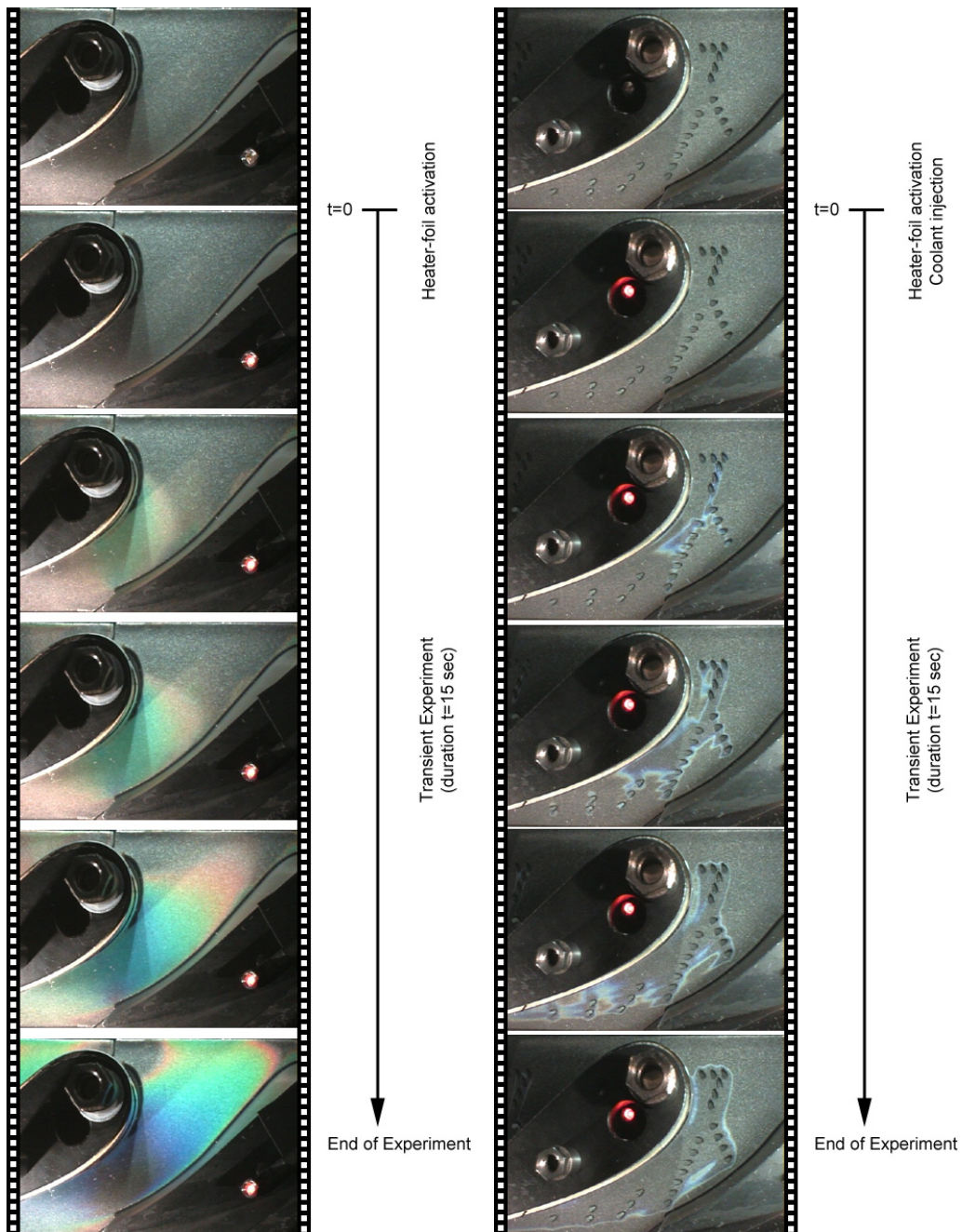


Figure 6-7: Liquid Crystal Signals on Platform for a Baseline (left) and a Film-Cooled (Right) Transient Experiment

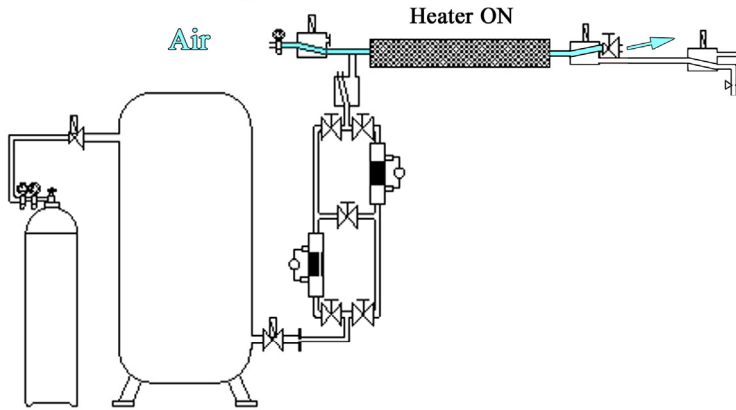
6.2.2.1 Coolant Supply for the Film-Cooled Platform

Coolant supply is the same as the one used by the film-cooled vane experiments. Coolant flow is supplied by a bottle via a series of mass flow meters, vanes, and heater tubes as shown in Figure 6-8. The bottle is filled with CO₂ as coolant gas in order to replicate a high-density ratio occurring in the engine due to much higher mainstream and coolant gas temperature differences. For a clearer comprehension, only one platform model is represented on Figure 6-8. However, the plenum chambers of the two film-cooled casing models are feed at the same time with the same coolant supply device. As for the film-cooled vane experiments, there are three different operating modes of the coolant gas injection:

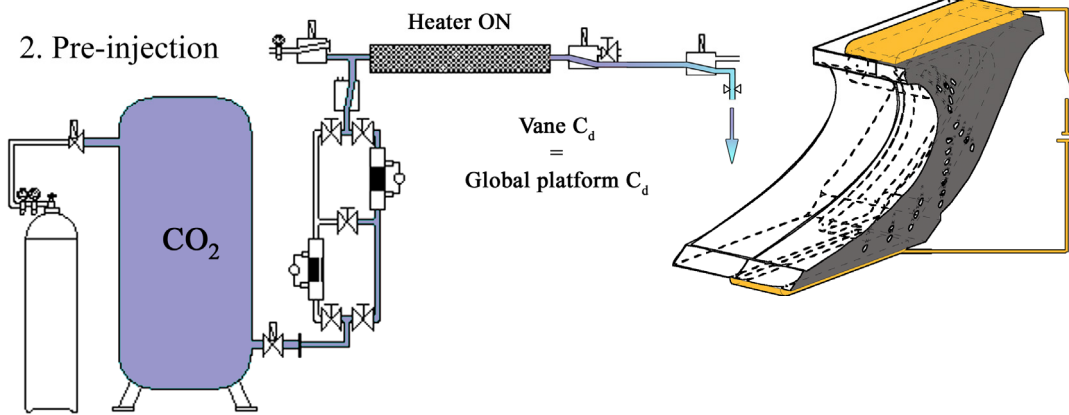
- The preconditioning mode allows setting up all the tubing installation so that the transient experiment will be performed at the desired coolant gas temperature. Preconditioning is usually performed with a higher mass flow rate experiment, so air is used in order to save CO₂.
- The pre-injection mode is then used a few minutes before the transient experiment starts. CO₂ replaces air and the mass flow regime is set to the required blowing ratio for the experiment. All the conditions are like for the transient test except that the flow does not go through the Perspex model but through an adjustable vane that has the same discharge coefficient as all the holes of the platform.
- The injection mode is the same as the previous one but this time with flow injected in the plenum chambers. Coolant gas injection is synchronized with the heater-foil activation.

During the transient experiment a pressure tube and a thermocouple in each plenum chamber measure the pressure and the temperature of the coolant gas injected. The discharge coefficient of each hole, issued from complementary experiments, allows determination of the local blowing ratio of each hole for a specific pressure level p_{tc} in the plenum chamber.

1. Preconditioning



2. Pre-injection



3. Injection

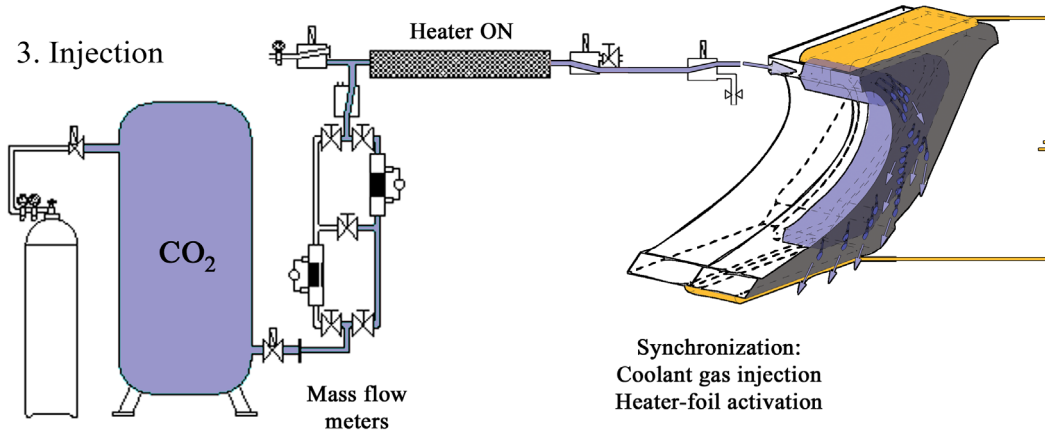


Figure 6-8: The Three Different Operating Modes of Coolant Gas Supply for the Film-Cooled Casing Platform.

6.2.3 Platform Heat Transfer Results

Baseline and film-cooled experiments are performed at the nominal flow condition defined in Table 2-5. Preliminary tests on both baseline and film-cooled situations did not show any difference between the right and the left channel walls. Moreover, injecting the coolant gas on one of the platforms did not have any influence on the results of the other platform. From these observations, film-cooled experiments were then carried out only on one casing wall channel, but with the coolant gas injected on both channels as a higher total coolant mass flow is more accurately determined by the mass flow meters. The resulting blowing ratio distribution for the different holes is only dependent on the p_{tc} pressure in the plenum chamber and is calculated by the help of the discharge coefficient measurements as described later in paragraph 6.2.3.5.

6.2.3.1 Reference Heat Flux Distribution of the Foil

For the baseline case, five to six experiments with different gain of heat flux G^i were performed. Heat flux values are chosen neither too low, in order to have signal detection on the tested surface, nor too high in order to avoid a liquid crystal video signal that is too fast, and consequently less accurate.

For the film-cooled case, as suggested by the measurement error analysis in the previous chapter, nine experiments issued from a combination of three coolant gas variations T_{tc} and three heat-flux gains G^i are performed.

Initial tests on the heater foils show that the use of the horizontal bus-bars with a curved and variable width of the foil does not give a good heat flux distribution, as the electrical current is using the path with less resistance thus the shortest distance (see Figure 6-9 upper graph). In order to generate better heat flux levels especially on the exit channel area, the bent foil connected to the bus bars is partly insulated and the electrical connections modified. The lower graph of Figure 6-9 shows the unwrapped foil with the improved copper bar connections. The electrical current streamlines are then forced to cover the area at the exit of the channel. As a consequence, it generates a better heat flux distribution. The color levels on the graphs represent the local heat flux ratio to the average global heat flux of the foil. The areas of zero or very low heat flux levels are indicated in blue, while the zones of high heat flux are indicated in red and can be up to three times higher than the average heat flux.

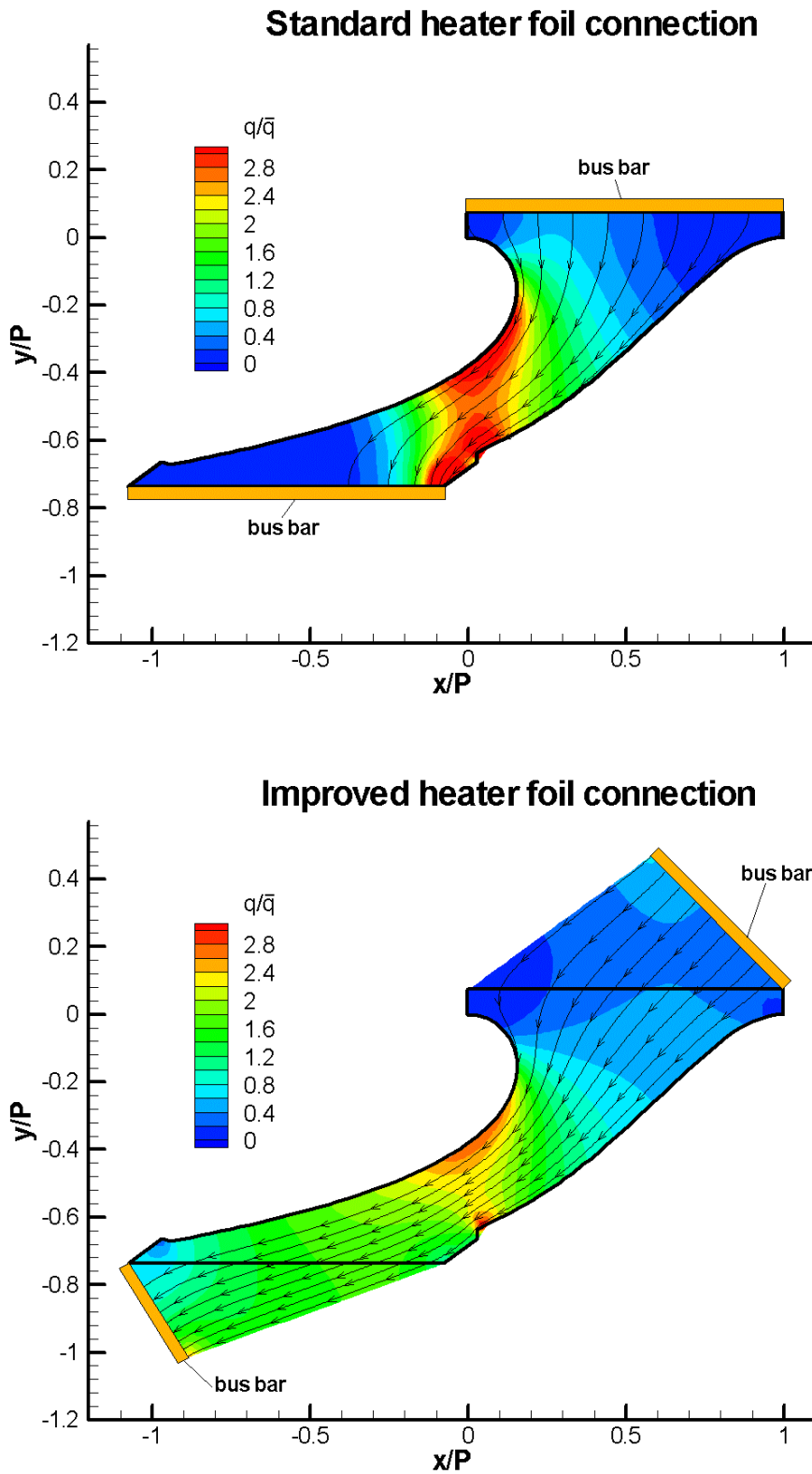


Figure 6-9: Improvement of the Heat Flux Distribution by Different Bus Bars Connections (streamlines represent the electrical current lines)

The new transient measurement technique gives the local heat-flux distribution generated by the foil as a by-product. Before focusing on the heat transfer coefficients and film-cooling effectiveness results, it is interesting to look at the reference heat flux issued from the data analysis. The heat flux ratios hence obtained are presented in Figure 6-10 for the baseline case and in Figure 6-12 for the film-cooled case.

In addition, numerical simulations of the heat flux ratio distribution on the surface, with the same method as already mentioned in the previous chapter, are performed and presented in Figure 6-11 for the baseline case and in Figure 6-13 for the film-cooled case. When compared with Figure 6-10 and Figure 6-12 respectively, the measurements issued from the multi-regression analysis show excellent agreement with the calculations. For a better comparison both results are presented together on the same graph by superposing the measured values (color levels) with the calculated values (lines) in Figure 6-14 for the baseline case and Figure 6-15 for the film-cooled case. By using the areas covered by the measurements, values are averaged once in the axial-wise direction and once in the pitch-wise direction. The resulting curves drawn on the same figures show excellent superposition for both cases.

Although the validation was already performed for the film-cooled flat plate in the previous chapter, the results of these much more complex heater-foils configurations validate again the new transient measurement technique regarding the determination of the reference heat flux distribution. Despite an inhomogeneous heat flux distribution for the film-cooled case due to the presence of the holes in the foil, values generated on the surface are suitable for the transient measurements. However, for both cases, regions of high heat-flux conduct to very fast transient liquid crystal signals and consequently to higher measurements uncertainties. This is particularly the case for the area close to the suction side before and around the channel throat location. The detailed distribution of the measurement uncertainties is given in paragraph 4.3.3.5.

In addition, regions of very low heat flux generation are not able to produce a transient liquid crystal signal on the surface; therefore, no result is available in these areas.

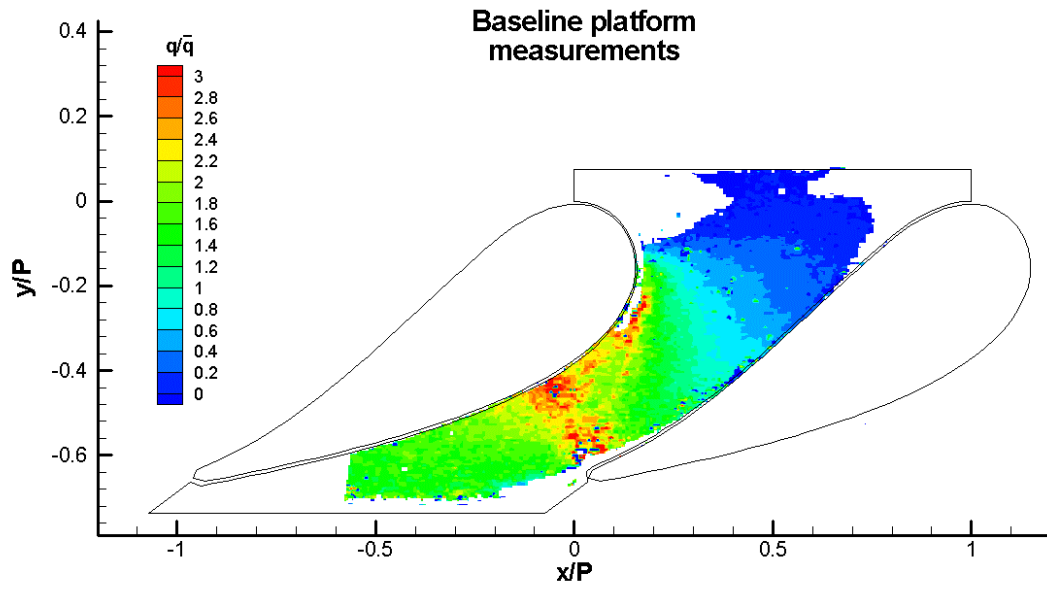


Figure 6-10: Reference Heat Flux Ratio Distribution Measured for the Baseline Case

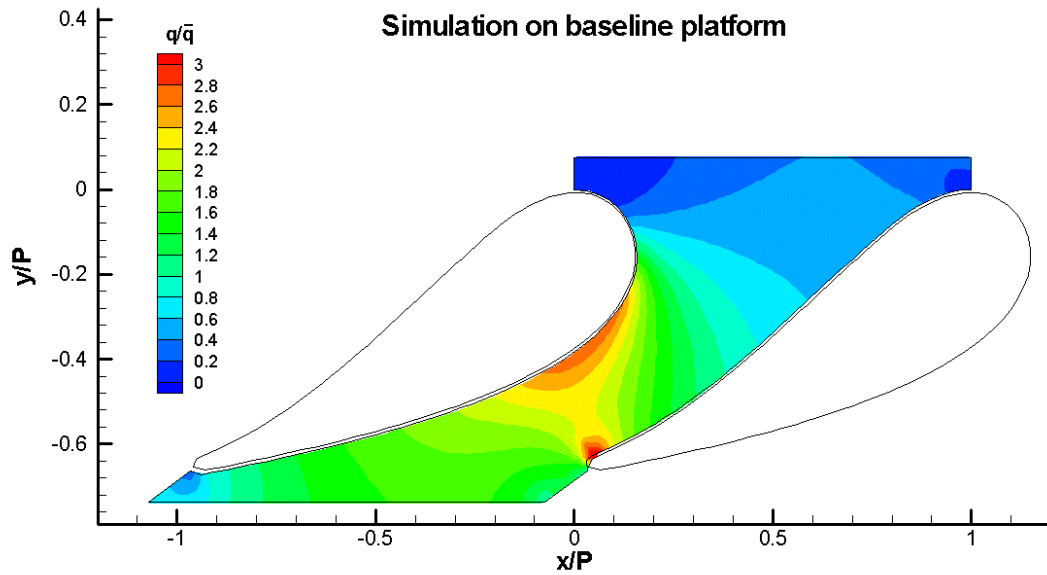


Figure 6-11: Heat Flux Ratio Calculated for the Baseline Case

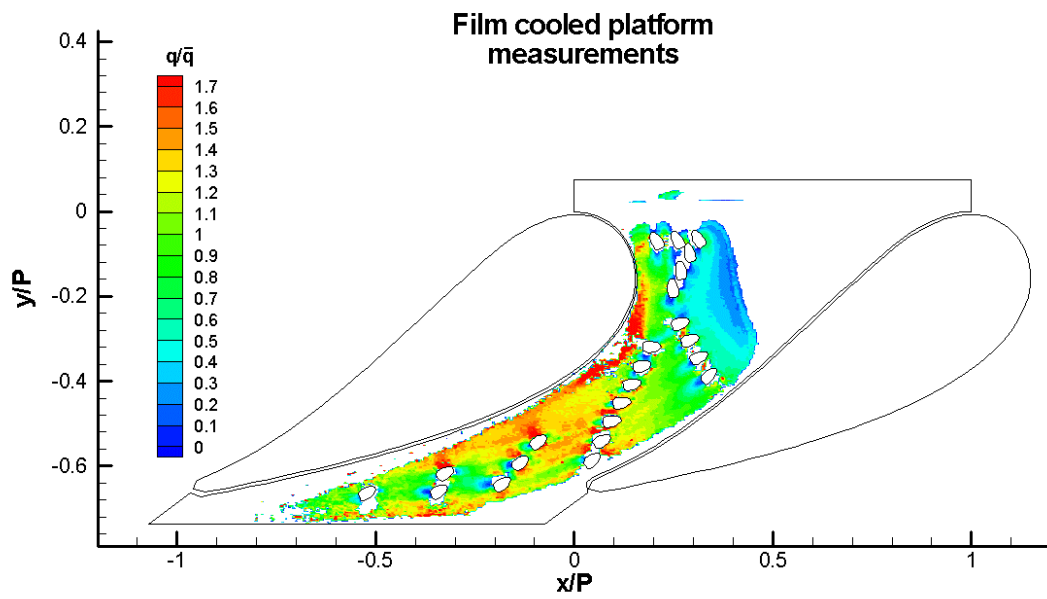


Figure 6-12: Reference Heat Flux Ratio Distribution Measured for the Film-Cooled Case

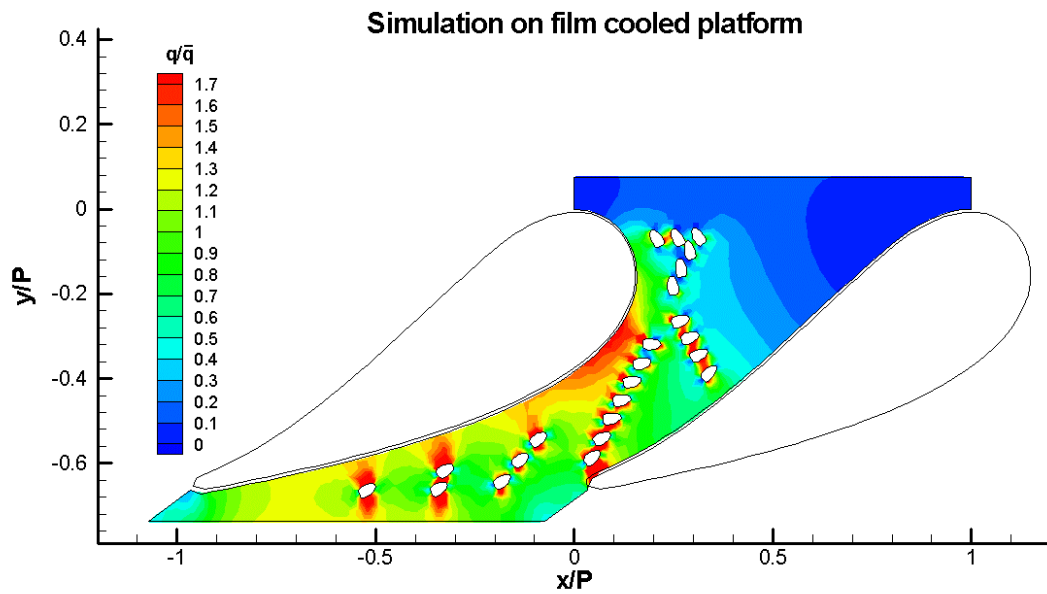


Figure 6-13: Heat Flux Ratio Calculated for the Film-Cooled Case

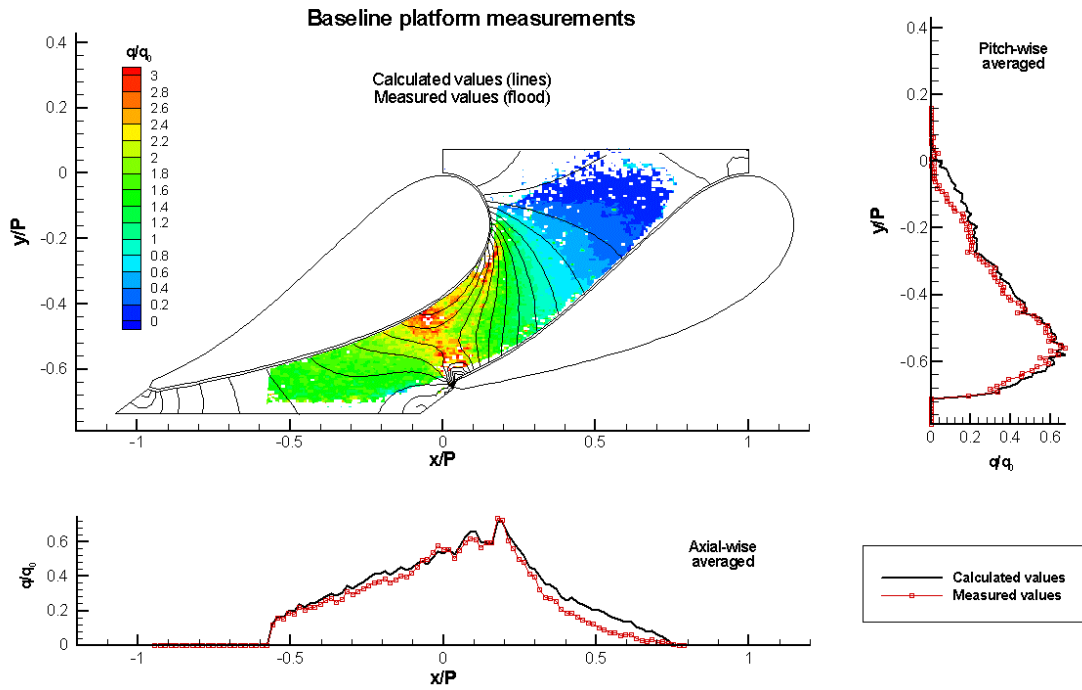


Figure 6-14: Comparison of the Baseline Heat Flux Ratio

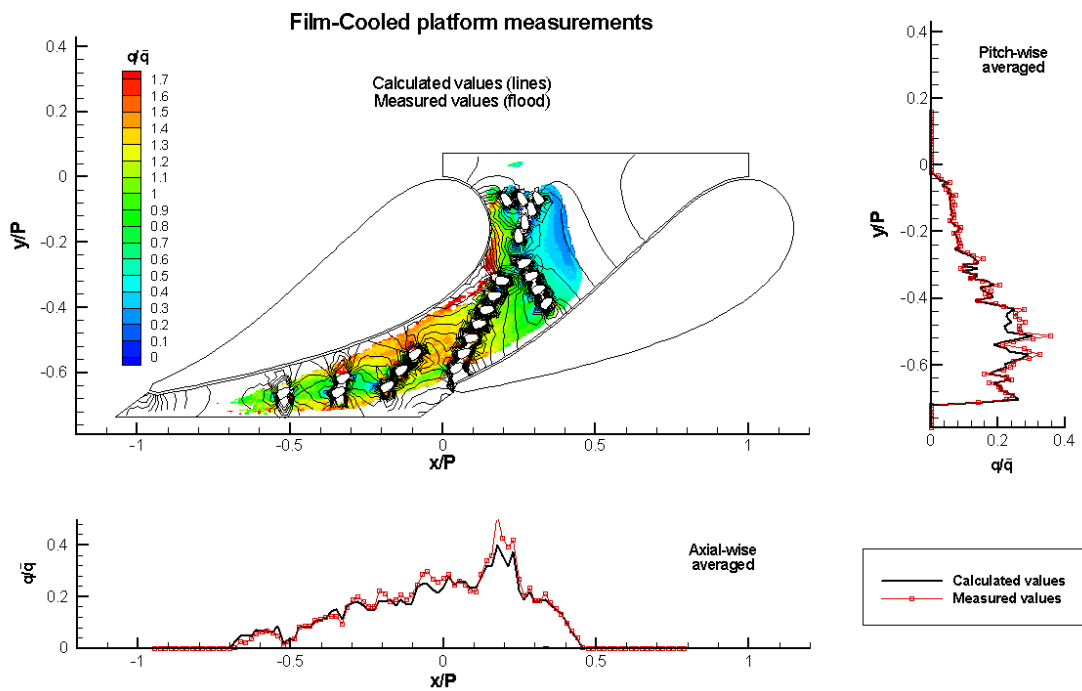


Figure 6-15: Comparison of the Film-Cooled Heat Flux Ratio

6.2.3.2 Heat Transfer Coefficient

Experimental results of the heat transfer coefficient distribution on the platform surface are present in Figure 6-18 for the baseline case and in Figure 6-20 for the film-cooled case. Here the average spatial resolution is of 8 pixels/mm, similar to the results of the vane airfoil experiments.

It is quite difficult to compare the results of this study with other data in literature, as the heat transfer coefficient distribution on the platform depends on the geometry configuration and the flow conditions. There is no adequate averaging method or representative dimensionless parameter that allows comparing cases of different platform geometries. A typical trend from other baseline experiments in literature (Wedlake et al., 1989; Harvey et al., 1990) is the detection of a low heat transfer coefficient on the area close to the pressure side and high values close to the leading edge, behind the trailing edge and on the area close to the suction side trailing edge. Excluding the leading edge area, as there is a lack of values in the results of the present work, a similar heat transfer coefficient distribution tendency is observed in Figure 6-18.

Kopper et al. (1981) observed a significant change in heat transfer distribution on a contoured platform relative to its flat counterpart. Indeed, the thermal transport near the platform is closely related to the secondary flows in the passage, the latter being different for a flat or contoured platform. Hence, for a better comprehension of the result of this work (Figure 6-18), an analysis of the secondary flow should be considered.

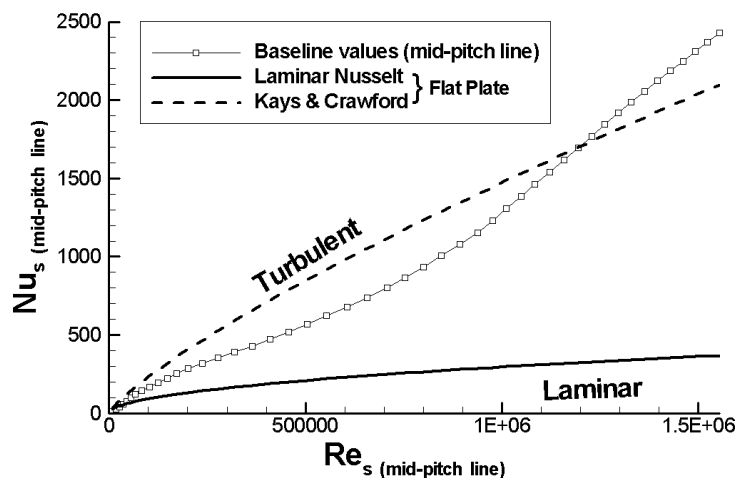


Figure 6-16: Comparison with Laminar and Turbulent Nusselt Number Correlations

In order to check the heat transfer coefficient levels obtained, data of the mid-pitch line (cf. black line on the graph) are extracted and presented in dimensionless form in Figure 6-16. Values are then compared with standard flat plate correlations, similar to those used in paragraph 4.2.4.1. Figure 6-16 shows clearly that the heat transfer coefficients measured have the correct tendency as they are between the values calculated by the laminar and turbulent correlations. For $Re_s > 1.3E+06$, however, the measurements show higher values than the curve of the turbulent case, certainly due to the fact that the flat plate correlation is here not suited for the vane contoured platform.

For the film-cooled configuration (Figure 6-20), heat transfer coefficients are slightly higher around the area of the first holes in the channel as compared to the baseline case (Figure 6-18). This tendency was also observed for the vane airfoil experiments and is a consequence of an increase in the turbulence level of the flow due to the coolant jet injection. Nevertheless, on the contoured platform at the exit of the channel passage, the film-cooled heat transfer coefficient values are lower than the baseline case. This is probably due to a change of the secondary flow intensity generated by the coolant gas injection. However, Chyu (2000) denotes that it is usually the characteristics of the film cooling that is affected by the secondary flows present in the vicinity and not the coolant flow that alters the secondary flows in the passage. This is the case for flat film-cooled platforms (Friedrichs, 1998) and probably has to be reconsidered for configurations of contoured platforms. In this case, as the contouring reduces the intensity of the secondary flows, the film-cooling layer is able to push the horseshoe or passage vortex away from the wall, which is responsible for high heat transfer coefficients at the channel exit in the baseline case. This shifting is clearly indicated by the separation lines on the vane in Figure 6-19 and Figure 6-21 (upper). They represent pictures of liquid crystal shear stress surface flow visualization on the contoured platform, with and without coolant injection. For the baseline case, separation lines of the horseshoe vortex can be clearly seen on the channel surface. For the film-cooled case, separation lines are less obvious. These pictures give an indication of the flow, but only a detailed analysis on the secondary flows would give more information about the passage and horseshoe vortex interaction and their influence on the heat transfer coefficient and aerodynamic losses. In this work, where the principal goal was to develop a new measurement technique applied for film-cooled platforms, the lack of time did not allow an opportunity to investigate more on the secondary flows. It can be mentioned that the secondary flows on a baseline platform region are the result of two main

pressure gradients in the vane passage. The first one is caused by the boundary layer velocity distribution and flow stagnation on the vane. It forces the flow toward the platform and to roll up into two legs of vortices giving the so-called horseshoe vortex. The second and stronger pressure gradient is due to the turning angle of the flow. It affects the path of the horseshoe vortex and causes a down-flow on the pressure surface and an up-flow on the suction surface. The pressure side leg of the horseshoe vortex combines with this flow near the wall and forms the passage vortex. The suction side leg of the horseshoe vortex starts wrapping around the passage vortex at a specific location depending on the cascade geometry. Figure 6-17 gives the aforementioned patterns, with exaggerated vortex motion as the actual number of rotations of the passage vortex are actually about two along the vane. These complex secondary flow distributions can significantly increase the heat transfer on the platform. The problem becomes very complex when the platforms are contoured and even more so when they are film-cooled.

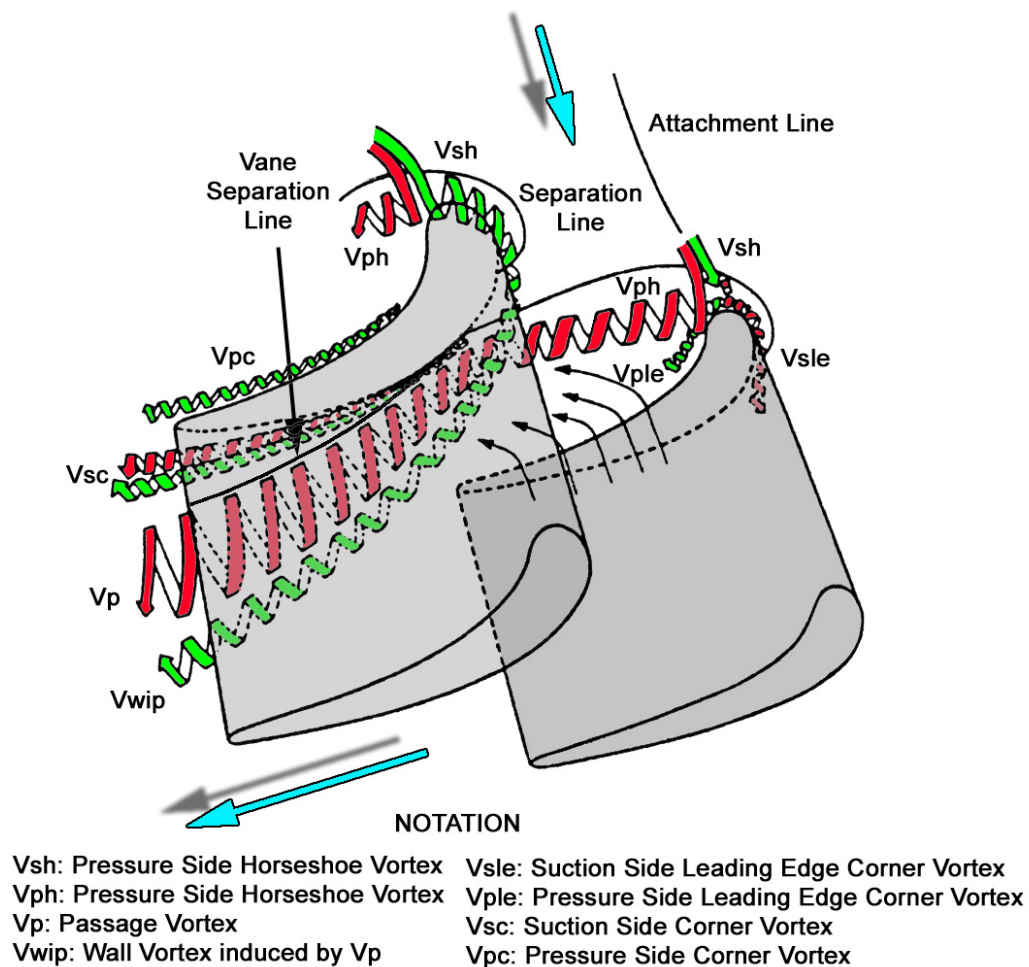


Figure 6-17: Platform Vortex Pattern (Goldstein & Spore, 1988)

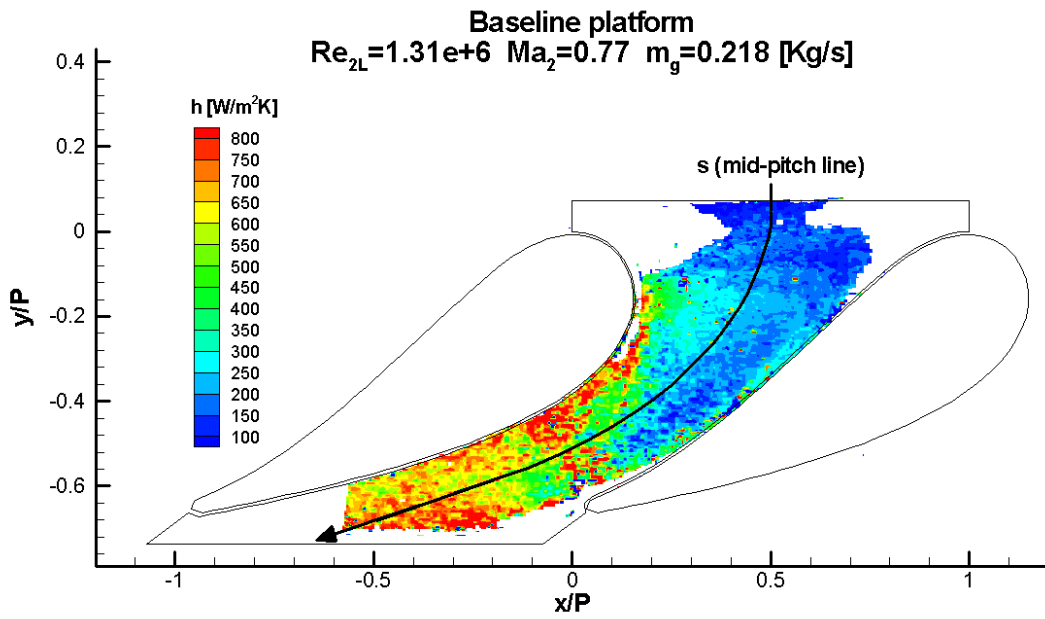


Figure 6-18: Baseline Heat Transfer Coefficients Measurement

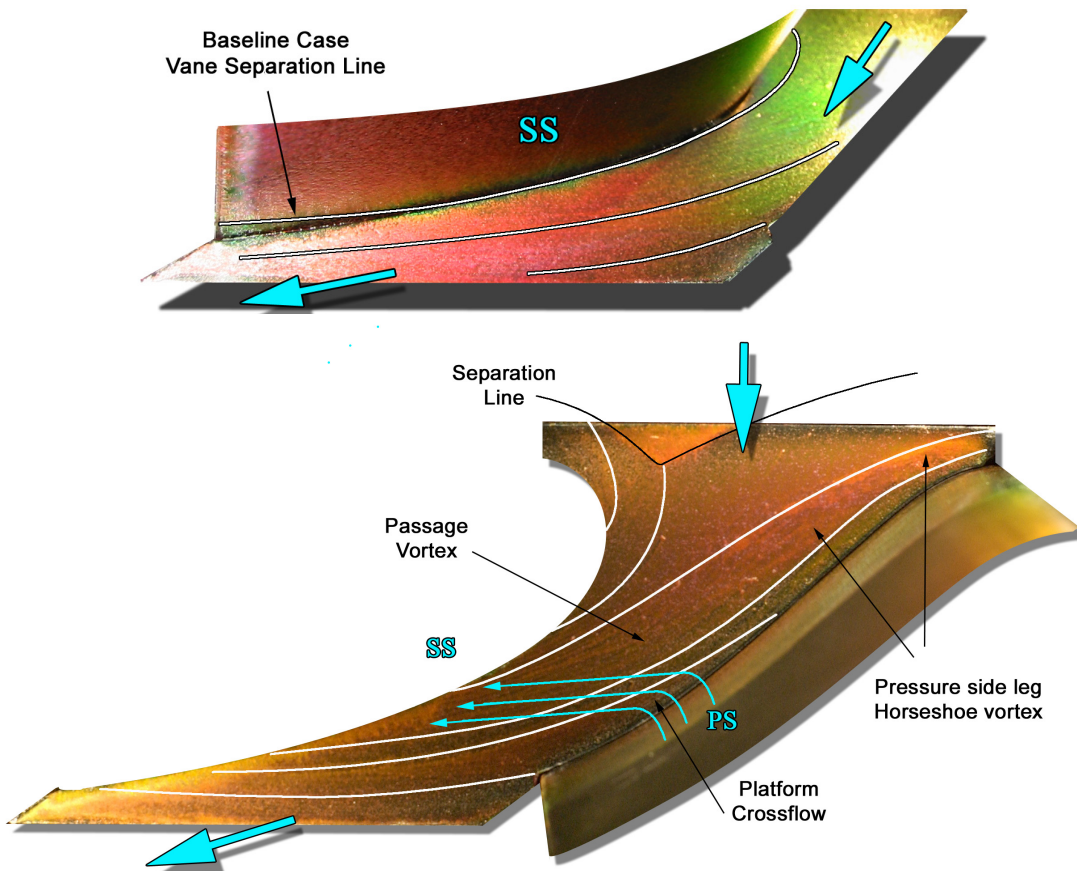


Figure 6-19: Surface Flow Visualization on the Baseline Casing Platform

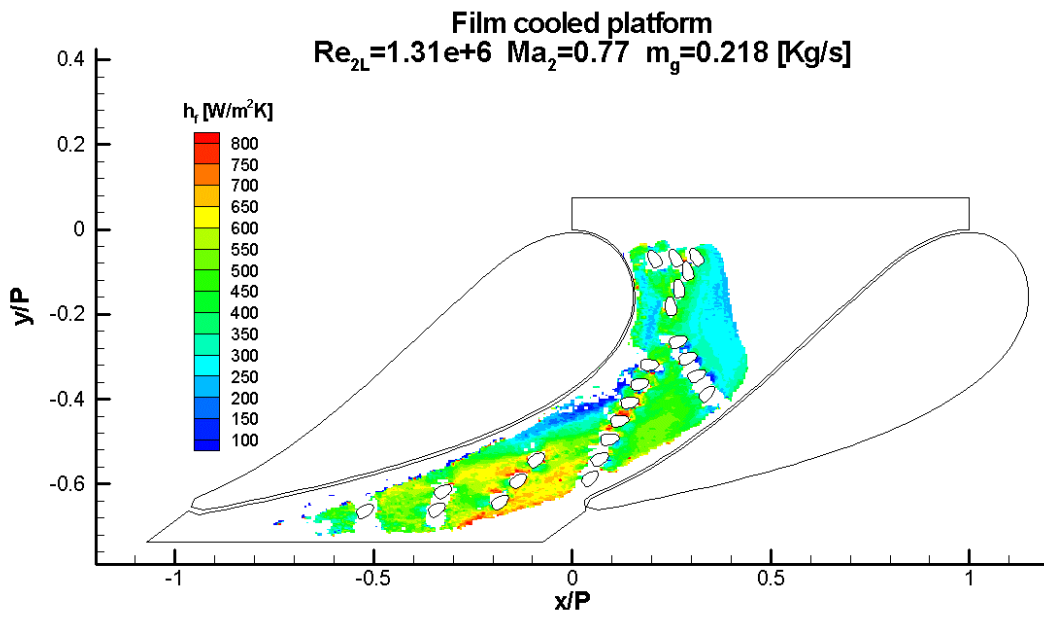


Figure 6-20: Film-Cooled Heat Transfer Coefficients Measurement

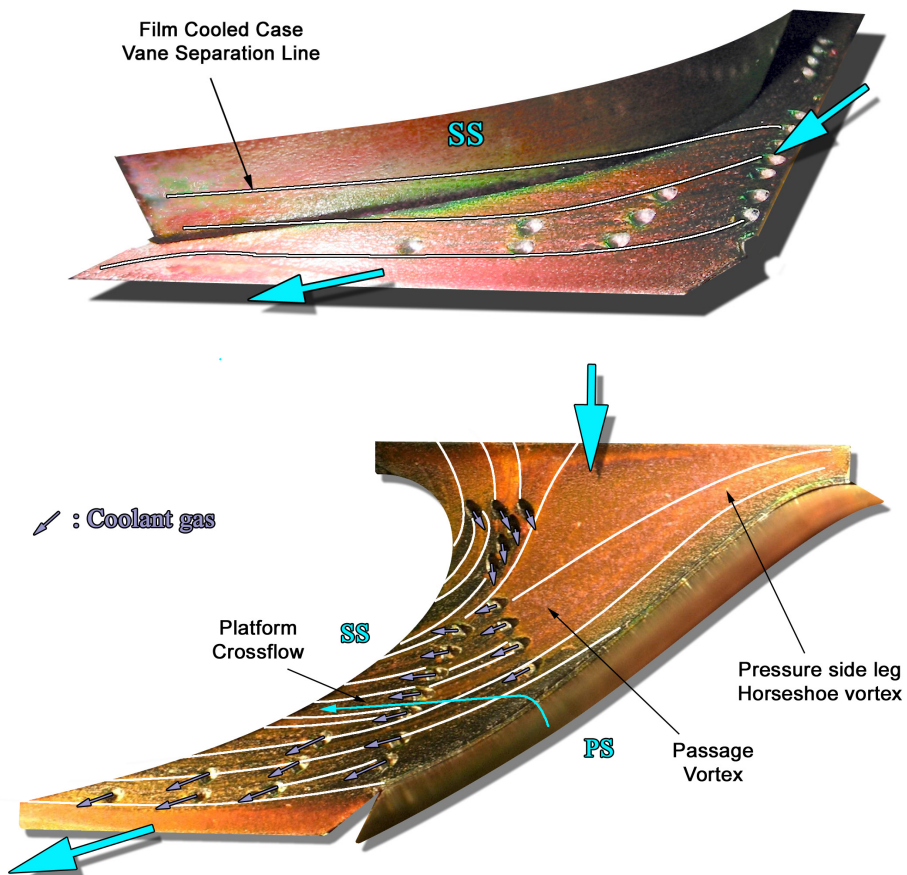


Figure 6-21: Surface Flow Visualization on the Film-Cooled Casing Platform

6.2.3.3 Film Cooling Effectiveness

Surface film cooling effectiveness results are presented in Figure 6-22. The 2D results show a clear indication of the direction of the cooling jets.

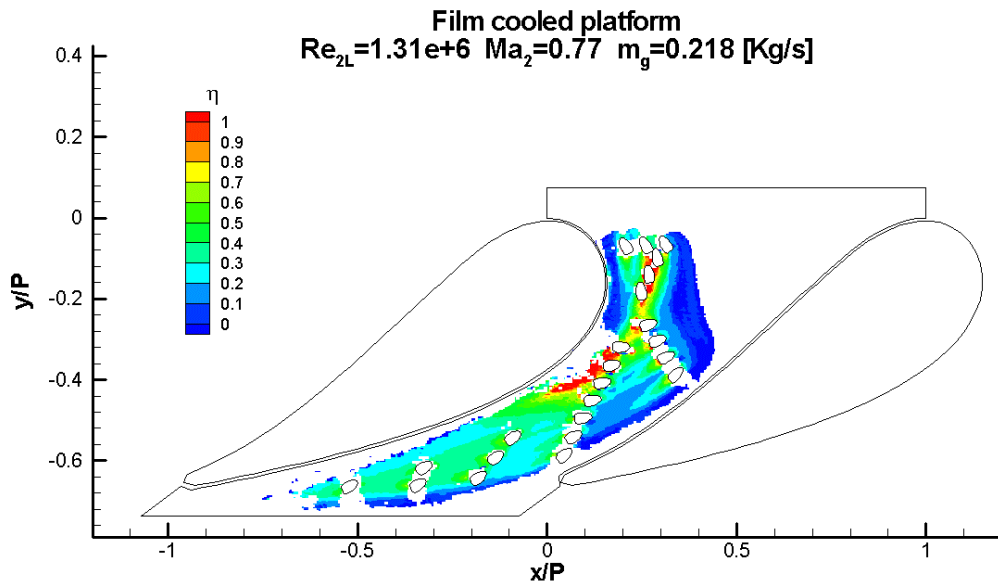


Figure 6-22: Film-Cooling Effectiveness Distribution with the Transient Technique

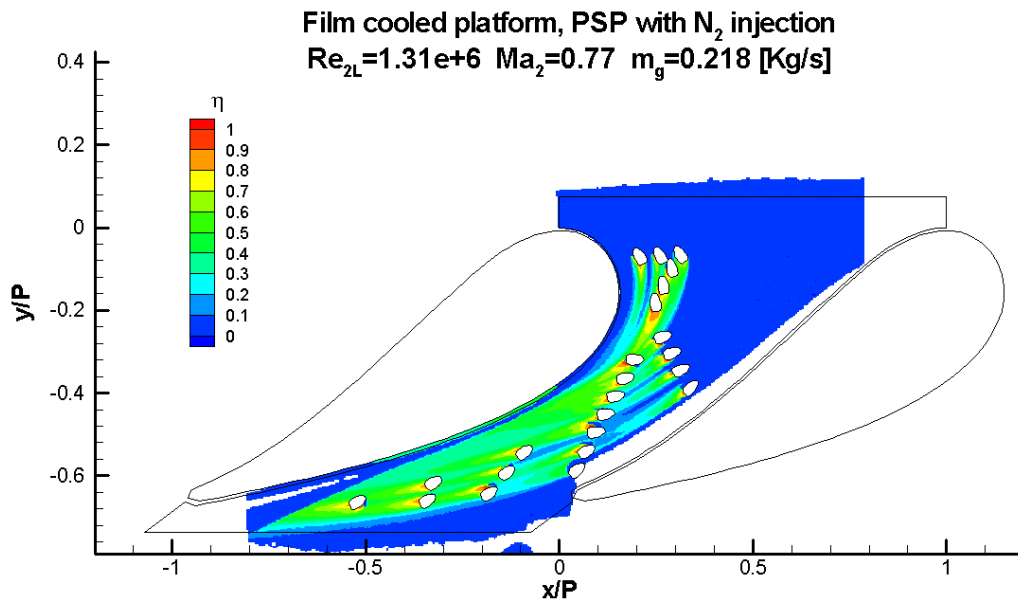


Figure 6-23: Film-Cooling Effectiveness Distribution for PSP with N_2 Injection

For the first group of holes (#1 to #6) the cooling jets are diverted towards the suction side vane. Hence, the upstream jets from holes #1 to #3 encounter the next cooling jets from holes #4 to #6 increasing effectiveness around this area to the maximum.

The second group of holes (#7 to #10) seems to have their exit angle aligned with the main flow direction and hence they produce some typical film-cooled jet patterns behind the hole. Effectiveness of this group varies from about 50% just behind the hole exit and decreases to a value of 10% close to the next group of holes.

The long row of holes (#11 to #17) starts the generation of a long film-cooled layer with a minimum effectiveness of 30%. This layer is reinforced by the injection of the following rows of holes. Note that due to the cross-flow on the wall the coolant jet pattern is diverted towards the suction side vane. Although for other geometries of film-cooled platforms, similar jet deviations were observed by Friedrichs et al., (1998) with the Ammonia and Diazo measurement technique.

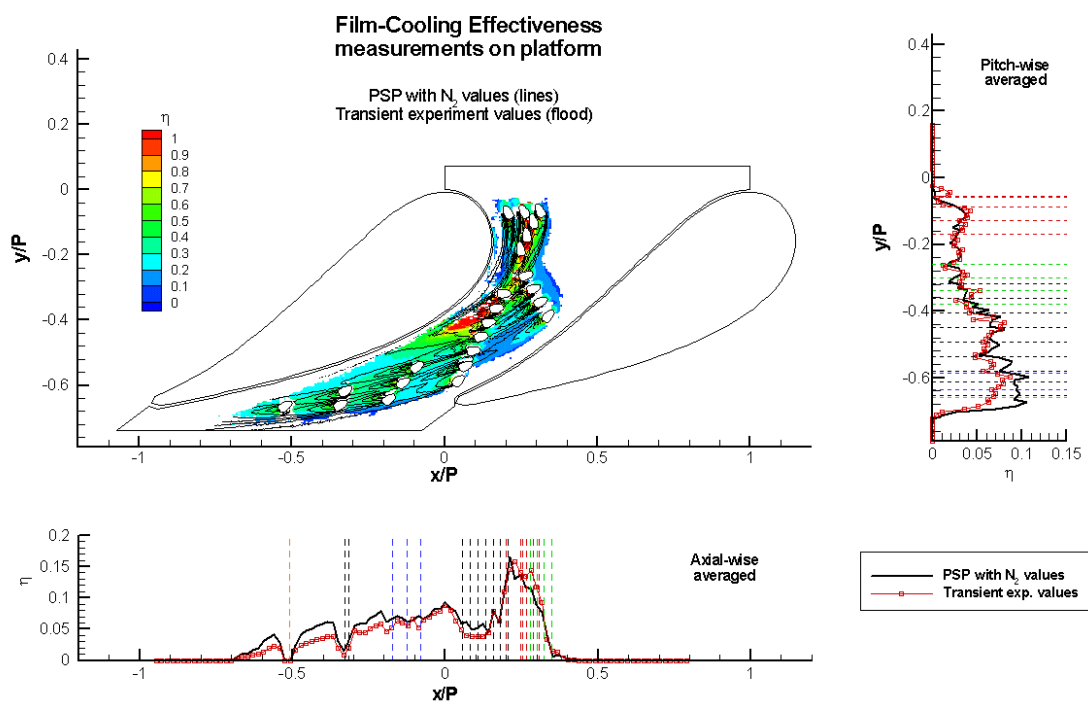


Figure 6-24: Comparison of the Transient and PSP Film-Cooling Effectiveness Results

In order to check the results of this geometry obtained by the new heater-foil measurement technique, additional PSP experiments with N_2 injection are performed. Film-cooling effectiveness can be obtained by the analysis of the partial pressure of

oxygen in a case with air injection (21% O₂, 79% N₂) and in a case with pure nitrogen (99.99% N₂) injection. Except for the use of N₂, the same PSP system as for the static pressure wall distribution (see paragraph 6.1.3) is used. In this case, the experiment consists of four captured images: a dark image (no light, no flow), a reference image (light, no flow), an air injection image and a N₂ injection image. The data analysis of this PSP technique using N₂ injection for film-cooling effectiveness is given in Appendix F. Care has to be taken to have the same coolant gas temperature in both cases, as the PSP is very sensitive to temperature variations. For the calibration of the paint used (Innovative Scientific Solutions Inc, UNI-001 Pt(TfPP)-Unicoat-Based PSP) a temperature variation of 0.2 K produces a variation on the film-cooling effectiveness of about 10%. Despite this sensitivity, film-cooling effectiveness levels and patterns shown in Figure 6-23 are very similar to the one issued from the new transient measurement technique.

In order to better compare the results obtained by the two measurement techniques, values are superimposed in the same 2D graph and averaged curves in the axial-wise and pitch-wise directions are plotted (Figure 6-24). The dashed lines represent the locations of the different cooling holes with their respective colors as given in Figure 2-11. From the graphs it can be clearly seen that results issued from the PSP technique give higher effectiveness values than those issued from the transient experiment. This difference can be explained by the high sensitivity of the PSP painting. On the other hand, PSP results close to the holes are much more correct than those obtained by the transient experiment as the latter case is sensitive to conduction effects around these areas.

6.2.3.4 Heat Flux Ratio

To demonstrate the advantage of film cooling, consider the heat flux ratio of the film-cooled and of the un-cooled case. As already mentioned, the heat transfer coefficient can increase in the film-cooled case due to higher turbulent flow conditions generated by the coolant jets issued from the first rows of holes in the channel. On the other hand, the coolant jets are cooler than the main flow, and if ideally spread on the surface, the heat flux q_f imposed to the casing wall decreases compared to the un-cooled case q_0 . Hence, the heat-flux ratio can be defined, as for the film-cooled vane experiments, by the relation given in (4.6) with the same overall cooling effectiveness Φ defined by (4.7). The latter is unfortunately not known but chosen, like for the film-cooled vane airfoil, to represent an engine environment ($\Phi = 0.5$) in order to have an indication of the cooling performances. The resulting surface heat

flux ratio distribution is given in Figure 6-25. In order to clearly see the beneficial or detrimental effects of film-cooling application, a special color legend is also used here, with a blue to green gradient for improved performances ($q_f/q_0 < 1$), and a red to yellow gradient for decreased performances ($q_f/q_0 > 1$).

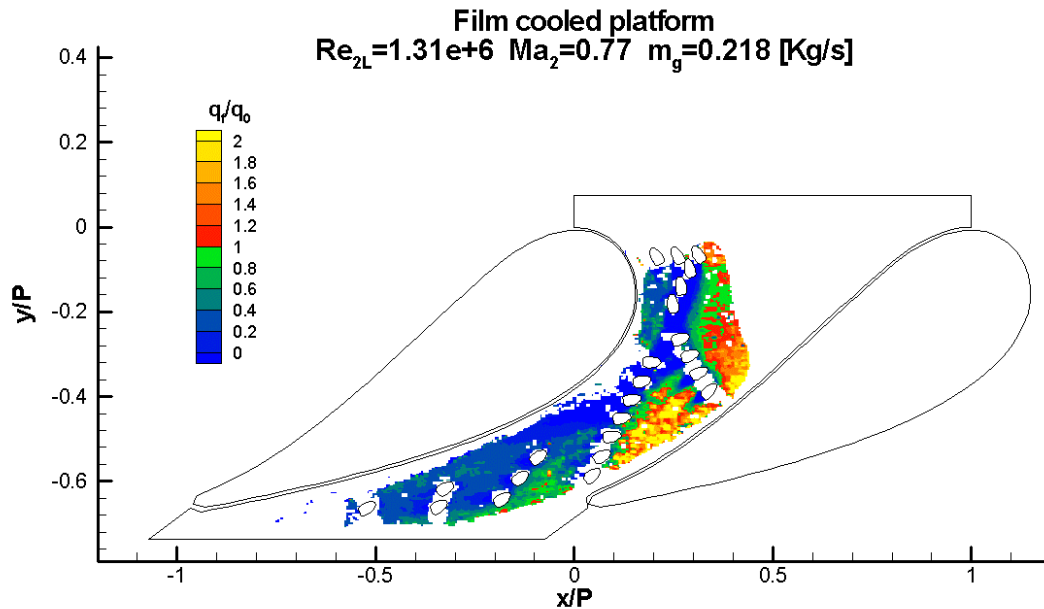


Figure 6-25: Film-Cooled and Un-Cooled Heat Flux Ratios Distribution

It appears now that the holes of the second group (#7 to #10) close to the pressure side vane do not yield good performance. However, the rest of the cooling holes give a very good protection of the casing wall, especially at the exit of the channel. Conclusions of these measurements have to be related to the coolant gas distribution applied during the experiments that is described in the next paragraph. To date, no other publication was found on the use of fan-shaped holes for film cooling on contoured platforms.

6.2.3.5 Coolant Gas Distribution

The determination of the coolant flow distribution is only based on the pressure in the plenum chamber and on the discharge coefficient values of each row. The static pressure at each exit hole is known; hence, the theoretical mass flow being injected can be calculated. The real mass flow is simply obtained by multiplying the theoretical mass flow with the discharge coefficient measured at the specific pressure ratio.

To measure the discharge coefficient of one hole of the physical model, others have to be sealed. 3M-Kapton tape is used for this but due to the proximity of some holes, it is only possible to perform a discharge coefficient measurement on rows or area of holes. For this reason six areas of holes are defined, as shown by the different colors in Figure 2-11. For each of them, a specific discharge coefficient function is determined despite the fact that in some cases for the same area, the static pressures at the hole exits vary slightly.

As for the film-cooling holes of the vane airfoil, the measurement procedure of the discharge coefficients consists of applying a certain coolant gas pressure level in the bottle connected to the plenum chamber. As coolant is coming out of the opened holes, the bottle becomes empty. The pressure level is then reduced and as a consequence, it reduces the mass flow injection. During this process, the effective coolant mass flow is measured and compared to the theoretical mass flow. Discharge coefficients are then measured by (4.4) and (4.5) with this time n being the number of holes in the considered area. Note that for the blowing ratio distribution, the local static pressure of each hole is used; only the discharge coefficient function $C_d(p_{tc})$ is considered the same for holes of a specific area. For verification, the total coolant mass flow obtained from the distribution is compared to the total coolant mass flow measured during the experiments. The result shows excellent agreement; hence, it indicates that the approximation of a unique discharge coefficient for a specific area of holes with similar flow conditions has no or negligible effect on the coolant distribution determination.

Based on the measurements of the discharge coefficient of each area of holes and by considering the nominal main flow conditions and the averaging coolant flow condition from the three different T_{tc} transient experiments, it is then possible to determine at each injection location the following coolant gas injection parameters:

1) p_{tc}/p_{sc} is the coolant gas pressure ratio and is given for each hole injection in Figure 6-26. p_{tc} is obtained by a pressure tap in the plenum chamber, while p_{sc} is obtained from the baseline aerodynamic measurements. As only one plenum chamber is used, hence one p_{tc} , holes located close to the entrance of the channel where main flow velocity is low have lower values than the holes at the channel exit where main flow velocity is higher.

2) DR present in Figure 6-27 is the coolant gas to main flow density ratio and has values of around 1.5 representatives from the conditions in the engine. This is achieved by the use of CO_2 coolant gas at an average temperature of 303K and a mainstream flow of air at 296K. The results are given locally with the main flow and the coolant gas densities based on the static conditions at local holes injection. Although both the main gas and the coolant gas densities decrease for areas with higher mainstream velocity, the slight decrease of the density ratio is a consequence of a coolant gas different than the main flow.

3) BR_i is the local (at injection location) coolant gas to local (also at injection location) main flow blowing ratio and is, like for the film-cooled vane experiments, defined by equation (4.8). Local velocity conditions are taken into account, as there is a change in the main flow velocity for each hole location. Values in Figure 6-28 go up to 2 at the channel entrance since the local velocity of the main flow is low. Despite a lower blowing rate of the holes after the long row (#11 to #17), they give a very efficient film-cooling effectiveness as already shown in Figure 6-22.

4) The coolant mass flow distribution is presented in Figure 6-29. Values are in percent relative to the main flow of one channel passage determined in paragraph 4.1.3. Hence, the total coolant mass flow used for all fan-shaped holes on the film-cooled casing platform is 0.87% of the main gas mass flow. This is quite representative of the engine condition as the total coolant mass flow on the platforms of the vane is usually of 1.6% (Cohen et al. 1996). The distribution in Figure 6-29 denotes a near doubled amount of coolant gas injected from the holes located at the exit of the channel as compared to the one located upstream. A better coolant gas distribution could be obtained by the use of different p_{tc} supplied by several plenum chambers, as in the case of the real engine.

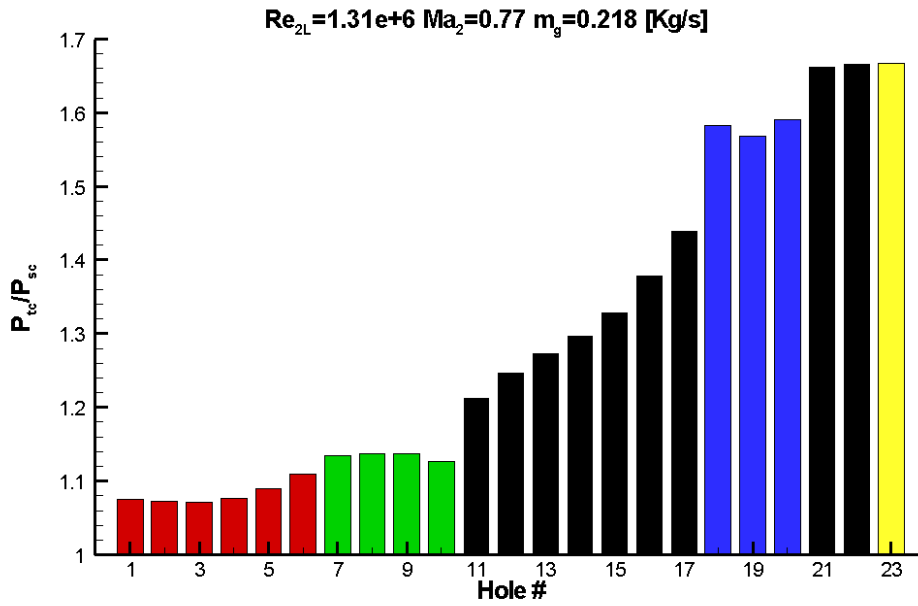


Figure 6-26: Pressure Ratio at the Different Coolant Gas Injection Positions

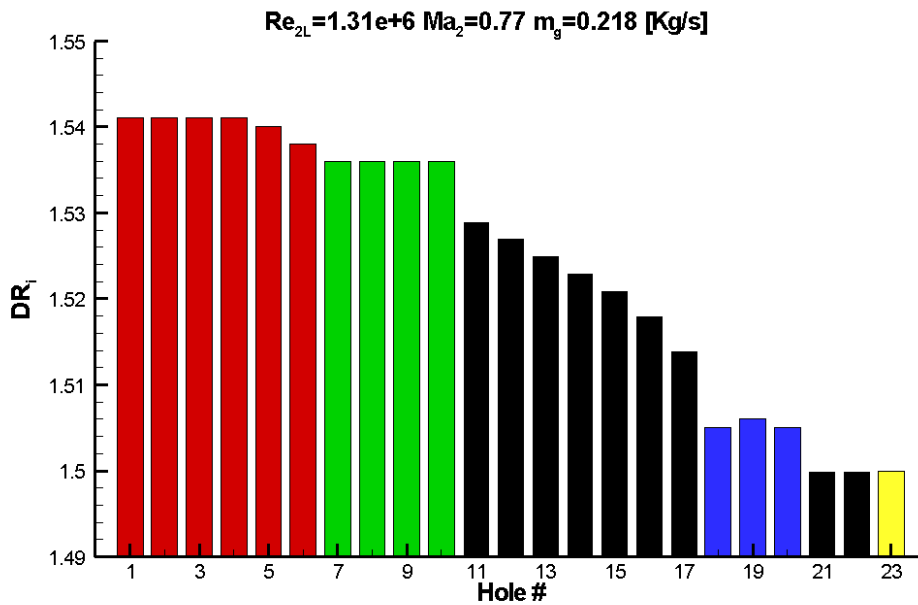


Figure 6-27: Density Ratio at the Different Coolant Gas Injection Positions

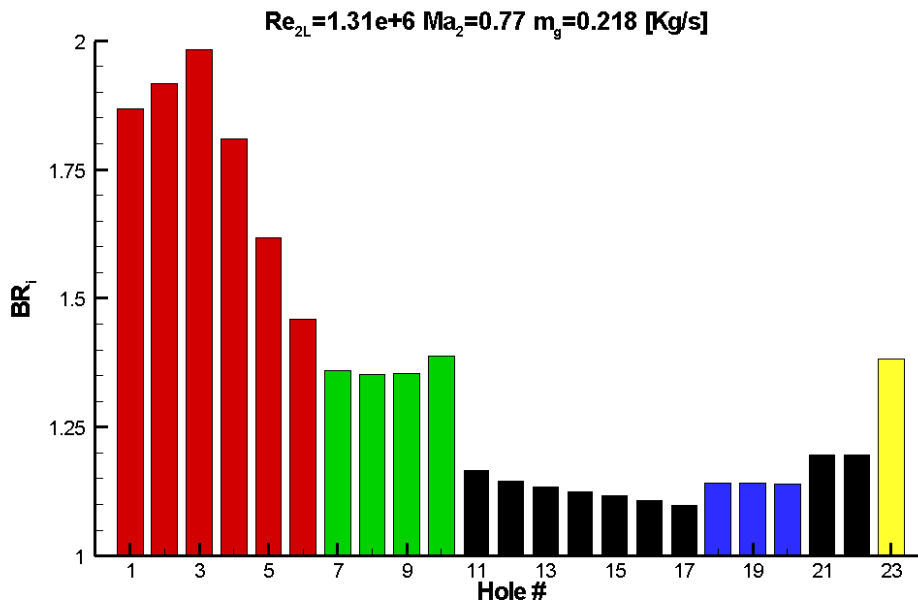


Figure 6-28: Blowing Ratio at the Different Coolant Gas Injection Positions

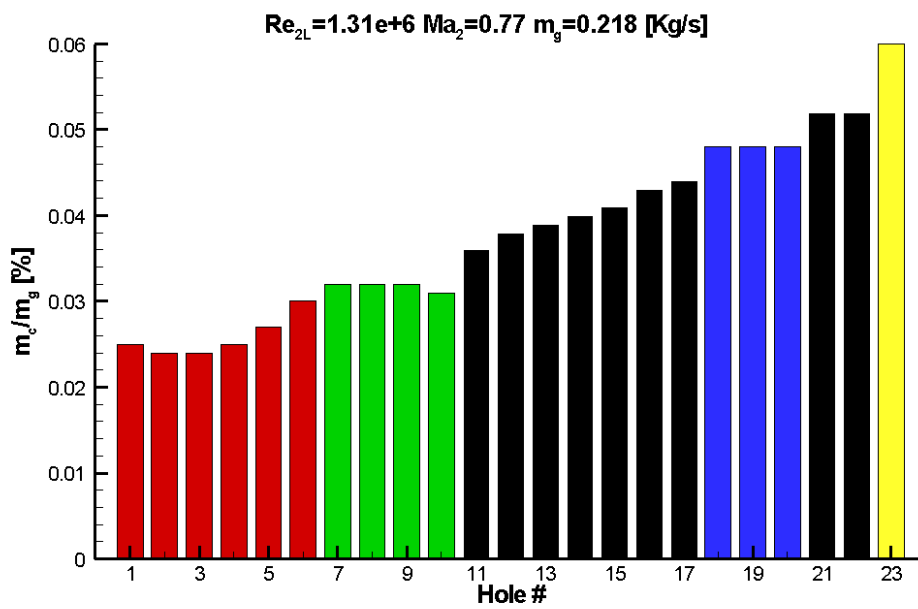


Figure 6-29: Coolant Mass Flow Distribution of the Different Holes

6.2.4 Measurement Uncertainties

Based on the existing measurement uncertainties for:

| | |
|---|--------------|
| Liquid Crystal Calibration T_{LC} | ± 0.1 K |
| Thermocouple Measurements T_{tg} T_o T_{tc} | ± 0.5 K |
| Time Resolution of Video Sequence | ± 0.04 s |
| Heat flux ratio G | $\pm 1\%$ |

For the case of nine experiments resulting from a combination of typical G_i and T_{tc} variations, an error calculation on the regression analysis used for the presented platform results of this work is performed. It is based on the same development as the one already presented for the validation of the technique on the flat plate in chapter 5. The uncertainties are calculated for each measured pixel; hence, it gives very detailed information on the quality of the results obtained for the film-cooled platform (Figure 6-30).

For the heat transfer coefficient h_f , values are with at least 4% error but with less than 9% on almost all the rest of the area. There is, however, a region close to the suction side leading edge area, where the error increases to 17% and more. This is due to the fact that during the transient experiment, the high heat fluxes applied here generate quite a fast transient liquid crystal signal. Thus it is essentially the uncertainty on the time event detection that leads to this level of error.

For the film cooling effectiveness, the same trend as for the heat transfer coefficient applies to the region close to the suction side leading edge area. Moreover, there is also an area at the entrance of the channel before the rows of holes where the error is high. This can be explained by the fact that this area has very low or zero film-cooling effectiveness. Over the rest of the area, error is only about 3%, confirming the accuracy of the transient liquid crystal and heater-foil technique.

Finally, the last graph of Figure 6-30 gives the measurement uncertainties on the reference heat-flux. Although being a by-product of the regression analysis, it is correlated to the film-cooling effectiveness error by the equations given in (5.2); and it is only because of low or acceptable error levels on the reference heat flux that this transient technique is able to give correct results. This low error level was already confirmed when the measured reference heat fluxes were compared to numerical simulations (Figure 6-15).

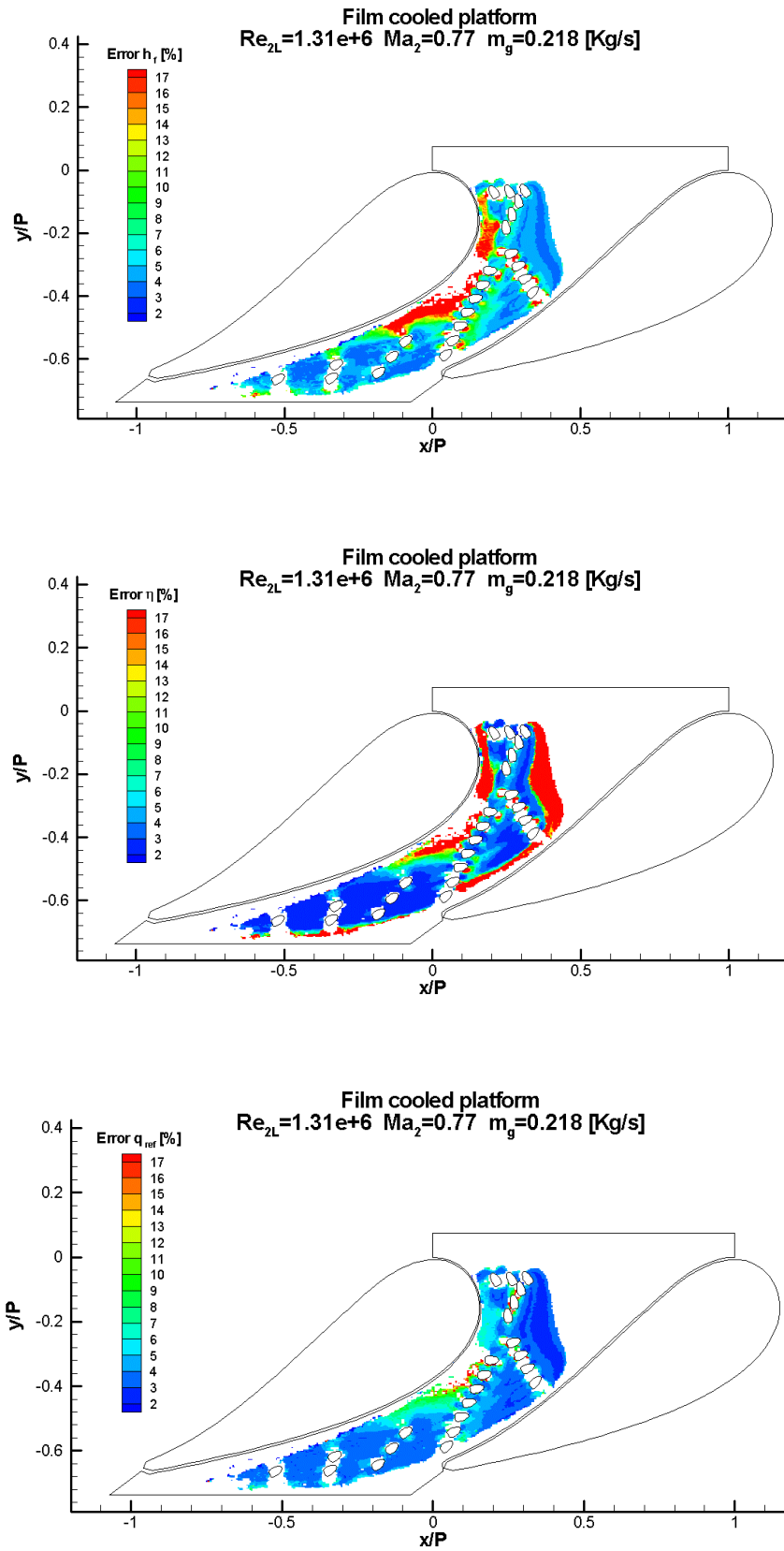


Figure 6-30: Detailed Measurements Uncertainties of the Film-Cooled Platform Results

6.3 Conclusion of the Platform Experiments

- The novel transient heater-foil measurement technique for heat transfer coefficient and film-cooling effectiveness measurements has been applied on the casing platform for the baseline and film-cooled configurations.
- All measurements were performed at nominal main flow conditions and a specific blowing ratio was used for the film-cooled experiments.
- Transient experiments were performed for the baseline and the film-cooled cases with different heat-flux ratios and coolant gas temperatures in order to apply the regression method. The result of reference heat-flux distribution generated by the foil has been compared to numerical simulations, which show very good agreement.
- One camera view was used and experiments were performed on one channel only with a blowing on both platforms. The results were presented in 2D with the casing surface projected. The baseline (h) and film-cooled (h_f) heat transfer coefficients and the adiabatic film cooling effectiveness (η) have been given. Based on this, a heat flux ratio between the film-cooled and the baseline case has been estimated, giving information on the performances of the film cooling holes design.
- Additional PSP experiments with N_2 injection were performed and gave very similar film cooling effectiveness results.
- The discharge coefficients of each row were measured and used to determine the coolant flow distribution. Parameters such as density ratio and blowing ratio of the experiment have been presented.
- Detailed measurement uncertainties were given to show the high accuracy of the results.

7 CONCLUSION

An experimental aerodynamic and thermodynamic investigation has been conducted on the film cooling of a complex nozzle guide vane geometry equipped with contoured platforms. The experiments were divided into two parts. The first one was dedicated to the vane airfoil, and the second part to the contoured platforms of the vane. In both cases, heat transfer coefficients and film-cooling effectiveness were performed by transient measurement techniques using liquid crystals.

For the vane airfoil, a preconditioning system followed by a rapid insertion was used. This installation has already been used during previous projects, but in the frame of this work, the liquid crystal technique was modified. A new signal analysis and image processing system were developed with the goal of improving the results obtained by this technique.

For the measurements on the platforms, a new measurement technique based on the use of a thin electrical heater-foil was developed. The innovation of this technique comes from the fact that it can be applied on complex geometries for which inhomogeneous heat flux is produced (curved surfaces, introduction of cooling holes). This novel measurement was first tested and validated on a simple geometry consisting of a film-cooled flat plate. The same technique was then applied to the film-cooled contoured platform and resulted in interesting heat transfer coefficient and film-cooling effectiveness distributions. The latter result was also compared to values obtained from another innovative measurement technique based on Pressure Sensitive Paint with Nitrogen injection.

The following summarizes the work and the major conclusions:

- The geometry of a new generation gas turbine nozzle guide vane has been carefully extracted to create a physical model for a linear cascade test facility. The resulting linear cascade was mounted on two discs for different inflow angle measurements. Experiments were carried out at engine representative flow conditions regarding the Ma and Re numbers except for the temperature levels. To respect the density ratio of the machine, CO₂ was used as coolant gas.
- The transient liquid crystal technique was used for the experiments. For this, a novel digital image acquisition and processing system for the transient liquid crystal technique have been developed. It allows performing experiments with

multiple cameras and is combined with a Digital Image Processing program on a computer providing powerful post-processing filtering, coordinate transformations and data reductions. It results in a higher spatial resolution and a better quality of the measurements.

- The criterion of the maximum allowable transient time has been analyzed in case of a semi-infinite or a finite wall model. Based on it, a new τ criterion, adapted for transient liquid crystal experiments has been defined.
- Aerodynamic measurements on the vane have been performed at nominal flow conditions with three different inflow angles: -12° , 0° and $+12^\circ$. Good flow periodicity was obtained and the surface Mach number distribution on the vane showed a non bi-dimensional behaviour due to the contouring of the walls. Loss measurements with a 5-Hole probe downstream from the cascade gave similar and quite low values for the three inflow configurations.
- Baseline heat transfer measurements have been performed for the same cases. The maximum values on the leading edge area occurred on a position different from the stagnation line. The maximum values are located on the suction side in the vicinity of the maximum flow acceleration. Heat transfer coefficient results were compared to laminar and turbulent Nusselt number correlations as well as to Texstan numerical simulations. They showed very good agreement.
- Film-cooled heat transfer measurements have been performed on the vane by using a regression of multiple experiments with different coolant gas temperatures. A new function better fitting the coolant gas temperature evolution was used for the data analysis. Six configurations were tested with different areas of opened holes. Despite variations of the amount of coolant injected per area, superposition of the results revealed close agreement. The film-cooled heat transfer coefficient h_f and the adiabatic film cooling effectiveness η results were used to estimate the film cooling performances of the vane. It showed a good overall coverage except for the leading edge area and for the last rows of cooling holes on the pressure and suction sides. This is a consequence of using a unique plenum chamber, resulting in a pressure ratio that is too low at the leading edge and one that is too high for the last rows of holes on both sides of the vane airfoil.
- A novel transient liquid crystal measurement technique with electrical heater-foils has been developed for the film-cooled platform experiments. It has the

advantage of working for heater-foil applications with inhomogeneous heat flux distributions, which is the case for film-cooled surfaces of representative engine geometries. Tests have been carried out on a film-cooled flat plate for configurations with homogeneous and inhomogeneous heat-flux distributions. Results showed excellent agreement with numerical simulations and data from literature. In addition, an error analysis has verified the accuracy of this novel measurement technique, hence validating its application for the heat transfer measurements on the film-cooled contoured platforms.

- Baseline and film-cooled platform experiments were performed by using the novel transient liquid crystal measurement technique with electrical heater-foils. The result of the inhomogeneous heat-flux distribution generated by the foils have been compared to numerical simulations, which show very good agreement. The baseline heat transfer coefficient values h were of a similar distribution as those found in the literature for non-contoured platforms. The result of the film-cooled h_f heat transfer coefficient and the film cooling effectiveness η were used to estimate the film cooling performances of the platform. Results showed an improvement at the channel exit probably due to the fact that the vortices were pushed away from the platform by the film-cooling injection. A study on the secondary flows would be necessary to better understand the heat transfer distribution on the platform.
- Additional PSP experiments with N_2 injection were performed on the film-cooled platforms and gave very similar film cooling effectiveness results to those obtained by the novel transient technique.

Future work:

The results of this experimental work dedicated to film cooling and applied on a complex geometry were obtained thanks to the development of novel measurement techniques. These techniques now afford the opportunity to perform systematic tests on film-cooled contoured platforms configurations in order to gain further insight into the physics of the film cooling process. In addition, useful heat transfer information would be obtained by performing detailed studies of the secondary flows. The film cooling performances should also be related to the reduction of the aerodynamic losses for which more measurements are required.

Finally, the promising PSP measurement technique should be improved to be less sensitive to temperature variations.

8 REFERENCES

Baldauf, S., Schulz, A., Wittig, S. and Scheurlen, M., 1997

An Overall Correlation of Film Cooling Effectiveness from One Row of Holes
ASME 97-GT-79.

Bölcs, A., 1993

Turbomachines Thermiques, Vol 1
Laboratoire de Turbomachines et de Thermique Appliqué, DGM, EPF-Lausanne.

Burd, S.W., Kasetta, R.W., Simon, T.W., 1996

Measurements in Film Cooling Flows: Hole L/D and Turbulence Intensities Effects
ASME-96-WA/HT-7.

Burd, S.W., Simon, T.W., 2000

Effect of Slot Bleed Injection Over a Contoured Endwall on Nozzle Guide Vane Cooling Performance: Part II- Thermal Measurements
ASME GT-200.

Carslaw, H.S. and Jaeger, J.C., 1992

Conduction of Heat in Solids
Sec. Ed., Oxford Science Publications, Clarendon Press, Oxford, UK.

Chyu, M.K., 2000

Heat Transfer near Turbine Nozzle Endwall
Heat Transfer in Gas Turbine Systems
Annals of the New York Academy of Sciences Vol 934, pp. 27-36.

Cohen, H., Rogers, GFC., Saravanamuttoo, HIH., 1996

Gas Turbine Theory, 4th edition
Longman Group Limited, England.

Crawford, M.E., 1986

Simulation codes for calculation of heat transfer to convectively cooled turbine blades VKI-LS, Convective heat transfer and film cooling in turbomachinery.

Day, C., Oldfield, M., Lock, G., Dancer, S., 1998

Efficiency measurements of an annular nozzle guide vane cascade with different film cooling geometries
ASME 98-GT-538.

Deich, M.E., Zaryankin, A.E., Phillipov, G.A., Zatsepin, M.F., 1960

Method of Increasing the Efficiency of Turbine Stages and Short Blades

Translation No. 2816, Associated Electrical Industries (Manchester) Ltd. April 1960.

Denton, J.D., 1993

Loss Mechanisms in Turbomachinery

ASME, Journal of Turbomachinery, **115**, pp. 621-656.

Dossena, V., Perdichizzi, A., Savini, M., 1998

The Influence of Endwall Contouring on the Performance of a Turbine Nozzle Guide Vane

ASME 98-GT-71.

Drost, U., 1998

An Experimental investigation of gas turbine airfoil aero-thermal film cooling performance

PhD Thesis 1817, EPFL, Switzerland.

Dullenkopf, K., Schulz, A., Wittig, S., 1991

The Effect of Incident Wake Conditions on the Mean Heat Transfer of an Airfoil

ASME, Journal of Turbomachinery, **113**, pp. 412-448.

Ekkad, S.V., Zapata, D., Han, J.C., 1997

Film effectiveness Over a Flat Surface with Air and Co₂ Film injection Through Compound Angle Holes Using a Transient Liquid Crystal Image Method

ASME, Journal of Turbomachinery, **119**, pp. 587-593.

Farmer, J.P., Seager, D.J., Liburdy, J.A., 1997

The Effect of Shaping Inclined Slots on Film Cooling Effectiveness and Heat Transfer Coefficient

ASME 97-GT-339.

Friedrichs, S., Hodson, H.P., Dawes, W.N., 1998

The Design of an Improved Endwall Film-cooling Configuration

ASME 98-GT-483.

Goldstein, R.J., 1971

Film Cooling. In Advances in Heat Transfer

Irvine T.F. and J.P. Hartnett Eds. Academic Press, New York, **7**, pp. 321-379.

Goldstein, R.J., Spores, R.A., 1988

Turbulent Transport on the Endwall in the Region Between Adjacent Turbine Blades

ASME J. of Heat Transfer, **110**, pp. 862-869.

Graf, A., 2001

Theoretical Consideration about the Heat Transfer on a Heated Plate with Film Cooling

EPFL-DGM-LTT, internal report LTT-01-09.

Gritsch, M., Schultz, A., Wittig, S., 1998

Discharge Coefficient Measurements of Film Cooling Holes with Expanded Exits

ASME J. of Turbomachinery, **120**, pp. 557-563.

Häring, M., 1994

Experimentelle Untersuchung Der Örtlichen Wärmeübergangszahl an Gansturbinschaufeln Anhand Der Sublimationstechnik im Kompressiblen Strömungsbereich

PhD Thesis 1291, EPFL, Switzerland.

Han, J.C., Dutta, S., Ekkad, S.V., 2000

Gas Turbine Heat Transfer and Cooling Technology

Taylor & Francis, London.

Harasgama, S.P., Burthorn, C.D., 1992

Film Cooling Research on the Endwall of a Turbine Nozzle Guide Vane in a Short Duration Annular Cascade Part 1: Experimental Technique and Results

ASME, Journal of Turbomachinery, **114**, pp. 741-746.

Harvey, N.W., Wang, Z., Ireland, P.T. & Jones, T.V., 1990

Secondary Flows in Turbomachines

AGARD CP469, Jerusalem.

Ireland, P.T., Jones, T.V., 2000

Liquid crystal measurements of heat transfer and surface shear stress

Meas. Sci. Technol., **11**, pp. 969-985.

Isaacson, E., Keller, H.B., 1966

Analysis of Numerical Methods

Dover Publications.

Jähne, B., 1993

Digital Image Processing

Springer-Verlag, London.

Kays, W.M., Crawford, M.E., 1993

Convective Heat and Mass Transfer

McGraw Hill, New York.

Kopper F.C., Milano, R., Vanco, M., 1981

Experimental Investigation of Endwall Profiling in a Turbine Vane Cascade
AIAA Journal, **19** no.8, pp. 1020-1040.

Kline, S.J., McClintock, F.A., 1953

Describing uncertainties in single-sample experiments
Journal of Mechanical Engineering, January 1953, pp. 3-8.

Kunt, M. 1993

Traitement numérique des images
Presse Polytechniques et Universitaires Romandes, Lausanne.

Leontiev, A.I., 1999

Heat and Mass Transfer Problems for Film Cooling
ASME J. of Heat Transfer, **121**, pp. 509-527.

Reiss, H., 2000

Experimental study on film cooling of gas turbine airfoils using shaped holes
PhD Thesis 2209, EPFL, Switzerland.

Seager, D.J., Liburdy, J.A., 1997

Experimental Investigation of the Effects of Compound-Angle Holes on Film Cooling Effectiveness and Heat Transfer Performance Using a Transient Liquid Crystal Thermometry Technique

Optical Technology in Fluid, Thermal and Combustion Flow III, SPIE, 3172, pp. 173-182.

Schultz, D.L., Jones, T.V., 1973

Heat transfer measurements in short duration hypersonic facilities
NATO Advisory Group Aeronautical RD AGARDOGRAPH, Vol. 165.

Steiner, P., 2000

Application of the Pressure Sensitive Paint Technique to The Turbomachinery Environment

PhD Thesis 2297, EPFL, Switzerland.

Takeishi, K.I., Aoki, S., 2000

Contribution of Heat Transfer to Turbine Blades and Vanes for High Temperature Industrial Gas Turbines, Part1: Film Cooling

Heat Transfer in Gas Turbine Systems

Annals of the New York Academy of Sciences Vol 934, pp. 305-312.

Theuwissen, A.J.P., 1995

Solid-State Imaging with Charge-Coupled Devices
Kluwer Academic Publishers Dordrecht, NL.

Turnbull, W.N., Oosthuizen, P.H., 1999

A New Experimental Technique for Measuring Surface Heat Transfer Coefficients Using Uncalibrated Liquid Crystals
HTD-Vol. 364-4, Proceedings of the ASME Heat Transfer Division, **4**, pp. 121-126.

Vogel, G., Weigand, B., 2001

A New Evaluation Method for Transient Liquid Crystal Experiments
NHTC01-1511, 35th ASME National Heat Transfer Conference, Anaheim, USA.

Vogel, G., Bölcs, A., 2000

A Novel Digital Image Processing System for the Transient Liquid Crystal Technique applied for Heat transfer and Film Cooling Measurements
Heat Transfer in Gas Turbine Systems
Annals of the New York Academy of Sciences Vol 934, pp. 297-304.

Vogel, G., 1999

DIPS Report, Digital Image Processing System for liquid crystal measurements (without cooling) Manual
Internal Report LTT-99-08.

Vogel, G., 1998

5 Hole Probe: Calibration, Acquisition and Data reduction under LabView
Internal Report LTT-98-12.

Von Wolfersdorf, J., Hoecker, R., Sattelmayer, T., 1993

A Hybrid Transient Step-Heating Heat Transfer Measurement Technique Using Heater Foils and Liquid-Crystal Thermography
ASME J. of Heat Transfer, **115**, pp. 319-324.

Wedlake, E.T., Brooks, A.J., Harasgama, S.P., 1989

Aerodynamic and Heat Transfer Measurements on a Transonic Nozzle guide Vane
ASME Journal of Turbomachinery, **111**, pp. 36-42.

Wiedner, B.G. and Camci, C., 1996

Determination of Convective Heat Flux on Steady-State Heat Transfer Surface With Arbitrarily Specified Boundaries
Journal of Heat Transfer, **118**, pp. 850-856.

Zhang, L.J., Jaiswal, R.S., 2001

Turbine Nozzle Endwall Film Cooling Study Using Pressure-Sensitive Paint
ASME, Journal of Turbomachinery, **123**, pp. 730-738.

APPENDIX A : STEP HEATING, BASELINE CASE, FINITE MODEL

Consideration is given to the one dimensional, unsteady heat conduction in a material of finite thickness. The material exchanges heat by convection on both sides. The heat conduction problem for the material is described by the following equations:

$$\rho c \frac{\partial T}{\partial t} = \frac{\partial}{\partial x} \left(k \frac{\partial T}{\partial x} \right) \quad (\text{a.1})$$

with the boundary conditions:

$$\begin{aligned} t = 0: \quad T(x) &= T_0 \\ x = 0: \quad h_g (T_g - T(x=0)) + k \frac{\partial T}{\partial x} \Big|_{x=0} &= 0 \\ x = \delta: \quad h_c (T_c - T(x=\delta)) + k \frac{\partial T}{\partial x} \Big|_{x=\delta} &= 0 \end{aligned} \quad (\text{a.2})$$

In case of a Perspex wall, the properties of the solid can be assumed to be constant. If one introduces now the following dimensionless quantities into (a.1) and (a.2):

$$\Theta = \frac{T_g - T}{T_g - T_0}, \quad \alpha = \frac{k}{\rho c}, \quad \tau = \frac{\alpha t}{\delta^2}, \quad \tilde{x} = \frac{x}{\delta} \quad (\text{a.3})$$

one obtains these equations in dimensionless form:

$$\frac{\partial \Theta}{\partial \tau} = \frac{\partial^2 \Theta}{\partial \tilde{x}^2} \quad (\text{a.4})$$

$$\begin{aligned} t = 0: \quad \Theta &= 1 \\ \tilde{x} = 0: \quad Bi_g \Theta(0, \tau) - \frac{\partial \Theta}{\partial \tilde{x}} \Big|_{\tilde{x}=0} &= 0 \\ \tilde{x} = 1: \quad Bi_c (\Theta(0, \tau) - \Theta_c) + \frac{\partial \Theta}{\partial \tilde{x}} \Big|_{\tilde{x}=1} &= 0 \end{aligned} \quad (\text{a.5})$$

with the following abbreviations:

$$Bi_g = \frac{h_g \delta}{k}, \quad Bi_c = \frac{h_c \delta}{k}, \quad \Theta_c = \frac{T_c - T_g}{T_0 - T_g} \quad (\text{a.6})$$

The solution of (a.4) can be derived by splitting the temperature distribution into two individual parts:

$$\Theta = \Theta_s + \Theta_T \quad (\text{a.7})$$

where Θ_s indicates the steady-state solution of the problem. The second part in equation (a.7) indicates the transient behaviour of the temperature field. The steady-state solution is given by:

$$\Theta_s = \Theta_c \frac{Bi_c (1 + Bi_g \tilde{x})}{Bi_g (1 + Bi_c) + Bi_c} \quad (\text{a.8})$$

The transient part Θ_T of the temperature field can be obtained by the method of separation of variables. This results in the following expression for Θ_T :

$$\Theta_T(\tilde{x}, \tau) = \sum_{n=1}^{\infty} C_n \left[\cos(\beta_n \tilde{x}) + \frac{Bi_g}{\beta_n} \sin(\beta_n \tilde{x}) \right] \exp(-\beta_n^2 \tau) \quad (\text{a.9})$$

where the eigenvalues β_n of the problem have to be obtained from the following transcendental equation:

$$(Bi_c + Bi_g) \cos(\beta_n) + \left(\frac{Bi_c Bi_g}{\beta_n} - \beta_n \right) = 0 \quad n = 1, 2, \dots \quad (\text{a.10})$$

The constants C_n in (a.9) are given by:

$$C_n = \frac{A \left\{ \frac{\sin(\beta_n)}{\beta_n} + \frac{Bi_g}{\beta_n^2} (1 - \cos(\beta_n)) \right\} + B \left\{ \frac{\cos(\beta_n)}{\beta_n^2} - \frac{1}{\beta_n^2} + \frac{\sin(\beta_n)}{\beta_n} + \frac{Bi_g}{\beta_n^2} \left(\frac{\sin(\beta_n)}{\beta_n} - \cos(\beta_n) \right) \right\}}{\frac{1}{2} \left(1 + \left(\frac{Bi_g}{\beta_n} \right)^2 \right) + \frac{\sin(2\beta_n)}{4\beta_n} \left(1 - \left(\frac{Bi_g}{\beta_n} \right)^2 \right) + \frac{Bi_g}{\beta_n^2} \sin^2(\beta_n)} \quad (\text{a.11})$$

with the abbreviations:

$$A = 1 - \frac{\Theta_c Bi_c}{Bi_g (1 + Bi_c) + Bi_c} \quad (\text{a.12})$$

$$B = - \frac{\Theta_c Bi_c Bi_g}{Bi_g (1 + Bi_c) + Bi_c} = Bi_g (A - 1)$$

The complete solution of the problem is finally given by:

$$\Theta(\tilde{x}, \tau) = \frac{\Theta_c Bi_c (1 + Bi_g \tilde{x})}{Bi_g (1 + Bi_c) + Bi_c} + \sum_{n=1}^{\infty} C_n \left[\cos(\beta_n \tilde{x}) + \frac{Bi_g}{\beta_n} \sin(\beta_n \tilde{x}) \right] \exp(-\beta_n^2 \tau) \quad (\text{a.13})$$

For the simple case, where the heat transfer coefficients for the coolant and the hot gas side are equal ($Bi_c = Bi_g$), the above given equations simplify to expressions given by Carslaw and Jaeger (1992).

Dimensionless wall surface temperature of the main flow side is then given by:

$$\Theta(\tilde{x} = 0, \tau) = \Theta_{wall} = \frac{\Theta_c Bi_c}{Bi_g (1 + Bi_c) + Bi_c} + \sum_{n=1}^{\infty} C_n \exp(-\beta_n^2 \tau) \quad (\text{a.14})$$

and with the transient signal of the liquid crystals applied on the surface, the solution is given for:

$$\Theta_{wall} - \Theta_{LC} = 0 \quad (\text{a.15})$$

The unknown Bi_g is then finally obtained by an iterative process, such as a simple bisection method. However as Bi_g changes at each step of the iteration, new eigenvalues have to be recalculated. To reduce time calculation a pre-calculation of the first ten eigenvalues is required.

APPENDIX B : STEP HEATING GENERATED BY RAPID INSERTION, BASELINE CASE, SEMI-INFINITE MODEL

In the baseline case, the heat transfer coefficient, in a two-temperature convection situation is defined as follow:

$$q = h(T_g - T_w) \quad (b.1)$$

Using the theory of one-dimensional transient conduction into a semi-infinite solid model, the driving equation is given by:

$$\rho c \frac{\partial T}{\partial t} = \frac{\partial}{\partial x} \left(k \frac{\partial T}{\partial x} \right) \quad (b.2)$$

with the initial and boundary conditions:

$$\begin{aligned} T(x, 0) &= T_0 \\ \lim_{x \rightarrow \infty} T(x, t) &= T_0 \end{aligned} \quad (b.3)$$

as well as convective boundary condition on the wall surface:

$$\left[-k \frac{\partial T}{\partial x} \right]_{x=0} = h(T_g - T_w) \quad (b.4)$$

For incompressible flow, the gas temperature T_g is the total temperature of the main flow. For compressible flow ($Ma > 0.3$), the recovery temperature is given by:

$$T_r = T + r_0 (\text{Pr}) \frac{u^2}{2c_p} \quad (b.5)$$

with the recovery factor $r_0 = \text{Pr}^{1/2}$ for laminar flow, and $r_0 = \text{Pr}^{1/3}$ for turbulent flow (valid for $0 < Ma < 6$ and $0.5 < \text{Pr} < 5$).

The solution for the surface temperature T_w is then (Carslaw and Jaeger, 1992):

$$\frac{T_w - T_0}{T_g - T_0} = \left[1 - \exp \left(\frac{h\sqrt{t}}{\sqrt{\rho c_p k}} \right)^2 \text{erfc} \left(\frac{h\sqrt{t}}{\sqrt{\rho c_p k}} \right) \right] \quad (b.6)$$

and with the transient signal of the liquid crystals applied on the surface, the solution is given with the t_{LC} transient time detection by:

$$T_w - T_{LC} = 0 \quad (b.7)$$

The unknown h is then obtained by an iterative process on equation (b.7), such as a simple bisection method.

The graphs below shows the evolution of the wall surface temperature, T_w during a transient experiment for an initial model temperature, T_0 and a total gas temperature, T_{tg} , for a typical local heat transfer coefficient.

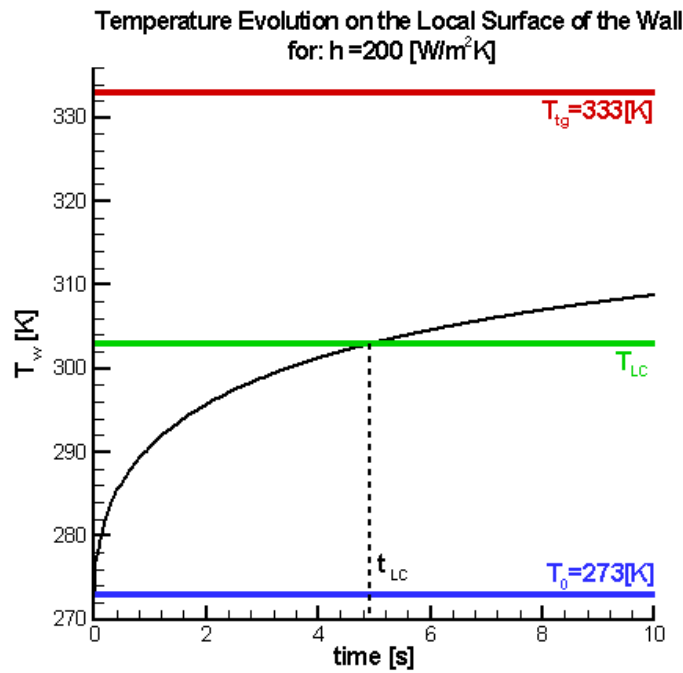


Figure b-1: Typical Wall Temperature Evolution of a Transient Liquid Crystal Experiment

APPENDIX C : STEP HEATING GENERATED BY RAPID INSERTION, FILM-COOLED CASE, SEMI-INFINITE MODEL

By analogy to the baseline case, the local heat flux onto a film-cooled surface can be written as follow:

$$q = h_f(T_{aw} - T_w) \quad (c.1)$$

where T_{aw} (called the adiabatic wall temperature) is the representative gas temperature at the wall. It can be put in dimensionless form by introducing the film cooling adiabatic wall effectiveness as:

$$\eta = \frac{T_{aw} - T_{tg}}{T_{tc} - T_{tg}} \quad (c.2)$$

The data analysis is based on the theory of one-dimensional heat conduction into a semi-infinite solid model. The governing differential equation for the temperature evolution of the solid is given by:

$$k \frac{\partial^2 T}{\partial x^2} = \rho c_p \frac{\partial T}{\partial t} \quad (c.3)$$

where k , ρ and c_p are the physical properties of the solid model.

The initial and boundary conditions on the solid side are given by:

$$T(x, 0) = T_0 \quad (c.4)$$

$$\lim_{x \rightarrow \infty} T(x, t) = T_0 \quad (c.5)$$

where (c.5) is valid only if the maximum transient measurement time is respecting the following criteria (Vogel and Weigand, 2001):

$$t_{\max} < \frac{\delta^2}{4\alpha} \quad (c.6)$$

At the physical model surface, the convective boundary condition is given by:

$$-k \left. \frac{\partial T}{\partial x} \right|_{x=0} = h_f (T_{aw} - T(x, t)) \Big|_{x=0} \quad (c.7)$$

Due to internal heat exchange with the preconditioned model, the coolant gas temperature injected during the transient experiment is not constant. This is accounted for by introducing a time dependent function for T_{tc} :

$$T_{ic}(t) = a e^{bt} + ct + d\sqrt{t} \quad (c.8)$$

where a, b, c and d are constants fitting the measured temperature evolution. This type of function is representative of the evolution obtained during the measurements. Note that it is also possible to use a more general power series function (Drost 1998).

The analytical solution for the heat conduction equation under the previous assumptions can be carried out by using the Laplace transform, yielding the surface ($x=0$) temperature evolution as:

$$T_w(h_f, \eta) = A(h_f) + \eta B(h_f) \quad (c.9)$$

where for $b > 0$:

$$A(h_f) = T_0 + (T_{rg} - T_0) \left[1 - e^{\beta^2} \operatorname{erfc}(\beta) \right] \quad (c.10)$$

$$B(h_f) = -T_{tg} \left[1 - e^{\beta^2} \operatorname{erfc}(\beta) \right] + \frac{h_f}{k} \left[\frac{a \cdot e^{b \cdot t}}{2} \left\{ \frac{\sqrt{\alpha}}{\frac{h_f}{k} \sqrt{\alpha} + \sqrt{b}} \operatorname{erfc}(-\sqrt{b \cdot t}) + \frac{\sqrt{\alpha}}{\frac{h_f}{k} \sqrt{\alpha} - \sqrt{b}} \operatorname{erfc}(\sqrt{b \cdot t}) \right\} - \frac{\alpha a}{\frac{h_f}{k} \alpha - \frac{kb}{h_f}} e^{\beta^2} \operatorname{erfc}(\beta) \right] - \frac{h_f}{k} \left[\frac{c}{\alpha \left(\frac{h_f}{k} \right)^3} \left(e^{\beta^2} \operatorname{erfc}(\beta) - \sum_{r=0}^{\infty} \frac{(-\beta)^r}{\Gamma\left(\frac{r}{2} + 1\right)} \right) \right] + \frac{h_f}{k} \left[\frac{d \sqrt{\pi}}{2 \sqrt{\alpha} \left(\frac{h_f}{k} \right)^2} \left(e^{\beta^2} \operatorname{erfc}(\beta) - \sum_{r=0}^{\infty} \frac{(-\beta)^r}{\Gamma\left(\frac{r}{2} + 1\right)} \right) \right] \quad (c.11)$$

$$\text{and } \beta = \left(\frac{h_f}{k} \right)^2 \alpha t$$

Γ is the gamma function and erfc is the complementary error function.

When $b < 0$ the term of $B(h_f)$ in {} is expressed as follows:

$$\left\{ \frac{\sqrt{\alpha}}{\frac{h_f}{k} \sqrt{\alpha} + \sqrt{b}} \operatorname{erfc}(-\sqrt{b t}) + \frac{\sqrt{\alpha}}{\frac{h_f}{k} \sqrt{\alpha} - \sqrt{b}} \operatorname{erfc}(\sqrt{b t}) \right\} = \left\{ \frac{2 \sqrt{\alpha}}{\left(\frac{h_f}{k} \right)^2 \alpha + b} \left(\frac{h_f}{k} \sqrt{\alpha} + 2 \sqrt{\frac{-b}{\pi}} \int_0^{\sqrt{-b t}} e^{-t^2} dt \right) \right\} \quad (c.12)$$

The two unknowns h_f and η present in equation (c.9) are then solved by a multiple-regression analysis applied to typically nine to ten different transient experiments with identical aerodynamic and thermal conditions except for the coolant temperature.

The graphs below show the typical multiple experiments for different coolant gas temperature T_{tc} evolution and the resulting wall temperature T_w .

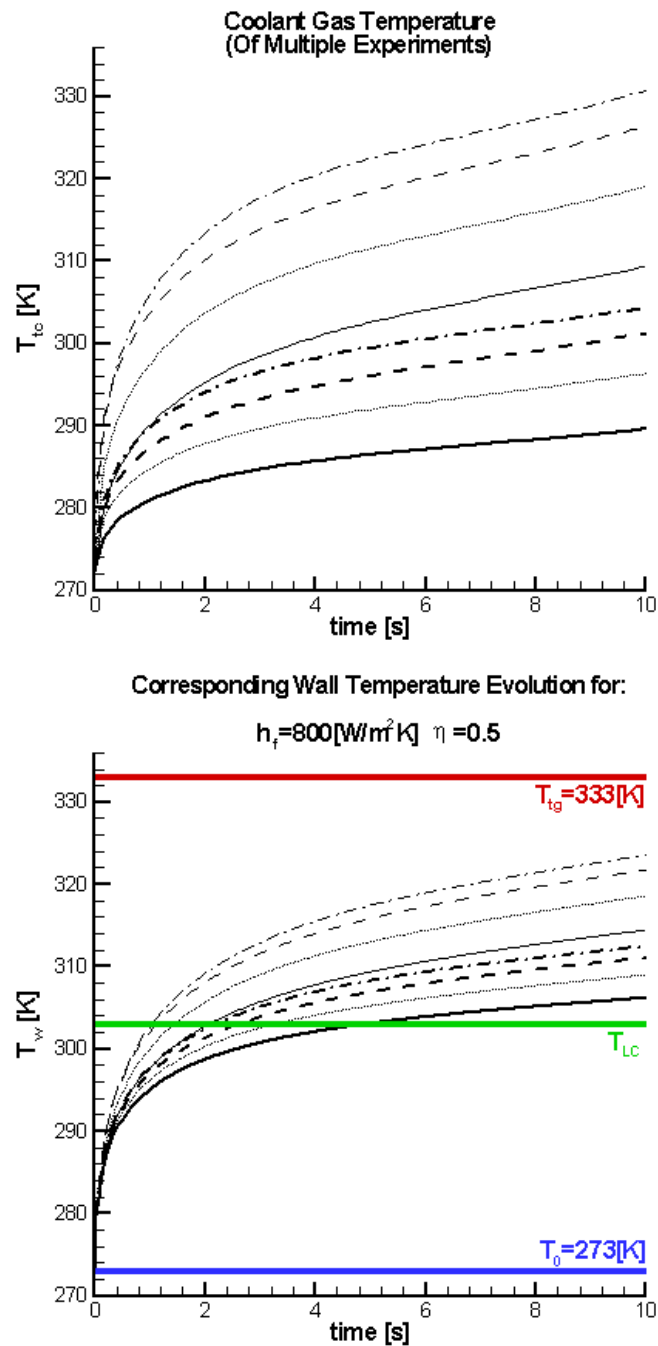


Figure c-1: Multiple T_{tc} Experiments and the Resulting T_w

APPENDIX D : STEP HEATING GENERATED BY HEATER FOIL, BASELINE AND FILM-COOLED CASES, SEMI-INFINITE MODEL

Figure 5-1 gives an overview of the physical model. A coolant fluid is injected into the main flow of gas over a flat plate. The latter is covered by a thin heater foil. At $t=0$, the plate is suddenly exposed to a heat flux through the foil, causing a temperature change in the wall of the plate. The evolution of the temperature field in the plate is assumed to be one-dimensional and the heat diffusion conduction equation in the plate in the absence of heat sources can be written as:

$$\frac{\partial T(x,t)}{\partial t} = \alpha \frac{\partial^2 T(x,t)}{\partial x^2} \quad \text{with} \quad \alpha = \frac{k}{\rho c_p} \quad (\text{d.1})$$

The heater-foil is supposed to be infinitely thin compared to δ . Its effect is thus taken into account in the boundary conditions and not in the heat conduction equation itself. This same assumption allows the plate to be considered homogenous.

The initial condition ($t=0$) is given by:

$$T(x,0) = T_0 \quad (\text{d.2})$$

whereas the boundary condition at the plate surface ($x=0$) is obtained using an energy balance:

$$q_w(t) = -k \frac{\partial T(0,t)}{\partial x} - h_f(T_{aw}(t) - T(0,t)) \quad (\text{d.3})$$

where $T_{aw}(t)$ stands for the adiabatic wall temperature. This value can be replaced by the adiabatic film cooling effectiveness, which is defined by:

$$\eta = \frac{T_{aw}(t) - T_{rg}}{T_{ic}(t) - T_{rg}} \quad (\text{d.4})$$

where T_{ig} and T_{rg} are determined using the flow conditions of the main stream of gas. Furthermore, it is assumed that the plate can be treated as half infinite (Vogel and Weigand 2001), i.e. the measurement time is so short that a heat pulse generated at the upper surface ($x=0$) will not reach the lower one ($x=\delta$). This can be expressed by the condition:

$$T(x \rightarrow \infty, t) = T_0 \quad (\text{d.5})$$

Solving equation (d.4) for $T_{aw}(t)$ and substituting it into equation (d.3) yields:

$$q_w(t) = -k \frac{\partial T(0,t)}{\partial x} + h_f(T(0,t) - T_{rg}) + h_f \eta (T_{ig} - T_{ic}(t)) \quad (d.6)$$

Equation (d.1) can be solved analytically under the conditions given by (d.2), (d.5) and (d.6) using the Laplace transform technique as described by Carslaw and Jaeger (1992). With $T^*(x,t) = T(x,t) - T_0$, the following transformed quantities are obtained:

$$\begin{cases} \hat{T}^*(x,s) = \sigma \exp\left(-\sqrt{\frac{s}{\alpha}}x\right) \\ \hat{q}_w(s) = -k \frac{\partial \hat{T}^*(0,s)}{\partial x} + h_f \hat{T}^*(0,s) + \frac{h_f(\eta T_{ig} + T_0 - T_{rg})}{s} - h_f \eta \hat{T}_{ic}(s) \end{cases} \quad (d.7)$$

where σ is an integration constant. In order to determine the latter, the following assumptions are made: at $t = 0$ a step in the surface heat flux is generated by the heater-foil and at the same time, a coolant gas is injected at a constant blowing ratio and with a given temperature evolution in time as defined below:

- The coolant temperature is a function of time since the cooling fluid is transferred from the plenum chamber to the test section, this transfer being accompanied by a heat loss. The temperature rise of the coolant is assumed to follow an expression as:

$$T_{ic}(t) = a \exp(bt) + ct + d\sqrt{t} \quad (d.8)$$

where a , b , c and d are constants fitted to the experimental profile of $T_{ic}(t)$.

- The surface heat flux follows a step function:

$$\begin{cases} q_w(t \leq 0) = 0 \\ q_w(t > 0) = Gq \end{cases} \quad (d.9)$$

where G stands for the known gain with respect to an unknown reference heat flux q .

Under the assumptions (d.8) and (d.9), the system of equations (d.7) has the following solution:

$$\hat{T}^*(x,s) = \left[\frac{Gq}{s} - \frac{h_f(\eta T_{ig} + T_0 - T_{rg})}{s} + h_f \eta \left(\frac{a}{s-b} + \frac{c}{s^2} + \frac{\sqrt{\pi d}}{2\sqrt{s^3}} \right) \right] \frac{\exp\left(-\sqrt{\frac{s}{\alpha}}x\right)}{h_f + k\sqrt{\frac{s}{\alpha}}} \quad (d.10)$$

The inverse Laplace transform of the expression above evaluated at $x=0$ yields for the wall temperature distribution:

$$T_w(t) = A + \eta B + q C \quad (d.11)$$

where:

$$A = T_0 + (T_{rg} - T_0)(1 - \exp(\beta^2) \operatorname{erfc}(\beta))$$

$$B = -T_{ig}(1 - \exp(\beta^2) \operatorname{erfc}(\beta)) + \frac{h_f}{k} \left[\frac{a \exp(bt)}{2} \mu - \frac{a \alpha}{\frac{h_f}{k} \alpha - \frac{kb}{h_f}} \exp(\beta^2) \operatorname{erfc}(\beta) \right] - \frac{h_f}{k} \left[\frac{c}{\alpha \left(\frac{h_f}{k} \right)^3} \left(\exp(\beta^2) \operatorname{erfc}(\beta) - \sum_{r=0}^2 \frac{(-\beta)^r}{\Gamma\left(\frac{r}{2} + 1\right)} \right) - \frac{d \sqrt{\pi}}{2 \sqrt{\alpha} \left(\frac{h_f}{k} \right)^2} \left(\exp(\beta^2) \operatorname{erfc}(\beta) - \sum_{r=0}^1 \frac{(-\beta)^r}{\Gamma\left(\frac{r}{2} + 1\right)} \right) \right]$$

$$C = \frac{G}{h_f} (1 - \exp(\beta^2) \operatorname{erfc}(\beta)) \quad (d.12)$$

with $\beta^2 = \alpha \left(\frac{h_f}{k} \right)^2 t \neq bt$ and:

$$\mu = \begin{cases} \frac{\sqrt{\alpha}}{\frac{h_f}{k} \sqrt{\alpha} + \sqrt{b}} \operatorname{erfc}(-\sqrt{bt}) + \frac{\sqrt{\alpha}}{\frac{h_f}{k} \sqrt{\alpha} - \sqrt{b}} \operatorname{erfc}(\sqrt{bt}) & \text{when } b \geq 0 \\ \frac{2\sqrt{\alpha}}{\left(\frac{h_f}{k} \right)^2 \alpha + b} \left(\frac{h_f}{k} \sqrt{\alpha} + 2\sqrt{\frac{-b}{\pi}} \left(\int_0^{\sqrt{-bt}} \exp(t^2) dt \right) \right) & \text{when } b < 0 \end{cases} \quad (d.13)$$

When considering the case of no film cooling (i.e. $\eta=0$) and a constant heat flux, the equations above reduce to the expression given by Von Wolfersdorf et al. (1993).

From the experiments, all parameters in equation (d.11) are assumed to be known *a priori* or measured except for h_f , η and q . These unknown quantities are determined below by a non-linear least-square regression using the transient experimental data. The latter includes temperature-time data pairs which are given by the coating of narrow-band liquid crystals applied on the plate and can be written as $(T_{LC}^i, t_{LC}^i)_{i=1}^N$ where i indexes the $N \geq 3$ independent experiments such that:

$$T_w(t_{LC}^i) = T_{LC}^i, \quad \forall i = 1, \dots, N \quad (d.14)$$

The above holds locally since the value of q is inhomogeneous across the surface of the plate as it depends upon the influence of the cooling holes and upon the possible variation in thickness of the heater-foil. For $N=3$, equation (d.14) yields exactly a solution triplet, if the latter exists. However, for $N>3$, the problem is over-defined and an optimal solution, if it exists, has to be sought. This solution should fit best all the N equations together, without necessarily satisfying each of them exactly. The above problem thus reduces to minimizing the following error function:

$$\varepsilon = \frac{1}{2} \left\| \vec{T}_w(t_{LC}) - \vec{T}_{LC} \right\|^2 = \frac{1}{2} \left\| \vec{A} + \eta \vec{B} + q \vec{C} - \vec{T}_{LC} \right\|^2 \quad (\text{d.15})$$

where each component of a vector corresponds to a distinct experiment and where $\|\vec{x}\|^2 = \langle \vec{x} | \vec{x} \rangle$, $\langle \cdot | \cdot \rangle$ being the Euclidean scalar product for $\vec{x} \in \mathbb{R}^N$. The above expression is minimal when:

$$\vec{\nabla} \varepsilon = 0 \Rightarrow \frac{\partial \varepsilon}{\partial \eta} = 0, \quad \frac{\partial \varepsilon}{\partial q} = 0, \quad \frac{\partial \varepsilon}{\partial h_f} = 0 \quad (\text{d.16})$$

which is a necessary but non-sufficient condition.

In the context of (d.11), the above three-parameter optimization process may be reduced to a one-parameter one. For this, η is expressed as a function of the two remaining unknowns as:

$$\frac{\partial \varepsilon}{\partial \eta} = 0 \Rightarrow \eta(h_f, q) = \frac{\langle \vec{T}_{LC} - q \vec{C} - \vec{A} | \vec{B} \rangle}{\|\vec{B}\|^2} \quad (\text{d.17})$$

Subsequently q is determined with respect to h_f as follows:

$$\frac{\partial \varepsilon}{\partial q} = 0 \Rightarrow q(h_f) = \frac{\left\langle \vec{T}_{LC} - \vec{A} - \frac{\langle \vec{T}_{LC} - \vec{A} | \vec{B} \rangle}{\|\vec{B}\|^2} \vec{B} \mid \vec{\omega} \right\rangle}{\|\vec{\omega}\|^2} \quad (\text{d.18})$$

$$\text{where } \vec{\omega} = \vec{C} - \frac{\langle \vec{C} | \vec{B} \rangle}{\|\vec{B}\|^2} \vec{B}$$

Equations (d.17) and (d.18) are inserted into (d.15), yielding an error function dependent solely upon h_f . This one-dimensional minimization may be done by classical methods of numerical analysis (Isaacson and Keller, 1966) such as the bisection rule. Once the optimal value of h_f is determined, the remaining unknowns are computed using equations (d.18) and (d.17) respectively.

The graphs on Figure d-1 show a typical multiple film-cooled experiments of three different heat flux ratios G with three different coolant gas temperature T_{tc} evolutions and the resulting wall temperature T_w .

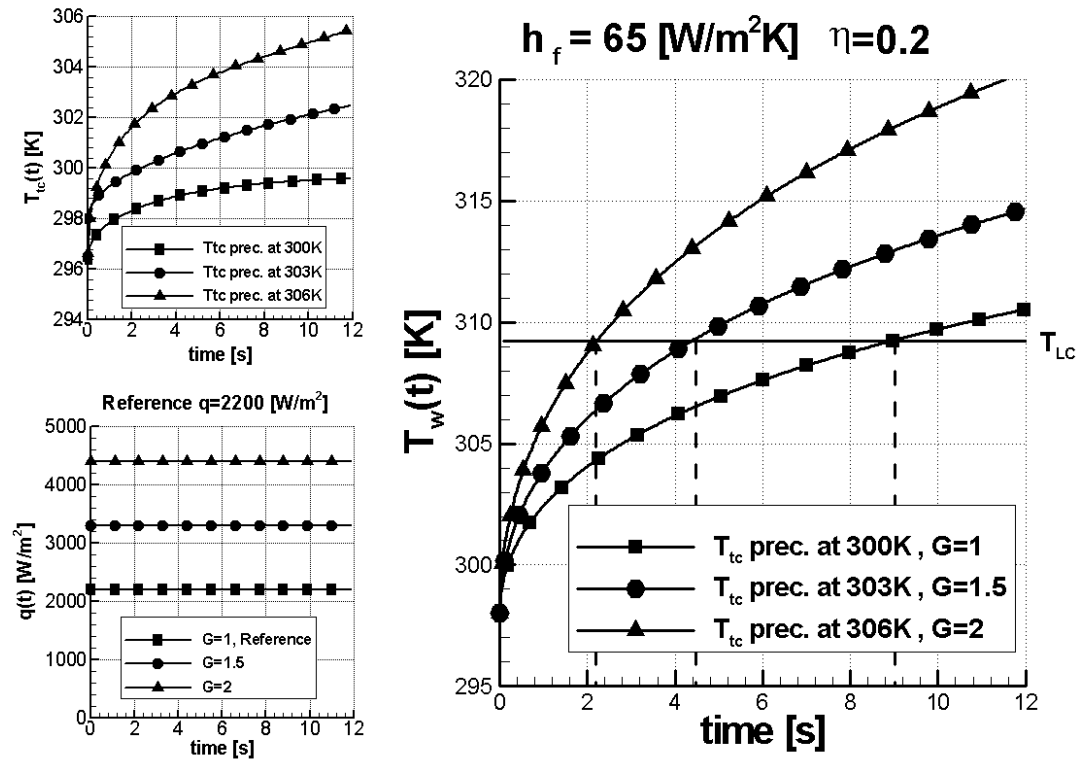


Figure d-1: Multiple G and T_{tc} Experiments and the Resulting T_w

APPENDIX E : PSP, ITERATIVE CORRECTION ON THE SURFACE TEMPERATURE DISTRIBUTION

PSP experiments are quite sensitive to temperature. For this reason, (PSP intensity I to pressure level p) coefficient calibrations $A(T)$, $B(T)$ and $C(T)$ cf. equation (6.1) are dependent on the surface temperature on which the painting is applied. A constant temperature level is often used as a first approximation. However such an approximation is not suited for surfaces with high flow acceleration, i.e., with significant temperature distribution. In this case, it is necessary to locally know within certain accuracy the temperature of the PSP. This can be given by a good approximation of the recovery temperature. The iterative method proposed here is based on a correlation relating the local recovery gas temperature to the local flow velocity. The latter, in turn, can be estimated by the static pressure distribution issued from the PSP.

The PSP equation (6.1) can be rewritten in a matrix form as follow:

$$p_s = p_{ref} \left(\left[1; \frac{I_{ref}}{I}; \left(\frac{I_{ref}}{I} \right)^2 \right] \cdot M_{calib} \begin{bmatrix} 1 \\ T_{rg} \\ T_{rg}^2 \end{bmatrix} \right) \quad (e.1)$$

Where (I_{ref}, p_{ref}) are reference values and M_{calib} the matrix of the calibration coefficients.

During the experiment the total flow conditions p_t and T_t are determined, and flow is considered as a perfect gas with the constant properties known.

Hence, for the first step of the iterative process:

Initial step:

$$T_0 = T_t$$

$$p_{s0} = p_{ref} \left(\left[1; \frac{I_{ref}}{I}; \left(\frac{I_{ref}}{I} \right)^2 \right] \cdot M_{calib} \begin{bmatrix} 1 \\ T_0 \\ T_0^2 \end{bmatrix} \right) \quad (e.2)$$

Then, for the iterative process with the step of the iteration given by i

Iterative process:

Velocity determination:

$$Ma_i = \left(\frac{2}{\kappa - 1} \left(\left(\frac{p_t}{p_{si}} \right)^{\frac{\kappa - 1}{\kappa}} - 1 \right) \right)^{1/2} \quad (e.3)$$

$$T_{si} = T_t \left(1 + \frac{\kappa - 1}{2} Ma_i^2 \right)^{-1} \quad (e.4)$$

$$a_i = \sqrt{\kappa R T_{si}} \quad (e.5)$$

$$v_i = Ma_i a_i$$

and with a recovery gas temperature estimated for a turbulent boundary layer:

$$T_{rgi} = T_{si} + \text{Pr}^{1/3} \frac{v_i^2}{2 c_p} \quad (e.6)$$

hence:

$$p_{si+1} = p_{ref} \left[\left[1; \frac{I_{ref}}{I}; \left(\frac{I_{ref}}{I} \right)^2 \right] \cdot M_{calib} \cdot \begin{bmatrix} 1 \\ T_{rgi} \\ T_{rgi}^2 \end{bmatrix} \right] \quad (e.7)$$

This process being convergent, the iteration is stopped when:

$$|p_{si+1} - p_{si}| < \Delta e \quad (e.8)$$

where Δe is the resolution factor of the convergence.

An important condition to respect is that the matrix of the calibration coefficients is defined for the range of the temperature levels used during the iterative process.

This was the case for the platform measurements for which a maximum of eight steps were required for any measured pixel on the surface with a $\Delta e = 1E-2$.

APPENDIX F : PSP TECHNIQUE WITH N₂ INJECTION FOR FILM-COOLING EFFECTIVENESS DETERMINATION

Film-cooling effectiveness can be obtained by the analysis of the partial pressure of O₂ in a case with air injection and in a case with N₂ injection (Zhang et al. 2001). Based on the O₂ concentration in the film C_{mix} , and on the concentration outside of the film C_{∞} the film-cooling effectiveness can be defined as follow (for incompressible flow):

$$\eta = 1 - \frac{C_{mix}}{C_{\infty}} \quad (f.1)$$

with:

$$C_{mix} = \frac{P_{O_2, N_2}}{P_{s, air}} = 0.21 \frac{P_{s, N_2}}{P_{s, air}} \quad (f.2)$$

$$C_{\infty} = 0.21$$

yielding:

$$\eta = 1 - \frac{P_{s, N_2}}{P_{s, air}} \quad (f.3)$$

In this case, the PSP experiment consists of four captured images; thus four intensities I were measured: I_{DK} for a dark image (no light, no flow), I_{ref} for a reference image (light, no flow), I_{air} for an air injection image and I_{N_2} for a N₂ injection image. For notation simplifications, considering that I_{ref} , I_{air} and I_{N_2} are intensities already corrected by the dark image. The data analysis of this PSP technique using N₂ injection for film-cooling effectiveness is then given as follow:

The case with air injection is first determined, with the same iteration method as described in Appendix E. It yields:

$$P_{s, air} = P_{ref} \left(\left[1; \frac{I_{ref}}{I_{air}}; \left(\frac{I_{ref}}{I_{air}} \right)^2 \right] \cdot M_{calib} \cdot \begin{bmatrix} 1 \\ T_{rg} \\ T_{rg}^2 \end{bmatrix} \right) \quad (f.4)$$

By using the same surface temperature, T_{rg} as the one determined in the case of air injection, it is not necessary to perform an iteration for the N₂ case. It directly yields:

$$p_{s,N_2} = p_{ref} \left(\left[1; \frac{I_{ref}}{I_{N_2}}; \left(\frac{I_{ref}}{I_{N_2}} \right)^2 \right] \cdot M_{calib} \cdot \begin{bmatrix} 1 \\ T_{rg} \\ T_{rg}^2 \end{bmatrix} \right) \quad (f.5)$$

Film-cooling effectiveness is finally given by injecting equations (f.4) and (f.5) into (f.3).

As the PSP is very sensitive to temperature variations, air or N₂ gas injection should preferably be made at the same temperature level as the mainstream temperature. Care has to be taken to have the same injected gas temperature of air and of N₂, as a difference of only 0.2K would conduct to a relative error on η of about 10%.

Curriculum Vitae

Name: Gregory Vogel
Date of Birth: 12th of June 1972
Place of Birth: Geneva, Switzerland
Nationality: Swiss & Dutch
Status: Single



EDUCATION:

1996-2002: EPFL-DGM-LTT,
Laboratoire de Thermique appliquée et de Turbomachines,
Thesis: "Experimental Study on a Heavy Film Cooled Nozzle
Guide Vane with Contoured Platforms".

1991-96: Swiss Federal Institute of Technology (EPF Lausanne),
Master of Mechanical Engineering,
Specialized in Fluid & Energetic,
Diploma Work: "Setup of a Micro Jet Engine Test Facility".

1987-91: Collège Claparède (Geneva),
Maturité Cantonale, type scientifique.

WORK EXPERIENCE:

1996-2002: Laboratoire de Thermique appliquée et de Turbomachines de
l'EPFL

- Development of transient liquid crystal measurement techniques and conception of a new test facility of film-cooled platforms for heat transfer measurements in collaboration with ALSTOM Power.
- Laboratory on a jet engine startup and its working principles.
- Laboratory on transient liquid crystal experiments.
- Invited lecturer in a post-graduate course in energy: "Introduction to gas turbines".

1988-94: Auxiliary work at the fire and rescue department in the city of Geneva. Responsible for the maintenance of breathing devices.

RELATED SKILLS:

Languages: French, English, Dutch, German.
Computers: LabViewTM, IDEAS, Fluent, Tecplot, Adobe Premère, Photoshop.
Technology: Turbomachines, Measurement Techniques, Data Analysis.
Interests: Member of the American Helicopter Society since 1993.